Ab initio Enhanced CALPHAD Modeling of Actinide Rich Metallic Nuclear Fuels

By:

谢玮 (Wei Xie)

A dissertation submitted in partial fulfillment of
the requirements for the degree of

Doctor of Philosophy
(Materials Science)
at the
UNIVERSITY OF WISCONSIN–MADISON
2014

Date of defense: November 25, 2014

MEMBERS OF THE THESIS COMMITTEE:

Dane Morgan, Professor, Materials Science and Engineering (Graduate Advisor)

Izabela Szlufarska, Professor, Materials Science and Engineering

Daniel Fredrickson, Assistant Professor, Chemistry

Donald Stone, Professor, Materials Science and Engineering

Sindo Kou, Professor, Materials Science and Engineering

Thesis Abstract

Metallic fuels are promising fuel candidates for Generation IV nuclear reactors currently under active research and development. The purpose of the researches in this thesis is to increase the understanding on the phase stability of U-Pu-Zr-MA (MA = Np, Am and Cm) alloy, which is the current basis for fast spectrum metallic fuel in a fully recycled closed fuel cycle. We focused on the Np-U-Zr system and its U-Zr, Np-Zr and Np-U binary and U, Np, Zr unary sub-systems and address two problems.

The first problem is to obtain accurate *ab initio* energetics for actinide systems due to challenges in modeling the *f*-electron many-body correlation and relativistic effects. We assessed density functional theory (DFT) in both its standard form and the so-called DFT plus Hubbard U (DFT + U) modification based on the generalized gradient approximation and established a consistent set of empirical U_{eff} parameter ranges for Np and U that can improve the calculated energetics for Np-U-Zr alloy and its sub-systems. We also determined quantitatively how much the calculated energetics are affected by spin-orbit coupling (SOC), a relativistic effect often neglected for lighter metals. The second problem is the lack of accurate thermodynamic models for Np-U-Zr due to limited experimental data. We mitigate the problem using *ab initio* predicted energetics to supplement existing experimental data and assist the thermodynamic modeling using the so-called *ab initio* enhanced CALculation of PHase Diagrams (CALPHAD) approach. Our work developed thermodynamic models for the U-Zr and Np-Zr systems that should be of good accuracy. For the Np-U and Np-U-Zr systems, we developed models that were restricted by limited experimental data available for these systems but

should also be acceptably accurate at the high temperatures at which metallic fuels are deployed in reactors.

Overall, understanding in the phase stability of Np-U-Zr and its subsystems acquired in the current thesis researches can help improve the design and use of metallic fuels. The *ab initio* approach and CALPHAD models established in this thesis should be applicable for studying additional properties and other related systems of metallic nuclear fuels.

Acknowledgements

Firstly, I would like to extend my sincerest gratitude to Dane Morgan for his wonderful advising and support in the past five years. In December 2009 when the financial crisis hitting the United States was still at its height and everyone's research proposal was rejected, Dane was very brave to accept me, who at that time with only a bachelor degree in polymer engineering knew nothing of solid state physics—having not even heard of the Drude model, to work with him on electronic structure calculations of actinides. I hope Dane finds this thesis worth his enormous time and efforts in the past years teaching me electronic structure calculations from the scratch.

I am also very grateful to Liqun Zhang for providing me the first formal scientific research opportunity in my life, training me to follow my curiosity and explore my interest with scientific methodology, and encouraging me to pursue an academic career.

Formal collaborations while working on this thesis with Chris Marianetti, Wei Xiong, Chao Shen, Chao Jiang, Chuan Zhang, Ying Yang and late Professor Y. Austin Chang are acknowledged. Suggestions of Daniel Fredrickson on this thesis are gratefully recognized.

I benefited very much from many individual suggestions and also general advising of Izabela Szlufarska over the years, for which I am deeply thankful.

Dane Morgan, Izabela Szlufarska, Daniel Fredrickson, Donald Stone, and Sindo Kou's service as the thesis committee is greatly appreciated.

I want to thank everyone whom I have worked with in my past and present research groups over the years, but here choose not to list any specific name so that I cannot miss anyone whom I cannot miss. I learned 80% of what I learned from you, and more

importantly, with you I know that when codes I write never really run, jobs I submit always crash, and calculations I do take forever to converge, I am not alone.

Words cannot describe how much I am thankful to Diana Rhodes for everything she has done over the years, so simply: Diana is the best non-academic colleague one can have.

由衷感谢我的母亲，岳父，岳母，外公，奶奶，姐姐和其他所有家人对我的支持和鼓励。

Finally, this thesis can never be possible without Minjing Tao. Minjing did everything she could to keep me motivated, sometimes even by sacrificing herself, for example, getting a PhD herself.

This research was funded by the US Department of Energy Office of Nuclear Energy's Nuclear Energy University Programs under Contract No. 00088978. We acknowledge computing time from Idaho National Laboratory's Center for Advanced Modeling and Simulation, TeraGrid resources provided by Texas Advanced Computing Center under Grant No. [TG-DMR090023], and High Performance Computing cluster hosted by Center for High Throughput Computing at University of Wisconsin-Madison. The uses of Thermal-Calc software from Thermo-Calc Software, Sweden, and Pandat software from CompuTherm LLC in Madison, WI are also acknowledged.

Table of Contents

Thesis Abstract .... **i**

Acknowledgements .... **iii**

Table of Contents .... **v**

List of Figures .... **xi**

List of Tables .... **xv**

1 General Introduction **1**

1.1 Background and Motivation 1

1.2 Challenges in Studying Metallic Nuclear Fuels 2

1.3 Thesis Objectives 4

1.4 Scientific Approach 5

1.5 Summary of Research Tasks 7

1.5.1 Ab initio Calculations 8

1.5.2 CALPHAD Modeling 9

1.6 Overview of Chapters 9

1.7 Publications and Author Contributions 10

1.7.1 Publications 10

1.7.2 Author Contributions 10

2 CALPHAD Modeling of the U-Zr System **13**

2.1 Chapter Abstract 13

2.2 Introduction 13

2.3 Literature Review 14

2.4 Thermodynamic Models 24

2.4.1 Disordered Solution Phases 24

2.4.2 Ordered Intermetallic Compound 25

2.5 *Ab initio* Calculations for the BCC and δ Phases 27

2.6 Results and Discussion 29

2.6.1 Phase Diagram and Phase Equilibria 29

2.6.2 Thermodynamic Properties 34

2.7 Conclusions 40

3 *Ab initio* calculations of the U and U-Zr systems 42

3.1 Chapter Abstract 42

3.2 Introduction 43

3.3 Computational Details 47

3.4 Results and Discussion 56

3.4.1 Energetics 56

3.4.2 Volume 65

3.4.3 Magnetic Moments 74

3.4.4 Electronic Structure 78

3.4.5 Theoretical Hubbard *U* for U and U-Zr 91

3.5 Conclusions 92

4 Additional validations of DFT + *U* on the U and U-Zr systems 95

4.1 Introduction 95

4.2 Choice of U_{eff} in DFT + *U* 96

4.3 Computational Details 98

4.4 Results and Discussion 99

4.4.1 γU and γ(U,Zr) 99

4.4.2 αU 116

4.4.3 The magnetic moments issue 118

4.5 Conclusions 120

5 CALPHAD Modeling and *Ab initio* Calculations of the Np and Np-Zr systems..122

5.1 Chapter Abstract 122

5.2 Introduction 123

5.3 Literature Review 124

5.3.1 Experimental Data on Np-Zr Phase Diagrams 124

5.3.2 Reported *Ab initio* Calculations and Thermodynamic Modeling of Np-Zr...127

5.4 Thermodynamic Models used in the CALHPAD modeling 127

5.4.1 Solution phase..128

5.4.2 Intermetallic Compounds..129

5.5 *Ab initio* Calculations 131

5.6 Results and Discussion 135

5.6.1 Low Temperature Stability of Pure Zr..136

5.6.2 Comparison of Calculated Phase Diagrams and Experimental Data.............138

5.6.3 Calculation of Thermodynamic Properties..139

5.7 Conclusions 147

6 CALPHAD Modeling and *Ab initio* Calculations of the Np-U System..................149

6.1 Chapter Abstract: 149

6.2 Introduction 150

6.3 Methodology 151

6.3.1 CALPHAD Methodology..151

6.3.2 *Ab initio* Methodology..155

6.4 Results and Discussion 159

6.4.1 CALPHAD Phase Diagram...159

6.4.2 Validation of *Ab initio* Methods on α(Np), β(Np), α(U), β(U) and γ(Np,U).161

6.4.3 *Ab initio* predictions for ζ phase 168

6.5 Conclusions 173

7 CALPHAD Modeling and *Ab initio* Calculations of the Np-U-Zr Systems 175

7.1 Chapter Abstract 175

7.2 Introduction 176

7.3 Methodology 179

7.3.1 CALPHAD Methodology 179

7.3.2 *Ab initio* Methodology 181

7.4 Model Validations 186

7.4.1 CALPHAD Model 186

7.4.2 *Ab initio* Method 190

7.5 Model Predictions 195

7.5.1 BCC Np-U-Zr solution behavior 196

7.5.2 BCC Np-U-Zr atomic volume and volume of mixing 200

7.5.3 Solidus and liquidus of Np-U-Zr 203

7.6 Conclusions 204

8 Concluding Remarks 207

8.1 Summary 207

8.2 Suggestions for Future Work 209

9 Appendix: Supplementary Material for Chapter 3 214

9.1 Evaluating Experimental Structural Data for U Metal 214

9.1.1 αU 215

9.1.2 βU 215

9.1.3 γU 216

9.2 Quasiharmonic Theory for the Zero-Point and Finite *T* Effects 217

9.3 Summary of Experimental Volumes for U, Zr Metals and U-Zr Alloys 220

10 References 222

List of Figures

Figure 1.1: *Ab initio* enhanced CALPHAD approach to phase stability prediction. 6
Figure 2.1. Comparison of phase diagram between experimental data [37, 42-44] and this work for temperatures above 1400 K. 15
Figure 2.2. Comparison of the solid phase diagram between experimental data [14, 42, 45-53] and thermodynamic descriptions [11, 40], (b) is the comparison among different CALPHAD modeling, (c) (d) (e) and (f) are magnified parts of (a). 17
Figure 2.3. Comparison of heat capacity of the U-Zr alloys between CALPHAD model-prediction [11, 40] and experimental data [45, 52, 53, 60]. (a) Summary of the experimental information provided by different research groups [45, 52, 53, 60], (b) Comparison for the U-13, 14 and 14.3 Zr alloys, the CALPHAD-type results are plotted for U-13.5Zr alloy; (c) comparison for the U-20Zr alloy; (d) comparison for the U-35, 41, and 61 Zr alloys. S denotes the unit for shifting the heat capacity in the plot to facilitate reading; (e) Comparison for the U-72 and 73Zr alloys, the CALPHAD-type results are plotted for U-72.5Zr alloy; (f) Comparison for the U-89 and 91Zr alloys, the CALPHAD-type results are plotted for U-90Zr alloy; (g) Comparison for pure U; (f) Comparison for pure Zr. 20
Figure 2.4. Comparison of activity of U in the δ phase between experimental results by Murakami *et al*. [61] and CALPHAD model-prediction in this work 22
Figure 2.5. Comparison of activity of U and Zr in the U-Zr alloys at different temperatures. Reference for U is the liquid phase, while for Zr is hcp α (Zr). Different colors indicate different temperatures for both symbols (experimental data) and curves (calculations). 23
Figure 2.6. Comparison of the excess entropy of mixing at 2200 K for the liquid phase among different thermodynamic modeling [11, 40]. 30
Figure 2.7. Model-predicted BCC miscibility gap of the U-Zr system according to different CALPHAD type modeling [11, 40] 33
Figure 2.8. Comparison of the enthalpy of formation of the γ (U,Zr) phase between *ab initio* calculations at 0 K and CALPHAD modeling at 298 K. SOC means Spin-Orbit Coupling 35
Figure 2.9. (a) Comparison of the enthalpy of formation for the δ phase among *ab initio* [66], CALPHAD [11, 40] and experimental data [62]. In CALPHAD modeling from the present work, case 1A is using the energy difference of (Zr) between α-hcp and δ structures as 1000 J/mol for model 1 $(Zr)_1(U,Zr)_2$, while case 1B is using 527.5 J/mol for model 1 $(Zr)_1(U,Zr)_2$. (b) Magnification of (a) from 98 to 100 at.% Zr. 36
Figure 3.1 Enthalpy of mixing for γ (U,Zr) calculated from DFT-noSOC with different degrees of structural relaxations. 53
Figure 3.2. Energetics for U metal: a) cohesive energy for α U; enthalpy of formation for b) β U and c) γ U. The vertical dash reference line is at U_{eff}=1.24 eV. Experimental cohesive energy of αU is from Ref. [136]; CALPHAD models are from Xiong *et al*. [33], Kurata[11], and Chevalier *et al*[40] which all use the same SGTE data for pure elements[69] and give the same enthalpy of formation for β U and γ U. 56
Figure 3.3. Enthalpy of formation for U-Zr alloy: a) α(U) (6.3 at.% Zr), b) β(U) (3.3 at.% Zr), c) δ (U,Zr) (66.7 at.% Zr) and d) α(Zr) (93.8 at.% Zr), The vertical dash reference line is at U_{eff}=1.24 eV. Experimental enthalpy of formation for δ(U,Zr) -0.04±0.11 eV/atom is from Nagarajan *et al.*[62]; the very large error bar is not plotted in c). CALPHAD models are from Xiong *et al.*[33], Kurata[11], and Chevalier *et al.*[40]. 59
Figure 3.4. RMS of enthalpy differences between *Ab initio* and CALPHAD for all solid phases of U metal and U-Zr alloy except αU and γ(U,Zr). DFT is at U_{eff}=0 eV while DFT + *U* is at $U_{\text{eff}} > 0$ eV. CALPHAD models are from Xiong *et al*. [33], Kurata[11], and Chevalier *et al.*[40]. See Table 3.3 for quantitative statistics 60
Figure 3.5. Enthalpy of mixing for γ (U,Zr). DFT results are from Landa *et al.*'s noSOC calculations[66]; CALPAHD models are from Xiong *et al.*[33], Kurata[11] and Chevalier *et al.*[40]. U_{eff} used for DFT + *U* is given in parentheses in the legend. 63

Figure 3.6 Volume for all solid phases of U metal and U-Zr alloy as a function of U_{eff}: a) αU; b) α(U) (6.3 at.% Zr); c) βU; d) β(U) (3.3 at.% Zr), e) γ U; f) γ (U,Zr) (6.3 at.% Zr); g) γ (U,Zr) (25.0 at.% Zr); h) γ (U,Zr) (50.0 at.% Zr); i) γ (U,Zr) (75.0 at.% Zr); j) γ (U,Zr) (93.8 at.% Zr); k) δ (U,Zr) (66.7 at.% Zr); and l) αZr (93.8 at.% Zr). The vertical dash reference line is at U_{eff}=1.24 eV. Experiments data are from those referenced in Table 3.4; no direct experimental data are found for b), d), f), j) and k). 72

Figure 3.7. Spin, orbital and total magnetic moments for all solid phases of U metal and U-Zr alloy as functions of U_{eff}: a) αU; b) α(U) (6.3 at.% Zr); c) βU; d) β(U) (3.3 at.% Zr), e) γ U; f) γ (U,Zr) (6.3 at.% Zr); g) γ (U,Zr) (25.0 at.% Zr); h) γ (U,Zr) (50.0 at.% Zr); i) γ (U,Zr) (75.0 at.% Zr); j) γ (U,Zr) (93.8 at.% Zr); k) δ (U,Zr) (66.7at.% Zr); and l) αZr (93.8 at.% Zr). The vertical dash reference line is at U_{eff}=1.24 eV. The unsmooth segment between 1.5 and 2.0 eV for γ (U,Zr) (75.0 at.% Zr) might be metastable solutions. 75

Figure 3.8. Band structure (left panel) and density of states (right panel) for α U. The respective experimental references are ARPES spectra from Opeil *et al.*[116] and UPS spectra from Opeil *et al.*[115] for α U(001) single crystal. All experimental spectra are plotted as blue circles, while DFT and DFT + *U* (U_{eff}=1.24 eV) calculated results are plotted as black and red curves, respectively; solid and dash line style distiguish noSOC and SOC. On the left, green arraws indicate two representative improvements of bands going from DFT to DFT + *U*. On the right, the positions of peaks from experiment, DFT and DFT + *U* are marked with blue, black and red arrows, respectively. Gray areas on the left and dash arrows on the right indicate spectra features from surfaces states that are not modeled in the calculations. Only the occupied part between -4.5 and 0 eV relative to Fermi level is shown. See FIG. 2 in Ref.[116] for an illutration of Brillouin zone and the special *k*-points used here. 78

Figure 3.9. Density of states for α U as a function of U_{eff}. The vertical dash reference line is Fermi level. Experimental reference is Baer and Lang's XPS and BIS spectra[151]. The full valence band, both occupied and unoccupied is shown. 84

Figure 3.10. Total, *d*- and *f*-orbital projected density of states for all solid phases of U, Zr metal and U-Zr alloy as functions of U_{eff}. The vertical dash reference line is Fermi level.The first column is calculated by DFT, the second, third and fourth by DFT + *U* at U_{eff}=1.24, 2.49, and 3.99 eV, respectively. Results from both noSOC (dash) and SOC (solid) are given. The highest unoccupied part of the valence band is missing for some systems due to limited number of bands included in the calculations. 87

Figure 3.11. Total *f*-orbital occupation for all solid phases of U metal and U-Zr alloy as a function of U_{eff}. Low and intermediate temperature phases α U, α (U), β U, β (U), α (Zr) and δ (U,Zr) are plotted in the left panel; high temperature phase γ U and γ (U,Zr) are in the right. Solid curves are from SOC calculations, while dash from noSOC. 89

Figure 4.1. γ(U,Zr)'s a) volume, b) volume expansion due to spin-orbit coupling (SOC), and c) volume of mixing. γU is one end member of γ(U,Zr) with 0 at.%Zr and β Zr is the other end member with 100 at.%Zr. SOC and noSOC denote calculations without and with SOC included, respectively. Volume expansion due to SOC is calculated as $(V_{\text{SOC}}\text{-}V_{\text{noSOC}})/V_{\text{noSOC}}$. Volume of mixing for γ(U,Zr) is defined as where *x* is Zr mole fraction. Experimental volume of mixing for Akabori *et al.*[14] and Basak *et al.* [162] is calculated by referencing to Lawson *et al.* for γU[80] and Heiming *et al.* for β Zr[83], while Huber and Ansari[126] is neglected due to its unrealistic convex curvature (see text for details on these choices). Estimated 0 K values are plotted here for the three experiments Lawson *et al.* [80], Akabori *et al.*[14], and Heiming *et al.* [83] that directly measured volumes at high temperatures where γ(U,Zr) is stable, while the original values are plotted for the other two experiments, Huber and Ansari[126] and Basak *et al.* [162] that measured quenched samples at room temperature. 104

Figure 4.2. Bulk modulus for a) α U and b) γ U as a function of U_{eff}. SOC and noSOC in the legend denote calculations without and with spin-orbit coupling (SOC) included, respectively. For α U, the two FPLMTO results are from Le Bihan *et al.* [144] and Söderlind[105], respectively while the experimental value extrapolated to 0 K is from Lawson and Ledbetter[172]. For γ U, the

referenced *ab initio* results are from Söderlind *et al.*[157] and the experiment values extrapolated to 0 K (see texts) is from Yoo *et al.*[166]. 112

Figure 5.1. Comparison of the phase diagram of Np-Zr between the CALPHAD modeling and experimental data [183-185]. (a) calculated phase diagram in this work and experimental data; (b) calculated phase diagram in the work by Bajaj *et al.* [182] and experimental data [183-185]; (c) magnified part of (a); (d) magnified part of (b). 124

Figure 5.2. The Hexagonal_C32 structure of the δ -NpZr phase. 129

Figure 5.3. Total energy for Zr metal as a function of volume. noSOC means that spin-orbit coupling effect was not considered in the *ab initio* calculations, while SOC means the spin-orbit coupling was taken into account. 137

Figure 5.4. *Ab initio* energetics for Np metal at 0 K: (a) cohesive energy for α Np, and enthalpy of formation for (b) β Np and (c) γ Np. The data from SGTE and experiments are considered at 298 K. Experimental data in (a) are taken from Ref. [136]. 140

Figure 5.5. Comparison of the enthalpy of formation for Np-Zr alloy phases at 0 K: (a) (α Np) (6.3 at.% Zr); (b) (β Np) (6.3 at.% Zr); (c) (α Zr) (93.8 at.% Zr). The CALPHAD values are calculated at 298 K. The model 1 by Bajaj *et al.* [182] considering HCP as the stable structure for pure Zr is used for comparison. 140

Figure 5.6. RMS of enthalpy differences between *ab initio* and CALPHAD in this work. β Np, γ Np, (α Np) (6.3 at.% Zr), (β Np) (6.3 at.% Zr) and (α Zr) (93.8 at.% Zr) are considered. The lines connecting the *ab initio* results are used for guiding the eyes. 141

Figure 5.7. Comparison of the enthalpy of formation of the δ phase between *ab initio* calculations and CALPHAD modeling. The dotted lines connecting the *ab initio* results are used for guiding the eyes. Model 1 in the work by Bajaj *et al.* [182] takes hcp as the stable structure for pure Zr, while model 2 takes the ω phase. (a) Is the case for *ab initio* calculations with noSOC and (b) is the case for *ab initio* calculations with SOC. 143

Figure 5.8. Comparison of the enthalpy of mixing of the BCC structure between *ab initio* calculations and CALPHAD modeling. The dotted lines connecting the *ab initio* results are used for guiding the eyes. (a) Is the case for *ab initio* calculations with noSOC and (b) is the case for *ab initio* calculations with SOC. 143

Figure 5.9. Comparison of the excess entropy of mixing of the liquid phase at 2500 K between this work and Bajaj *et al.* [182]. 147

Figure 6.1. Phase diagram of the Np-U system from the CALPHAD models of this work and Kurata[12], compared to the experimental data of Mardon and Pearce[19]. 152

Figure 6.2. Enthalpy of formation for a) α (Np) (6.3 at.%U), b) β (Np) (6.3 at.%U), c) α (U) (93.7 at.%U), and d) β (U) (96.7 at.%U) from *ab initio* at different U_{eff}(Np) and U_{eff}(U) compared with those from the CALPHAD models of this work (cyan) and Kurata (magenta)[12]. Only the points marked with black balls are actually calculated data, and the surfaces connecting them are from spline interpolation as guides to the eyes. 163

Figure 6.3. Enthalpy of mixing for γ (Np,U) from *ab initio* compared with those from the CALPHAD models of this work (cyan) and Kurata (magenta)[12]. The results from U_{eff}(Np) = a) 0, b) 0.4, c) 0.65, d) 0.9, e) 1.4 eV are shown in the respective panel. In all panels the results from U_{eff}(U) = 0 (black), 0.49 (red), 0.99 (green) and 1.49 (blue) eV are shown as different curves. Only the points marked with symbols are actually calculated data, and the lines connecting them are from spline interpolation as guides to the eyes. 166

Figure 6.4. Enthalpy of formation for ζ from DFT and DFT + U at (U_{eff}(Np), U_{eff}(U)) = (0.65, 1.24) eV. 169

Figure 6.5. Site occupations for ζ predicted by DFT (solid) and DFT + U (dash) at (U_{eff}(Np), U_{eff}(U)) = (0.65, 1.24) eV for the five lattice site groups I-V defined in Table 6.4. 170

Figure 7.1. The 28 compositions of BCC Np-U-Zr studied in *ab initio* calculations and the three representative series of isopleth paths that they form. 181

Figure 7.2. U_{eff} used for Np and U in DFT + U calculations. 184

Figure 7.3. Isothermal sections of the phase diagram of Np-U-Zr at a) 793.15 K, b) 868.15 K, and c) 973.15 K. Greek phase labels for dominant component(s) of single-phase and BCC two-phase

regions are given. Additionally, BCC and BCC+BCC' are used to denote BCC single- and two-phase regions, respectively. 186

Figure 7.4. Enthalpy of mixing for BCC Np-U-Zr from CALPHAD (300 K) and *ab initio* (0 K) at different U_{eff}'s. DFT corresponds to the point at U_{eff}(Np)= U_{eff}(Np)=0 (bottom left), while DFT + *U* to all others. 191

Figure 7.5. Root mean square (RMS) of the differences in enthalpy of mixing for BCC Np-U-Zr between CALPHAD (300 K) and *ab initio* (0 K) at different U_{eff}'s. DFT corresponds to the point at U_{eff}(Np)= U_{eff}(Np)=0 (bottom left), while DFT + *U* to all others. *Ab initio* calculated values are marked black balls and the remaining in the surface are their spline interpolations. The bottom plane is projection of the 3D surface. 194

Figure 7.6. Enthalpy of mixing for BCC Np-U-Zr from CALPHAD and DFT + *U* at (U_{eff}(Np), U_{eff}(U))=(0.6, 0.99) eV viewed from a) Np-, b) U-, and c) Zr-rich corner. The front of CALPHAD and DFT + *U* surface is filled by the color palette given in the legend, while the back of them is filled by dark cyan and gray, respectively. The top and bottom plane are projections of the CALPHAD and DFT + *U* 3D surface, respectively. See Figure 7.4 for the result from DFT. 195

Figure 7.7. Phase diagram of Np-U-Zr showing only BCC and Liquid phases viewed from a) Np-, b) U-, and c) Zr-rich corner. The surface outlined by red, black and the inner curled piece of green curves is the lower while the surface of Solidus is the upper boundary of BCC single-phase region. The surface outlined by red and green curves is the upper boundary of BCC+BCC' two phase (i.e., miscibility gap) region. Green curves outline the interface shared between solidus and BCC+BCC' miscibility gap. The front of solidus and liquidus surface is filled the color palette given in the legend, while the back of them is filled by dark cyan and dark yellow, respectively. 197

Figure 7.8. Projections of BCC Np-U-Zr's stable phase boundary from CALPHAD compared to enthalpy of mixing from DFT + *U* at (U_{eff}(Np), U_{eff}(U))=(0.6, 0.99) eV on the left and miscibility gap temperature from CALPHAD on the right. The units for enthalpy and temperature are eV/atom and K, respectively. 198

Figure 7.9. Atomic volume and volume of mixing for BCC Np-U-Zr from DFT and DFT + *U* at (U_{eff}(Np), U_{eff}(U))=(0.6, 0.99) eV. The front of DFT and DFT + *U* surface is filled by the color palette given in the legend, while the back of them is filled by dark cyan and gray, respectively. The top and bottom flat surfaces are projections of the DFT and DFT + *U* 3D surfaces, respectively. 204

Figure 9.1. Thermal expansion of U metal from quasi-harmonic theory and experiment. See section 9.1 for references to the plotted experimental data. Two points exist at 0 K, corresponding to the rigid lattice and the zero-point of the vibrating lattice, respectively. 218

Figure 9.2. Thermal expansion of Zr metal from quasiharmonic theory and experiment. The experimental references for α Zr and β Zr are Goldak *et al.*[82] and Heiming *et al.*[83], respectively. Two points exist at 0 K, corresponding to the rigid lattice and the zero-point of the vibrating lattice, respectively. 218

List of Tables

Table 1.1. Binary and ternary systems formed by U-Pu-Zr and one of Np, Am and Cm minor actinides. 3
Table 1.2. Intermediate compound phases in binary alloy systems of U-Pu-Zr-Np. 3
Table 2.1. Comparison of invariant reaction in the U-Zr phase diagram[Δ]. 19
Table 2.2. Crystal structure information of solid phases in the U-Zr system 24
Table 2.3. Thermodynamic models and optimized CALPHAD type parameters for different phases of the U-Zr system in this work (Case 1B). 25
Table 3.1. Solid phases of U, Zr metal and U-Zr alloy. 47
Table 3.2. Energetics[a] for solid phases of U, Zr metal and U-Zr alloy (unit: eV/atom). 61
Table 3.3. Differences in energetics between DFT, DFT + *U* (1.24 eV) and CALPHAD for all solid phases of U metal and U-Zr except α U and γ (U,Zr)a (unit: eV/atom). 62
Table 3.4. Volume for U, Zr metal and U-Zr alloy (Å^3/atom) 67
Table 3.5. Theoretical Hubbard U for Uranium in all solid phases of U metal and U-Zr alloy evaluated with the linear response approach of Ref. [124]. 91
Table 4.1. γ(U,Zr)'s volume in unit of Å^3/atom from a) experiment, b) theory in this work, and b) theory in the literature, SOC and noSOC denote calculations with and without spin orbit coupling (SOC) included, respectively. 99
Table 5.1. Thermodynamic models and optimized CALPHAD type parameters for different phases of the Np-Zr system in this work 128
Table 5.2. Crystal information on Np and Zr allotropy and their solution phases used in the *ab initio* modeling of this work 130
Table 6.1. Stable solid phases of the Np-U system, their crystal structures and settings in *ab initio* calculations. 152
Table 6.2. Wyckoff sites of ζ phase given in the conventional tetragonal setting. This whole table, including the atomic environment is quoted from Ref.[207] and provided here for easier reference. The original experimental crystal structure data are from Ref.[15] 153
Table 6.3. Thermodynamic model and optimized CALPHAD type parameters for stable phases of the Np-U system. 154
Table 6.4. Groups of the lattice sites of ζ in *ab initio* calculations according to atomic environment. 155
Table 7.1. Supercell structures used in *ab initio* calculations of BCC Np-U-Zr. 182
Table 7.2. Melting temperature at U-rich corner of Np-U-Zr compared with solidus and liquidus temperatures predicted from CALPHAD in this work. 188
Table 7.3. Root mean square (RMS) of the differences in enthalpy of mixing for BCC Np-U-Zr between CALPHAD (300 K) and *ab initio* (0 K) at different U_{eff}'s averaged over compositions illustrated in Figure 7.2. DFT corresponds to the point at U_{eff}(Np)= U_{eff}(Np)=0 (bottom left), while DFT + *U* to all others. The units of enthalpy and U_{eff} are eV/atom and eV, respectively. .. 192
Table 7.4. Atomic volume of BCC Np-U-Zr from DFT and DFT + *U* at (U_{eff}(Np), U_{eff}(U))=(0.6, 0.99) eV (unit: eV/atom). The same values are given multiple times where the isopleth paths cross. ... 202
Table 9.1. Experimental lattice constant and volume of γ U 216
Table 9.2. Experimental volume for U, Zr metals and U-Zr alloys (Å^3/atom) 220

1 General Introduction

1.1 Background and Motivation

The nuclear energy industry is currently undertaking major research and development activities towards the next generation (so-called Generation IV) nuclear reactors[1]. Central to the design principles of Generation IV reactors are to use nuclear fuel efficiently, reduce radiotoxicity and heat in spent fuel, and avoid separated Pu that might lead to nuclear weapon proliferation. Among the six Gen IV nuclear reactor designs recommended by the Generation IV International Forum as most promising[2], all the three fast spectrum neutron reactors[3] proposed to use metallic fuel[4] as a leading candidate. The current basis for metallic fuel in a fully recycled closed fuel cycle is U-Pu-Zr-MA (where MA are minor actinides Np, Am, Cm) alloy[7]

Comparing to oxide fuels, metallic nuclear fuels have advantages in thermal conductivity, burn-up rate, recycling, fabrication and most significantly safety[4, 5]. However, metallic fuels are also subject to some possible issues like fuel constituent redistribution, fuel cladding interaction, and fuel swelling[4, 6]. Moreover, the melting temperatures of Np and Pu are close to or even lower than the maximum operating design temperatures of some Gen VI fast reactors, which poses safety concern.

These issues should be properly addressed to achieve safe and optimal uses of metallic fuels. On the fundamental level, addressing them needs thorough understanding of relevant materials properties, including microstructure, melting temperature, density, thermal conductivity, mechanical properties, diffusion constants, etc.[4]. All of these materials properties couple strongly to the phases present under operating and potentially transient conditions. In addition to phase stability, the underlying thermodynamic functions for the alloy are necessary for quantitative understanding of the fuels, on which more accurate design and precise control are relied. For example, Kurata *et al.* [8] observed that the constituent migration is greatly affected by MA and rare earth (RE) elements present in the U-Pu-Zr fuel. Since the constituent migration is driven by chemical potential gradient along the temperature gradient, the thermodynamic properties and phase equilibria of the U-Pu-Zr-MA alloy are essential for understanding the migration mechanisms. While significant experimental data on the U-Pu-Zr system exists, the phase stability and thermodynamic properties of minor actinide containing systems are relatively unknown[9].

1.2 Challenges in Studying Metallic Nuclear Fuels

Despite the strong application needs reviewed above, metallic nuclear fuels are challenging to study both experimentally and theoretically.

On the experimental side, actinides and possible fission products in the fuels are radioactive and toxic, so special facilities, for example, glove box are needed to handle these materials, increasing of course the time and cost. Most actinide elements in the fuel are non-naturally occurring, and thus are difficult and expensive to get in the form and quantity desired in scientific research. Moreover, actinide elements, in particular Pu are politically sensitive and still only limitedly available in a few countries. As a result, relevant experimental data for actinide materials in general are scarce, if not unavailable at all.

For example, the current availability of experimental phase diagram data for U-Pu-Zr-MA metallic nuclear fuel, according to Refs.[10-13] are summarized in Table 1.1. It is clear that only the systems of U-Pu-Zr are well studied. Several Np containing systems also have some experimental data available, but most of them are not sufficient to guide reliable thermodynamic modeling according to our assessment.

Table 1.1. Binary and ternary systems formed by U-Pu-Zr and one of Np, Am and Cm minor actinides.

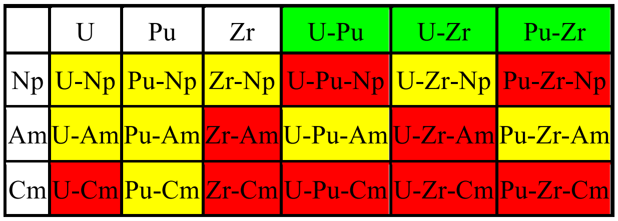

	U	Pu	Zr	U-Pu	U-Zr	Pu-Zr
				🟩	🟩	🟩
Np	🟨 U-Np	🟨 Pu-Np	🟨 Zr-Np	🟥 U-Pu-Np	🟨 U-Zr-Np	🟥 Pu-Zr-Np
Am	🟨 U-Am	🟨 Pu-Am	🟥 Zr-Am	🟨 U-Pu-Am	🟥 U-Zr-Am	🟨 Pu-Zr-Am
Cm	🟥 U-Cm	🟨 Pu-Cm	🟥 Zr-Cm	🟥 U-Pu-Cm	🟥 U-Zr-Cm	🟥 Pu-Zr-Cm

Green, yellow and red represent systems with sufficient, insufficient and no experimental data, respectively available to guide reliable thermodynamic modeling based on our assessment of the data reviewed in Refs.[10-13].

Table 1.2. Intermediate compound phases in binary alloy systems of U-Pu-Zr-Np.

System	Phase	Chemical Formula	Lattice System	Space Group	Size (atom/cell)	Wyckoff Known?	Occupation Known?	Reference
U-Zr	δ	UZr_2	Hexagonal	P6/mmm	3	yes	yes	[14]
Pu-U	ζ	?	Rhombohedral	$R\bar{3}m$	58	yes	no	[15]
	η	?	Tetragonal	?	52	no	no	[16]
Pu-Zr	ζ	$Pu_{28}Zr$	Tetragonal	$I4_1/a$	116	yes	yes?	[17]
	θ	Pu_4Zr	Tetragonal	P4/ncc	80	no	no	[18]
Np-U	δ (ζ)	?	Rhombohedral	$R\bar{3}m$	58	yes	no	[19]
Np-Pu	η	?	Orthorhombic	?	54	no	no	[20]
Np-Zr	δ	$NpZr_2$	Hexagonal	P6/mmm	3	yes	yes	[21]
	θ	Np_4Zr	Tetragonal	P4/ncc	80	no	no	[22]

As a further example, we also review the current knowledge of the crystal structures of the intermediate compound phases in binary alloy systems of U-Pu-Zr-Np in Table 1.2. We can see that except for δ phases of U-Zr and Np-Zr, the crystal structure information is incomplete for all other systems, usually with the site occupation missing. Most significantly, for η phases of Pu-U and Np-Pu, even the space group is undetermined.

On the other hand, theoretical study of actinide metals and alloys is also more difficult than other common metals. The actinide series is expected to have electron correlation increasing from weak to strong at higher atomic number, with Pu near the critical point[23]. *Ab initio* modeling of actinide metals is still at the forefront of modern many-body electronic structure theory[23, 24]. Moreover, with actinides locating near the end of the periodic table, the relativistic effects are expected to be stronger than lighter metals. At a structural level, the peculiar electronic structure and *f* electron bonding also results in the crystal structures of these materials being more complicated[23], and thus *Ab initio* modeling of them can be more computationally expensive. Finally, related to the scarcity of experimental data due to experimental challenges we just explained above, theoretical study of actinide systems is also hampered due to lack of proper validation, or simply due to lack of essential starting information on which modeling needs to be based. For example, thermodynamic modeling using the traditional CALculation of PHAse Diagrams (CALPHAD) [25] method of even a binary alloy system needs to know at least what phases are present in the system. Without such information traditional CALPHAD cannot provide any prediction beyond some elementary extrapolations. This means that those systems listed in Table 1.1 as having no experimental phase diagram data cannot be reliably modeled using the traditional CALPHAD method alone. Similarly, *ab initio* modeling of the intermediate phases we reviewed in Table 1.2 that have missing or incomplete crystal structure also faces major uncertainty, if even possible at all.

1.3 Thesis Objectives

Motivated by the application needs of safer and more efficient uses of metallic nuclear fuels, this thesis is endeavored to increase the knowledge of phase stability and thermodynamic properties of U-Pu-Zr-MA metallic fuels. We focus on Np as the minor actinide and also exclude Pu to keep the work scope practical, leaving Pu, Am, and Cm containing systems for future study. That is to say, this thesis studies Np, U and Zr unary, Np-Zr, U-Zr and Np-U binary and Np-U-Zr ternary systems. Due to the challenges in experiment, we take a modeling approach with the overall objective to develop a thermodynamic model and establish an *ab initio* approach for Np-U-Zr that is reasonably accurate and can contribute towards improving and controlling reactor fuels. Because of the challenges in applying the two modeling approaches of *ab initio* and CALPHAD individually, we pursue the so-called *ab initio* enhanced CALPHAD modeling approach, as detailed in the next section.

The overall objectives of this thesis are to

1. Establish a best-practice *ab initio* approach for predicting Np-U-Zr energetics for thermodynamic modeling.

2. Develop a thermodynamic model for Np-U-Zr and its binary subsystems.

1.4 Scientific Approach

The standard approach for constructing thermodynamic models of phases in a multicomponent system is the CALPHAD approach[25]. As we discussed above, however, only limited experimental thermodynamic and phase equilibrium data are available for U-Pu-Zr-MA that we can fit to in CALPHAD modeling. We therefore supplement existing experimental data with *ab initio* energetics. However, due to the challenges in *ab initio* modeling of these *f* electron systems, we need to first validate *ab initio* approaches to ensure the accuracy of the calculated energetics. Such an approach involving iterative cross-validation between experiment, CALPHAD, and *ab initio* and predictions from the validated models is called the *ab initio* enhanced CALPHAD approach, as illustrated in Figure 1.1.

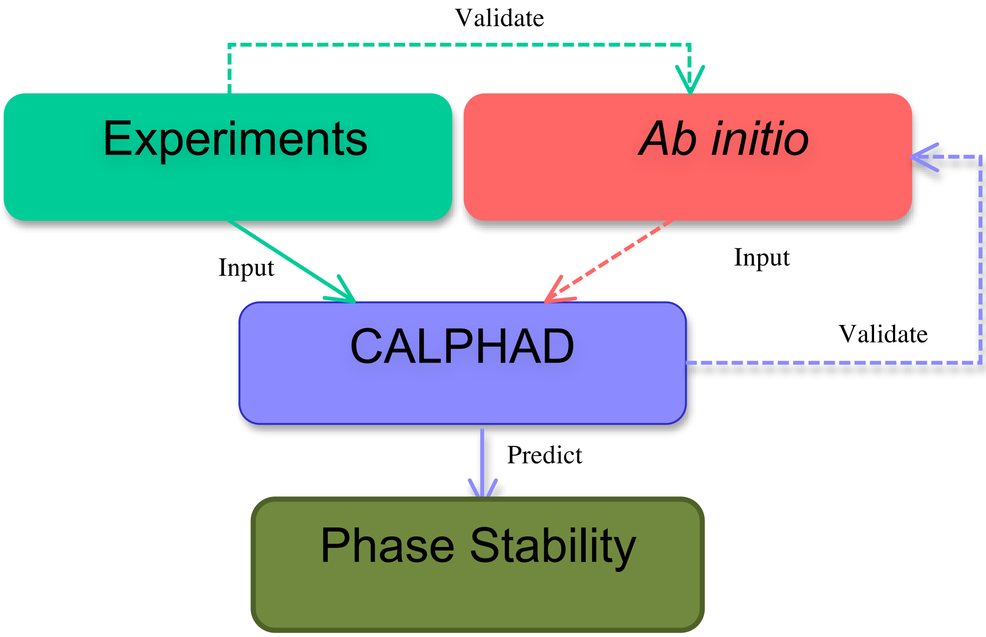

Figure 1.1: *Ab initio* enhanced CALPHAD approach to phase stability prediction. Solid lines denote the conventional CALPHAD approach, while dashed lines indicate how *ab initio* calculations are involved in the *ab initio* enhanced CALPHAD approach.

The *ab initio* enhanced CALPHAD approach for a multicomponent alloy contains the following steps:

1) Develop optimized Gibbs energy models for the binary subsystems that have sufficient thermochemical and/or phase equilibrium data available from experiment, following the traditional CALPHAD approach.

2) Validate *ab initio* approaches against the thermodynamic models developed in step 1) and, if available, also experimental thermochemical data. Specifically, enthalpies of formation/mixing for stable solid phases are compared. Focus in this step will be put on the phases with known crystal structures that are modeled with good accuracy in the CALPHAD models.

3) Use the validated *ab initio* approaches to calculate energetics for the remaining systems that have insufficient or no experimental data. The following energetics can be calculated and used in CALPHAD modeling: (a) Enthalpies of formation of end-member compounds, which are essential to constrain the CALPHAD optimization but are often metastable and therefore difficult to obtain experimentally. (b) Enthalpies of formation of mixtures to get interaction energies that might otherwise take extensive experimental investigation. (c) Enthalpies of formation of candidate compounds in order to identify where new compounds might be stable. (d) Sublattice and antisite defect energies that can guide the accurate choice of sublattice model in CALPHAD, which must be as simple as possible without ignoring active degrees of freedom. In addition, the finite temperature effects of vibrational and electronic excitations can also treated in *ab initio* calculations, for example as Ref.[26] did for Ni and Ni_3Al. However, due to the limited time and large errors in just the zero temperature enthalpies, we did not consider such effects, leaving them for future study.

4) Build a thermodynamic model for the target multicomponent alloy by extrapolating the models for its subsystems. Usually *ab initio* calculations is not performed in this step. However, Ref.[27] suggested it may be beneficial for example to estimate the multicomponent interaction parameters by referencing to *ab initio* energetics as well.

1.5 Summary of Research Tasks

As explained in section 1.3, researches reported in this thesis is divided into two main tasks:

- Task 1 – *Ab initio*: Establish a best-practice *ab initio* approaches for calculating Np-U-Zr energetics through comparison to CALPHAD models identified and developed in Task 2.

Use the optimized approach to predict key energetics of Np-U-Zr alloys for developing improved CALPHAD models.

- Task 2 – CALPAHD: Construct a CALPAHD model for the thermodynamics of Np-U-Zr using existing experimental data and thermodynamic models with additional input *ab initio* data from Task 1.

Next we explain in more details what were performed for each task.

1.5.1 *Ab initio* **Calculations**

We performed *ab initio* calculations in the general framework of density functional theory (DFT)[28, 29] for all the known stable solid phases of U, Np, Zr unary systems and U-Zr, Np-Zr and Np-U binary systems. In particular, we calculated all the intermediate binary compound phases of these three binary systems. However, despite significant efforts, we did not reach satisfactory results for the θ phase of Np-Zr that has undetermined Wyckoff atom position information and the results we obtained for it are thus not included in this thesis. In addition to stable phases, metastable end members are also calculated whenever it helped improve CALPHAD modeling in Task 2. Finally, we also calculated the body center cubic (BCC) phase of the Np-U-Zr ternary system.

Based on the generalized gradient approximation[30] to the exchange and correlation potential, we explored how well the electron-electron correlation effects are modeled by both the standard DFT and the so-called simplified rotationally invariant DFT + U functionals[31] in a wide range of effective Hubbard U (U_{eff}) parameters for Np and U (from 0 to 4 eV for U/U-Zr and Np/Np-Zr, and from 0 to at least 1.5 eV for Np-U and Np-U-Zr). Moreover, we also validated how large the relativistic effect of spin orbit coupling is for the U/U-Zr and Np/Np-Zr systems. We focused on ground state energy as the primary material property of interest, but atomic volume, bulk modulus, electronic structure, magnetic moments, and elastic constants are also calculated, analyzed and reported in this thesis when necessary.

1.5.2 CALPHAD Modeling

We reviewed existing experimental phase diagram and thermochemical data and developed CALPHAD models for the U-Zr, Np-Zr and Np-U binary and the Np-U-Zr ternary systems. The U-Zr system was modeled by fitting to experimental data. The Np-Zr was also fitted to experimental data except for the lattice stability of pure Zr with the structure of αNp and βNp, and that of pure Np with the structure of αZr, which were from *ab initio* calculations of Task 1. The Np-U systems is being studied by *ab initio* enhanced CALPHAD modeling approach for the low temperature part, but the current thesis reports a CALPHAD model that is fitted only to available experiment data, which we will show to be already satisfactorily accurate for the high temperature part (i.e., BCC and liquid phase) of the Np-U system. The CALPHAD model for the Np-U-Zr ternary system is developed from Muggianu extrapolation[32] of the models for the U-Zr, Np-Zr, and Np-U binary systems.

1.6 Overview of Chapters

This thesis is divided into the following chapters.

Chapter 1 contains the current general introduction to this thesis.

Chapter 2 reports a CALPHAD model for the U-Zr binary system and *ab initio* enthalpies for δ and BCC γ phases of the U-Zr system.

Chapter 3 reports *ab initio* calculations for the U unary and the U-Zr binary systems. The properties calculated included enthalpy, volume, magnetic moments, and electronic structure.

Chapter 4 reports *ab initio* calculations for γU and αU's bulk modulus and presented additional discussions on γ(U,Zr)'s volume and enthalpy of mixing, αU's volume as well as the magnetic moments issue overall for the U unary and the U-Zr binary systems.

Chapter 5 reports both a CALPHAD model for the Np-Zr binary system and *ab initio* calculations for the Np unary and the Np-Zr binary systems.

Chapter 6 reports both a CALPHAD model and *ab initio* calculations for the Np-U binary system.

Chapter 7 reports both a CALPHAD model for the Np-U-Zr ternary system and *ab initio* calculations for BCC γ phase of the Np-U-Zr system.

Finally, Chapter 8 contains a summary of this thesis and offers some suggestions for future work.

1.7 Publications and Author Contributions

1.7.1 Publications

Chapter 2 has been published as a peer-reviewed journal article[33] of which I was the second author. Chapter 3 has been published as a peer-reviewed journal article[34] of which I was the first author. The content of chapter 4 has gone through peer-review and been accepted for publication as a journal article of which I will be the first author. Chapter 5 has been published as a peer-reviewed article[35] of which I was a equal-contributing co-first author. The contents of both chapter 6 and chapter 7 have gone through internal review and will be submitted for peer-review as journal articles both of which I will be the first author.

1.7.2 Author Contributions

This thesis mainly reports the researches of myself as the thesis author. However, it also includes related results obtained by my collaborators in order to make the presentation complete as possible. Contributions of the thesis author and the collaborators are as follows.

1.7.2.1 Contribution of the thesis author:

For the *ab initio* part, I determined what calculations were needed, planned the work, performed all the calculations and analyzed all the data, and wrote all the texts related to them in journal papers and this thesis; for the CALPHAD part, I provided *ab initio* inputs, discussed the results and provided the analyses, particularly in light of *ab initio* data. I also edited the texts related to them for the U-Zr and Np-Zr systems, and analyzed the CALPHAD results and wrote all the texts related to them for the Np-U and Np-U-Zr systems in journal papers and this thesis.

1.7.2.2 Contributions of the collaborators:

Wei Xiong performed the CALPHAD modeling for the U-Zr, Np-Zr, Np-U and Np-U-Zr systems, and also wrote the texts for the CALPHAD results of the U-Zr and Np-Zr systems. Chao Shen developed some early CALPAHD models for the U-Zr, Np-Zr and Np-U systems and wrote some texts for his CALHPAD work. Both the work and the texts of Chao Shen were nevertheless not adopted in the journal papers and this thesis. Chao Jiang generated a new ternary BCC supercell used in Chapter 7. Chuan Zhang assisted the analysis of the CALPHAD results for the Np-U-Zr systems in Chapter 7.

Dane Morgan conceived, proposed and supervised the whole thesis project and edited all the journal papers and this thesis. Ying Yang contributed to the proposal of this thesis project. Chris Marianetti advised the *ab initio* work and edited the manuscripts that Chapters 3 and 4 are based on. Y. Austin Chang supervised Chao Shen before passing away in August, 2011.

2 CALPHAD Modeling of the U-Zr System

Note: This chapter has been published as a peer-reviewed article[33] in Journal of Nuclear Materials, and the article was adapted for use in this thesis.

2.1 Chapter Abstract

A new thermodynamic description of the U-Zr system is developed using the CALPHAD method with the aid of *ab initio* calculations. Thermodynamic properties, such as heat capacity, activities, and enthalpy of mixing, are well predicted using the improved thermodynamic description in this work. The model-predicted enthalpies of formation for the BCC and δ phases are in good agreement with the results from DFT + *U ab initio* calculations. The calculations in this work show better agreements with experimental data comparing with the previous assessments. Using the integrated method of *ab initio* and CALPHAD modeling, an unexpected relation between the enthalpy of formation of the δ phase and energy of Zr with hexagonal structure is revealed and the model improved by fitting these energies together. The present work has demonstrated that *ab initio* calculations can help support a successful thermodynamic assessment of actinide systems, for which the thermodynamic properties are often difficult to measure.

2.2 Introduction

U-Zr based alloys are promising nuclear fuels because of their advantages in thermal conductivity, evolution under burn-up, and other factors [4]. For example, U-Zr is an important binary of the U-Pu-Zr system which has been used as the metallic fuel for Fast Breeder Reactors since its thermal and neutronic behavior has some advantages compared to oxide ceramic fuels [36]. Thorough understanding of phase stability of the U-Zr system is essential for the safe and optimal use of nuclear fuels based on this alloy. Although extensive work has appeared in the literature, the available experimental data are inadequate in scope and reliability for a robust understanding of the thermodynamics of the U-Zr system.

In terms of thermodynamic modeling, the first CALPHAD-type assessment of the U-Zr system was performed by Leibowitz *et al*. [37], and then revised further by several other groups [11, 38-40]. However, in the previous work [11, 38-40] some details of the U-Zr phase diagrams and thermodynamic properties have not been well described.

The present work aims to provide an improved CALPHAD modeling of the U-Zr system through revisiting the CALPHAD modeling of thermodynamic and phase stability data combined with *ab initio* calculations. The *ab initio* calculations are used to provide the computational-experimental values of thermodynamic properties of the U-Zr alloys and also to guide the choice of thermodynamic models in the CALPHAD approach.

Following this introduction, Section 2 gives a review of the previous literature on thermodynamic experiments and modeling of the U-Zr system. Section 3 describes the thermodynamic modeling approach used in this work, Section 4 the *ab initio* calculations, and Section 5 gives the resulting thermodynamic model, phase diagram, and discussion.

2.3 Literature Review

Some previous thermodynamic evaluations were carried out with comprehensive literature reviews. For example, Sheldon and Peterson [41] reviewed the experimental data of the U-Zr system published in the literature up to 1989, and constructed its phase diagram. Therefore, in this section, only the most important and new (since the work of

Sheldon and Peterson [41]) experimental datasets useful for the thermodynamic modeling are critically reviewed.

The experimental phase equilibria with the liquid phase were determined by four groups [37, 42-45], as shown in Figure 2.1. However, the region on the Zr-rich side deserves further investigations. It should be noted that the experimental data from the work by Kanno *et al*. [44] was extrapolated indirectly from the thermodynamic activity measurements and their dataset for phase transformation temperatures shows significant deviations from the ones reported by other groups [42, 43].

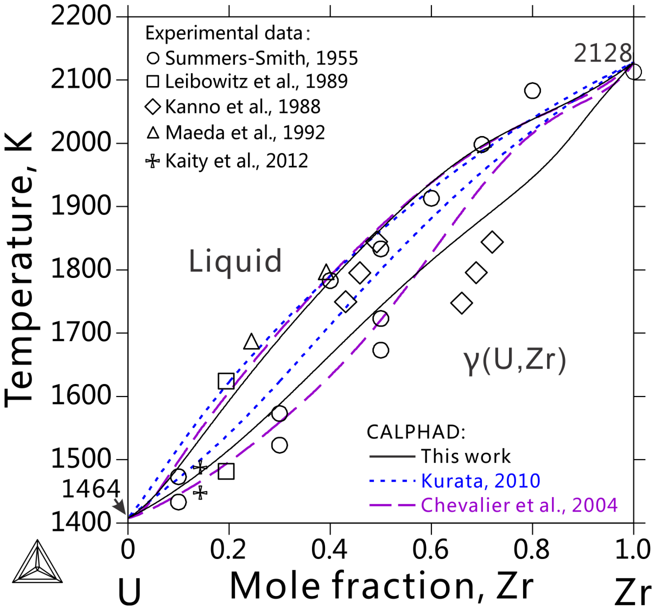

Figure 2.1. Comparison of phase diagram between experimental data [37, 42-44] and this work for temperatures above 1400 K.

Regarding the solid phase equilibria, the major contributions are from five research groups [42, 46-50]. The first comprehensive determination of the solid phase equilibria was carried out by Summers-Smith [42] using metallographic, dilatometric, and X-ray diffraction (XRD) methods. It is noteworthy that the intermetallic phase δ was not observed instead a eutectic reaction was assumed to be occurring in the phase region of the δ phase. Therefore, the ageing time of samples in the work by Summers-Smith [42] may be inadequate, and the experimental data should not be considered with a high weight during thermodynamic optimization. According to the work done by Akabori *et al*. [49], the experimental tie-lines between γ(U,Zr) and α(Zr) shows a significant deviation from the one reported by Summers-Smith [42]. In the work by Akabori *et al*. [49], the homogeneity range of the δ phase was determined using electron probe microanalysis, XRD, and differential thermal analysis. It should be emphasized that the static measurement (XRD) is consistent with the determination by the kinetic method (thermal analysis) in the same work performed by Akabori *et al*. [49]. As can be seen in Figure 2.2, the compositional homogeneity range, i.e. single phase region, of the δ phase determined by Duffey and Bruch [47] is smaller than the one determined by Akabori *et al*. [49]. A possible reason for this discrepancy is the higher contaminant of the samples used in the work of Duffey and Bruch [47], because contamination by oxygen has been shown to reduce the homogeneity range of the δ phase [46]. It is also likely that the metallographic observation of the phases used by Duffey and Bruch [47] will be less precise than XRD performed by Akabori *et al*. [49] due to the greater challenges associated with metallographic vs. XRD analysis. Furthermore, a homogeneity limit of the δ phase, in agreement with Akabori *et al*. [49] was recently determined by Basak [51], who determined the tie-line between α(U) and δ at the temperature of 873 K using the Energy-dispersive X-ray spectroscopy. Given the above observations, in this work we will fit primarily to the data from Akabori *et al*. [49] for the δ phase boundaries.

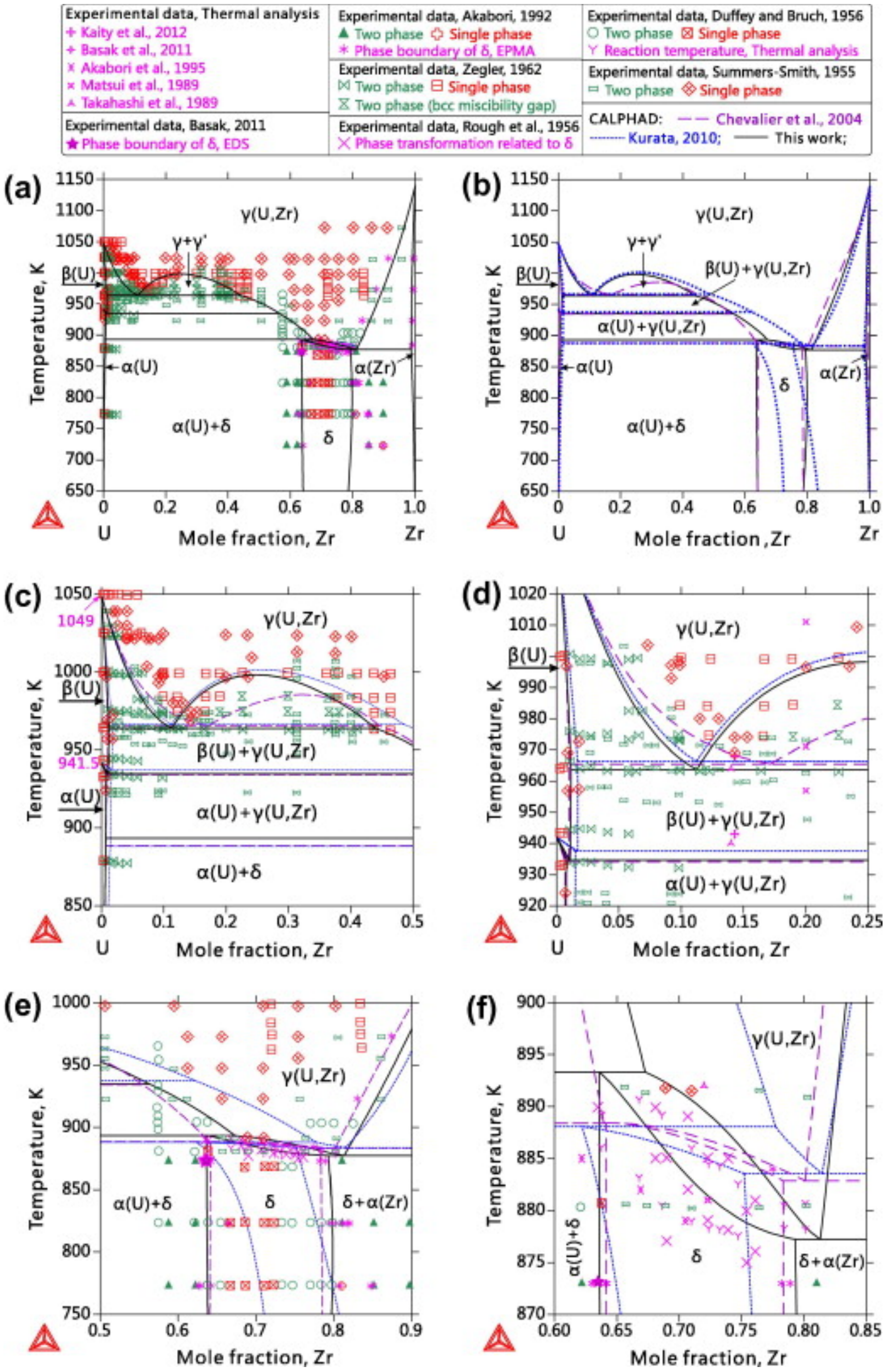

Figure 2.2. Comparison of the solid phase diagram between experimental data [14, 42, 45-53] and thermodynamic descriptions [11, 40], (b) is the comparison among different CALPHAD modeling, (c) (d) (e) and (f) are magnified parts of (a).

In the U-Zr system, as can be seen in Figure 2.2 (c), the BCC structure will form a miscibility gap in the range between 960 and 1020 K through a monotectoid reaction.

However, there are large discrepancies of the experimental phase boundary determined by Summers-Smith [42] and Zegler [48]. It is rather common to observe such differences of the results from different work. In particular, there are aspects of each study that might lead to errors. Firstly, as mentioned before, the sample examined in the work of Summers-Smith [42] was not sufficiently aged. Secondly, the contaminants, e.g., oxygen or nitrogen, will significantly reduce the precision of the experimental construction of the BCC miscibility gap.

Although Zegelr [48] claimed the experimental alloy for determination of the BCC miscibility gap had an oxygen contamination of 150 ppm (lower than the critical value of 160 ppm to influence the accuracy of the measurement [48]), the ageing time for the sample are rather short as 7 days, which could be insufficient annealing to reach the phase equilibria.

It is also noteworthy that martensitic structures were found frequently in the annealed samples for the BCC miscibility gap by Zegler [48], which may interfere with accurate microstructure analysis for the equilibrium alloys. In many cases, due to the above mentioned challenges and others, the experimental determination of the miscibility gap with high accuracy is difficult (e.g., in Al-Zn [54, 55] and Fe-Cr [56, 57] binary alloys). Consequently, the experimental miscibility gap data by Summers-Smith [42] and Zegler [48] should not be considered with a high weight during thermodynamic modeling.

Table 2.1. Comparison of invariant reaction in the U-Zr phase diagram$^{\Delta}$.

Reaction	Phase composition, at.% Zr			T, K	Reference *
$\gamma \leftrightarrow \gamma' + \beta(U)$	17.2	44.6	1.0	965.5	[40] C
	11.0	48.0	1.9	967.7	[11] C
	11.2	44.0	1.2	963.7	This work
	10.9	42.4	1.1	966	[41] V
	9.7	47	—	961	[58] V
	14.5	~57	2.5	966 ± 3	[42] E
	11.0	42.4	1.06	966	[48] E
$\beta(U) \leftrightarrow \alpha(U) + \gamma$	1.0	0.7	55.4	934.2	[40] C
	1.9	1.7	62.6	937.0	[11] C
	1.1	0.8	56.3	934.7	This work
	0.8	0.5	60	935	[41] V
	1.1	—	57	932	[58] V
	~1.5	~1	61	935 ± 2	[42] E
	—	0.55	—	935	[48] E
$\gamma \leftrightarrow \alpha(U) + \delta$	64.1	0.7	64.0	888.4	[40] C
	77.9	1.6	63.5	887.8	[11] C
	67.3	0.69	63.6	893.3	This work
	~66	~0.5	63	890	[41] V
$\gamma + \alpha(U) \leftrightarrow \delta$	68	0.5	65	885	[58] V
	—	—	—	~885	[59] E
	—	—	62.5	890	[47] E
	—	—	—	880	[46] E
$\gamma \leftrightarrow \delta + \alpha(Zr)$	80.1	78.3	99.5	882.9	[40] C
	81.4	75.2	98.2	883.5	[11] C
	81.3	79.3	98.7	877.2	This work
	~81	~78	99.6	879	[41] V
	78	76	99.6	883	[58] V
	—	—	—	~868	[59] E
	76.1	—	—	879	[47] E
	—	—	—	866	[46] E

Δ The calculated result according to this work is taken from case 1B shown in Figure 2.9.

* “C” stands for CALPHAD modeling, “E” stands for experimental work, and “V” denotes thermodynamic evaluation only based on literature review.

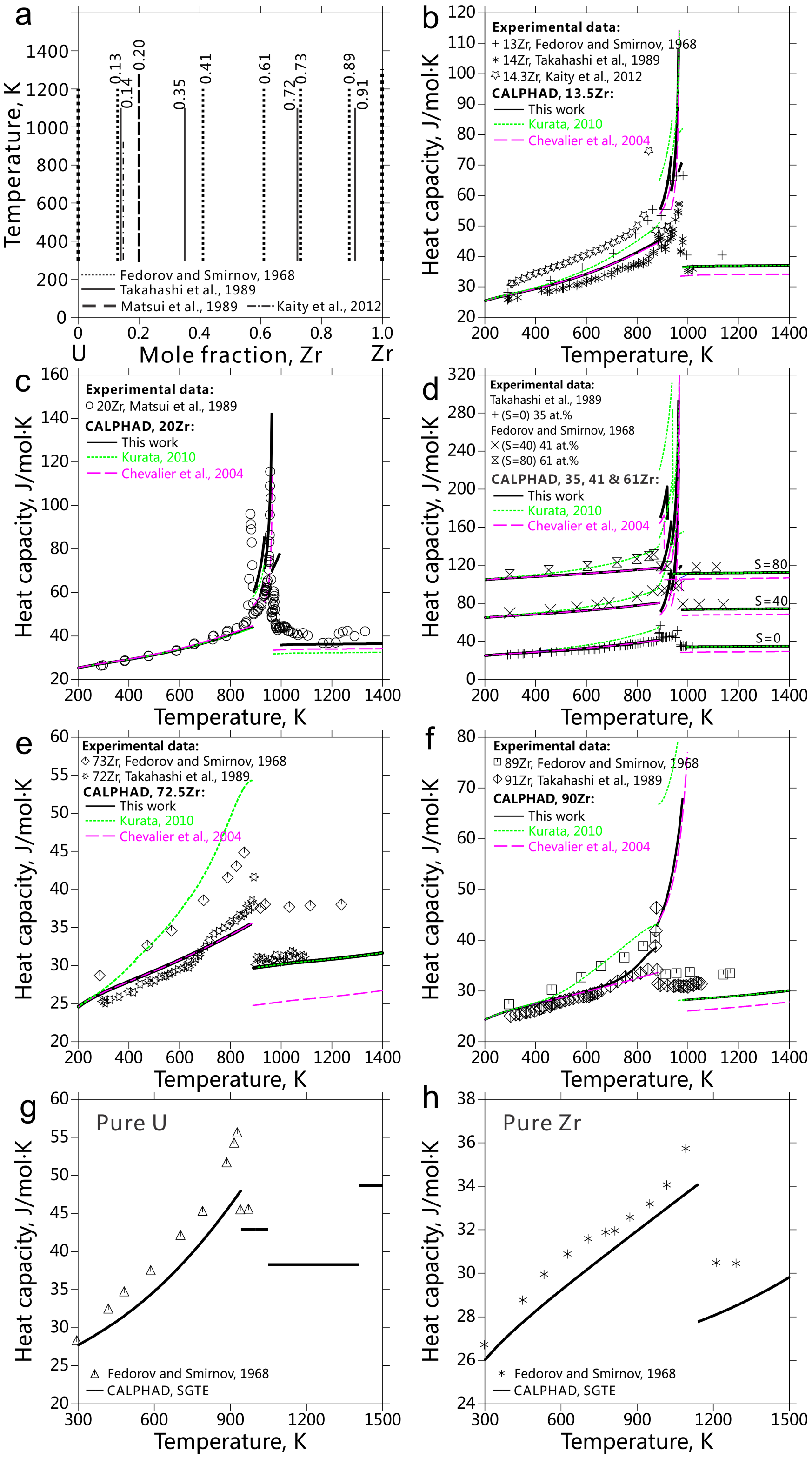

Figure 2.3. Comparison of heat capacity of the U-Zr alloys between CALPHAD model-prediction [11, 40] and experimental data [45, 52, 53, 60]. (a) Summary of the experimental information provided by different research groups [45, 52, 53, 60], (b) Comparison for the U-13, 14 and 14.3

Zr alloys, the CALPHAD-type results are plotted for U-13.5Zr alloy; (c) comparison for the U-20Zr alloy; (d) comparison for the U-35, 41, and 61 Zr alloys. S denotes the unit for shifting the heat capacity in the plot to facilitate reading; (e) Comparison for the U-72 and 73Zr alloys, the CALPHAD-type results are plotted for U-72.5Zr alloy; (f) Comparison for the U-89 and 91Zr alloys, the CALPHAD-type results are plotted for U-90Zr alloy; (g) Comparison for pure U; (f) Comparison for pure Zr.

There are four invariant reactions in the U-Zr system in total, which are listed in Table 2.1. The largest discrepancies among different measurements can be found in the one related to the δ phase as shown in Figure 2.2(f), which is mainly caused by the difference of the experimental homogeneity range of the δ phase (see Figure 2.2(e)). As discussed previously, the experimental results reported by Akabori *et al*. [49] are considered to be the most accurate. Therefore, the results by Duffey and Bruch [47] will not be rigorously fitted during the thermodynamic optimization.

There are a considerable number of experimental measurements of thermodynamic properties of U-Zr alloys. Fredorov and Smirnov [60] and Takahashi *et al*. [53] determined the heat capacities of a series alloys from room temperature up to 1200 K. Matsui *et al*. [52] determined the heat capacity of $U_{0.8}Zr_{0.2}$ alloy from 300 to 1300 K. Very recently, the heat capacity of the U-14.3 at.% Zr alloy were measured again using differential scanning calorimetry by Kaity *et al*. [45]. The information of alloy composition and temperature ranges for the experiments on heat capacity is summarized in Figure 2.3 (a). The determined phase transition temperatures in thermal analysis are plotted in Figure 2.2 for comparison.

Limited experiments were designed for measuring activities in the U-Zr alloys by several research groups. Very recently, Murakami *et al*. [61] determined the activity of uranium in the δ phase between 700 and 839 K through the electrochemical reaction (see Figure 2.4). However, since the concentration of Zr in the δ phase was not clearly determined, the results by Murakami *et al*. [61] should not be considered to be accurate enough for thermodynamic optimization. Kanno *et al*. [44] determined the activities of U and Zr in solid and liquid at 1723, 1773, and 1823 K, respectively, using the Knudsen effusion mass spectrometry. It should be noticed that the concentration of impurity of the determined U-Zr samples are rather high in the work of Kanno *et al*. [44]. Later, Maeda *et al*. [43] use the same method determined the activities of uranium in U-Zr alloys at 1673, 1723, 1773, 1823 and 1873 K. The measurements show significant difference with the one reported by Kanno *et al*. [44] as shown in Figure 2.5.

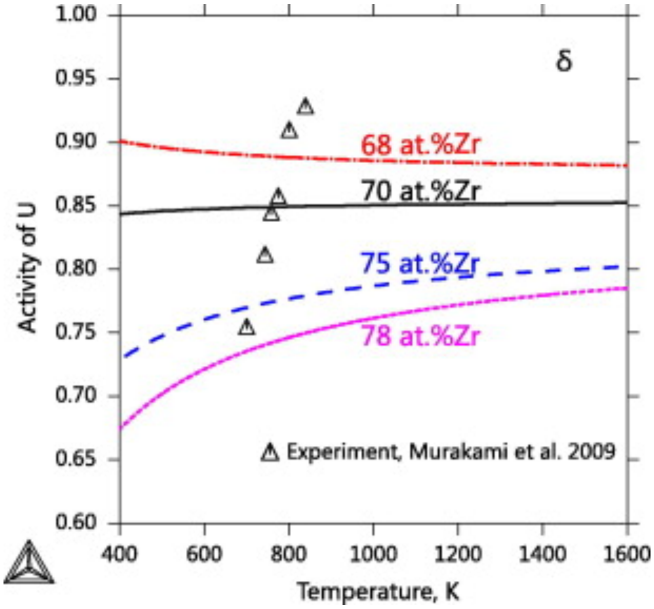

Figure 2.4. Comparison of activity of U in the δ phase between experimental results by Murakami *et al*. [61] and CALPHAD model-prediction in this work

There is scarce experimental information on the enthalpy of mixing for the solid phase. The only one available is from the work by Nagarajan *et al*. [62], who determined the enthalpy of formation of the δ phase with 66.7 at.% Zr using high temperature solution calorimetry. However, the experimental uncertainty is as high as ± 10.1 kJ/mol, since the thermal effects of dissolution of pure uranium, zirconium and δ compounds in liquid aluminum solvent have a large experimental uncertainty. As a consequence, the *ab initio* calculations on the enthalpy of mixing for the δ phase performed in this work will help us to gain insight into thermodynamic properties of the δ phase.

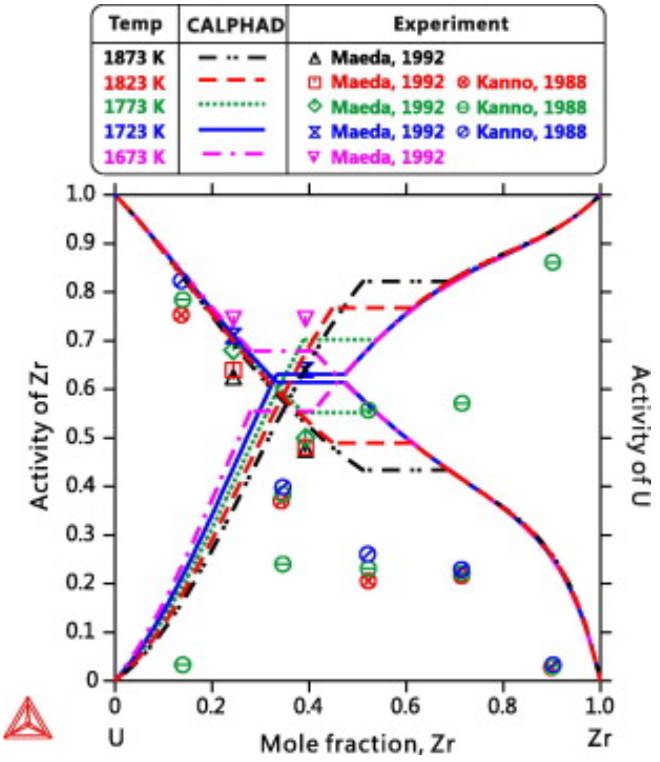

Figure 2.5. Comparison of activity of U and Zr in the U-Zr alloys at different temperatures. Reference for U is the liquid phase, while for Zr is hcp α(Zr). Different colors indicate different temperatures for both symbols (experimental data) and curves (calculations).

The U-Zr system has been investigated in *ab initio* studies [63-67] only recently. Landa, Soderlind and Turchi [65-67] are among the first to do so. They calculated the ground state properties of the BCC and δ phases in the U-Zr system based on Density Functional Theory in the General Gradient Approximation (GGA). The resulted enthalpy of mixing of BCC phase from their calculations using the Korringa–Kohn–Rostoker method in the Atomic Sphere Approximation (KKR-ASA) was very close to those from their own calculations using the Full Potential Linear Muffin-Tin Orbitals (FP-LMTO) method and a previous CALPHAD modeling by Kurata [10]. The partial ordering of the δ phase was also confirmed in their study. However, they did not calculate other phases, and beyond GGA correlation and relativistic effects were not explicitly explored in their study. To further understand the thermodynamic behavior of the U-Zr system, all solid phases of U-Zr are treated and the strong on-site correlation effects and relativistic effects especially spin-orbit coupling (SOC) are taken into account in the present *ab initio* calculations.

2.4 Thermodynamic Models

Table 2.2. Crystal structure information of solid phases in the U-Zr system

Phase	Structure name	Pearson Symbol / Space Group / Prototype
γ(U,Zr)	Bcc_A2	cI2 / Im$\bar{3}$m / W
β(U)	Tetragonal_A$_b$	t*P*30 / *P4$_2$/mnm* / β(U)
α(U)	Orthorhombic_A20	o*C*4 / *Cmcm* / αU
α(Zr)	Hcp_A3	h*P*2 / *P6$_3$/mmc* / Mg
δ	Hexagonal_C32	h*P*3 / *P6/mmm* /AlB$_2$

There are six phases in the U-Zr system: liquid, γ(U,Zr), α(U), β(U), δ, α(Zr). The crystal structural information of different solid phases is listed in Table 2.2, and the models used in different assessments [11, 37-40, 68] are given in Table 2.3.

2.4.1 Disordered Solution Phases

There are five disordered phases in the U-Zr system: α(Zr), α(U), β(U), γ(U,Zr), and the liquid phase, which are described by the substitutional solution model. The Gibbs energy of a substitutional solution phase is described by the following equation:

$$G_m^\varphi = x_U \, {}^oG_U^\varphi + x_{Zr} \, {}^oG_{Zr}^\varphi + RT\left(x_U \ln x_U + x_{Zr} \ln x_{Zr}\right) + {}^{ex}G_m^\varphi \qquad (1)$$

where x_{U} and x_{Zr} are the mole fractions of component elements respectively. ${}^oG_U^\varphi$ and ${}^oG_{Zr}^\varphi$ represent the Gibbs energies of pure U and pure Zr with the φ structure. The

Gibbs energy of pure element *i*, ${}^{o}G_{i}$, was taken from the SGTE (Scientific Group Thermodata Europe) database [69], which is referred to the enthalpy of its stable state at 298.15K. The next term is the Gibbs energy from ideal mixing, while R is the gas constant and T is the temperature. The last term, the excess Gibbs energy of the φ phase, is described by the Redlich-Kister polynomial [70]:

$$ {}^{ex}G_{m}^{\varphi} = x_{U}x_{Zr}\sum_{i=0}^{n} {}^{i}L_{UZr}^{\varphi}\left(x_{U}-x_{Zr}\right)^{i} \qquad (2) $$

where ${}^{i}L$ are the binary interaction parameters and take the form of $a + b \cdot T$ with "*a*" and "*b*" being the model parameters to be optimized in terms of experimental data.

Table 2.3. Thermodynamic models and optimized CALPHAD type parameters for different phases of the U-Zr system in this work (Case 1B).

Phase	Model	Thermodynamic parameters (Energy unit: J/mol·atom)
Liquid	(U,Zr)	${}^{0}L_{U,Zr}^{Liquid} = 33465.2 - 14.55 \cdot T$
		${}^{1}L_{U,Zr}^{Liquid} = 19809.4 - 18.07 \cdot T$
γ(U,Zr)	(U,Zr)	${}^{0}L_{U,Zr}^{\gamma} = 23296.9 - 8.97 \cdot T$
		${}^{1}L_{U,Zr}^{\gamma} = 21149.0 - 16.93 \cdot T$
		${}^{2}L_{U,Zr}^{\gamma} = 2841.6$
β(U)	(U,Zr)	${}^{0}L_{U,Zr}^{\beta} = 27980.5$
α(U)	(U,Zr)	${}^{0}L_{U,Zr}^{\alpha} = 30312.4$
α(Zr)	(U,Zr)	${}^{0}L_{U,Zr}^{\alpha(Zr)} = 24184.4$
δ	$(Zr)_{1/3}(U,Zr)_{2/3}$	${}^{o}G_{Zr}^{\delta} = 527.5 + {}^{o}G_{Zr}^{\alpha(Zr)}$
		${}^{o}G_{Zr_1U_2}^{\delta} = 588.19 + 2.768 \cdot T + 0.333 \cdot {}^{o}G_{Zr}^{\alpha(Zr)} + 0.667 \cdot {}^{o}G_{U}^{\alpha(U)}$
		${}^{0}L_{Zr:U,Zr}^{\delta} = -2209.76 + 6.740 \cdot T$
		${}^{1}L_{Zr:U,Zr}^{\delta} = 236.686 - 5.874 \cdot T$

2.4.2 Ordered Intermetallic Compound

The δ phase is the only intermetallic phase in this binary system, and it can be modeled using the sublattice model [71]. The δ phase has a hexagonal structure with three atoms in the conventional cell (see Table 2.2 for detailed symmetry information). The (0, 0, 0) sites (which we will call the A sublattice) are preferentially occupied by Zr atoms and the (2/3, 1/3, 1/2) and (1/3, 2/3, 1/2) sites (which we will call the B sublattice) are occupied by U and Zr atoms randomly. The sublattice sites occur with stoichiometry AB_2. Landa *et al.* [65, 66] confirmed that this configuration has the lowest energy from their density functional study. It is noteworthy that there are different choices of the sublattice model for describing the δ phase in the U-Zr system. In the work by Chevalier *et al.* [39], the δ phase was modeled as the stoichiometric phase as U_3Zr_7, which is not reasonable, and thus was later revised by the same authors [40] to $(Zr)_1(U,Zr)_2$. Another type of sublattice model was adopted by Kurata *et al.* [11, 38] as $(U,Zr)_1(U,Zr)_2$. Therefore, there will be four end-members available: U, U_1Zr_2, U_2Zr_1 and Zr, which covers the whole composition range, and thus may generate more freedom to adjust the phase range of the δ phase in higher-order systems. In order to illustrate the difference of these two sublattice models, *ab initio* calculations are performed in this work to calculate the Gibbs energy term for the end-members. With these end-member values one can select the reasonable thermodynamic model from the above two. A detailed discussion is performed in Section 5.

In this work, the Gibbs energy function of the δ phase can be described by compound energy formalism [71], and the Gibbs energy per mole of atoms of the $(Zr)_1(U,Zr)_2$ phase could be described by the following equation:

$$G_m^{\delta} = y_U^{II} \cdot {}^{o}G_{Zr:U}^{\delta} + y_{Zr}^{II} \cdot {}^{o}G_{Zr:Zr}^{\delta} + (2/3)RT\left(y_U^{II}\ln y_U^{II} + y_{Zr}^{II}\ln y_{Zr}^{II}\right) + y_U^{II} y_{Zr}^{II} L_{Zr:U,Zr}^{\delta} \qquad (3)$$

where y_U^{II} and y_{Zr}^{II} are the site fractions of U and Zr in the second sublattice respectively. ${}^{o}G_{Zr:U}^{\delta}$ and ${}^{o}G_{Zr:Zr}^{\delta}$ are the Gibbs energies of the end-members: Zr_1U_2 and Zr of the δ phase. $L^{\delta}_{Zr:U,Zr}$ represents the interaction energy term between U and Zr in the second sublattice with only Zr being present in the first sublattice. The model of $(U,Zr)_1(U,Zr)_2$ adopted by Kurata *et al.* [11, 38] can be described in a similar way.

2.5 *Ab initio* Calculations for the BCC and δ Phases

All calculations are performed in the general framework of DFT[28, 29] using the Vienna *Ab initio* Simulation Package (VASP)[72, 73]. The electron-ion interaction is described with the projector-augmented-wave (PAW) method[74] as implemented by Kresse and Joubert[75]. The PAW potentials used treat $6s^2 6p^6$ $7s^2$ $5f^3$ $6d^1$ and $4s^2 4p^6 5s^2 4d^2$ as valence electrons for U and Zr, respectively. The exchange-correlation functional parameterized in the GGA[76] by Perdew, Burke and Ernzerhof (PBE)[30] is used. All of our calculations were spin-polarized, and in more accurate calculations Spin-Orbit Coupling (SOC) effects were also included. The SOC was included by starting with the magnetization density from non-SOC calculations and relaxing both the magnitude and direction of the spin magnetic moments self-consistently. To describe correlation effects beyond GGA, we used the DFT + U method [77] in the simplified rotationally invariant implementation of Dudarev *et al.* [31] The double counting term used was the so called fully localized limit (FLL) [77]. In this implementation DFT + U adds an additional orbital dependent potential to the Hamiltonian that is a function of the effective Hubbard parameter U_{eff}. The stopping criteria for self-consistent loops used were 0.1 and 1 meV tolerance of total energy for the electronic and crystal structure relaxation, respectively. We did not explicitly set stopping criterion for forces on ions, but they were generally 0.1 eV/Å or smaller when the total energy was converged according to the criteria above. Cut-off energies of 450 eV were used throughout all calculations. The

Brillion zone was sampled with k-point meshes generated according to Monkhorst–Pack's formalism [78]. The number of k-points used depends on the crystal unit cell size; generally, 1000 k-points per reciprocal atom (KPPRA) or more were used in structural relaxation calculations, and over 5000 KPPRA were used in more accurate static calculations afterwards. We have tested both k-point mesh and cut-off energy convergences for each system studied using spin-polarized scalar relativistic DFT-GGA calculations, and verified that using above settings the total energy is converged to within 3 meV/atom, and closer to 1 meV/atom in most cases.

We here describe the types of structural cells used in the calculations. For pure U and Zr allotropes, that is, α(U), β(U), γ(U), α(Zr) and γ(Zr), we used the known primitive unit cells [79-83]. Alloy phases in the study usually contain at least some configurational disorder, so we used supercells with the proper composition and crystal structure that were generated and optimized to yield the most random possible correlations within the first four nearest-neighbour pairs using the Special Quasi-random Structure (SQS) technique [84], as implemented in the Alloy Theory Automated Toolkit (ATAT) [85]. For the intermediate δ phase, three supercells at 33.3, 66.7 and 100 at.% Zr were used, of which the two at 33.3 and 100 at.% Zr correspond to the two end-members, $(Zr)_1(U)_2$ and $(Zr)_1(Zr)_2$, and the one at 66.7 at.% Zr has 12-atom and is generated and selected using SQS. For the BCC solid solution phase γ(U, Zr), five 16-atom supercells at 6.3, 25.0, 50.0, 75.0 and 93.8 at.% Zr were used. Among them, the three cells with 25.0, 50.0, and 75.0 at.% Zr were exactly those recommended by Jiang *et al.* [86]. The other two at 6.3 and 93.8 at.% Zr were generated and selected using SQS as well. Calculations were initiated with lattice parameters obtained directly or extrapolated from the best available experimental data [49, 79-83]. Low and intermediate temperature structures were relaxed afterwards. For the high temperature structures of γ(U, Zr), we found that after full relaxation they collapsed into lower symmetry structures similar to α(U) and β(U), which shows alloyed γ(U, Zr) has similar lattice instability as elemental γ-U that has been reported previously [87]. As a result, only volume relaxation was performed for them to best model their cubic crystalline symmetry. The enthalpy of formation for any $U_xZr_{(1-x)}$ phase, except the BCC solid solution, was obtained from the calculated energies by the relation:

$$E^{form}_{U_xZr_{1-x}} = E^{0}_{U_xZr_{1-x}} - x \cdot E^{0}_{\alpha(U)} - \left(1-x\right) \cdot E^{0}_{\alpha(Zr)} \quad (4)$$

where U_xZr_{1-x} is the chemical formula for the alloy, $E^{0}_{U_xZr_{1-x}}$ is the calculated ground state total energy, and x is the mole fraction of U with $0 \leq x \leq 1$. α(U) and α(Zr) are used as end point references. The enthalpy of formation for the solid solution phase γ(U, Zr) with formula U_xZr_{1-x} is defined as follows:

$$E^{form}_{\gamma(U_xZr_{1-x})} = E^{0}_{\gamma(U_xZr_{1-x})} - x \cdot E^{0}_{\gamma(U)} - \left(1-x\right) \cdot E^{0}_{\gamma(Zr)} \qquad (5)$$

for which γ(U) and γ(Zr) are used as the references. The above two enthalpies can be straightforwardly converted to each other using the energetic difference between the two sets of references. Further details on the *ab initio* methods and data is given in Ref. [34].

2.6 Results and Discussion

2.6.1 Phase Diagram and Phase Equilibria

The thermodynamic description of the U-Zr system was performed using the Thermo-Calc software package [88]. Optimization for the self-consistent parameters was carried out by the PARRROT module of the Thermo-Calc software [89]. According to the assessed parameters in this work, the phase diagram of the U-Zr system is plotted in Figure 2.1 and Figure 2.2, which also show the comparison between reported experiments and available thermodynamic descriptions.

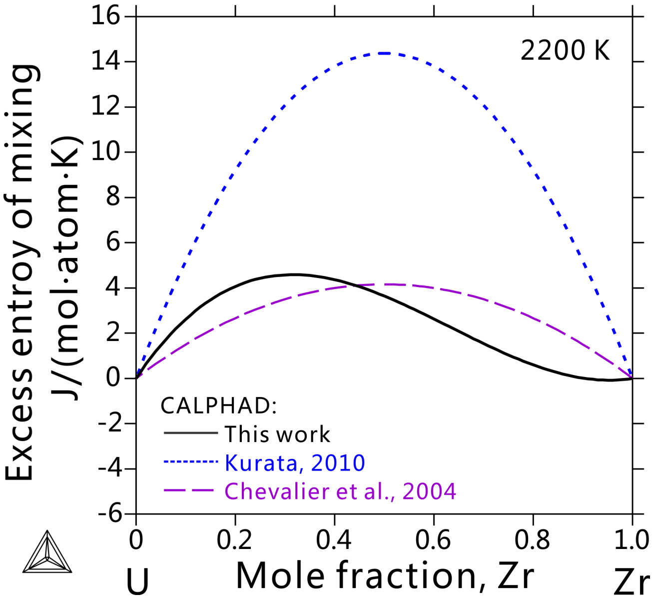

Figure 2.6. Comparison of the excess entropy of mixing at 2200 K for the liquid phase among different thermodynamic modeling [11, 40].

In Figure 2.1, experimental information [37, 42-45] of the phase boundary shows consistency only up to 50 at.% Zr. Furthermore, experimental data from Summers-Smith [42] and Kanno *et al*. [44] show large discrepancies. Both thermodynamic assessments performed in this work and the one performed by Chevalier *et al*. [40] fit to the experimental phase transition temperature measured in the work of Refs. [37, 42, 43] but not the one by Kanno *et al*. [44]. As will be discussed later, the measured activity of U and Zr by Kanno *et al*. [44] also show significant difference with other experimental data [43] and our assessment.

Since the experimental information of the phase equilibria related to the liquid phase are rather limited, it is helpful to have some additional criteria to judge the quality of different liquid thermodynamic descriptions. Here we consider the values of the excess entropy of mixing of the liquid. In Figure 2.6, the excess entropy of mixing is plotted at 2200 K for the liquid phase. Obviously, the calculation according to the work by Kurata [11] shows a much larger excess entropy of mixing than the ones by Chevalier *et al*. [40] and this work. This large value indicates that Kurata has a strong interaction between atoms even in the high temperature range in the liquid phase, which would be quite unusual for a metallic alloy. As discussed in the work by Okamoto [90], the excess entropy of mixing of an intermetallic liquid phase is normally in the range of –10 and 5 J/(mol·atom·K), which can be found in many different metallic systems [57, 90-92]. Thus the excess entropy values of Kurata [11] are likely too large, while ours are consistent with other intermetallic alloys.

A detailed comparison of the solid phase diagram between experiments and different thermodynamic calculations is shown in Figure 2.2. Although the U-Zr system has been thermodynamically assessed several times before, it is easy to observe that there are some considerable differences among these calculations. It should be noted that since the thermodynamic assessments performed by Ogawa *et al*. [68] and Leibowitz *et al*. 1989 [37] were not based on the lattice stability by SGTE [69], they are not considered in the present discussion for comparison. To keep the comparison tractable, only the most updated version of the thermodynamic modeling performed by Chevalier *et al*. [40] and Kurata [11] (but not their earlier versions [38, 39]) are considered for comparison. However, one should also notice that in the work by Chevalier *et al*. [40], the thermodynamic description of the tetragonal (Zr) as the unstable structure is described differently than in the SGTE database [69]. The use of the SGTE database for the pure elements is very widely adopted in CALPHAD modeling to make it easy to construct thermodynamic databases based on the same basis of unary, and the reason for this unconventional approach in Chevalier's model [40] is not clear.

According to Figure 2.2, the homogeneity range of the δ phase calculated from this work is distinctly different from the previous assessments [11, 40]. This difference is at least in part because the experimental data reported in the work by Akabori [49] was assigned with the highest weight during the present thermodynamic optimization. For this same reason the calculated homogeneity range of the δ phase in this work agrees well with the one by Akabori [49] within the experimental uncertainty. The arguments for weighing the Akabori data preferentially, which are based on purity and accuracy of the experimental techniques, are given in Section 2.

Another discrepancy with previous models is the thermodynamic description of the BCC miscibility gap below 50 at.% Zr, which is plotted in Figure 2.2 (c). As mentioned in Section 2, the experimental phase boundary of the BCC miscibility gap should not be considered to have high accuracy. A comparison of the BCC miscibility gap between different models over the whole composition and temperature ranges is shown in Figure 2.7. The model-described consolute temperature and composition of the BCC phase, γ(U,Zr), in this work agree with the one by Kurata [11], but not Chevalier *et al.* [40]. Further experiments to validate the model-predictions on the BCC miscibility gap are needed.

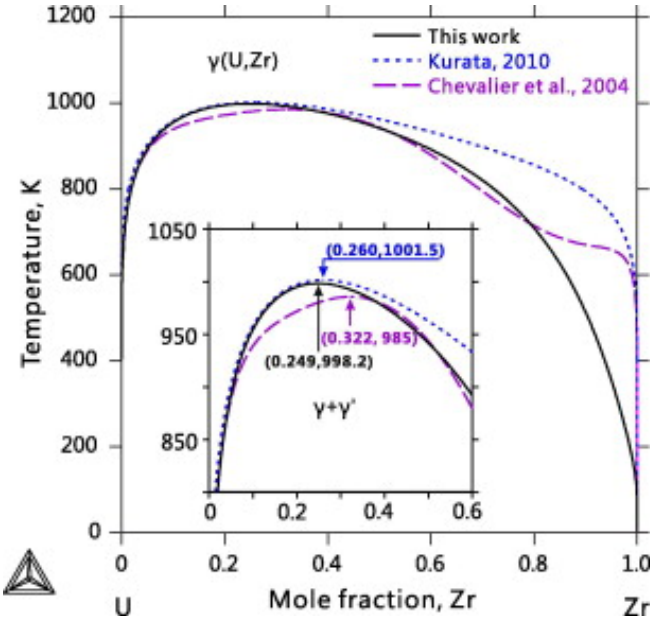

Figure 2.7. Model-predicted BCC miscibility gap of the U-Zr system according to different CALPHAD type modeling [11, 40].

A comprehensive comparison of the invariant equilibria between the experiments and models is presented in Table 2.1. It should be noted that the composition of the reaction related to the δ phase is not well determined yet. The difference of the reaction temperature among CALPHAD modeling is relatively large for the eutectoid reaction: γ(U,Zr) = δ + α(Zr). It is also worth noting that the present calculation agrees well with the experimental temperature measured by Holden [59], Duffey and Bruch [47], and Rough *et al*. [46], as well as the one evaluated by Sheldon [41]. While the other two CALPHAD calculations [11, 40] show higher temperatures, and only agree with the phase diagram compilation in the ASM handbook [58]. More seriously, the peritectoid reaction, γ(U,Zr) + α(U) = δ, was described as the eutectoid type: γ(U,Zr) = α(U) + δ, by Chevalier *et al*. [40] as shown in Figure 2.2 (c) and Table 2.1. It is noteworthy that the present calculation agrees well with the experimental data of the phase boundary for the γ(U,Zr) to δ transformation determined by Rough *et al*. [46] (see Figure 2.2 (c)).

2.6.2 Thermodynamic Properties

Figure 2.4 and Figure 2.5 show the comparison of the activity of U and Zr in different phases. In Figure 2.5**,** the model-predicted activity of Zr agree with the one measured by Maeda [43], but not Kanno [44]. According to Maeda [43], the disagreement may be due to the choice of material used for the Knudsen cells in the experiment. Obviously, from Figure 2.5, the experimental phase transition temperature by Kanno [44] is inconsistent with the other experimental data. During optimization, we found that any attempt to fit experimental activities from Kanno [44] makes the model inconsistent with other experimental data for the phase diagram and thermodynamic properties related to the liquid phase. We therefore believe that the Zr activity data from Kanno [44] should not be used in fitting the thermodynamic model.

Figure 2.4 is the comparison of the activity of U in the δ phase between this work and experimental data by Murakami *et al*. [61]. The calculated results generally agree well with the experimental data. However, the activity of U in the δ phase apparently varies a lot with the concentration of Zr in the δ phase. Assuming Zr dissolves homogenously in the δ phase, the increase of the activity of U determined by experiment [61] is more rapid than the model-prediction. This disagreement can be due to the small composition fluctuation of the solute in experiments, and will not have a significant impact on the phase diagram or other essential thermodynamic properties. Moreover, as pointed out in Section 2, the accuracy of the measurement by Murakami *et al*. [61] should be questioned, since the concentration of Zr in the δ phase of samples was not well-determined. Further experiments to confirm the current model-prediction are warranted.

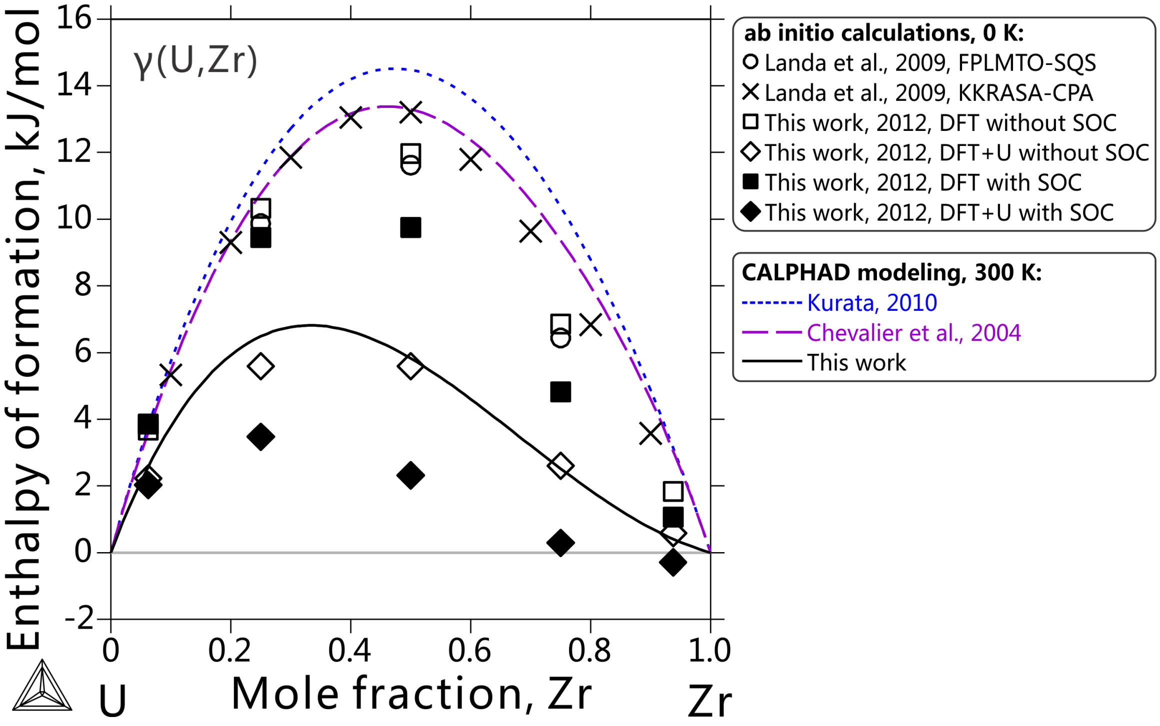

Figure 2.8. Comparison of the enthalpy of formation of the γ(U,Zr) phase between *ab initio* calculations at 0 K and CALPHAD modeling at 298 K. SOC means Spin-Orbit Coupling.

The comparison of enthalpy of formation of the γ(U,Zr) phase is shown in Figure 2.8. Since there are no direct experimental data available, model-predictions extracted from the phase equilibria are quite valuable. The *ab initio* calculations by Landa *et al.* [66, 67] using DFT agree well with the previous assessments by Chevalier *et al.* [40] and Kurata [11], which are all quite close to our own *ab initio* claculations using DFT as well. The CALPHAD modeling and *ab initio* calculations using DFT + *U* in this work also agree with each other, but show notably lower and more asymmetric values than the previous CALPHAD and *ab initio* studies. While it is not possible at this point to rigorously determine which values are correct, it is worth noting that the DFT + *U ab initio* methods used in this work are shown in Ref.[34] to be more accurate for U-Zr alloying energetics than the DFT methods used in previous studies [66, 67]. We therefore believe that the somewhat lower and more asymmetric enthalpy of mixing found in the present studies is likely to be closer to the true U-Zr thermodynamics than that obtained in the previous thermodynamic [11, 40] and *ab initio* [66, 67] models.

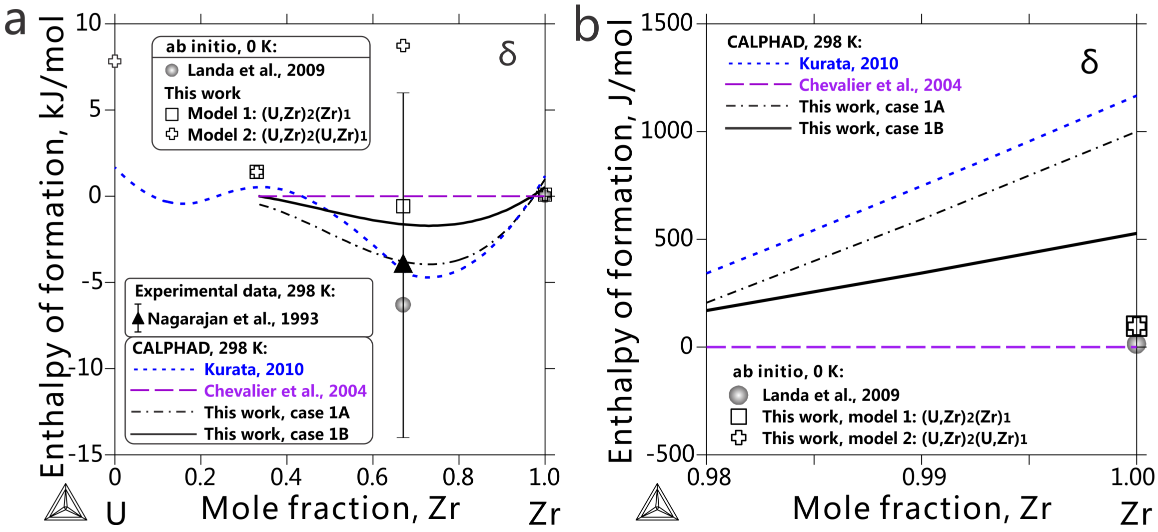

Figure 2.9. (a) Comparison of the enthalpy of formation for the δ phase among *ab initio* [66], CALPHAD [11, 40] and experimental data [62]. In CALPHAD modeling from the present work, case 1A is using the energy difference of (Zr) between α-hcp and δ structures as 1000 J/mol for model 1 $(Zr)_1(U,Zr)_2$, while case 1B is using 527.5 J/mol for model 1 $(Zr)_1(U,Zr)_2$. (b) Magnification of (a) from 98 to 100 at.% Zr.

In Figure 2.9**,** the enthalpy of formation of the δ phase at 298 K is calculated in this work in order to compare with the previous assessments [11, 40], *ab initio* calculations [66] as well as experiments by Nagarajan *et al.* [62]. As noted in section 3.2., there are two choices of the thermodynamic model for the δ phase in the previous assessments. According to the crystal structure information, the most suitable model for the δ phase is: $(Zr)_1(U,Zr)_2$. This is named as model 1 in the discussion, which was employed by Chevalier *et al.* [40]. The second model (model 2) is the one proposed in the work of Kurata [11], which is $(U,Zr)_1(U,Zr)_2$. This model 2 may allow more flexibility than model 1 as U is allowed to occupy the first sublattice, which generate four end-members cover the whole composition range. To assess if this occupation is likely we compared the model 2 U_1Zr_2 energy with that of a candidate model 1 δ-phase structure $(Zr)_1(U,Zr)_2$. The details of the calculation are given in Ref. [34]. As shown in Figure 2.9, the enthalpy of formation with 66.7 at.% Zr calculated using the model 1 $(Zr)_1(U,Zr)_2$ structure (open square symbol) yields a significantly lower energy than the model 2 U_1Zr_2 structure (open cross symbol). These calculations suggest that the more constrained model 1 is the most appropriate model for the δ phase.

It should be noted that even though the model adopted in the work by Kurata [11] is the second model: $(U,Zr)_1(U,Zr)_2$, the calculated enthalpy agrees well with the experimental data determined by Nagarajan *et al*. [62] and the *ab initio* calculations reported by Landa *et al*. [66, 67]. However, this apparent agreement with experiment cannot be considered as a strong reason to believe either the previous *ab initio* data or Kurata's model over the *ab initio* data and model found for the δ phase in this work, since the uncertainty of the measurement by Nagarajan *et al*. [62] is as large as 10.1 kJ/mol and therefore includes all the calculated and modeled values being considered.

The disagreement in the enthalpy of the δ phase between the previous *ab initio* studies of Landa *et al*. [66, 67] and the *ab initio* studies shown here does suggest that there is significant work still to be done to establish a robust *ab initio* approach. However, as mentioned above, Xie *et al*.[34] have shown that when using an approximate exchange-correlation term[30], the DFT + U functional we are using gives more accurate energetics than the standard DFT functional. This result would argue that our are possibly closer to the true values. However, it should also be noted that Landa *et al*. [66, 67] treat the disordered phase with the Coherent potential Approximation (CPA), while we have used an SQS approach to disorder, and use an exact Muffin-Tin Orbitals (EMTO) code, while we have used the PAW approach in a plane wave code (VASP). These differences can also play a significant role. As these energy differences are relatively small between the different methods a large number of comparisons would have to be made to establish which approach is truly the most robust and what are the typical error bars for each technique when compared to experiment. Such benchmarking has been initiated by Xie *et al*., and can be found further discussed in Ref. [34].

Interestingly, it is found that the CALPHAD model-prediction is strongly influenced by the thermodynamic description of the pure Zr end-member for the δ phase. The energy difference of pure Zr between the δ and α-hcp structure considered in the present thermodynamic modeling is different with the conventional value 5000 J/mol used in the CALPHAD community for database construction. In the present thermodynamic modeling, we found that 5000 J/mol is too large to consider as a reasonable value to describe the δ phase, as this large value can cause errors when extending the composition homogeneity range of the δ phase to the Zr-rich side during the thermodynamic assessment. Moreover, according to the *ab initio* calculations in Landa's work [66, 67] and ours, the energy difference for pure Zr between the δ and hcp phase are rather small (97 J/mol in this work, less than 50 J/mol in the work by Landa *et al*. [66]). Since the *ab initio* predictions are for 0 K, in this work, we assume that there will be a somewhat larger energy difference of (Zr) between δ and hcp structure at 298 K, which may not necessary to be exactly the same as, but should be close to, the value calculated from DFT in this work. As a consequence, the energy difference of (Zr) between these two different structures, $\Delta E_{(Zr)}$, is also assessed during the thermodynamic modeling of the δ phase in this work. During thermodynamic optimization, it is found that a higher value of $\Delta E_{(Zr)}$ will generate a lower enthalpy of formation for the δ phase at 66.7 at.% Zr, as shown in case 1A in Figure 2.9 ($\Delta E_{(Zr)} = 1$kJ/mol). A reasonable assessed $\Delta E_{(Zr)}$ = 527.5 J/mol will generate a value for δ-phase enthalpy of formation at 66.7 at.% as -1627.5 J/mol at 298 K, which agrees fairly well with the *ab initio* results in this work using DFT + *U* (-579 J/mol at 66.7 at.% Zr). This coupling between the $\Delta E_{(Zr)}$ and the δ-phase formation enthalpy is reasonable and can be easily explained by the tie-line construction using the common tangent of the Gibbs energy curves at 298 K. However, according to the present optimization, it should be noted that the phase diagram will not be significantly affected by mildly different descriptions of the α(Zr) and δ phases. Although both model-predicted enthalpies of formation of the δ phase are within the range of experimental uncertainty, we believe the one consistent to the DFT + *U* is preferable, because it generates reasonable energetic value that is consistent with both experiments and optimized *ab initio* calculations.

The comparison of the heat capacities from thermodynamic modeling in this work and experimental studies we found is given in Figure 2.3. For U-Zr alloys, the comparison in Figure 2.3 (b) – (f) shows that the present CALPHAD results agree well with the experimental data reported by Takahashi *et al.* [53] and Matsui *et al.* [52] in the full measured temperature range, while the model by Chevalier *et al.* [40] seems to only reproduce well the data in the temperature range below about 900 K and the one by Kurata [11] mainly those in the temperature range above about 900 K. Further, Figure 2.3 (g) and (h) compare the heat capacity for pure U and Zr between the SGTE database and the experimental data by Fedorov and Smirnov [93]. We find that the experimental heat capacities of Fedorov and Smirnov [93] for U and Zr are higher than the SGTE values, which are in agreement with the finding that their heat capacity for U-Zr alloys are also systematically higher than the model-predicted results shown in Figure 2.3. We believe SGTE data as more reliable source as they were obtained from evaluated reliable sources and have been tested over many systems, and therefore believe its possible that the discrepancy between our model and Fedorov and Smirnov [93] may be due to uncertainty included in the experimental data. Finally, we comment that the experimental data of Kaity *et al*. [45] may also have overestimated the heat capacity, since their values for U-14.3Zr in Figure 2.3 (b) are even higher than those of Fedorov and Smirnov [93].

2.7 Conclusions

The U-Zr system has been re-assessed using the CALPHAD approach assisted by *ab initio* calculations. Different choices of thermodynamic models of the δ phase have been explored with the help of *ab initio* calculations. The resulted thermodynamic model of the δ phase reproduces existing experimental data favorably. The thermodynamic parameters of the liquid phase in the current model are expected to have some improvement over those in the previous model[11], as supported by the fact that the predicted liquid phase boundary showed improved agreement with the assessed reliable experimental data. In addition, the modeled predicted heat capacity of this work shows good agreement with assessed reliable experiments data both at low and high temperatures, which was not the case for the two previous CALHAD models[11, 40]. However, some controversy exists on the BCC phase for which our model predicts the enthalpy of formation to be considerably smaller than the previous two CALPHAD models[11, 40] and DFT calculations [65-67], which are nevertheless closer to the DFT +

U results in this work. Further experiments need to be performed to resolve this controversy. Finally, this work demonstrates that a combined approach of *ab initio* and CALPHAD modeling can be used to develop a full thermodynamic description of an actinide alloy system, and we expect that this approach can be extended to other systems.

3 *Ab initio* calculations of the U and U-Zr systems

Note: This chapter has been published as a peer-reviewed article in Physical Review B[34], and the article was adapted for use in this thesis document.

3.1 Chapter Abstract

Ab initio calculations have been performed on all solid phases of U metal and U-Zr alloy, the basis of a promising metallic fuel for fast nuclear reactors. Based on generalized gradient approximation (GGA), both density functional theory (DFT) in its standard form and the so-called DFT plus Hubbard U (DFT + U) modification are evaluated. The evolution of calculated energetics, volume, magnetic moments, electronic structure and f-orbital occupation as functions of the effective Hubbard U parameter U_{eff} is carefully examined at U_{eff} from 0 to 4 eV. DFT is found to overestimate energetics, underestimate volume, downward shift some f-bands near Fermi level and overestimate f-orbital occupation against existing experimental and/or computational data. The error is ~0.07 eV/atom in terms of enthalpy which affects phase stability modeling for δ(U,Zr) and γ(U,Zr). DFT + U at U_{eff}=1-1.5 eV offers clear improvement on these calculated properties (~0.05 eV/atom in terms of enthalpy) and in general still neither promotes ordered magnetic moments nor opens unphysical band gap, which occur at higher U_{eff} values. The empirical U_{eff} values of 1-1.5 eV are close to but smaller than the theoretical estimations of 1.9-2.3 eV that we obtain from the linear response approach. U_{eff} is found to vary only slightly (≤0.24 eV) between different phases and at different compositions of U and U-Zr, and thus a single U_{eff} =1.24 eV, which is the statistical optimal from

energetic fitting is suggested for both U and U-Zr. Besides correlation, the relativistic effect of spin orbit coupling (SOC) is also systematically explored. SOC is found to lower energy, increase volume and split the 5*f* shell above Fermi level and reduce *f*-orbital occupation. The effect predominates in the unoccupied states and is very small on all these calculated ground state properties (<0.02 eV/atom in terms of enthalpy).

3.2 Introduction

U-Pu-Zr-MA (MA=Minor Actinides Np, Am, Cm) alloy is a promising metallic fuel for fast nuclear reactors with advantages in thermal conductivity, burn-up, recycling, and other factors[4]. Its safety and efficiency are nevertheless affected by issues like constituent redistribution and fuel swelling, which are closely related to its phase stability. Better modeling of the phase stability will help improve the design and guide the safe and optimal use of this fuel, and model validation is important towards this objective. U metal and U-Zr alloy are the primary constituents of this multicomponent fuel and have most experimental and computational data available[41, 94-97], and hence are ideal systems for validating *ab initio* approaches.

Many DFT[28, 29] based *ab initio* calculations of U metal have been reported[63, 98-113] since the 1970s. An important conclusion of some early studies[99, 101] is that for U metal, GGA[76] improves local density approximation (LDA)[29] to the exchange-correlation functional, with which the calculated structural and elastic properties reproduce experimental data quite well. However, how accurate GGA can calculate the total energy is less certain due to the lacking of direct experimental thermochemical data for validation. Moreover, βU is often neglected and has been calculated only recently

[109, 113]. Different from U metal, U-Zr alloy has just been explored in *ab initio* studies[50, 64, 66, 114] recently. Landa *et al.*[66] calculated the BCC solution phase γ(U,Zr) with the Korringa–Kohn–Rostoker method in the Atomic Sphere Approximation (KKRASA). The resulted enthalpy of mixing is very close to that from their own Full Potential Linear Muffin-Tin Orbitals (FPLMTO) calculations and a previous CALPHAD model[38]. Interfacing with Monte Carlo simulation and adding phonon contribution they further calculated its decomposition temperature, which is about 350 K higher than experimental miscibility gap. Besides γ(U,Zr), they also confirmed the partial ordering of the intermediate phase δ(U,Zr) with the Exact Muffin-Tin Orbital (EMTO) method and explained its existence in the U-Zr system using *d*-orbital occupation change relative to ωZr. Other studies[50, 64, 114] used the Projector Augmented Wave (PAW) method. Huang and Wirth[64, 114] calculated the defect formation energy and migration barriers in α(U). Basak *et al.*[50] obtained the energy difference between γ(U,Zr) and δ(U,Zr) at 66.7 at.%Zr to be 4.87 kJ/mole. As far as we are aware, previous calculations of U-Zr alloy have not treated the terminal solution phases β(U) and α(Zr), and the accuracy of calculated energetics is just starting to be assessed.

In general, when studying actinide systems, it is important to understand the extent of and validate modeling approaches on correlation and relativistic effects. Here we briefly summarize recent experimental and computational studies of these effects in U metal. Opeil *et al*[115, 116] compared the density of states and band structure calculated from DFT-GGA to their experimental photoemission spectra and band energy dispersion intensity map of a αU single crystal. They find that overall the experimental spectral characteristics are reproduced, however, one of the calculated DOS peaks and several *f*-

bands just below Fermi level are shifted downwards with respect to measured spectra. Going beyond LDA/GGA, Chantis *et al.*[117] calculated the electronic structure of αU with the many-body quasiparticle self-consistent *GW* (QSGW) method. They found that, compared to DFT-LDA, *f*-band from QSGW is shifted with respect to remaining metallic bands by about 0.5 eV and also significantly narrower leading to smaller *f*-orbital occupation. They conclude that the correlations predominate in the unoccupied part of the *f* states, and explain that LDA/GGA can reproduce the structural and elastic properties of U metal well because of the overall low *f*-orbital occupation. However LDA/GGA still misplace several bands just below Fermi level and overestimates *f*-orbital occupation, which may have more pronounced effects on other properties like energetics, the accuracy of which have not been systematically tested yet. Regarding the relativistic effects, Soderlind[105] found that SOC mainly changes the unoccupied part of the density of states for αU and explained that its effect on calculated properties is not large again due to the relatively small *f*-orbital occupation. Alloying with Zr further complicates the situation because Zr may change the *f*-orbital occupation and promote both correlation and relativistic effects, as in many heavy fermion U intermetallics[118]. However, previous *ab initio* studies[50, 64, 66, 114] of U-Zr have not tested any beyond DFT approach and have neglected SOC, to the best of our knowledge.

Summarizing the existing literature, several important questions remain open: how accurate can DFT based on LDA/GGA alone calculate energetics for U and U-Zr? How much better can we get going beyond them? To answer them, we validate based on GGA the standard DFT and also the beyond DFT functional DFT + *U*[119] in this study. DFT + *U* has shown success on many U intermetallic alloys. For example, DFT + *U* correctly reproduces the electronic and magnetic structures of U intermetallic compounds $UGe_{2[120]}$, UPd_3[121] and $UPt_{3[122]}$ that DFT-GGA fails to. It is therefore interesting to see if similar improvement also exists on U-Zr. For U metal, there is an initial evaluation of DFT + U on αU[123]. However, merely two U_{eff} points at 0.5 and 3 eV are tried for αU phase only. A more systematic study covering broader U_{eff} range for all solid phases would be favored. Moreover, if DFT + U turns out to be a good model for U and U-Zr, what Hubbard U parameters should be used for them is also unsettled. Previous studies use U=0.7 and J=0.44 eV for UGe_2 in Ref. [120] and U=2 and J=0.5 eV for UPd_3 in Ref. [121] and for UPt3 in Ref. [122]. Such values are chosen based primarily on intuition rather than systematic empirical fitting, theoretical estimation or direct experiment measurement. Therefore, we seek to determine U_{eff} for U and U-Zr here as well.

This paper studies all stable solid phases of both U and U-Zr. Based on GGA, we validate both the standard DFT and the DFT + U functionals at a wide range of U_{eff} from 0 to 4 eV and explore the effect of SOC in terms of calculated energetics, volume, magnetic moments, electronic structure and *f*-orbital occupation. The accuracy of calculated energetics is determined by comparing them to best-established thermodynamic models in addition to available experiments. The Hubbard U parameters for U metal and U-Zr alloy are determined both empirically by fitting to existing experimental and/or computational data and also theoretically by using the linear response approach[124].

This manuscript proceeds as follows. Section II describes the computational details including materials systems, *ab initio* methods and parameters, definitions of energetics, as well as approximations adopted and their justifications. In Section III, the evolution of energetics, volume, magnetic moments, electronic structure and *f*-orbital occupation as functions of U_{eff} is examined from $U_{\mathrm{eff}} = 0$ to 4 eV in calculations both with and without SOC included. The empirically fitted U_{eff} is compared to theoretically calculated Hubbard U values and suggestions are given on choosing U_{eff} for U and U-Zr. Finally, Section IV summarizes the conclusions of this study.

3.3 Computational Details

Table 3.1. Solid phases of U, Zr metal and U-Zr alloy.

Phase^a	Structure name	Space Group	Composition (Zr at.%)	Cell Size (atoms/cell)	SQS used?	*k*-point mesh	Expt. Refs.
αU	Orthorhombic_A20	Cmcm	0	2	No	8×8×8	Ref. [125]
α(U)			6.3	16	Yes	5×5×5	
βU	Tetragonal_A$_b$	P4$_2$/mnm	0	30	No	3×3×6	Ref. [80]
β(U)			3.3	30	Yes	3×3×6	
γU	Bcc_A2	$Im\bar{3}m$	0	1	No	17×17×17	Ref. [81]
γ(U,Zr)			6.3 25.0 50.0 75.0 93.8	16	Yes	6×6×6	Ref. [126]
βZr			100	1	No	17×17×17	Ref. [127]
δ(U,Zr)	Hexagonal_C32	P6/mmm	66.7	12	Yes	9×9×9	Ref. [49]
ωZr			100	3	No	9×9×13	Ref. [128]
α(Zr)	Hcp_A3	P6$_3$/mmc	93.8	16	Yes	4×4×4	Ref. [82]
αZr			100	2	No	8×8×8	

[a] A phase is elemental/alloyed when labeled without/with parenthesis.

All solid phases of U metal, Zr metal and U-Zr alloy, as summarized in Table 3.1 are calculated in this study. Zr metal is not the main object of this study but is also calculated to serve as an end member reference. Among them, elemental U and Zr metal phases, that is, αU, βU, γU, αZr, ωZr and βZr are modeled using their primitive unit cells[80-82, 125, 127, 128]. U-Zr alloy phases, that is, α(U), β(U), α(Zr), γ(U,Zr), and δ(U,Zr) all have certain structural disorder, and thus are modeled using supercells that are generated based on their experimental crystal structures[49, 80, 82, 125, 126] using the Special Quasi-random Structure (SQS) method[84] as implemented in the Alloy Theory Automated Toolkit (ATAT)[85]. Firstly, the terminal solution phases α(U), β(U) and α(Zr) are studied with one solute atom in supercells of 16, 30 and 16 atoms, respectively. The solute concentrations have exceeded the solubility limit, but we believe they are acceptable model systems to probe the dilute alloying effect, as the solute atoms are at least 5.2, 5.6, and 7.7 Å apart in these cells, respectively. Secondly, the single solution phase BCC γ(U,Zr) is studied by five 16-atom supercells with composition 6.3, 25.0, 50.0, 75.0, 93.8 at.% Zr (i.e., 1, 4, 8, 12, and 15 Zr atoms in supercells of 16 atoms), respectively. Among them, the three at 25.0, 50.0, 75.0 at.% Zr are exactly those recommended by Jiang *et al.*[86]. The other two at 6.3 and 93.8 at.% Zr are generated and selected in the same spirit. 16-atom has already been found in Ref. [86] to well reach energy convergence. Finally, the only intermediate phase δ(U,Zr) has crystal structure of C32[49] in Strukturbericht designation which is isomorphous with ωZr[128]. More specifically, it has two distinct Wyckoff sites—site A is of Wyckoff Symbol 1*a* and coordinate (0, 0, 0) and site B of 2*d* and (1/3, 2/3, 1/2). The occupation is 100 at.% Zr on site A and approximately 50 to 70 at.% Zr on site B. Here we calculate a representative structure with 50 at.% Zr occupation on site B that has the overall chemical formula UZr_2. We find that 12-atom already converges the energy and therefore a 12-atom SQS supercell structure is selected and used in this study.

All calculations are performed in the general framework of DFT[28, 29] using the Vienna *Ab initio* Simulation Package (VASP)[72, 73]. The electron-ion interaction is described with the projector-augmented-wave (PAW) method[74] as implemented by Kresse and Joubert[75]. The PAW potentials used treat $6s^2 6p^6$ $7s^2$ $5f^3$ $6d^1$ and $4s^2 4p^6 5s^2 4d^2$ as valence electrons for U and Zr, respectively. The exchange-correlation functional parameterized in the GGA[76] by Perdew, Burke and Ernzerhof (PBE)[30] is used. The stopping criteria for self-consistent loops used are 0.1 meV and 1 meV tolerance of total free energy for the electronic and ionic relaxation, respectively. We do not explicitly set force as a stopping criterion, but when the total free energy is converged according to the criteria above, the Hellmann-Feynman forces on atoms are generally <0.1 eV/Å or smaller. Cutoff energy of 450 eV is used throughout all calculations. The Brillouin zone is sampled with Monkhorst–Pack[78] k-point meshes given in Table 3.1.We have tested that such k-point meshes and cutoff energy converge the total energy at least to 3 meV/atom, most even to 1 meV/atom. The partial occupancies are set using the Methfessel-Paxton method[129] of order one with a smearing width of 0.2 eV. All calculations have included spin polarization.

DFT as a theory is exact, but the exchange-correlation functional such as GGA used in this study is approximate. We hereinafter refer to the standard DFT functional and the DFT + U[119] functional simply as DFT and DFT + U, respectively. When we "compare" DFT and DFT + U below, it is important to remember that we are only comparing the two functionals based on GGA, not the two theories that are usually referred to under the same acronyms.

DFT + U[119] is an effective action theory that uses a functional of both the spin density, as in DFT, and the local spin-density matrix of some correlated subspace. The correlated subspace is typically defined using local, atomic-like orbitals as basis sets, and in this work we use the standard implementation[130] in VASP. The screened interactions for these orbitals must be determined (i.e., U and J) and then the local interaction potential for this subspace is constructed within Hartree-Fock formalism. Given that one typically employs standard approximations (i.e., LDA/GGA) for the density dependent potential, a double counting correction must be used to remove the local correlations that are already present in LDA/GGA, and in this work we use the standard fully localized limit (FLL) double courting correction[77]. Following Dudarev *et al.*[31], we use a version of DFT + U functional that does not introduce explicit local exchange J term and is dependent on the effective value of $U_{\mathrm{eff}}=U-J$. The functional recovers DFT exactly at $U_{\mathrm{eff}}=0$. This practice should be justified given that we are using a spin-density functional which already contains the effects of local exchange. Note that VASP still needs input of U and J parameter separately even though only $U_{\mathrm{eff}}=U-J$ is used. Due to historical reasons, we do not set J to 0 but instead to 0.51 eV and vary U from 0.51 to 4.5 eV. Therefore, U_{eff} spans between 0 and 4 eV (strictly, 3.99 eV). The Hubbard U potential is applied only on U sites for U metal and U-Zr alloys, and is not used at all for elemental Zr metal.

The additional local spin-density matrix in the DFT + U functional introduces vast spin and orbital degrees of freedom, which pose a significant challenge to numerical optimization algorithms and often result in metastable solutions. We frequently encounter such problem in our systems. To avoid metastable solution, Dorado *et al.*[131] suggested to perform a manual combinatorial search for the ground state orbital configuration and impose it afterwards. We cannot afford such search here due to the large numbers of systems and U_{eff} points we pursue. Alternatively, Meredig *et al.*[132] proposed in the *U*-ramping method to perform a series of calculations starting from DFT and extending adiabatically towards the point at desired U_{eff} with each step initializing from the charge density and relaxed structure of its previous one. We find Meredig *et al.*'s original approach cannot always guarantee low energy solution for our systems. In general calculated properties of our systems are smooth functions of U_{eff} that have a clear three-stage pattern, as detailed in Section III. Metastable solutions are quite easy to identify as they break the pattern. Take αU as an example. We find that DFT correctly reproduces its experimental paramagnetic structure[79, 133]; DFT + *U* promotes spin and orbital polarization, which are still quenched at small U_{eff} by kinetic energy but will eventually overcome it after U_{eff} is larger than a critical value. So the ground state solutions of DFT + *U* to αU should have zero magnetic moments at small U_{eff}'s until a critical point after which moments emerge. Metastable solutions are characterized by wrong magnetic moments. If we follow Meredig *et al.'s* original proposal[132] to do *U*-ramping starting from DFT (i.e., U_{eff} =0), we obtain solutions without moments even when U_{eff} is larger than 2.5 eV which has passed the critical U_{eff} and should have moments. On the other hand, if we do reverse *U*-ramping starting from large U_{eff} (large enough to promote net polarization, e.g., 4 eV for U and U-Zr) and gradually reducing U_{eff}, we always obtain solutions with large moments even when U_{eff} is smaller than 1.5 eV which has passed the critical U_{eff} and should have no or small moments. Fortunately, low energy solutions are usually successfully obtained from the first series below 1.5 eV and from the second series above 2.5 eV. The problem lies within a critical region of 1.5-2.5 eV where solution from the two series, though have very different magnetic moments, are very similar in energy. We thus have to manually select the low energy solution from the two series in the critical region between 1.5-2.5 eV. With such care and efforts, we should have removed most metastable solutions in this study.

To compare with the U_{eff} from empirically fitting, we implement the linear response approach proposed by Cococcioni and de Gironcoli[124] in VASP and theoretically evaluate Hubbard U for U(ranium) in both U metal and U-Zr alloy with self-consistent calculations described in the following. For elemental phases αU, βU and γU, 2×2×2, 1×1×1 and 3×3×3 supercells of their primitive cells that have 16, 30 and 27 atoms with Monkhorst–Pack k-point meshes of 6×6×4, 3×3×6 and 5×5×5, respectively are used. For alloyed phases α(U), β(U), α(Zr), δ(U,Zr) and γ(U,Zr), the same supercells and *k*-point meshes given in Table 3.1 are used. All other numerical details are also the same as given above. Localized potential perturbations of -0.1, -0.05, 0, 0.05, and 0.1 eV are applied on symmetrically distinct U atomic site (called Hubbard site) to build the full response matrix and ultimately calculate U_{eff} following the procedures outlined in Ref. [124].

Regarding the relativistic effects, VASP always includes the mass-velocity and Darwin corrections using the methods proposed in Refs. [134, 135] and thus all of our calculations are at least so-called scalar-relativistic. In more accurate calculations, we have included the effect of SOC in the *LS*-coupling limit. For convenience, in this paper we designate calculations as SOC and noSOC, respectively for those with and without SOC included. SOC uses quantization axis (0, 0, 1) (i.e., z axis), starts with the charge density from noSOC and relaxes both the magnitude and the direction of the magnetic moments self-consistently. All noSOC calculations treat magnetism collinearly while

SOC non-collinearly, with one exception: when evaluating the band structure of αU, noSOC calculations also treat magnetism non-collinearly to avoid a bug that corrupts the calculated band structure.

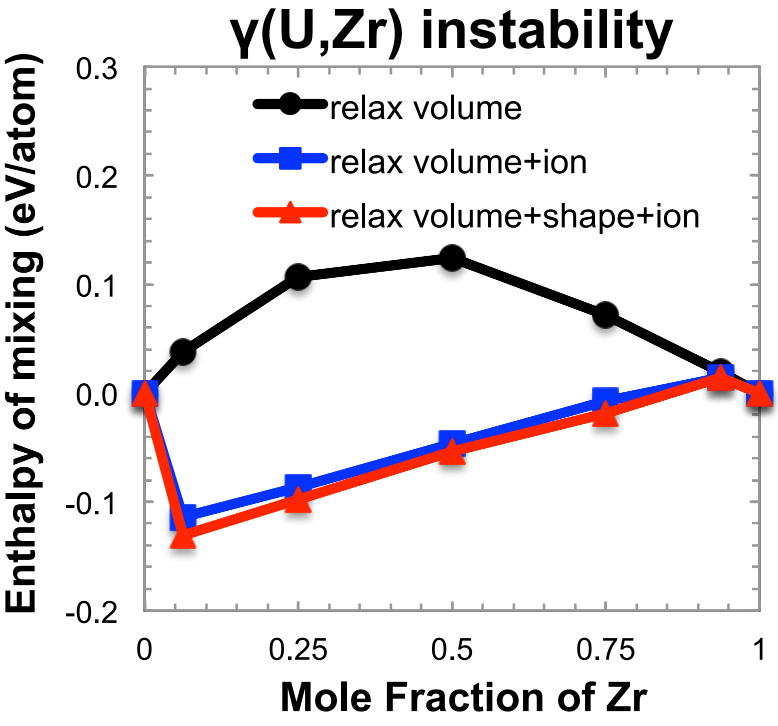

Figure 3.1 Enthalpy of mixing for γ(U,Zr) calculated from DFT-noSOC with different degrees of structural relaxations.

We define the enthalpy of formation for any U and U-Zr phase as $E^{\text{form}}_{\text{U}_{1-x}\text{Zr}_x} = E^{0}_{\text{U}_{1-x}\text{Zr}_x} - (1-x)E^{0}_{\alpha\text{U}} - xE^{0}_{\alpha\text{Zr}}$, where $\text{U}_{1-x}\text{Zr}_x$ is the chemical formula, x is the mole fraction of Zr with $0 \leq x \leq 1$, and $E^{0}_{\text{U}_{1-x}\text{Zr}_x}$, $E^{0}_{\alpha\text{U}}$, $E^{0}_{\alpha\text{Zr}}$ are the calculated total energy per atom for $\text{U}_{1-x}\text{Zr}_x$ and the two references αU and αZr at zero K, respectively. For elemental phases, enthalpy of formation defined here is essentially what the CALPHAD community refers to as lattice stability. Similarly, we define the enthalpy of mixing specifically for the solution phase γ(U,Zr) as $E^{\text{mix}}_{\text{U}_{1-x}\text{Zr}_x} = E^{0}_{\text{U}_{1-x}\text{Zr}_x} - (1-x)E^{0}_{\gamma\text{U}} - xE^{0}_{\beta\text{Zr}}$ for which γU and βZr are used as the references. The two enthalpies can be straightforwardly converted to each other using the energetic differences between the two sets of references. Besides, the two ground state phases αU and αZr's cohesive energies are also calculated by referencing to U and Zr atom, respectively. They are each modeled in their respective atomic ground state with a simple cubic cell of 14Å using a Γ point only k-point mesh.

All calculations have relaxed all structural degrees of freedom—volume, ion position, and cell shape—for all phases except γU and γ(U,Zr), which are only volume-relaxed. γU has been proved to be strongly mechanically unstable at low temperatures[87, 97]. Indeed we find that fully relaxing even its one-atom primitive cell may collapse γU's cell shape from BCC, especially in SOC calculations .We could not find γ(U,Zr)'s structural instability documented in the literature, nor have we performed any elastic constants or phonon dispersion calculations for it as Refs. [87, 97] did for γU, but we suggest that γ(U,Zr) should also be mechanically unstable based on the following evidence. As shown in Figure 3.5 the enthalpy of mixing for γ(U,Zr) is significantly negative as long as we allow the ion positions to relax, especially on the U-rich end, which is in contradiction with the existence of miscibility gap for γ(U,Zr); examining the relaxed structures, ions displace significantly from the vicinities of BCC superlattice sites and approach those of βU, resulting in quasi-β(U) solution structures; similar is true if we only relax cell shape, although the extent is small because these SQS supercells are already of very low symmetry (monoclinic or triclinic). To mitigate the strong mechanical instability in our zero K calculations, we follow the practices of the previous calculations[16, 27] and perform only volume relaxation for γU and γ(U,Zr). Such practice is physical for γU because it has no ion position or cell shape degree of freedom in its one-atom primitive BCC cell that we use. For γ(U,Zr), not relaxing the lattice should also only have minimal effect because the lattice constants are based on experiments and these low-symmetry SQS supercells have no internal structural degree of freedom, which is demonstrated by the closeness between the enthalpies from volume+shape and volume+shape+ion relaxed calculations in Figure 3.1. However, the lacking of ion relaxation for γ(U,Zr) sounds unsettling because ions need to be relaxed to accommodate the size mismatch between U and Zr. Nevertheless, the radius for U and Zr atom is 1.56 and 1.60 Å in U and Zr metal[136], respectively, differing only by 2.5%. In γ(U,Zr), Huber and Ansari[126] suggest that the size of U and Zr atom should also be comparable based on their lattice constant measurements. As a result, such constrained relaxation should only introduce trivial error due to the small size mismatch between U and Zr. However, it may still entangle with the differences between DFT and DFT + *U* and between noSOC and SOC that are our main objects of model validation. Therefore, we should put less weight on γ(U,Zr) than other phases next.

We do not include finite temperature effects and focus only on exploring relativistic and correlation effects in this study, which is a reasonable and necessary first step for future model validation including them. As a result, our calculated energetics are for zero K, and corresponding experimental data—the most common standard for model validation—are mostly not available. A common approach to mitigate this problem is to extrapolate experimental energetics using thermodynamic models such as those developed with the CALPHAD method[25]. The extrapolations in CALPHAD models are generally most reliable only at room temperature and above, and it is commonly assumed that energetics do not change much from 0 to 300 K. Therefore, here we choose enthalpies at 300 K from three best-established recent CALPHAD models[11, 33, 40] of U-Zr and the SGTE database for pure elements[69] to validate our *ab initio* energetics. Relevant experimental data[62, 137] are also employed. The comparability between CALPHAD and *ab initio* energetics is still debatable due to temperature difference and issues like mechanical instability[138-140]. Our premise is that we consider all solid phases of U and U-Zr in this study and if we obtain statistically significant results on energetics that are also consistent with other properties like electronic structure, the conclusion should be robust.

3.4 Results and Discussion

3.4.1 Energetics

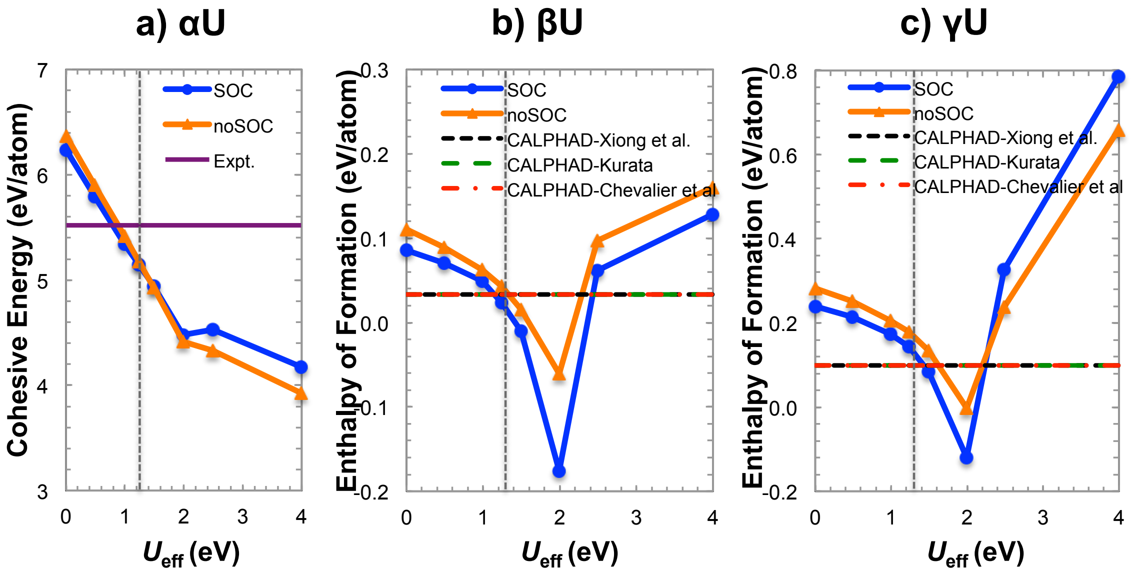

Figure 3.2. Energetics for U metal: a) cohesive energy for αU; enthalpy of formation for b) βU and c) γU. The vertical dash reference line is at U_{eff}=1.24 eV. Experimental cohesive energy of αU is from Ref. **[136]**; CALPHAD models are from Xiong *et al.* **[33]**, Kurata**[11]**, and Chevalier *et al***[40]** which all use the same SGTE data for pure elements**[69]** and give the same enthalpy of formation for βU and γU.

The enthalpies of formation for all solid phases of U metal and U-Zr alloy except γ(U,Zr) are plotted in Figure 3.2 and Figure 3.3, respectively. αU is used as a reference when calculating the enthalpies, so its cohesive energy is given instead. A major observation is that DFT (i.e., U_{eff}=0 eV) overestimates the energetics considerably for all the systems calculated here. The deviation is over 0.8 eV/atom for cohesive energy of αU and mostly over 0.05 eV/atom for enthalpy of formation of other phases (The values are given in Table 3.2 and their statistics in Table 3.3). Particularly, for δ(U,Zr) which is stable at low temperature and therefore should have negative enthalpy of formation at 0 K, DFT calculation gives a considerably positive enthalpy of formation, 0.043 eV/atom, while CALPHAD models gave -0.013[33], -0.045[11] and 0 eV/atom[40] and an available calorimetry experiment*[62]* gave -0.04±0.11 eV/atom (-4.0±10.1 kJ/mole). Our DFT result is, however significantly different from Landa *et al.*'s DFT result of -0.065 eV/atom[66], which is quite negative. We give a detailed analysis of the discrepancy here. The key differences between Landa *et al.*'s *ab initio* approach and ours are 1) method to treat the disordered B site—we use SQS and they use the CPA; and 2) basis sets and potential—we use PAW and they use EMTO, although neither PAW nor EMTO is a strictly full potential method. The first difference (i.e., CPA vs. SQS) can probably be ruled out as a source of large discrepancy, because as we will show later below our DFT calculations using PAW-SQS do well reproduce the enthalpy of mixing for γ(U,Zr) from Landa *et al.*'s KKRASA-CPA calculations[66], which is also very close to their FPLMTO-SQS calculations. Now consider the second difference (EMTO vs. PAW). PAW is fully capable of modeling both U and U-Zr. For U metal, PAW was shown in a number of previous studies[108-110] to reproduce its structural, elastic and phase stability properties reasonably well. As an example, we compare our calculated enthalpy of formation for γU in Table 3.2. Our PAW calculation gives 0.241 eV/atom, which is very close to FPLMTO's 0.223 eV/atom[105], FPLAPW's 0.265 eV/atom[102], and LCGTO-FF's 0.249 eV/atom[102] and is essentially the same as that of another PAW study[108] (0.24 eV/atom, not tabulated in Table 3.2). Besides U metal, our PAW calculations reproduce the mixing enthalpy of γ(U,Zr) from Landa *et al.*'s EMTO and FPLMTO calculations as already mentioned above. What about EMTO? Interestingly, the same group of authors Bajaj and Landa *et al.* in another study[141] found a similarly large difference between their calculations using EMTO and FPLMTO for δ (U,Ti) that has the same C32 crystal structure as δ(U,Zr). For δ(U,Ti), their EMTO calculations gave a formation enthalpy of –0.402 eV/atom (-38.806 kJ/mole) while their FPLMTO gave -0.268 eV/atom (-25.865 kJ/mole)—the difference is -0.134 eV/atom (12.941 kJ/mole). Besides, they also estimated PAW would give -0.368 eV/atom (-35.483 kJ/mole) based on a third party calculation[142], which is also 0.034 eV/atom (3.323 kJ/mole) higher than EMTO's. Because δ(U,Ti) is completely ordered on both A and B site, SQS or CPA is not necessary to model it. So it is clear that the difference should be between EMTO and FPLMTO/PAW methods themselves. Considering EMTO gives a significantly lower enthalpy than FPLMTO for δ(U,Ti) and also that FPLMTO is one of the most accurate full potential method, it is possible that EMTO similarly underestimates enthalpy for δ(U,Zr) and hence explaining the large difference between our and Landa *et al.*'s DFT results.

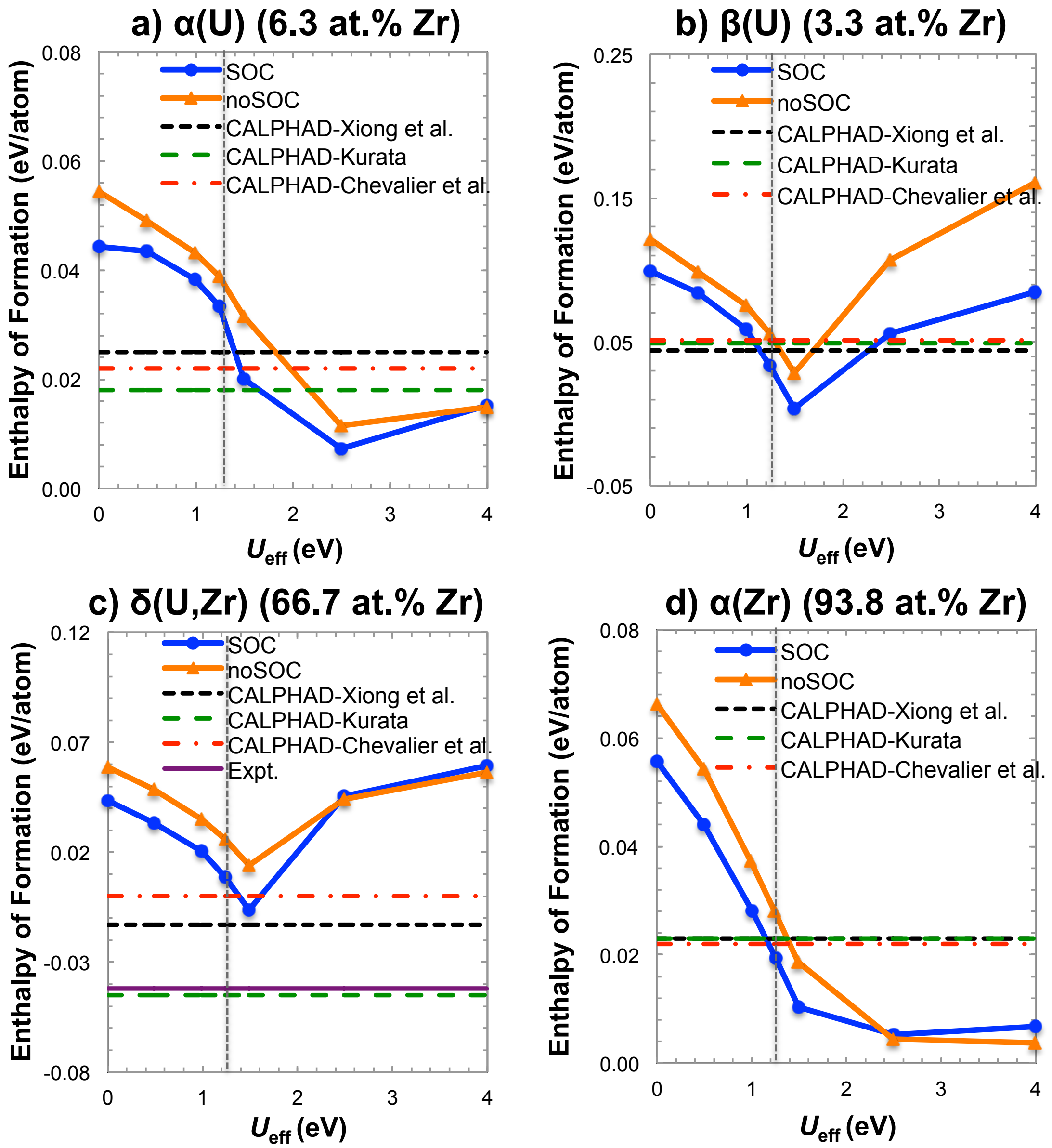

Figure 3.3. Enthalpy of formation for U-Zr alloy: a) α(U) (6.3 at.% Zr), b) β(U) (3.3 at.% Zr), c) δ(U,Zr) (66.7 at.% Zr) and d) α(Zr) (93.8 at.% Zr), The vertical dash reference line is at U_{eff}=1.24 eV. Experimental enthalpy of formation for δ(U,Zr) -0.04±0.11 eV/atom is from Nagarajan *et al.***[62]**; the very large error bar is not plotted in c). CALPHAD models are from Xiong *et al.***[33]**, Kurata**[11]**, and Chevalier *et al.***[40]**.

What about DFT + *U*? Figure 3.2 and Figure 3.3 show that when we apply DFT + *U* with a gradually increased U_{eff}, calculated energetics will firstly decrease and approach CALPHAD values. For example, DFT + *U* gives 0.009 and -0.006 eV/atom at U_{eff}=1.24 and 1.49 eV, respectively for the enthalpy of formation of δ(U,Zr), which are finally reasonable comparing to both experiment and CALPHAD models. *Ab initio* energy curves generally cross the CALPHAD lines in the range between U_{eff} =1 and 1.5 eV. The point of crossing varies somewhat among different systems, and is usually before the point where the energy drops to minimum near U_{eff}=2 eV. After the minimal points, the curves rise drastically and for most systems they will cross the CALPHAD lines again. We stress that neither the minimal nor the second cross should be picked as the empirical U_{eff} and we will explain the reason when we discuss the electronic structure below. Finally SOC and noSOC energetic curves in Figure 3.2 and Figure 3.3 show very similar qualitative features as functions of U_{eff}, but those of SOC are almost always below noSOC in the whole range of 0-4 eV range, showing including SOC will improve the energetics, which reflects correct physics and is totally expected for these actinide systems.

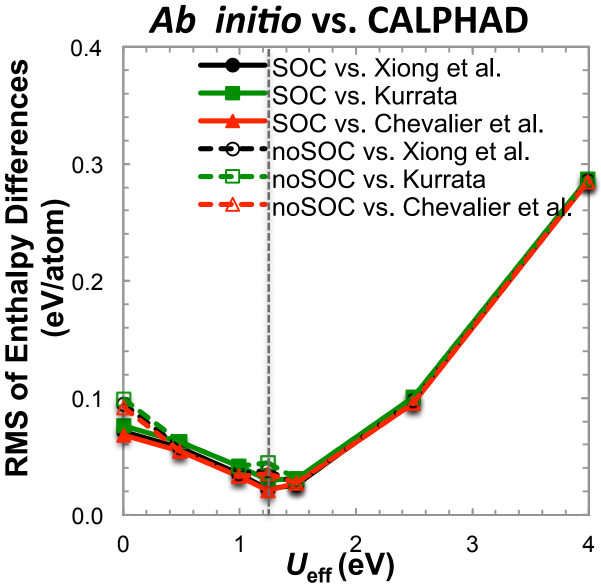

Figure 3.4. RMS of enthalpy differences between *Ab initio* and CALPHAD for all solid phases of U metal and U-Zr alloy except αU and γ(U,Zr). DFT is at U_{eff}=0 eV while DFT + U is at $U_{\mathrm{eff}} > 0$ eV. CALPHAD models are from Xiong *et al*. [33], Kurata[11], and Chevalier *et al.*[40]. See Table 3.3 for quantitative statistics.

Table 3.2. Energetics[a] for solid phases of U, Zr metal and U-Zr alloy (unit: eV/atom).

Phase	Composition (at.% Zr)	DFT (0 K)		DFT+U[b] (0 K)		CALPHAD (300 K)			DFT-Refs. (0 K)	Expt. (var. T)
		noSOC	SOC	noSOC	SOC	Xiong *et al.* [33]	Kurata [11]	Chevalier *et al.* [40]		
αU	0	6.375	6.246	5.421	5.326					5.55[g]
α(U)	6.3	0.058	0.044	0.046	0.041	0.025	0.018	0.022		
βU	0	0.110	0.063	0.086	0.049	0.033	0.033	0.033		
β(U)	3.3	0.125	0.099	0.078	0.062	0.044	0.049	0.051		
γU	0	0.282	0.239	0.205	0.173	0.099	0.099	0.099	0.223/ 0.265/ 0.249[c]	
γ(U,Zr)	6.3	0.038	0.040	0.018 (0.023)	0.006 (0.021)	0.026	0.038	0.036		
	25.0	0.107	0.098	0.037 (0.058)	0.006 (0.036)	0.067	0.119	0.112	0.102[d]	
	50.0	0.124	0.101	0.036 (0.058)	-0.006 (0.024)	0.060	0.150	0.138	0.120[d]	
	75.0	0.071	0.050	0.013 (0.027)	-0.012 (0.003)	0.026	0.107	0.097	0.067[d]	
	93.8	0.019	0.011	0.001 (0.006)	-0.007 (-0.003)	0.004	0.031	0.030		
βZr	100	0.079	0.078			0.076	0.076	0.076		
δ(U,Zr)	66.7	0.058	0.043	0.026 (0.014)	0.009 (-0.006)	-0.013	-0.045	0.000	-0.065[e]	-0.04±0.1[h]
ωZr	100	0.001	0.001			0.005	0.011	0.000	0.006[f]	
α(Zr)	93.8	0.067	0.056	0.042	0.044	0.023	0.023	0.022		
αZr	100	6.160	6.158							6.25[g]

[a] Cohesive energy for αU/αZr, enthalpy of mixing for γ(U,Zr), and enthalpy of formation for all other phases.

[b] Result at U_{eff}=1.24 eV for all is given; additional result at U_{eff}=0.99 eV for γ(U,Zr) and at U_{eff}=1.49 eV for δ(U,Zr) is also given in parenthesis. DFT+U is not applied on Zr in all calculations.

[c] Soderlind's FPLMTO in Ref. [105], and Boettger's FPLAPW and and LCGTO-FF in Ref. [102].

[d] FPLMTO-SQS result of Landa *et al.* in Ref. [66]; their KKR-ASA-CPA result is similar and not tabulated but plotted in Figure 3.5.

[e] EMTO-CPA results of Landa *et al.* in Ref.[66].

[f] Estimated from Landa *et al.*'s FPLMTO result (FIG. 9 in Ref. [66]).

[g] Kittel in Ref. [136].

[h] Experimental result at 298 K from Nagarajan *et al.* in Ref. [62].

Putting all these energetic data together, let us look at the root mean square (RMS) of the differences between *ab initio* and CALPHAD energetics as a function of U_{eff} in Figure 3.4. It shows that no matter which CALPHAD model we compare to, DFT always overestimates enthalpies significantly, and DFT + U always matches CALPHAD values better than DFT at $U_{\mathrm{eff}} \sim$ 1-1.5 eV. A statistically optimal U_{eff} is 1.24 eV although the RMS of differences is very close in the whole 1-1.5 eV range. Note we do not include the cohesive energy for αU in Figure 3.4. The reason is that cohesive energy does not directly impact phase stability as modeled in CALPHAD and including it will sweep the statistics because it is an order of magnitude larger than the formation enthalpies that are our major interest. However, the trend in cohesive energy as a function of U_{eff} is similar to those found for the enthalpies in Figure 3.2 and Figure 3.3.

Table 3.3. Differences in energetics between DFT, DFT + U (1.24 eV) and CALPHAD for all solid phases of U metal and U-Zr except αU and γ(U,Zr)a (unit: eV/atom).

CALPHAD Model	Statistics of Differences[a]	DFT		DFT+*U*	
		noSOC	SOC	noSOC	SOC
Xiong *et al.*[c]	RMS	0.095	0.071	0.038	0.022
	Mean	0.081	0.060	0.027	0.009
	Max positive	0.183	0.140	0.079	0.045
	Max negative[f]	N/A	N/A	N/A	-0.010
Kurata[d]	RMS	0.099	0.076	0.045	0.030
	Mean	0.086	0.065	0.032	0.014
	Max positive	0.183	0.140	0.079	0.053
	Max negative[f]	N/A	N/A	N/A	-0.015
Chevalier *et al.*[e]	RMS	0.092	0.069	0.035	0.021
	Mean	0.077	0.057	0.024	0.006
	Max positive	0.183	0.140	0.079	0.045
	Max negative[f]	N/A[e]	N/A[e]	N/A[e]	-0.017

[a] αU is used as reference and γ(U,Zr) is controversial due to mechanical instability.

[b] RMS is root mean square. Positive/negative difference means *ab initio* enthalpy is larger/smaller than CALPHAD's.

[c] Xiong, *et al.* in Ref [33].

[d] Kurata in Ref.[11].

[e] Chevalier *et al.* in Ref. [40]

[f] N/A means none of *ab initio* values is smaller than CALPHAD's.

The above visual impressions from Figure 3.4 are confirmed by quantitative statistics listed in Table 3.3. The RMS of the differences in energetics between DFT and CALPHAD is approximately 0.10 and 0.07 eV/atom without and with SOC included, respectively. DFT + U at U_{eff}=1.24 eV reduces it to 0.04 and 0.02 eV/atom. These together show that the improvement of DFT + U over DFT is ~0.05 eV/atom (~5 kJ/mole) and the effect of SOC is ~0.02 eV/atom (~2 kJ/mole). The former is a substantial amount of energy in the context of CALPHAD modeling, and the latter, despite smaller in extent, is not negligible either. Our systematic model validation here shows that DFT significantly overestimates energetics, so it is necessary to go beyond DFT to treat correlation in U and U-Zr for applications that requires high energetic accuracy and DFT + U with U_{eff} =1.24 eV seems a promising option. The relativistic effect of SOC is relatively small but should be included for applications that demand best accuracy.

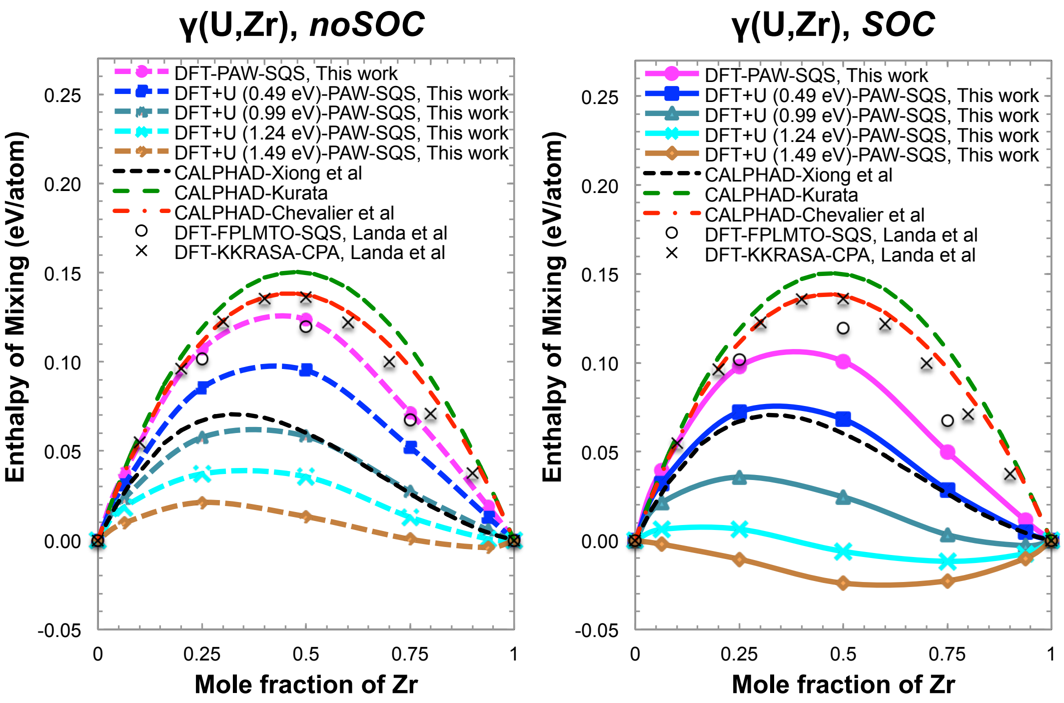

Figure 3.5. Enthalpy of mixing for γ(U,Zr). DFT results are from Landa *et al.*'s noSOC calculations**[66]**; CALPAHD models are from Xiong *et al.***[33]**, Kurata**[11]** and Chevalier *et al.***[40]**. U_{eff} used for DFT + U is given in parentheses in the legend.

With experiences gained on the above well established phases, we now proceed to the controversial high temperature BCC solid solution phase γ(U,Zr), and show its enthalpy of mixing in Figure 3.5. First of all, our DFT calculations using PAW-SQS give the enthalpy to be strongly positive (>0.1 eV/atom) and overall symmetric as a function of composition in the whole region from 0 to 100 at.%Zr. As mentioned above when discussing δ(U,Zr), it is almost identical to Landa *et al.*'s DFT result from FPLMTO-SQS**[66]** (Figure 3.5**,** circles), which is also very close to their DFT result from KKRASA-CPA**[66]** (crosses). Note they do not include SOC in neither of the calculations and we should compare their results to ours in the left figure of Figure 3.5. These DFT results also reproduce Kurata**[11]** (green dash curve) and Chevalier**[40]** *et al*'s (red dash curve)'s CALPHAD results well, all suggesting strong demixing of BCC U and Zr. However, the latest CALPHAD model**[33]** (black dash curve) gives a mixing enthalpy that is 1) only slightly positive and 2) asymmetric with the U-rich end higher. Based on our experience on the other phases in Figure 3.2 and Figure 3.3, our most accurate predictions should be from DFT + *U* at U_{eff} 1-1.5 eV, which very interestingly all also give weekly positive (or even slightly negative on the Zr rich end) and asymmetric mixing enthalpy. It should be pointed out that this latest CALPHAD model by Xiong *et al.*[33] was developed in our group with knowledge of *ab initio* results reported here; however, attempt was deliberately made *not* to fit its model parameters to our *ab initio* results but only to best available experiments in order to provide an independent source of reference. Showing excellent match with experimental phase boundary and heat capacity data in wide composition and temperature ranges, Xiong *et al.*'s CALPHAD model**[33]** is in no way less accurate, and in some ways more accurate than previous CALPHAD models, suggesting that the weaker demixing found here is possible and does not contradict with existing experimental data. Note that our DFT + *U* result at 1.24 eV from SOC is slightly negative on the Zr rich end, and is about 0.04 eV/atom below at the maximum point from that of Xiong *et al.*'s, while the one at U_{eff}=0.99 eV or even 0.49 agrees with it better. It is possible that we should use a smaller U_{eff} value for example 1eV for γ(U,Zr), rather than 1.24 eV, because as we see inFigure 3.2 and Figure 3.3, the point of U_{eff} where DFT + U curves cross CALPHAD does vary slightly between 1 and 1.5 eV among different phases. However, due to the possible error in our *ab initio* energetics resulted from constrained relaxation and other approximations and also considering the error bar of CAPHAD energetics, the two sets of energetics can still be considered as reasonably consistent. Besides all the above modeling studies, one experimental measurement of the mixing enthalpy of γ(U,Zr) by emf at 1073 K**[137]** is available (not plotted in Figure 3.5). The emf result is substantially negative explaining the complete miscibility between BCC U and Zr at such high temperature. Due to the huge temperature difference, our modeling results cannot be directly compared to it in terms of quantitative values. Yet it is interesting to note that the emf enthalpy is also *asymmetric* with U-rich end higher. The fact that both our DFT + U calculation and the latest CALPHAD model**[33]** reproduce the same asymmetry of the experimental emf data suggests that our prediction is possibly closer to the true value. Overall, there are still controversies on this high temperature phase due to the scattering of previous results, the scarcity of direct experimental thermochemical data, and the uncertainty resulted from our model approximations, and we call for more experimental measurements to resolve this controversy.

3.4.2 Volume

Next we present the calculated volume, which is tabulated in Table 3.4 for all systems of U, Zr metal and U-Zr alloys at the two U_{eff} points of 0 and 1.24 eV only, as well as plotted in Figure 3.6 for U metal and U-Zr alloy only in the whole region of U_{eff} =0-4 eV. Again, we discuss the results in terms of DFT vs. DFT + *U*, and noSOC vs. SOC.

First, for the three phases of U metal, volumes calculated by DFT are smaller than the experimental data. The point is best illustrated by αU, as it is the stable phase of U metal at 0 K (the ground state phase) that has direct low-temperature experimental data[125] available. As tabulated in Table 3.4 the experiment in Ref. [125] measured its volume to be 20.53 Å/atom at 45 K (just above charge density wave states at 43 K and below), which is corrected to be 20.48 $Å^3$/atom at 0 K with Debye-Gruneisen quasiharmonic model[143]. Using PAW, we get 20.06 and 20.07 Å/atom from noSOC and SOC calculations, respectively, which are about 2% smaller than experimental values. They are quite close to what was obtained in a previous PAW study:[108] 20.19 and 20.07 Å/atom from noSOC and SOC calculations, respectively (not tabulated in Table 3.4). To see if the error is due to the pseudopotential approximation of PAW, we further compare them to *ab initio* results obtained from full-potential methods. The FPLMTO method[105] obtained ~20.40 (estimated from fig. 6 in Ref. 16) and 20.67 Å/atom from noSOC and SOC calculations, respectively.

Table 3.4. Volume for U, Zr metal and U-Zr alloy (Å^3/atom).

Phase	Composition (at.% Zr)	DFT (0 K)		DFT + U(1.24 eV) (0 K)		DFT refs.	Expt. (var. T)	Expt. (Corrected to 0 K)[f]
		noSOC	SOC	noSOC	SOC			
αU	0	20.06	20.07	20.75	20.94	20.40/20.67; 20.41/20.76; 20.34 (0 K)[a]	20.53 (45 K) (Ref. [125])	20.48
α(U)	6.3	20.50	20.57	21.19	21.39			
βU	0	20.49	20.49	21.51	21.91		21.81 (955 K) (Ref. [80])	21.19
β(U)	3.3	20.63	20.62	21.75	22.07			
γU	0	20.13	20.17	21.28	22.77	20.43/20.74;20.51 (0 K)[b]	22.05 (1060 K) (Ref. [80])	21.46
γ(U,Zr)	6.3	20.36	20.41	21.96	22.79			
	25.0	21.10	21.18	22.62	23.20	22.25 (300 K)[c]	22.37 (room T) (Ref. 48[126])	22.15
	50.0	21.97	22.06	23.02	23.33	22.90 (300 K)[c]	22.29 (room T) (Ref. 48[126])	22.07
	75.0	22.43	22.60	23.04	23.23	23.52 (300 K)[c]	22.75 (room T) (Ref. 48[126])	22.63
	93.8	22.88	22.86	23.01	22.97			
βZr	100	22.91	22.91			22.98 (0 K)[d]	23.70 (1253 K) (Ref. [83])	23.10
δ(U,Zr)	66.7	22.61	22.68	22.99	23.17	22.49 (0 K)[e]	22.49(room T) [Ref. [49])	22.36
ωZr	100	23.28	23.31			23.14 (0 K)[d]	22.75(room T) ([128]Ref.)	22.65
α(Zr)	93.8	23.54	23.55	23.66	23.68			
αZr	100	23.52	23.55			23.43 (0 K)[d]	23.22 (4.2 K) (Ref. [82])	23.19

[a] Soderlind’s FPLMTO noSOC/SOC results in Ref.[105] (noSOC estimated from Fig. 6); Jones *et al.*’s FPLAPW noSOC/SOC results in Ref. [103]; and FPLMTO SOC result from Le Bihan *et al*. in Ref. [144] (noSOC not given).

[b] Soderlind’s FPLMTO noSOC/SOC results in Ref.[105] (both estimated from Fig. 6); Boettger’s FPLAPW noSOC result in Ref. [102] (SOC not given).

[c] Landa *et al.*’s KKRASA-CPA noSOC results at 300 K in Ref. [66] (estimated from Fig. 1).

[d] Landa *et al.*’s FPLMTO noSOC results at 0 K in Ref. [66].

[e] Landa *et al.*’s EMTO-CPA noSOC results at 0 K in Ref. [66].

[f] Based on Debye-Gruneisen quasiharmonic model in Ref.[143](See the Supplementary Material).

However, an earlier SOC calculation[99] by the same author using the same

FPLMTO method and GGA functional obtained 19.49 Å/atom (not tabulated in Table IV). Another full-potential method, FPLAPW [102, 103] gives 20.41 and 20.76 Å/atom from noSOC and SOC calculations, respectively. The full-potential values are about 2% larger than our PAW values, so the pseudopotential approximation probably has contributed part of the underestimation. However, there is another subtle difference that may play an even more important role. αU has an internal parameter (often denoted *y*) that determines the atom positions and early full potential calculations usually either set *y* to experimental value and do not relax the atom positions when relaxing the lattice constants, or as Ref. [105] did, manually perform loops of sequential relaxation of lattice constants and *y* parameter that stop when certain convergence criteria is met. In contrast, our pseudopoetntial PAW calculations fully relaxed the lattice constants and atom positions simultaneously with conjugate-gradient (CG) algorithm. Interestingly, a more recent full potential SOC calculation with FPLMTO[144] that also did simultaneous relaxation of all structural degrees of freedom of αU with CG algorithm obtained a value of 20.34 Å/atom, which is over 1.5% smaller than the full potential results in Refs. [103] and [105] and much closer to our PAW value. Ref. [144] did not report any result from noSOC calculation but the effect of relaxation should be similar. In short, full-potential values, at least from noSOC calculations, are smaller than the experimental value by about 1% and perhaps more if the structure is also properly relaxed with CG algorithm; those from SOC calculations are not all consistent—the smallest value is 5% below, the largest is about 0.5% over, and the latest and perhaps most accurate value in Ref. [144] is about 0.7% below the experimental value. This is unusual because DFT calculations based on GGA more often overestimate volume. For example, in a previous high-throughput study[145] of 10768 compounds in the International Crystal Structure Database, it is found that the median error for DFT-GGA's volume prediction is positive (i.e., overestimated) 3.2%; also as a specific example, as listed in Table 3.4, our own calculations show that DFT-GGA overestimates the volume of αZr by about 1.3%. So, if it is still debatable to suggest that DFT-GGA underestimates the volume of U metal in the absolute sense, it is reasonable to argue that at least DFT-GGA's volume prediction for U metal is biased toward the negative (i.e., underestimated) end in the statistical distribution of the volume prediction errors. Such a finding is not surprising. In fact, it follows the general trend of DFT-GGA's underestimation of the volume of actinide metals.[103] The trend debatably starts at U, as we have discussed above, and becomes more significant as the atomic number increases—for Np and Pu, the calculated volumes are clearly smaller than experimental values, even in the most accurate full-potential calculations with SOC included (see Table I of Ref. 14). Since the correlation effects become more pronounced with higher atomic number along the actinide series, it is expected that the volume underestimation is due to correlation effects.

Next we discuss Zr metal. Table 3.4 shows that our PAW results for Zr metal match the full potential results from FPLMTO[27][66] very well for all the three solid phases of Zr. In comparison, we note that our earlier calculations using a different PAW pseudopotential for Zr that only treated $5s^2 4d^2 5p^0$ as valence orbital obtained considerably smaller volumes, which prompted us to adopt the current pseudopotential for Zr. Comparing to experimental data, our current DFT-GGA calculations overestimate the volume of αZr and ωZr by about 1.3% and 2.6%, respectively, while marginally underestimate the volume of βZr (<0.8%).

Now we discuss U-Zr alloy. We have found experimental volume data for γ(U,Zr) at 25, 50, and 75 at.% Zr and for δ(U,Zr) at 66.7 at.% Zr. For γ(U,Zr), DFT also underestimates the volumes to different extents, and if we consider it together with γU metal, the error seems to decrease as Zr concentration increases and becomes negligible at 50 and 75 at.%Zr. The result is expected because γ(U,Zr)'s end members are βZr and γU (they all have BCC structure) and we have shown above that DFT almost reproduces the volume for βZr but underestimates that for γU significantly. δ(U,Zr)'s volume are 22.61 and 22.68 Å/atom from noSOC and SOC calculations, respectively, which, different from all other U and U-Zr phases are nevertheless larger than the experimental value[49] of 22.49 Å/atom at room *T* (22.36 if corrected to 0 K). This result seems to be an anomaly but is totally expected because the volume of ωZr, which is the end member of δ(U,Zr) that also has C32 structure, is overestimated by a significant extent of 2.6%--in contrast with βZr whose volume is even slightly underestimated. Our PAW results based on both Zr PAW potentials are again different from the EMTO result of Landa *et al.*[66], which does not include SOC but matches the experimental value almost perfectly. The discrepancy can be due to reasons similar to those that explain the difference in our calculated enthalpies for δ(U,Zr) discussed above but can also stem from approximations in our calculations, such as the pseudopotential. Other alloy phases do not have direct experimental volume data, but we can assume the trend will be similar.

Now we consider the effect of adding + *U* potential on volume. Qualitatively, Figure 3.6 shows that the calculated volumes increase monotonically with U_{eff} from 0 to 4 eV for all 12 systems. The evolution can be differentiated into three linear stages with the first having the smallest slope and the second the largest. The phenomenon is negligible at 93.8 at.% Zr for both γ(U,Zr) and α(Zr) but becomes more pronounced with increased U concentration and is most obvious in αU. We will keep finding such three-stage differentiation on other calculated properties below. Next we make quantitative comparison of calculated volume with experimental results that we find for seven systems, as listed in Table 3.4.

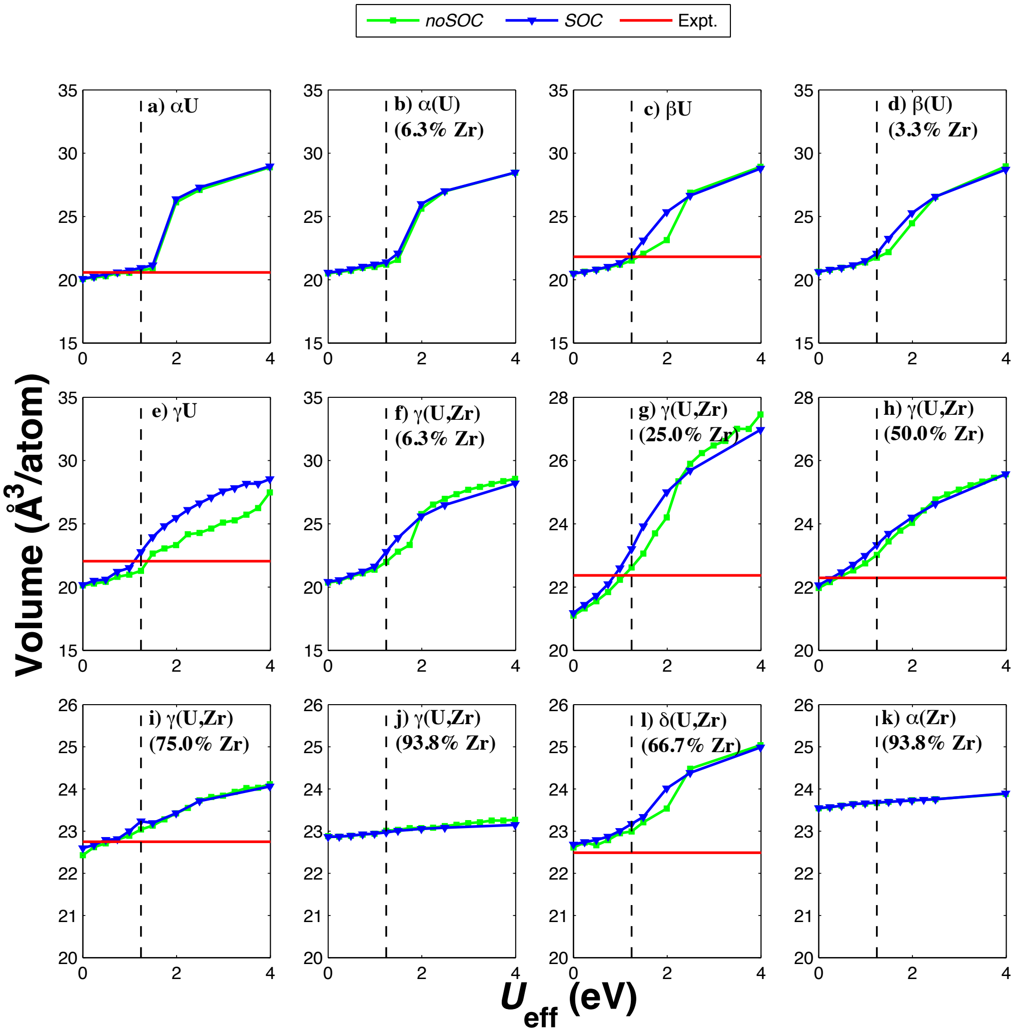

Figure 3.6 Volume for all solid phases of U metal and U-Zr alloy as a function of U_{eff}: a) αU; b) α(U) (6.3 at.% Zr); c) βU; d) β(U) (3.3 at.% Zr), e) γU; f) γ(U,Zr) (6.3 at.% Zr); g) γ(U,Zr) (25.0 at.% Zr); h) γ(U,Zr) (50.0 at.% Zr); i) γ(U,Zr) (75.0 at.% Zr); j) γ(U,Zr) (93.8 at.% Zr); k) δ(U,Zr) (66.7 at.% Zr); and l) αZr (93.8 at.% Zr). The vertical dash reference line is at U_{eff}=1.24 eV. Experiments data are from those referenced in Table 3.4; no direct experimental data are found for b), d), f), j) and k).

Firstly, for U metal and U-rich U-Zr alloy (i.e., αU, βU, γU and γ(U) at 25 at.% Zr), optimal match of calculated volume with experimental value seems to happen at U_{eff} around 1 eV. Secondly, for U-Zr alloy with higher Zr contents (i.e., γ(U,Zr) at 50 and 75 at.% Zr, and δ(U,Zr) at 66.7 at.% Zr), DFT already reproduces well or even overestimates the volume. Because DFT + *U* always gives larger volume than DFT, it obtains worse agreement with experimental data at almost any finite U_{eff}. Does this mean DFT + *U* is a worse model for Zr rich U-Zr alloy systems than DFT? The answer is certainly no. The reason is that for U-Zr alloy, DFT + *U* is only applied on the U sublattice, and any error on the Zr sublattice remains largely unchanged not matter what U_{eff} is used. The error on Zr sublattice carries negligible weight in the U rich system γ(U,Zr) at 25 at.% Zr discussed above, but becomes more important or even dominant when Zr content is larger. Take δ(U,Zr) at 66.7 at.% Zr as an example. DFT overestimates its volume by 1%. In comparison, DFT overestimates its end member ωZr's by 2.6%. The error for δ(U,Zr) is smaller than ωZr only because for δ(U,Zr) DFT's volume overestimation error on the Zr sublattice in δ(U,Zr) is partially canceled by the underestimation error on the U sublattice. Because Zr is dominant at 66.7 at.%Zr, the overall error is still positive (i.e., overestimation). When DFT + *U* is used, the error on the U sublattice is reduced and can cancel less the error on the Zr sublattice, which results in the net effect of increased overall error at larger U_{eff}. At U_{eff} = 1 eV, DFT + *U* gives volume of δ(U,Zr) that is overestimated by 2.9%, which is approximately the error for ωZr. This result suggests that the error on the U sublattice almost vanishes at 1 eV, which is in excellent agreement with the results for U metal and U-rich U-Zr alloy systems discussed above. Therefore, DFT + *U* is still more appropriate than DFT for δ(U,Zr). Similar argument holds for γ(U,Zr) although the trend is less clear due to noises in the data introduced by the various approximations mentioned above, especially the constrained relaxation. Overall, the above quantitative comparison shows that volume fitting gives an empirical optimal U_{eff} near 1 eV, with 1.24 eV being marginally worse. The situation for volume should be compared with that for enthalpy, for which Figure 3.4 shows the optimal U_{eff} is near 1.24 and 1 eV is only slightly inferior. For both enthalpy and volume, the difference between those at 1 and 1.24 eV is comparable to the combined error bar of our *ab initio* calculation, the experimental data and the temperature extrapolation. Therefore, we can consider fittings in volume and enthalpies to give consistent empirical U_{eff}.

Regarding the effect of SOC on volume, for all systems in Figure 3.6, volumes from SOC calculations are slightly larger than (<0.5%) or at least equal to those from noSOC when calculated using DFT. This is especially true for all three solid phases of U metal, which reflect correct physics[146] and agree with previous full-potential studies using FPLMTO[105], [146] and FPLAPW,[102, 103] as we have discussed above. For DFT + *U*, volumes from SOC calculations are also arger than noSOC, but by more extent. For example, at $U_{\text{eff}} = 1.24$ eV, using the volume data in Table 3.4 we can calculate that the volume expansion due to SOC is 7, 4, and 2.5% for γU and γ(U,Zr) at 6.3 and 25 at.%Zr, respectively and less than 2% for all other systems. It has been suggested that SOC volume expansion for U should be between 1 to 2 %[147], so the first three systems of γU and γ(U,Zr) probably have wrong volumes $U_{\text{eff}} = 1.24$ eV. We did not tabulate the numerical volume values at other U_{eff}, but comment that this problem does not exist for the three systems at $U_{\mathrm{eff}} = 1$ or smaller, but does exist and become more severe at larger U_{eff} values, as Figure 3.6 shows. The reason for too large SOC volume expansion for the three systems of γU and γ(U,Zr) is not clear, however, Figure 3.5 shows that the enthalpy of mixing for γ(U,Zr) does not show strange or sudden large jump in the whole range of U_{eff} from 0 to 1.49 eV, which suggests that whatever caused the volume expansion problem does not obviously affect the calculated enthalpy. These results suggest caution should be taken when using DFT + *U* to calculate the volume of γU and U-rich γ(U,Zr) using $U_{\mathrm{eff}} = 1.24$ or higher, but the enthalpy seems to be unaffected.

On the whole, the above results of calculated volumes suggest that correlation effects also have a significant impact on volume: based on GGA, DFT underpredicts the volume of U metal and the U sublattice in U-Zr alloy, and the error is somewhat corrected using DFT + *U*. The relativistic effect of SOC is also relevant, which increases the volume and brings in further improvement. Such results on volume are consistent with those on energetics discussed above.

3.4.3 Magnetic Moments

The calculated spin, orbital, and total magnetic moments integrated over the whole unit cell are given as functions of U_{eff} for all solid phases of U metal and U-Zr alloy in Figure 3.7. The magnetic moments evolve in three stages as well. Initially, total magnetic moments are zero for all systems; spin/orbital moments are also zero for U metal and U-Zr alloy with high U concentrations and are finite but small for U-Zr alloy with low U concentration. After a threshold value of U_{eff}, total magnetic moments emerge and start to increase with larger U_{eff}. Finally, these moments level out after reaching a certain saturation level. The empirical optimal $U_{\mathrm{eff}} = 1.24$ eV from energetic and volume fitting in general lies in the first stage.

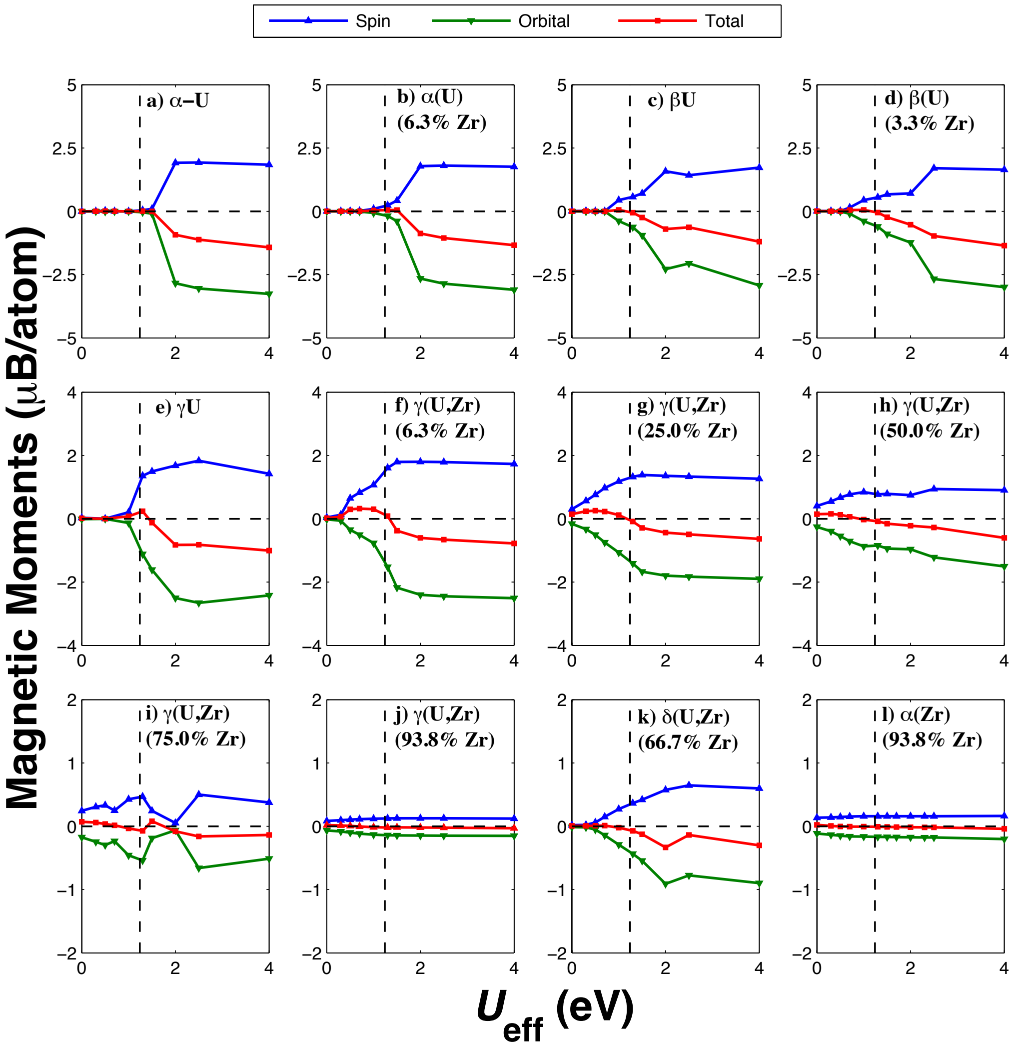

Figure 3.7. Spin, orbital and total magnetic moments for all solid phases of U metal and U-Zr alloy as functions of U_{eff}: a) αU; b) α(U) (6.3 at.% Zr); c) βU; d) β(U) (3.3 at.% Zr), e) γU; f) γ(U,Zr) (6.3 at.% Zr); g) γ(U,Zr) (25.0 at.% Zr); h) γ(U,Zr) (50.0 at.% Zr); i) γ(U,Zr) (75.0 at.% Zr); j) γ(U,Zr) (93.8 at.% Zr); k) δ(U,Zr) (66.7at.% Zr); and l) αZr (93.8 at.% Zr). The vertical dash reference line is at U_{eff}=1.24 eV. The unsmooth segment between 1.5 and 2.0 eV for γ(U,Zr) (75.0 at.% Zr) might be metastable solutions.

We comment on the magnetic configurations of U and U-Zr next. Experimentally, αU is confirmed Pauli paramagnetic with vanishing local magnetic moments (<0.005 μB /atom)[79, 133] and βU and γU show similar behavior in magnetic susceptibility measurements.[148] Our DFT calculations indeed get zero magnetic moments on every atomic site for the three phases of U metal and therefore correctly reproduce its magnetic structure. For U-Zr alloy, DFT also gets no local magnetic moments on the U-rich end but does yield some spin and orbital moments on the Zr-rich side, which are on U rather than Zr atomic sites, though. Note that γ(U,Zr)'s results here are from constrained relaxation only. If fully relaxed, they are also found to have vanishing local spin and orbital magnetic moments, so the presence of these moments may be an artifact of the constrained relaxations we are using to treat this unstable phase. On the other hand, DFT + U at U_{eff} = 1.24 eV in general gets non-zero local *spin* magnetic moments for at least some of the atomic sites, even in U metal. However, these moments are close to zero for U metal and not exceeding 2 μ_B even in the Zr-rich U-Zr alloy systems; moreover, the local spin moments are also largely canceled by orbital moments. Take αU as an example. At U_{eff} = 1.24 eV the spin moments for αU on each of the two atomic sites are 0.045 μ_B and the orbital moments are −0.043 μ_B. The uncompensated 0.002 μ_B total local moments are antiparallel between the two sites and give zero integrated total magnetic moments. For other systems with larger supercells, local magnetic moments, if existing, are quite random in terms of both magnitude and direction, and we do not observe any long-range ferromagnetic or antiferromagnetic ordering. Most importantly, the total magnetic moments on each atomic site are still zero or very small at U_{eff} = 1.24 eV. Therefore, DFT + U at U_{eff} = 1.24 eV still gives no ordered magnetism for U and U-Zr. In short, DFT + U promotes spin/orbital polarization, which is still quenched at small U_{eff} but emerges at larger U_{eff}. At the empirical 1.24 eV, total local magnetic moments are still zero or vanishingly small in general, which is consistent with experiments showing no local moments. However, our results do show significant local spin and orbital moments in some cases, although they almost completely cancel each other. These values are difficult to compare to experiment and we cannot be sure if they might exist in nature—it is quite possible that they are an artifact of the current DFT + *U* functional because the Hartree-Fock term in it is well known to promote magnetic polarization. This artifact can probably be avoided by employing an alternative double counting scheme so called around the mean field (AMF), as Ref. [149] showed that AMF gives magnetic polarization a much larger penalty than FLL double counting scheme that we are using in this study. In fact, AMF based DFT + *U* has been validated on δPu in Ref.[150] to yield a non-magnetic ground state in perfect agreement with experiment result while still reproduce the experimental volume, bulk modulus and important features of photoelectron spectra well and significantly better than DFT. We will leave it for future study to consider AMF based DFT + *U* for U and U-Zr. At present, we conclude the discussion by pointing out that it would be misguided to be overly concerned with the emergence of very small moments in isolated incidents when the energetics, volume and electronic structure (discussed next) are globally improved.

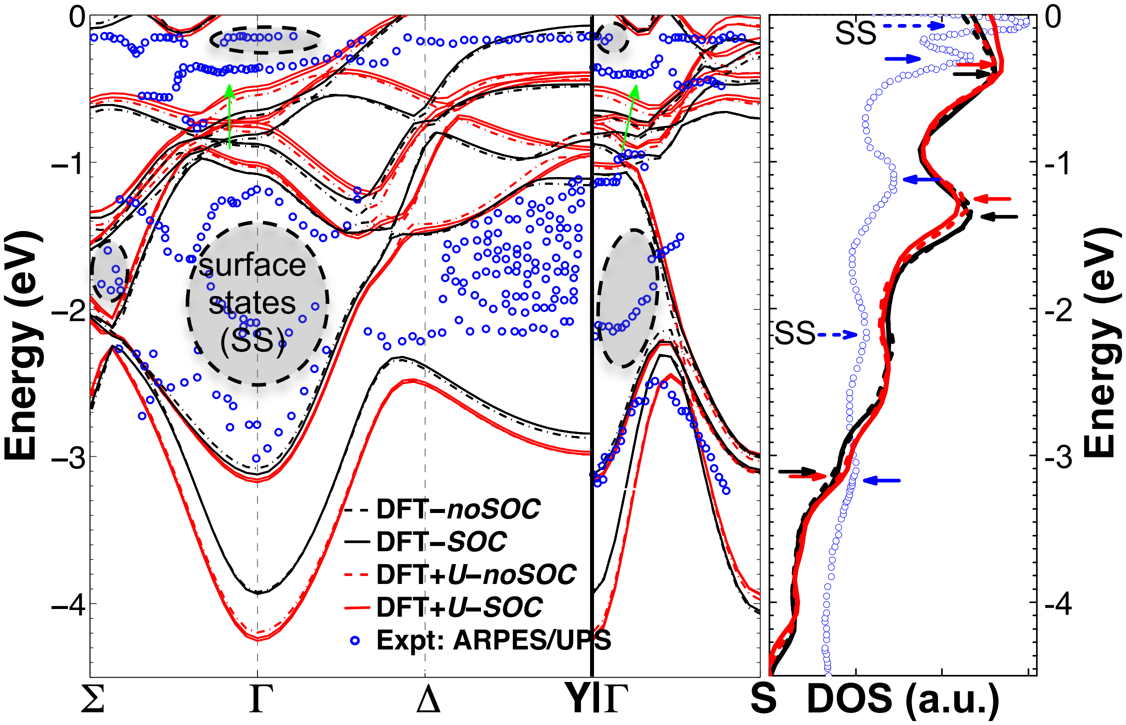

Figure 3.8. Band structure (left panel) and density of states (right panel) for αU. The respective experimental references are ARPES spectra from Opeil *et al.***[116]** and UPS spectra from Opeil *et al.***[115]** for αU(001) single crystal. All experimental spectra are plotted as blue circles, while DFT and DFT + *U* (U_{eff}=1.24 eV) calculated results are plotted as black and red curves, respectively; solid and dash line style distiguish noSOC and SOC. On the left, green arraws indicate two representative improvements of bands going from DFT to DFT + *U*. On the right, the positions of peaks from experiment, DFT and DFT + *U* are marked with blue, black and red arrows, respectively. Gray areas on the left and dash arrows on the right indicate spectra features from surfaces states that are not modeled in the calculations. Only the occupied part between -4.5 and 0 eV relative to Fermi level is shown. See FIG. 2 in Ref.**[116]** for an illutration of Brillouin zone and the special *k*-points used here.

3.4.4 Electronic Structure

Next we show that DFT + *U*’s improvement in the calculated energy and volume relative to DFT is not fortuitous—it is based on better account of the electronic structure. We make the case on experimentally most-characterized system αU by comparing its calculated valence band electronic structure to experimental photoelectron spectra in Figure 3.8 and Figure 3.9.

Let us first focus in Figure 3.8 on the occupied part between -4.5 and 0 eV relative to Fermi level. Here, latest experimental ARPES[116] and UPS[115] spectra of αU (001) single crystal are used as references for the calculated band structure (left panel) and density of states (DOS, right panel) of bulk αU, respectively. Before we start the comparison, a few clarifications regarding the experimental spectra should be made. Firstly, some features of the spectra are due to surface states as the escape depth of the phonon source used is "at most 2-3 atomic layers"[116]. Some of the possible surface states features are suggested based on DFT calculations of bulk αU[115, 116]. These features are marked roughly with gray areas on the left and dash arrows on the right panel of Figure 3.8. They are not expected to exist in our *ab initio* results. Second, the UPS spectra in Figure 3.8 reflect states mainly along the ΓZ direction (we follow the k-point designation given in FIG. 2 of Ref. [116]). Our calculated DOS is however total DOS (TDOS) integrated over the whole Brillouin zone and thus may show additional features not seen in the UPS spectra. On the other hand, the ARPES spectra reflect mainly states along k-vectors in the (001) plane that is normal to ΓZ, so the ARPES and UPS spectra may not strictly align with each other. However, the anisotropy of electronic states for such metallic system should be small and we can probably still make meaningful comparison between the three groups of data. Finally, the UPS spectra are not normalized, so their absolute intensity is not comparable to the calculated DOS, and we should focus the comparison on energy.

Now we start our discussion with the right panel of Figure 3.8. There the UPS spectra mainly show five peaks at -0.1, -0.3, -1.2, -2.2 and -3.2 eV, respectively, which are marked with blue arrows. The two at -0.1 and -2.2 eV are suggested to be surface states[115], and their arrows are dashed and annotated with text. The remaining three peaks all show up in the calculated TDOS, which are marked correspondingly with black and red arrows for DFT and DFT + *U*. Moreover, two additional small peaks also exist near -2.7 and -4.2 eV (not marked) in the calculated TDOS, which are not seen in the UPS spectra (not to confuse the TDOS peak near -2.7 eV with the UPS surface state peak near -2.2 eV). As explained above, they are presumably from electronic states along other directions of the Brillouin zone, for example those shown on the left panel of Figure 3.8. In fact, these additional two DOS peaks' positions are consistent with where some bands turn around on the left. We neglect the two UPS peaks due to surface states and the two TDOS peaks not existent along the ΓZ direction, and focus on the three peaks near -0.3, -1.2, and -3.2 eV. For the sake of convenience, we will refer to them as peak I, peak II and peak III, respectively in the next. Figure 3.8 shows that peak I and peak II from DFT shift downwards to -0.4 eV and -1.4 eV, respectively, while peak III does not change much relative to UPS. To see if the difference is due to the direction of the UPS spectra, we cite the directional DOS (DDOS) calculated exactly along ΓZ with DFT-GGA in Ref. [115], which shows that peak I also downshifts to -0.6 eV, while peak II and III are rather well reproduced. So the error of downward shifting of peak I should be real while that of peak II is possibly artificial and due to anisotropy. Such result is totally expected. If we look at the orbital projected DOS of αU in the first row of Figure 3.10, we will find that *f*-states dominate mainly between 0 and -1.3 eV. So peak I is mainly due to *f*-states, while peak II and III are probably more of other states (i.e., *s*- and *d*- states). The above analysis points to peak I as a key indicator of the correlation effects and how well they are modeled. Now we present a key point of Figure 3.8: peak I from DFT + *U* is shifted upwards with respect to DFT to around -0.35 eV, partially correcting the downward shifting error and is therefore in better agreement with UPS. The shift in energy seems relatively small (about 0.1 eV), but peak I is directly below Fermi level and has the largest magnitude among the peaks below Fermi level, so the effect is still significant. Besides position, the magnitude of peak I from DFT + *U* is also larger than DFT. It is in fact another improvement that is not evident in Figure 3.8 in which UPS spectra's absolute magnitude is not meaningful, as mentioned above, but will become clear below when we compare them to the properly normalized spectra in Figure 3.9. All these factors make the seemly small change in peak I a substantial improvement.

Next we show that we can draw similar conclusions from band structure, which is shown along the three *k*-vectors Σ-Γ, Γ-Δ-Y, and Γ-S on the left panel of Figure 3.8. In general, six bands exist between -0.2 to -4.5 eV in all the three directions although the highest one of them actually extends above Fermi level between Δ-Y. We will name them band I, II, …, and VI from top to bottom, respectively. They can be easily identified near Γ although band II and III are almost degenerate at Γ. The band that is directly above the six also has some segments extending below Fermi level to about -0.2 eV, which show up in the Σ-Γ and Γ-S directions, but its major parts are above it and unoccupied, and thus we will neglect it in our discussion below. For the band structure calculated by DFT (black curves), our result is generally consistent with Opeil *et al.*'s DFT calculation[116] (not shown in Figure 3.8); but two major differences exist, which may be due to factors like the pseudopotential approximation used in our calculation and the lacking of structural relaxation in the theirs[116]. The first difference is that band V and band VI are almost degenerate at Γ in Ref. [116] but are about 0.8 eV split in Figure 3.8. Nevertheless, bands V and VI are low-lying and mostly not *f*-states, so they are expected not to affect the property of U metal much. The other difference happens on all the five bands II-VI along Δ-Y (remember band I is above Fermi level there). For example, Ref. [116] gives that band II is also above Fermi level like band I, while our calculation obtains band II to be between -0.1 and -0.8 eV. Despite so, it should be noticed that Δ and Y are relatively low-symmetry *k*-points and carry much less weight comparing to high-symmetry *k*-points such as Γ. Encouragingly, our calculations show good agreement with Opeil *et al.*'s for bands I-IV around Γ (i.e., Σ-Γ, Γ-Δ, and Γ-S*)*, which exist mainly between -1.5 to 0 eV, and we will focus on them when making the comparison between DFT, DFT + *U* and ARPES spectra next. The ARPES spectra[116] we reference to in Figure 3.8 are to our knowledge the latest and probably the best experimental data of such kind so far. Yet they still do not reach the resolution that can differentiate the six bands without ambiguity and are also contaminated by surface states. By projecting their DFT calculated bands of bulk αU onto (001) plane, Ref. [116] identified some possible surfaces, which are marked in Figure 3.8 with shaded areas. It should be noted that those intensive spectra features between -1.3 and -2.3 eV along Δ-Y are not among such states. We nevertheless doubt that some of them may still be artificial, especially those below -1.6 eV where the corresponding DOS is quite flat. Despite all the above imperfections, we can get the following key conclusion from band structure results in Figure 3.8: bands I-IV around Γ from DFT + *U* are shifted upwards by about 0.1 eV or more with respect to DFT. The effect is most obvious for band I around *Γ* (marked with two green arrows) above which some ARPES spectra features happen to exist. The upward shifting brings calculated band I closer to these spectra, which is consistent with what happens for peak I of DOS on the right panel of Figure 3.8.

Overall, Figure 3.8 shows that DFT + *U* at U_{eff}=1.24 eV obtains better electronic structure for αU than DFT by shifting upwards and intensify some *f*-states directly below Fermi level, which we argue is the underlying mechanism that leads to the improvement in the calculated energetics and volume shown above.

Figure 3.8 also provides some insights on the relativistic effect of SOC. In terms of DOS, the intensity of peak I increases, peak II decreases, and peak III also increases due to SOC (the increasing/decreasing is illustrated with the directions of the arrows Figure 3.8). The effect seems most pronounced for peak I from DFT + *U* calculation (compare red solid and red dash peak I). The positions of these peaks however almost stay the same. Not surprisingly, Figure 3.8 also shows that there is no significant shifting or splitting of bands due to SOC below Fermi level. In general, there is only small difference between noSOC and SOC in the calculated DOS in the occupied part of valence band shown in Figure 3.8, which is in agreement with the previous study by FPLMTO [105]. The major effect of SOC that leads to the slight improvement in calculated properties for αU is to adjust the intensity of electronic states. The adjustment is small, and hence the improvement is also not large, about 0.02 eV/atom in terms of energetics, as we have found above.

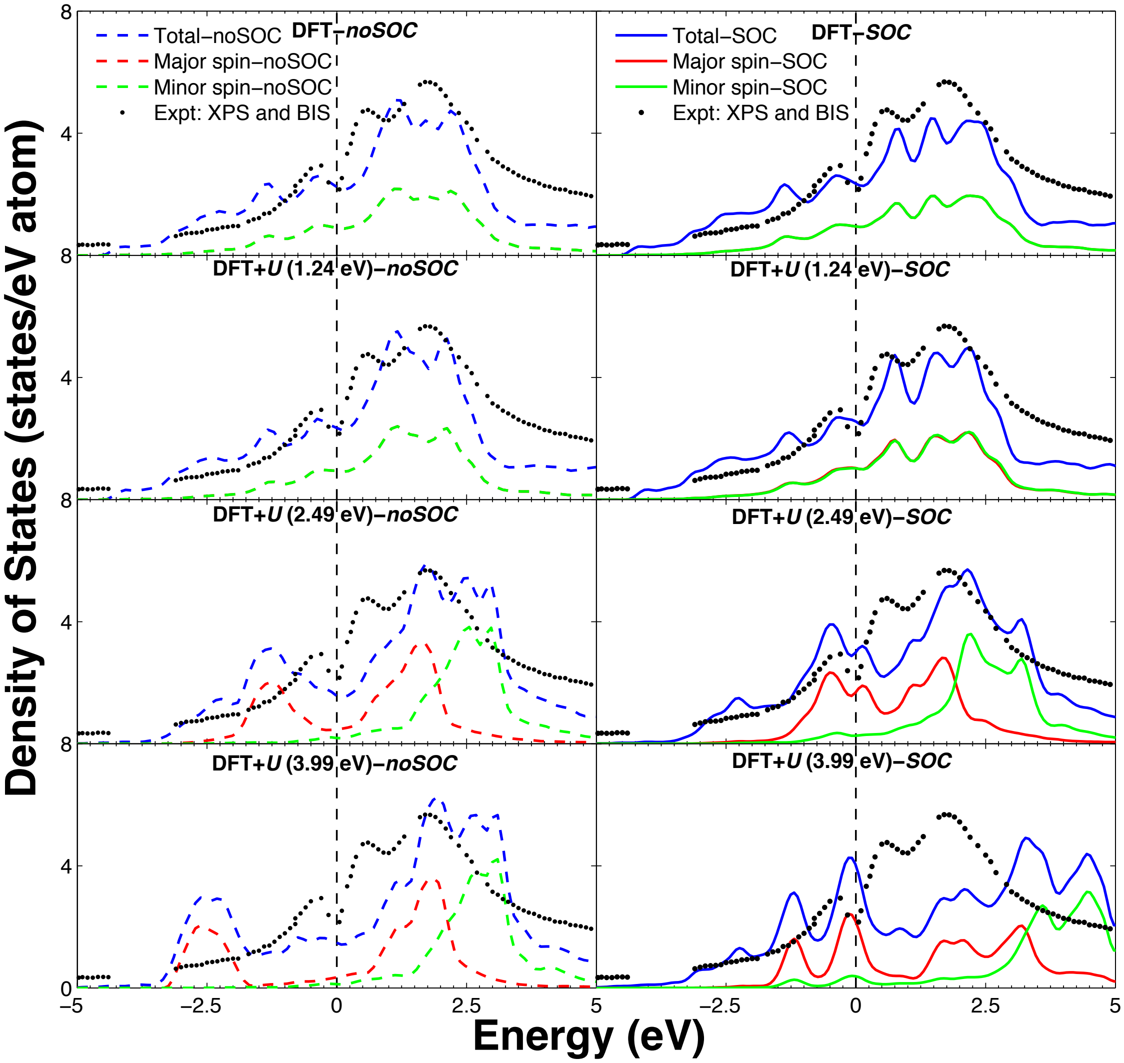

Figure 3.9. Density of states for αU as a function of U_{eff}. The vertical dash reference line is Fermi level. Experimental reference is Baer and Lang's XPS and BIS spectra**[151]**. The full valence band, both occupied and unoccupied is shown.

Next we look at the full valence band of αU in Figure 3.9. Here instead of the UPS spectra from Ref. [115] that is used above, we use the X-ray photoemission (XPS) and the bremsstrahlung isochromat spectroscopy (BIS) spectra from Ref. [151] as the experimental references. They have both been properly normalized, so we can also compare the peak intensity as well. The major features of αU's valence band from XPS and BIS spectra are the three peaks near -0.3, 0.4 and 2.3 eV, respectively. The first one is just peak I that we have discussed above; the latter two will be referred to as peak A and peak B, respectively. Above Fermi level, Peak A was suggested[152] to be the $5f_{5/2}$ subshell, while peak B the $5f_{7/2}$ subshell. Note peak B should further split into two sub-peaks, as seen in the DOS from the calculations of ours and also of the previous one by FPLAPW[152]. Such feature is not resolved in the BIS spectra probably due to the core-hole lifetime broadening of about 1 eV[152]. Now we discuss our calculated results and compare them to the XPS/BIS spectra. Firstly, going from DFT to DFT + U at U_{eff}=1.24 eV in SOC calculations (i.e., going from the first to the second row on the right column), peak I slightly shifts upwards and becomes higher but narrower, as has been shown more clearly in Figure 3.8; peak A becomes higher and narrower as well but shifts downwards, by much larger extent than that of peak I; peak B also evolves in similar ways. All these changes are towards better agreement with the measured XPS/BIS spectra, which are similar to what was found when going from DFT-LDA to QSGW[117].

Next we discuss the effect of SOC by comparing the left and the right column of the first (i.e., DFT) or second row (i.e., DFT + U at U_{eff}=1.24 eV) row. Again we focus on the unoccupied part. On the left (i.e, *nosOC*), peak A and the left subpeak of B are mixed/overlapped, which together make a single peak near 1 eV. In comparison, on the right, peak A and the left subpeak of peak B split into two, which are near 0.7 and 1.5 eV, respectively. Such splitting is the so-called spin-orbit splitting. We estimate based on the distance between the two split peaks that SOC parameters for U metal is about 0.8 eV, which is very close to the literature value of 0.77 eV[153]. Atomic spectra gave that neutral U atom has a much smaller SOC parameter of 0.22 eV (1773 cm^{-1})[154]. It seems that SOC is much enhanced in U metal than U atom. Lastly, as previous studies[105, 117] suggested, correlation and relativistic effects predominate in the unoccupied part, which is clearly seen in our results in that the relative extent of improvement (e.g., peak shifts) in the unoccupied part (i.e., peak A and B) is much larger than that of the occupied part (i.e, peak I) when going from DFT to DFT + U at 1.24 eV and from noSOC to SOC.

Another main point of Figure 3.9 is to demonstrate the evolution of DOS as a function of U_{eff}. From 0 to 1.24 eV, peaks evolve and change their positions and shapes, but the up and down spin lobes are still mostly overlapped. At 2.49 eV, the two spin lobes are split apart and no longer overlap. This corresponds to the emergence of spin magnetic moments as we show in Figure 3.7. Such splitting is large enough that the positions and shapes of the DOS peaks already deviate substantially from the experimental spectra. From 2.49 eV to 3.99 eV, the two spin lobes are split further apart. Especially in those from noSOC calculations at 3.99 eV (bottom left panel), there even is a gap open between the up and down spin channels of the *f*-band although overall the valence band is still continuous across Fermi level and the system remains metallic. Based on the evolution of DOS, we can characterize the three stages constantly observed in the evolution of calculated properties as functions of U_{eff} roughly as metal, metal-gap transition and gap stages, where the gap refers to splitting between the up and down spin channels of *f*-band. Overall, the comparison of calculated DOS with experimental spectra here align with those of energetics, volume and magnetic moments above, which suggests that a reasonable U_{eff} should be smaller than 2.49 eV, and 1.24 eV seems a good choice.

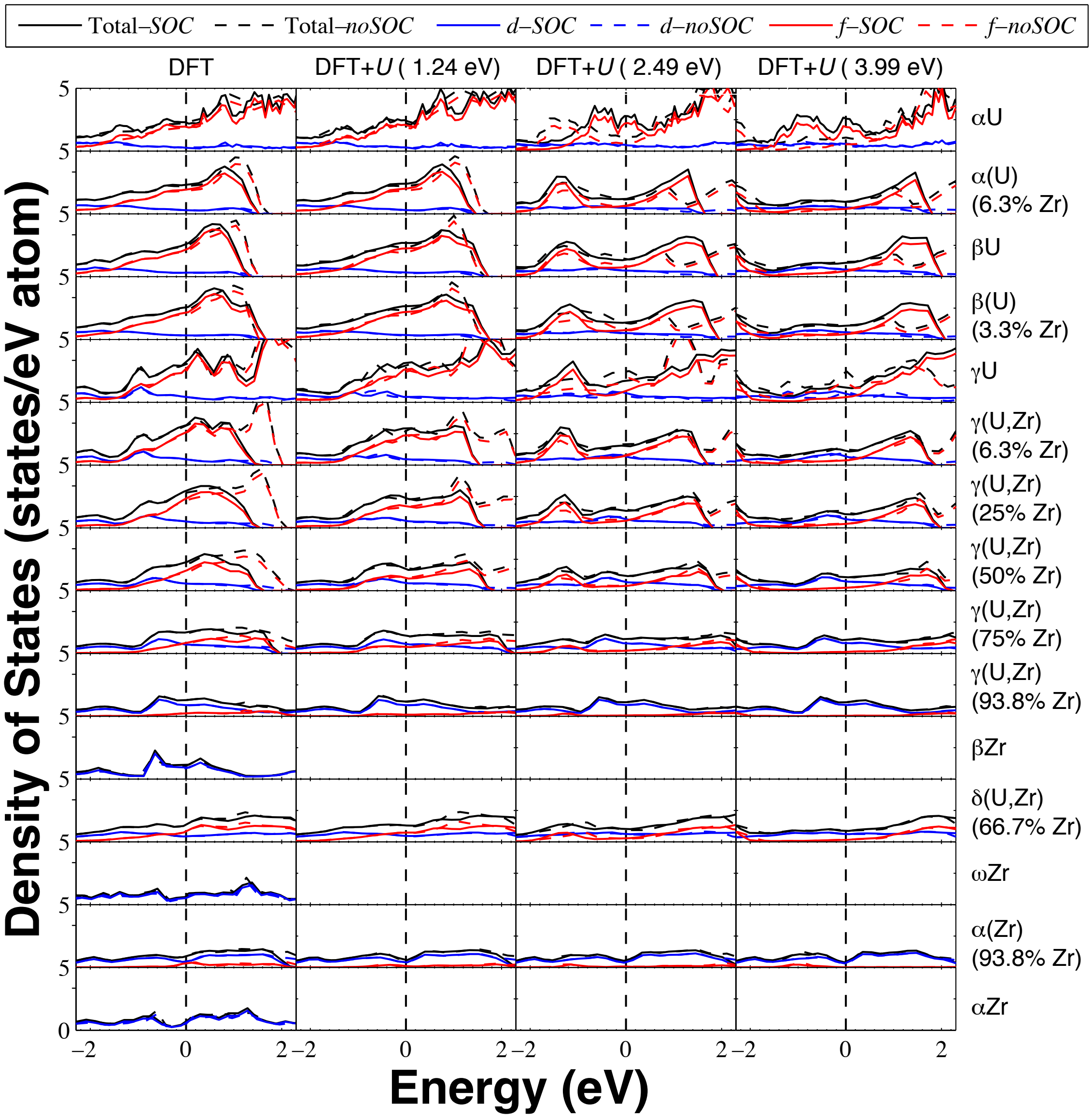

Figure 3.10. Total, *d*- and *f*-orbital projected density of states for all solid phases of U, Zr metal and U-Zr alloy as functions of U_{eff}. The vertical dash reference line is Fermi level.The first column is calculated by DFT, the second, third and fourth by DFT + U at U_{eff}=1.24, 2.49, and 3.99 eV, respectively. Results from both noSOC (dash) and SOC (solid) are given. The highest unoccupied part of the valence band is missing for some systems due to limited number of bands included in the calculations.

Such pattern for the change of DOS as a function of U_{eff} is actually quite similar for all solid phases of U metal and U-Zr alloy, as we can see in Figure 3.10. Although the highest unoccupied part of the valence bands are not shown because they are not included in our calculations due to computing capability limits, the available data in Figure 3.10 are enough to offer the following insights. Firstly, slightly different from αU, in some systems, like α(U) (6.3at.% Zr) and γU, the two 5*f* lobes already separate enough at U_{eff} =2.49 eV to open a gap for the *f*-band although the whole valence band only shows a pseudo-gap because the *d* band (blue curves) stays essentially unchanged. The U_{eff}'s corresponding to the minimum in enthalpy or the second cross with the CALPHAD lines in Figure 3.2 and Figure 3.3 are in this region. Such pseudo-gap should be unphysical for these metallic systems and hence the U_{eff}'s should not be picked as the optimal U_{eff}. Moreover, the DOS curves in Figure 3.10 also show the impact on U electronic properties upon alloying with Zr. No significant changes of the position and shape of the valence bands happen after U and Zr is alloyed. This phenomenon is most evident if we look at the DOS curves for γ(U,Zr) at various Zr concentrations between the sixth and the tenth row in Figure 3.10. They look quite like linear suppositions of the DOS curves for γU and βZr metal end members in the fifth and eleventh row. These trends show that alloying with Zr does not dramatically impact the qualitative U electronic structure, and therefore U-Zr alloy should have similar correlation strength as U metal.

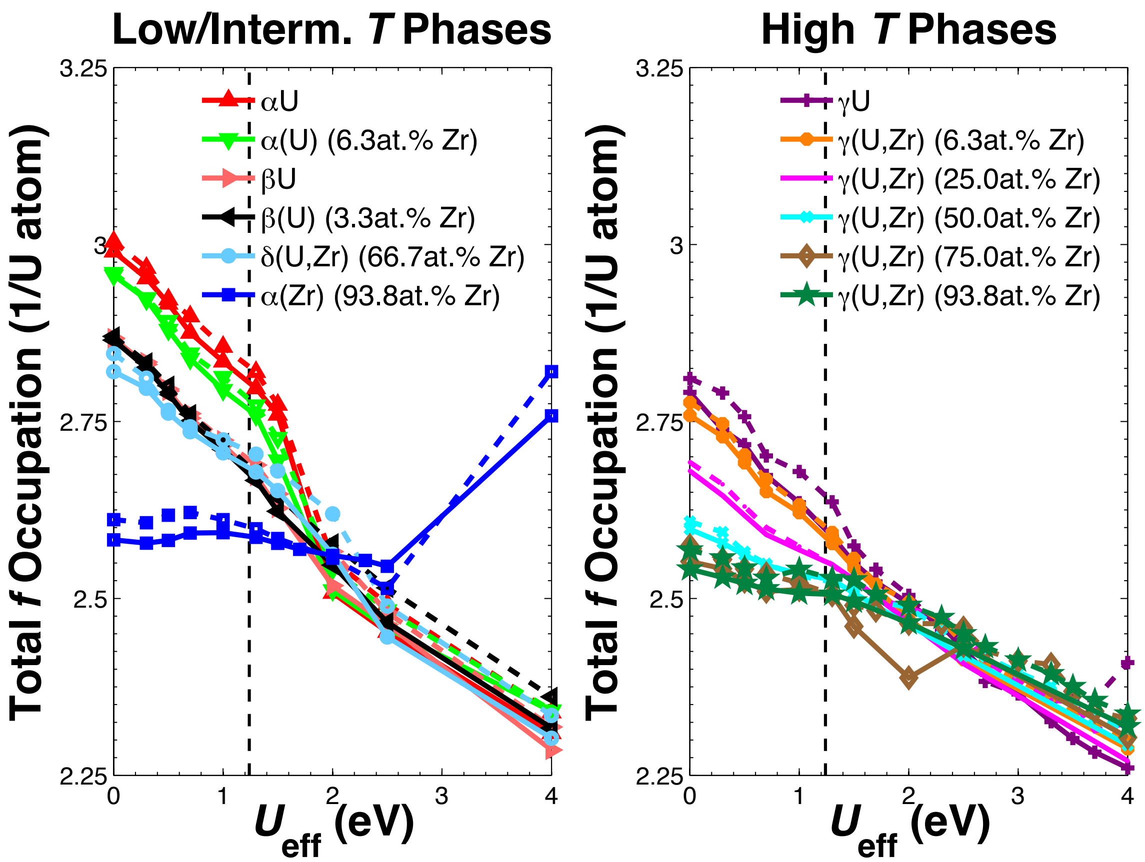

Figure 3.11. Total *f*-orbital occupation for all solid phases of U metal and U-Zr alloy as a function of U_{eff}. Low and intermediate temperature phases αU, α(U), βU, β(U), α(Zr) and δ(U,Zr) are plotted in the left panel; high temperature phase γU and γ(U,Zr) are in the right. Solid curves are from SOC calculations, while dash from noSOC.

The total *f*-orbital occupation for U and U-Zr as a function of U_{eff} is shown Figure 3.11. First consider the magnitude of the occupation as calculated by DFT. We point out beforehand that our values presented next are calculated using the quick projection scheme (LORBIT=11) implemented in VASP, and are probably underestimated to some extent possibly because the projection sphere radii are not sufficiently large. For the three allotropes of U metal—αU, βU to γU, the *f* occupation decreases consecutively from 3.01, to 2.87 and 2.81, respectively. Let us compare our values to the literature. Chantis *et al.*[117] obtained the *f*-orbital occupation of αU to be 3.57 and 3.19 respectively from DFT-LDA and QSGW calculations, respectively. Our DFT-GGA calculation gets 3.01

due to the projection issue. U atom has three *f* electron in the ground atomic state[23]; in crystal it should have less than three due to hybridization with other orbitals such as 6*d*. Despite the projection issue, our DFT calculations still get a value larger than 3, and hence has reproduced the previous observation[117] that DFT overestimates the *f*-orbital occupation for U metal. Alloying with Zr in general reduces the *f*-occupation. The reduction is negligible when the Zr concentration is small. For example, at 3.3 at.%Zr, β(U)'s *f*-occupation curves are almost indistinguishable from βU's. However, it becomes more significant when the Zr concentration gets higher. This is most evident if we look at γ(U,Zr), which has *f*-orbital occupations of 2.78, 2.69, 2.60, 2.57 and 2.57 at 6.3, 25.0, 50.0, 75.0 and 93.8 at.%Zr, respectively, suggesting that at higher Zr concentration the *f* orbitals of U have stronger hybridization with Zr. Secondly, Figure 3.11 also shows that similar to QSGW, DFT + *U* reduces *f*-orbital occupation relative to DFT for all the systems considered, which serves as another evidence that it models the correlation effects better. These lost charges can be due to the hybridization of *f* orbitals with other orbitals of U atoms, which is presumably the only mechanism for U metal. For U-Zr alloy, *f* orbitals can also hybridize with orbitals of Zr atoms—mostly *d* orbitals, as evidenced by the slightly increased *d*-orbital occupation of Zr (not shown in Figure 3.11). Thirdly, SOC also reduces the occupation when U_{eff} is in the reasonable range of < 2eV (i.e., the dashed curves from noSOC are generally above the solid curves from SOC in this region); the change is marginally small, on the order of 0.001. Finally, for most systems, the total *f*-orbital occupation decreases in the whole U_{eff}=0-4 eV range, and there seems to be a slight change of slope near U_{eff}= 2eV. However, for α(Zr) at 93.8at.% Zr, the occupation starts to recover at U_{eff} near 2.5 eV. We point out this is probably not an anomaly because in a few systems we also perform calculations that go beyond U_{eff}=4 eV and find that for them the total *f*-occupation also goes up at some higher U_{eff}'s. Therefore, total *f*-occupation can also be considered to evolve in three stages as a function of U_{eff}. In general, Figure 3.11 suggests that the total *f*-occupation is a good parameter to characterize the correlation effects and how well they are modeled.

3.4.5 Theoretical Hubbard *U* for U and U-Zr

Table 3.5. Theoretical Hubbard U for Uranium in all solid phases of U metal and U-Zr alloy evaluated with the linear response approach of Ref. [124].

Phase	Composition (at.% Zr)	Hubbard *U* (eV)
αU	0	1.87
α(U)	6.3	1.95
βU	0	2.10
β(U)	3.3	2.20
γU	0	2.10
γ(U,Zr)	6.3	2.15
	25.0	2.27
	50.0	2.34
	75.0	2.20
	93.8	2.15
δ(U,Zr)	66.7	2.21
α(Zr)	93.8	2.33

Summarizing all the fitting results above suggests that empirical U_{eff} for U and U-Zr should be between 1-1.5 eV with the statistical optimal from energetic fitting to be 1.24 eV. How does it compare to theoretical Hubbard *U*? Note correlation is normally characterized by the ratio *U*/*W* where *U* is Hubbard *U* and *W* is valence bandwidth. Therefore, an appropriate energy scale to characterize the magnitude of *U* is ~4 eV which is *W* for αU. Table 3.5 gives that theoretical *U* goes from 1.87 eV for αU to 2.34 eV for γ(U,Zr) at 50 at.%Zr. So theoretical *U*'s are close to but larger than the empirical U_{eff} by 0.63 to 1.1 eV, or 16% to 28% *W*. This result is not surprising because DFT + *U* is a based on Hartree-Fock that is known to overestimate spin/orbital polarization and so in real calculations smaller U_{eff} should be used to compensate the effect. The difference suggests that 1) it may not be optimal to use theoretical U directly in DFT + U calculations of U and U-Zr, and 2) theoretical U's are still reasonably close to and can definitely provide the guideline for empirical U_{eff}. Moreover, Table 3.5 also illustrates the important point that there is only small change of Hubbard U for Uranium between different phases and at different compositions of U and U-Zr. Among different phases, for example, αU, βU and γU have theoretical U values of 1.87, 2.10 and 2.10 eV, respectively and the span is 0.23 eV, or 6% of W. The effect of composition is best illustrated when we look at the BCC phases, γU and γ(U,Zr). We see that when going from 0 to 93.75 at.%Zr, U reaches a maximum of 2.34 eV at 50 at.%Zr, which is about 0.24 eV higher than the minimum at 0 at.%Zr, or 6% W again. The small variations in U suggest that we may use a single U_{eff} for DFT + U calculations of U and U-Zr. Based on our study, we suggest to use U_{eff}=1.24 eV. Its magnitude is much smaller than that for U oxides like UO_2 for which Ref. [123] suggests the empirical U_{eff} to be 3 eV.

3.5 Conclusions

We have explored the correlation and relativistic effects in U metal and U-Zr alloy. All solid phases of U metal and U-Zr alloy have been studied in both DFT and DFT + U calculations without and with SOC included using the effective Hubbard U parameter U_{eff} ranging from 0 to 4 eV.

DFT overestimates the formation energetics of phases relative to the stable end-members by 0.10 and 0.07 eV/atom without and with SOC as compared to best-established CALPHAD models; DFT + U improves the energetics which matches

CALPHAD at U_{eff}=1-1.5 eV. A statistically best agreement is found at U_{eff}=1.24 eV with which DFT + U reduces the error to 0.04 and 0.02 eV/atom without and with SOC. Our validated DFT + U approach predicts that the BCC solution phase γ(U,Zr) only has a weakly positive and asymmetric mixing enthalpy, quite different from DFT and previous CALPHAD's results but consistent with a latest CALPHAD model.

Besides energetics, DFT also underestimates volume, misplaces bands immediately below Fermi level, and overestimates *f*-orbital occupation, while DFT + U with U_{eff}=1-1.5 eV consistently improve all these properties, and in general still neither promotes ordered magnetic moments nor opens unphysical band gap, consistent with experiment.

The calculated properties in general evolve as functions of U_{eff} in three stages, roughly corresponding to metal, metal-gap transition and gap states, where the gap refers to splitting between the up and down spin channels of *f*-bands.

The empirical U_{eff} values of 1-1.5 eV are close to but smaller than theoretical estimation of 1.9-2.3 eV that we obtain from the linear response approach. U_{eff} is found to vary only slightly between different phases and at different compositions of U and U-Zr, and thus a single U_{eff}=1.24 eV, which is the statistical optimal from energetic fitting is suggested for both U and U-Zr.

The relativistic effect of SOC is found to lower energy by 0.02 eV/atom, increase volume by <0.5%, adjust intensities of states below Fermi level and split bands above it, and also very slightly reduces the *f*-orbital occupation. It predominates in the unoccupied part of the valence band, so the effect on all these calculated ground state properties is small.

Finally, alloying with Zr generally reduces the *f*-orbital occupation and increases

Hubbard U slightly but does not change the qualitative features of valence bands. U-Zr alloy therefore should have similar strength of correlations as U metal.

4 Additional validations of DFT + *U* on the U and U-Zr systems

Note: This chapter has been accepted for publication as a peer-reviewed article[155] in Journal of Nuclear Materials, and the article was adapted for use in this thesis document.

4.1 Introduction

Our results in the previous two chapters showed that DFT + *U* can be of value in studying the U and U-Zr systems. However, some concerns[156, 157] are still not fully addressed: 1) the γU phase of elemental U metal's volume from DFT + *U* is too large while bulk modulus too small at higher U_{eff} values, for example 2 eV. 2) At U_{eff} =1.24 eV, for γU and U-rich γ(U,Zr) systems, the relative volume expansion due to SOC calculated using DFT + *U* is larger than expected, which is probably wrong. 3) At U_{eff} =1.24 eV, γ(U,Zr)'s volume of mixing from DFT + *U* is larger than that from DFT, which people may believe as erroneous. 4) At U_{eff} =1.24 eV, when spin orbit coupling (SOC) is included, γ(U,Zr)'s enthalpy of mixing is calculated by DFT + *U* to be slightly negative when mole fraction of Zr is larger than about 0.4 (the minimum is around -0.012 eV/atom at 75 at.%Zr). 3) DFT + *U* also predicts magnetic moments for U and U-Zr when U_{eff} is larger than certain limits—about 1.5 eV for U, and 1 eV for βU and γU.

In this chapter, we carefully analyze *ab initio* results for γU and γ(U,Zr) from both standard DFT and DFT + *U* that are both calculated by ourselves and from the literature and compare to experimental data whenever possible. In addition to γU and γ(U,Zr), we will also include relevant results and discussions on the ground state phase of αU.

Overall, we will show that although considerable uncertainty exists due to γU and γ(U,Zr)'s thermal and mechanical instability at 0 K, DFT + *U* at U_{eff} near 1 eV shows good promise of improving the predicted volume of γU and γ(U,Zr) compared to DFT. We will also show that bulk modulus of γU can also be improved by DFT + *U* with an optimal match with estimated 0 K experimental data also near $U_{\mathrm{eff}} = 1$ eV, which is consistent with the corresponding bulk modulus result for αU, with optimal match with estimated 0 K experimental data happening near $U_{\mathrm{eff}} = 1.5$ eV. In addition, we explain why magnetic moments are predicted in DFT + *U* for U and U-Zr after U_{eff} is large than certain limits, show that other ground state solutions are not affected by the magnetic moments and propose future work that may alleviate or avoid this issue. We therefore believe that DFT + *U* can be of value in studying U metal and U-Zr alloys.

4.2 Choice of U_{eff} in DFT + *U*

In order to assess if the DFT + *U* method is of value, one must use appropriate U_{eff} parameters. Here we discuss which values we feel are appropriate and why. We begin by defining a material's empirical U_{eff}, which is the U_{eff} with which DFT + *U* calculation reproduces a specified physical observable. The applicability of DFT + *U* for modeling a target property of a material is then decided by whether a reasonable empirical U_{eff} can be found. A material may of course have many properties of practical interests and another question to ask, which is related to some people's doubt on the physical meaning of U_{eff} parameter is whether empirical U_{eff} for different properties of a same material is consistent. Based on our results in Ref.[4] and additional results to be presented below, we show that empirical U_{eff}'s for the 12 different systems of U and U-Zr can indeed be found, and they vary approximately between 1- 1.5 eV among different structures.

Moreover, we will show in this chapter that for a given system of U and U-Zr the empirical U_{eff} for various properties is indeed roughly the same. For example, γU's empirical U_{eff}'s for volume found in Ref. [34] and bulk modulus to be shown below are all close to 1 eV. The BCC solution phase γ(U,Zr)'s empirical U_{eff} is also approximately 1 eV, similar to its BCC end member γU. Finally, different phases seem to have different empirical U_{eff}'s, For example, different from γU, αU's empirical U_{eff} may be as large as 1.5 eV. That was why in fact different empirical U_{eff}'s were used for different systems in Ref. [3]. In particular, for γ(U,Zr) we used $U_{\text{eff}} = 1$ eV, as γU and γ(U,Zr) share the same BCC structure and this value was found to be best for γU. We used $U_{\text{eff}} = 1.5$ eV for δ(U,Zr) as this was the largest value we generally found to give improved results for U-Zr and such a large value was necessary to give δ(U,Zr) a negative formation energy, consistent with its observed formation.

Having to determine appropriate U_{eff} for each system of U and U-Zr is laborious and not practical for general modeling of these systems with DFT + U. Hence we suggested that a single optimal U_{eff} for U and U-Zr is close to 1.24 eV, which was found in Ref. [34] to on average give enthalpies closest to those from the CALPHAD models. Clearly this value is only optimal in a statistical sense, and we call 1.24 eV statistically optimal U_{eff} for U and U-Zr, to differentiate it from individually optimal U_{eff} (empirical U_{eff}) of a particular system. Using such a single statistically optimal U_{eff} for all systems of U and U-Zr is of course an approximation, and less satisfactory results may still be obtained for certain systems. For example, the statistically optimal $U_{\text{eff}} = 1.24$ eV is not particularly accurate for γU and γ(U,Zr), as we will show below.

Overall, we believe that an evaluation of DFT + U for U metal and U-Zr alloy in general should consider U_{eff} not at 2 eV but in the range 1-1.5 eV. For example 1 eV, which is γU and γ(U,Zr)'s individual empirical U_{eff}, or 1.24 eV, which is the statistically optimal U_{eff} for enthalpies when considering the multiple systems of U and U-Zr together.

Our empirical U_{eff} values discussed above (U_{eff} = 1-1.5 eV), which were obtained from empirical fitting, are found to be reasonable based upon theoretical estimation of the Hubbard *U*. For example, our theoretical calculations based on the linear response approach[124] estimate that U and U-Zr's Hubbard *U* is in the range of 1.9 – 2.3 eV, and the exact value depends mainly on structure but also varies with composition. Another calculation also obtained a value of about 2 eV for αU[158]. While these theoretical values are somewhat larger than our empirically determined range of U_{eff} = 1-1.5 eV, this discrepancy is to be expected, because DFT + *U* is the Hartree-Fock approximation to DFT + DMFT, and DFT + *U* is expected to overestimate the effects of the Hubbard *U*[159]. Therefore, it is natural that one would arrive at smaller values of the Hubbard *U* when fitting DFT + *U* results to observable properties like formation enthalpy as compared to direct computation of *U* theoretically using approaches like the linear response.

4.3 Computational Details

All calculations were performed using the Vienna *Ab initio* Simulation Package (VASP) based on the generalized gradient approximation (GGA) to the exchange-correlation potential parameterized by Perdew, Burke, and Ernzerhof[30]. The electron-ion interaction is described with the projected augmented wave (PAW) method[74] as implemented by Kresse and Joubert[75]. For U and U-Zr, the difference between results from PAW and full potential methods like full potential linear muffin-tin orbital

(FPLMTO)[160] and full potential linear augmented plane wave (FPLAPW)[161] has been shown by both Ref.[157] and many references cited in Ref.[34] to be significantly smaller when comparing to that between DFT and DFT + *U* results. We will also compare our PAW results to full potential results below whenever possible. The simplified rotationally invariant form[31] of DFT + *U* that reproduces the standard DFT functional at U_{eff} = 0 eV was used. Other details, in particular the method to combat metastable DFT + *U* solutions are the same as we gave in Ref. [34].

4.4 Results and Discussion

4.4.1 γU and γ(U,Zr)

4.4.1.1 Volume for γU and γ(U,Zr)

Here we make a thorough assessment of experimental volume data for γ(U,Zr) in the whole composition range (and thus including the two end members γU and βZr), compare our PAW as well as full potential *ab initio* data from the literature to the most reliable experimental data and show that 1) DFT based on GGA underestimates the volume of γ(U,Zr); 2) DFT + *U* using U_{eff} = 1 eV shows promise of improving volume of γ(U,Zr), but there is major uncertainty. 3) DFT + *U* using higher U_{eff} values of 1.24 and 2 eV becomes clearly worse than U_{eff} = 1 eV and does show large volume errors. All data discussed in this section is tabulated in Table 4.1and plotted in Figure 4.1.

Table 4.1. γ(U,Zr)'s volume in unit of $Å^3$/atom from a) experiment, b) theory in this work, and b) theory in the literature, SOC and noSOC denote calculations with and without spin orbit coupling (SOC) included, respectively.

a) Experiment. The three experiments Lawson *et al.* [80], Akabori *et al.*[14], and Heiming *et al.* [83] directly measured volumes at high temperatures where γ(U,Zr) is stable, and both the original finite temperature data and the estimated 0 K values are given here (see supplementary materials of Ref.[34] for details of the estimation). The other two experiments, Huber and

Ansari[126] and Basak *et al.* [162] measured quenched samples at room temperature and the original data are tabulated directly here.

Mole Fraction of Zr	Lawson *et al.*	Huber and Ansari (room *T*)	Akabori *et al.*	Basak *et al.* (room *T*)	Heiming *et al.*
0	22.05/21.46 (1060/0 K)				
0.25		22.37			
0.3		22.24			
0.4		22.05			
0.5		22.29			
0.5		22.29			
0.6		22.52			
0.7		22.62			
0.707			23.11/22.78 (925/0 K)		
0.723				22.87	
0.749		22.75			
0.8		22.8			
1					23.7/23.1 (1253/0 K)

b) Theory in this work. All were calculated using PAW and have been reported in Table IV and FIG. 6 of Ref.[34] except the DFT + *U* (1eV) SOC value (explained in note 1 below).

Mole Fraction of Zr	DFT (0 K)		DFT + *U* (1eV) (0 K)		DFT + *U* (1.24eV) (0 K)	
	noSOC	SOC	noSOC	SOC	noSOC	SOC
0	20.13	20.17	20.98	21.18[1]	21.28	22.77
0.0625	20.36	20.41	21.38	21.63	21.96	22.79
0.25	21.10	21.18	22.23	22.60	22.62	23.20
0.5	21.97	22.06	22.75	22.99	23.02	23.33
0.75	22.43	22.60	22.89	23.00	23.04	23.23
0.9375	22.88	22.86	22.94	22.94	23.01	22.97
1[2]	22.91	22.91				

Note 1: We reported a solution with volume of 21.51 Å^3/atom in Fig. 6 of Ref.[34], but recently found another solution to be 0.001 eV/atom lower in energy, the volume of which (21.18 Å^3/atom) is then used here as the ground state solution.

Note 2: DFT + *U* is not applied on Zr.

c) Theory in the literature. The two references are Söderlind *et al.*[157] and Landa *et al.*[66].

Mole Fraction of Zr	DFT-KKRASA (300 K)[3]	DFT-FPLMTO (0 K)[4]	DFT-FPLAPW (0 K)[5]	
	noSOC	noSOC	noSOC	SOC
0	21.4		20.3	20.6
0.1	21.7			
0.2	22.0			
0.3	22.3			
0.4	22.7			
0.5	23.0			
0.6	23.2			
0.7	23.4			
0.8	23.6			
0.9	23.7			
1	23.8	22.98		

Note 3: From Fig.1 (a) of Landa *et al.*[66].

Note 4: From Fig. 9 of Landa *et al.*[66]. The original numerical values were provided to us by Söderlind in a private communication on November 20th, 2013.

Note 5: From Table 1 of Söderlind *et al.*[157].

We first review existing experimental data, as given in Table 4.1 a). We have done such a review already for the two end members γU and βZr in Ref. [34] and thus for each of them only the experimental values that were evaluated to be most accurate will be referenced here—Lawson *et al.* for γU[80] and Heiming *et al.* for βZr[83]. Both these experimental values were measured at high temperature and are corrected to give approximate 0 K volumes appropriate for comparison to *ab initio* values (see the supplementary materials of Ref.[34] for the review of experimental data for γU and βZr and the details of the correction). For γ(U,Zr), we found three experimental volume measurements—Huber and Ansari[126], Akabori *et al.*[14] and Basak *et al.*[162]. Both Huber and Ansari and Basak *et al.* measured quenched samples at room temperature. Basak *et al.*[162] found that two of the three quenched γ(U,Zr) samples actually phase separated into mixtures of γ(U,Zr) and δ(U,Zr), and thus we will only refer to the value from the sample that did not phase separate next. We suspect phase separation may have happened in some of Huber and Ansari's samples as well, because their data show convex shape. Such a shape differs from all other experimental and *ab initio* data and is counterintuitive for a phase separating alloy like γ(U,Zr), and thus is possibly incorrect. Especially, we expect the problem to be more severe near δ(U,Zr)'s stable composition range of about 60-80 at.%Zr. Therefore, we should put less weight on the data from Huber and Ansari, despite the fact that it is the only study that measured a wide composition range. The only data point for γ(U,Zr) measured directly at high-temperature is from Akabori *et al.*[14], which is particularly valuable as it probes the true structure of γ(U,Zr) that is only stable at high temperatures. The original value again has been corrected to give an approximate 0 K volume appropriate for comparison to *ab initio* values, as done above for other high-temperature data. As we can see in Figure 4.1 a), Basak *et al.*'s and Akabori *et al.*'s values are very close, so they should be considered especially trustworthy.

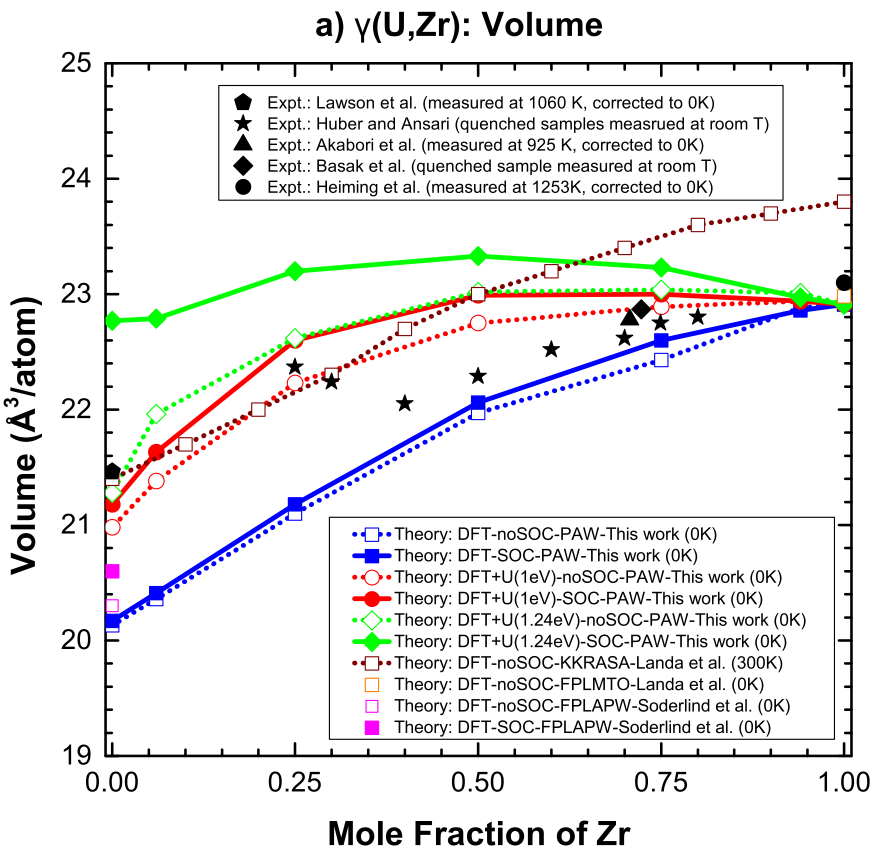

a) γ(U,Zr): Volume

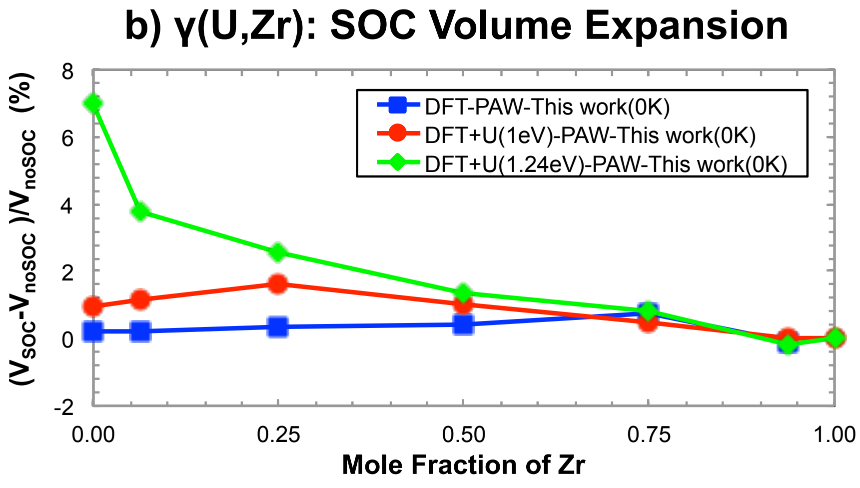

b) γ(U,Zr): SOC Volume Expansion

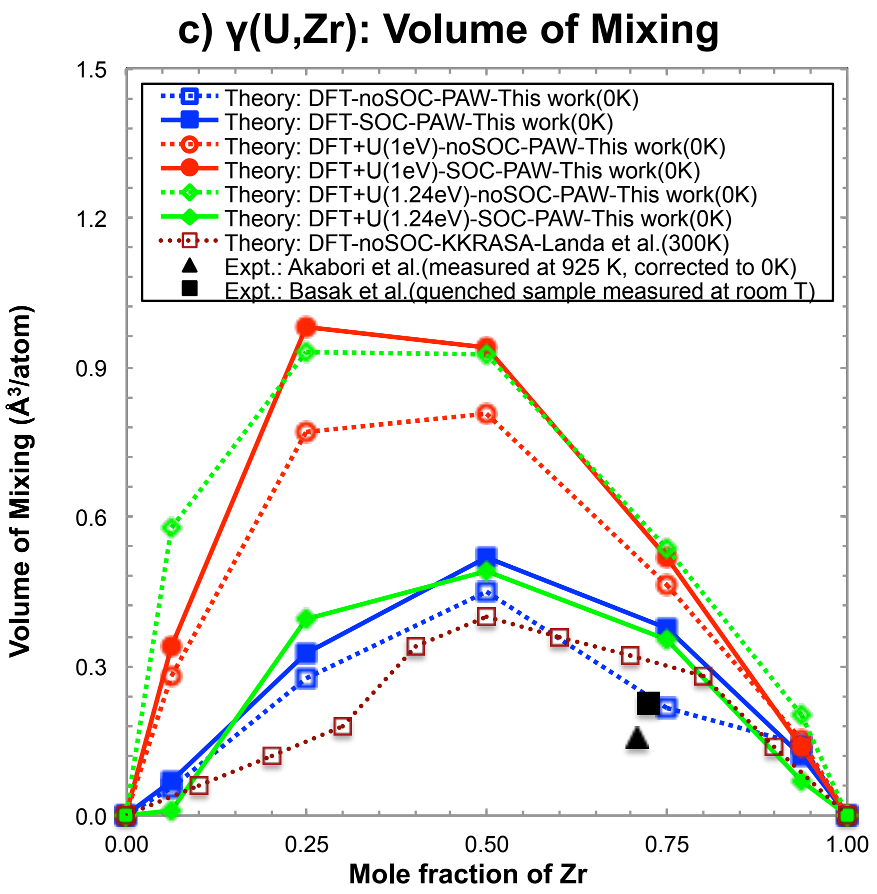

Figure 4.1. γ(U,Zr)'s a) volume, b) volume expansion due to spin-orbit coupling (SOC), and c) volume of mixing. γU is one end member of γ(U,Zr) with 0 at.%Zr and βZr is the other end member with 100 at.%Zr. SOC and noSOC denote calculations without and with SOC included, respectively. Volume expansion due to SOC is calculated as $(V_{\text{SOC}}\text{-}V_{\text{noSOC}})/V_{\text{noSOC}}$. Volume of mixing for γ(U,Zr) is defined as $V^{\text{mix}}_{\gamma(\text{U,Zr})} = V_{\gamma(\text{U,Zr})} - (1-x)V_{\gamma\text{U}} - xV_{\beta\text{Zr}}$ where x is Zr mole fraction. Experimental volume of mixing for Akabori *et al.*[14] and Basak *et al.* [162] is calculated by referencing to Lawson *et al.* for γU[80] and Heiming *et al.* for βZr[83], while Huber and Ansari[126] is neglected due to its unrealistic convex curvature (see text for details on these choices). Estimated 0 K values are plotted here for the three experiments Lawson *et al.* [80],

Akabori *et al.*[14], and Heiming *et al.* [83] that directly measured volumes at high temperatures where γ(U,Zr) is stable, while the original values are plotted for the other two experiments, Huber and Ansari[126] and Basak *et al.* [162] that measured quenched samples at room temperature.

Next we compare our *ab initio* results calculated using PAW to other *ab initio* studies of γ(U,Zr) in the literature to clarify any issues on differences between the *ab initio* methods. For this purpose, let us look at Table 4.1 b) and c). It shows that our DFT noSOC/SOC calculations using PAW predict γU's volume to be 0.2/0.4 $Å^3$/atom smaller than Söderlind *et al.*[157]'s calculated using FPLAPW (magenta square symbol). For βZr, our DFT calculations using PAW obtained essentially the same result as Landa *et al.*[66]'s DFT calculations using FPLMTO (open orange square symbol; estimated from Fig 9 of Ref.[66]). These results show that our noSOC/SOC PAW results are about 1%/2% smaller than the FPLAPW calculations for γU, which is likely in part due to pseudopotential effects but may also come from other differences in the two calculations. Additional calculations from Landa *et al.*[66]'s (brown open symbol and dash line) using the Korringa-Kohn-Rostoker method in the Atomic Aphere Approximation (KKRASA) obtained values that are larger than all the other three calculations using FPLAPW, FPLMTO and PAW by approximately 1.0 $Å^3$/atom in the whole composition range, even for βZr. It should be noted that KKRASA values were from model temperature of 300 K and the other three calculations were from 0 K, but the temperature effect should be quite small (<0.2 $Å^3$/atom based on our estimation in Ref.[34]) and cannot explain the majority of the large discrepancy of about 1.0 $Å^3$/atom. This comparison suggests that the range of DFT values can be relatively large depending on the methods. However, if we exclude the KKRASA results as involving additional approximations over FPLAPW, then the discrepancies between PAW and FPLAPW for γU are still significantly smaller than the difference between the *ab initio* DFT results and the experiment values, which are about 6% for PAW and 5% for FPLAPW. This suggests that in exploring DFT + *U* effects on volume our PAW calculations can be considered to yield results that are close enough compared to best *ab initio* calculations using full potential methods like FPLAPW, and weakly enough influenced by the pseudopotential and other approximations, to allow meaningful comparison to experiments and assessment of effects of adding Hubbard *U* potential.

Before we compare *ab initio* results to experimental data for γU and γ(U,Zr), we stress that such a comparison will certainly face major uncertainty and is potentially very misleading. We feel this way for three reasons. Firstly, γU and γ(U,Zr) are high temperature phases and thermodynamically unstable at 0 K, so no corresponding experimental volume data at low temperature are directly available. We have to extrapolate experimental data from the actual measurement temperatures over 1000 K to 0 K, which necessarily introduces considerable uncertainty. Secondly and more importantly, γU and γ(U,Zr) are also mechanically unstable[34, 87] at 0 K and can only be modeled in 0 K *ab initio* calculations with lattice shape and ion position constrained relaxations. Thirdly, such a constrained relaxation approach appears to worsen the problem of metastable solutions with DFT + *U*[131], which otherwise can be quite well mitigated with approaches like U-ramping[132] as we did in Ref.[34]. For example, we recently found that for γU calculated by DFT + *U* at U_{eff} = 1 eV, another solution exists that is 0.001 eV/atom lower in energy than the solution we reported in FIG. 6 of Ref.[34].

This new solution has a volume of 21.18 Å^3/atom, while the old solution despite being very close in energy, has a volume of 21.51 Å^3/atom.

However, to address the concern about the calculated γ(U,Zr)'s volume, we still proceed and compare our *ab initio* volume data for γ(U,Zr) (including γU and βZr) calculated using PAW by us or full potential methods from the literature to the above reviewed experimental results in Figure 4.1. The numerical values are also given in Table 4.1.

Firstly, we focus on absolute volume in Figure 4.1 a). In general, we see that our DFT calculations using PAW underestimate the volume of γ(U,Zr) in the whole composition range. The error is larger at smaller Zr concentration. For example, for the γU end member, the error is about 1.3 Å^3/atom from our PAW calculations, and about 0.9/1.2 Å^3/atom from Söderlind *et al.*[157]'s FPLAPW noSOC/SOC calculations. Admittedly, there should be error in our estimation of γU's volume at 0 K from the original experimental data[80] measured at 1060 K. Based on our validation against experimental data shown in FIG. S1 of Ref. [34], we can estimate that such an error in the temperature correction may be as large as 0.5 Å^3/atom for γU, which is still much smaller than the total error of over 0.9 Å^3/atom between DFT and experimental volume for γU. Therefore, it should be reasonable to expect that γU's volume is considerably underestimated by DFT based on GGA. In comparison, DFT + U gives larger volume than DFT, and at $U_{\text{eff}} = 1$, our DFT + U volume results are closer to the most reliable values discussed above than DFT (specifically Lawson *et al.* for γU[80] (filled black pentagon symbol), the high-temperature γ($U_{0.707}Zr_{0.293}$) data from Akabori *et al.*[14] (filled black triangle symbol), and the quenched γ($U_{0.723}Zr_{0.277}$) sample of Basak *et* *al.*[162] that did not phase separate (filled black rhombus symbol)). The improvement is particularly significant for γU. However, at a slightly larger U_{eff} of 1.24 eV, DFT + *U*, especially when SOC is included, gives volumes that are much larger than the experimental values, and the error is also most significant for γU. The exact source of the error at U_{eff} = 1.24 eV is still unknown, but the large changes in predicted volume suggest that something significant has changed in the electronic structure. Indeed, we can see in FIG.10 of Ref. [34] that for γU and γ(U,Zr) the density of states (DOS) differs significantly between those calculated by DFT and by DFT + *U* at U_{eff} = 1.24 eV, while for other systems like αU, βU and δ(U,Zr) the DOS is still quite similar between DFT and DFT + *U* at U_{eff} = 1.24 eV. In addition, the lack of a smooth volume curve in Fig. 1 a) for U_{eff} = 1.24 eV with SOC also suggests some systems, for example γU, are probably failing to relax to the proper lowest energy state. However, we were not able to converge any state with a lower volume at this point.

Secondly, given the particularly large increase of volume from the noSOC to SOC case at U_{eff} = 1.24 eV it is useful to consider explicitly the relative volume expansion due to SOC, which is given in Figure 4.1 b). A normal range of SOC volume expansion is about 1-2% for U metal[146, 147]. We see in Figure 4.1 b) that our DFT and DFT + *U* calculations of γ(U,Zr) at U_{eff} = 1 eV is in the expected range (even the previous metastable solution for γU with a larger volume of 21.51 Å^3/atom still only has an expansion of about 2.5%), while at U_{eff} = 1.24 eV the expansion is as high as 7% for γU, which is abnormally large. This result may be in part due to some convergence errors, but overall suggests an unphysical interaction of SOC with U_{eff} = 1.24 eV.

Finally, we consider how volume vs. composition curves deviate from linearity (perfect linear relationship between volume and composition is known as Zen's law[163]). The deviation from linearity can be quantitatively calculated as $V_{\gamma(\mathrm{U,Zr})} - (1-x)V_{\gamma\mathrm{U}} - xV_{\beta\mathrm{Zr}}$ where x is Zr mole fraction. We call this deviation the "volume of mixing" and plot it in Figure 4.1 c). It shows that DFT + *U* does give larger volume of mixing than DFT, reaching a maximum of about 1 Å^3/atom (5%) at 0.25 mole fraction of Zr at U_{eff}= 1 eV, although at U_{eff}= 1.24 eV with SOC included it actually drops back to be very close to DFT's. As references, we calculate the volume of mixing for the two experiment data Akabori *et al.*[14] and Basak *et al.* [162] by using the end member volumes from Lawson *et al.* [80] and Heiming *et al.* [83]. Figure 4.1 c). shows that DFT gives volume of mixing that is closer to the two particular estimated experimental points than DFT + *U* at U_{eff}= 1 eV by about 0.2 Å^3/atom (1%). However, given that the alloy and the end member data used to calculate the two points come from different experimental sources, the experimental volume data must be extrapolated from high temperature to 0 K (which is an 0.5 Å^3/atom effect for γU), and that we are modeling a dynamically unstable phase with constrained *ab initio* calculations, we do not think that this level of error is very meaningful. Furthermore, we point out that significant deviation from Zen's law is not in itself a sign of an error. For example, Hafner[164] reviewed experimental volumes of mixing (called volume of formation in his paper) for 49 compounds of different categories, and found that many of them have volumes of mixing greater than our calculated maximum 5% volume of mixing for γ(U,Zr) at U_{eff} = 1 eV. Although the compounds summarized by Hafner were ordered phases, not solid solutions as is γ(U,Zr), these results suggest that our volume of mixing for γ(U,Zr) is not excessively abnormal.

Overall the above analysis shows that DFT based on GGA significantly underestimates the volume of γ(U,Zr), especially the end member γU, and DFT + U at $U_{\mathrm{eff}} = 1$ eV gives agreement with assessed experimental absolute volume data as good as or better than DFT. The predicted volume of mixing by DFT + U at $U_{\mathrm{eff}} = 1$ eV does appear to be quite large compared to DFT, but it is not clear that this is incorrect given the constrained nature of the calculations, the limited experimental data and the necessity to extrapolate experimental data from over 1000 K to 0 K. DFT + U at $U_{\mathrm{eff}} = 1.24$ eV, especially for the SOC case does seem to give some unusual behavior and must be considered somewhat unreliable in this phase. Despite the uncertainty, these findings are consistent with the idea that DFT + U, with proper U_{eff} can yield improved results for the U-Zr system, even for γ(U,Zr), if appropriate U_{eff} is used.

4.4.1.2 Bulk Modulus for γU

Next we consider bulk modulus. Again, we review the experimental data first. We point out first that it is the consensus of more recent studies[144, 165] that early high pressure X-ray measurements of U metal's bulk modulus, including Yoo *et al.* [166] were performed in nonhydrostatic media and systematically overestimated the measured bulk modulus values due to nonhydrostatic stress (see TABLE 1 and discussion of it in Ref. [144]). The error associated with the nonhydrostatic media is difficult to estimate for γU due to limited data so we will estimate it based on similar studies of αU. The latest and perhaps most accurate value of αU's bulk modulus obtained from X-ray studies in quasihydrostatic media is 114.5 GPa at room temperature (298 K)[165], which is consistent with values from both ultrasonic (115 GPa [167, 168] and 114 GPa [169]) and neutron-diffraction (112 GPa [170]) measurements at room temperature, and is very close to the value estimated from specific heat (107 GPa[171]) measurement at almost 0 K. In contrast, Yoo *et al*. [166] reported a significantly larger value of 135.5 GPa at room temperature, which suggests that the error due to nohydrostatic stress in their study[166] was about 135.5 – 114.5 = 21 GPa. Yoo *et al*. [166] also reported γU's bulk modulus at 1100 K to be 113.3 GPa. Because they used the same nonhydrodstatic media when measuring both αU and γU, similar error to what we just calibrated for αU might be expected to occur in the γU measurements. Therefore, the true value for γU's bulk modulus at 1100 K is likely closer to 113.3 – 21 = 92.3 GPa. Before comparing to our *ab initio* results at 0 K, we need to extrapolate experimental bulk modulus values measured at finite temperatures to zero temperature (0 K). There are accurate measurements of αU's bulk modulus at multiple temperatures between 298 and 923 K [168] that span the major part of its stable temperature range. Based on these data, Lawson estimated αU's bulk modulus at 0 K to be 114.4 GPa[172]. Unfortunately, there is no similar data for γU on the evolution of bulk modulus with temperature as far as we are aware, and γU is not even stable below 1045 K[80]. Considering the challenges of obtaining the trend in γU's bulk modulus with temperature, we assume αU and γU have similar temperature dependence of bulk modulus and estimate that γU's bulk modulus should increase from 92.3 GPa at 1100 K to 109.5 GPa at 0 K based on αU's trend measured in Ref. [168]. We note that this effective bulk modulus for γU at 0 K is quite uncertain due to the necessity of extrapolating from high-temperature based on αU's trend and the fact that γU is not stable at lower temperatures. Normally we would not even attempt to compare 0K *ab initio* and high temperature experimental data in such details for a phase that is both thermodynamically and mechanically unstable at 0 K. However, to address the concern about the calculated γU’s bulk modulus, we believe that this is the best estimation presently available for γU’s bulk modulus at 0 K.

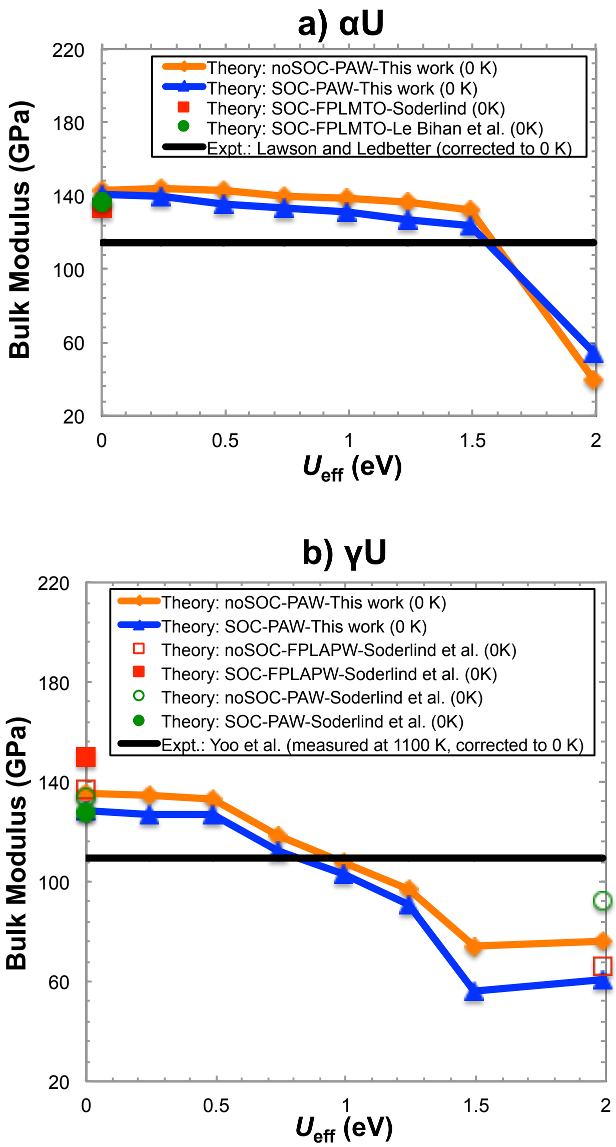

Figure 4.2. Bulk modulus for a) αU and b) γU as a function of U_{eff}. SOC and noSOC in the legend denote calculations without and with spin-orbit coupling (SOC) included, respectively. For αU, the two FPLMTO results are from Le Bihan *et al.* [144] and Söderlind[105], respectively while the experimental value extrapolated to 0 K is from Lawson and Ledbetter[172]. For γU, the referenced *ab initio* results are from Söderlind *et al.*[157] and the experiment values extrapolated to 0 K (see texts) is from Yoo *et al.*[166].

Now we compare our *ab initio* bulk modulus to the estimated 0 K experimental values of 114.4 and 109.5 GPa for αU and γU, respectively, in Figure 4.2. This figure shows several important points that are common for both αU and γU: 1) DFT overestimates the bulk modulus substantially (by about 20 GPa or more); 2) DFT + U obtains smaller bulk modulus (the larger U_{eff}, the smaller the bulk modulus) and is in better agreement with experiment than conventional DFT again when U_{eff} is in the range of 1-1.5 eV, in excellent agreement with the empirical U_{eff} range we determined in Ref.[34]; 3) DFT + U reproduces the experimental bulk modulus of αU and γU near U_{eff} = 1.5 eV and 1 eV, respectively, but considering the two phases together, DFT + U at U_{eff} = 1.24 eV seems again to be near the statistically optimal U_{eff} value, consistent with what we obtained from validations on energetics in Ref.[34].

Let us focus on γU and make quantitative comparison now. We find that DFT + U noSOC/SOC calculations at γU's individual empirical U_{eff} of 1 eV obtains its bulk modulus to be 107.6/103.3 GPa, respectively—only 1.9/6.2 GPa different from estimated 0 K experimental value of 109.5 GPa, which should be within the error bars of the experimental data and the finite temperature extrapolation. At U and U-Zr's statistically optimal U_{eff} of 1.24 eV, DFT + U noSOC/SOC calculations gives 97.1/90.9 GPa, respectively. The result is about 11/17% below the extrapolated 0 K experimental value, respectively. Even with these errors, the results are still comparable or better than those from conventional DFT noSOC/SOC calculations, which in our own study with PAW obtain 135.1/128.5 GPa (23/17% above the extrapolated 0 K experimental value), while Söderlind *et al.* [157] reported 134/128 GPa (23/17% above the extrapolated 0 K experimental value) with PAW and 137/150 GPa (23/37% above the extrapolated 0 K experimental value) with FPLAPW.

In short, we find that γU's volume and bulk modulus seem to be again improved by DFT + *U* at U_{eff} = 1 eV, but there is major uncertainty due to lacking of sufficient and reliable experimental volume data covering wide composition ranges, the mechanical instability of this phase, and the approximate estimation of finite temperature effects. Also, the calculated properties deteriorated going from U_{eff} = 1 to 1.24 eV. At present, we do not think the errors calculated at the particular U_{eff} of 1.24 eV is so severe that the whole DFT + *U* approach should be considered inappropriate. Instead, we should take the errors for γU and γ(U,Zr) at U_{eff} = 1.24 eV as a warning that using a single U_{eff} = 1.24 eV across different structures and compositions of U and U-Zr should be done with care. In particular, we have shown above that 1 eV is probably closer to γU and γ(U,Zr)'s empirical U_{eff}, with which DFT + *U* seems to be able to provide improved accuracy vs. experiments compared to DFT.

4.4.1.3 Enthalpy of Mixing for γ(U,Zr)

Next we show that γ(U,Zr)'s enthalpy of mixing results gave the same picture in terms of comparison between DFT and DFT + *U* at different U_{eff}'s. Such results were reported in FIG. 5 of Ref.[34]. From there we can see that the DFT calculations of ourselves[34] and Landa *et al.* [66] predicted essentially the same enthalpies that are large in value (0.12 eV/atom or higher at maximum near 50 at.%Zr) and quite symmetric as functions of composition. These DFT results agreed well with those from the two CALPHAD models of Refs. [11, 40], but differed significantly from what was predicted in the CALPHAD model that we reported in Ref.[33], which suggested the enthalpies to be mildly positive (about 0.07 eV/atom at maximum) and asymmetrically higher on the U-rich end. DFT + *U* in general predicted smaller values when U_{eff} was gradually increased. At U and U-Zr's overall statistically optimal U_{eff} of 1.24 eV, the enthalpies from DFT + U even became negative when mole fraction of Zr is larger than about 40 at.%Zr with the calculations included SOC, although they remained mostly positive without SOC. Although the former could still give a miscibility gap between 0 and 70 at.%Zr, which completely covers the experimental miscibility gap range of about 10-50 at.%Zr and hence can not be ruled out as wrong for sure, such a partial miscibility gap disagrees with the three CALPHAD models[11, 33, 40] that all suggest a miscibility gap extending the whole composition range, as we summarized in Fig.7 of Ref. [33]. This suggests again that $U_{\mathrm{eff}} = 1.24$, despite being statistically optimal U_{eff} when considering the many systems of U and U-Zr together, may not be best for γ(U,Zr) individually. However, again in consistency with DFT + U results for other properties, at $U_{\mathrm{eff}} = 1$ eV, which we have been suggesting to be closer to γ(U,Zr)'s individual empirical U_{eff}, DFT + U predicted enthalpies to be positive and hence a miscibility gap covering the whole composition range. It also reproduces the moderate and asymmetric enthalpy higher in the U-rich end from the CALPHAD model[33], although quite different from the other two CALPHAD models[11, 40] which both gave large and symmetric enthalpy. The controversy on the enthalpy's quantitative values are hard to resolve for this high temperature phase as we explained above, but the one on the shape of the enthalpy seems to be clarified to certain extent by an experimental result[137], which despite again being measured at high temperature, gave asymmetric enthalpy higher in the U-rich end seen in the CALPHAD model[33] and all of our DFT + U results, not in DFT and other CALPHAD models[11, 40].

4.4.2 αU

So far we have focused primarily on the high temperature BCC phases γU. However, due to the fact these BCC phases are not only thermodynamically but also mechanically unstable[34, 87] at 0 K they are potentially unreliable systems to focus on for validation. We believe that the ground state phase αU is a more appropriate case than γU and γ(U,Zr) to validate model approaches. We therefore briefly discuss here how DFT + *U* compared to conventional DFT for αU.

4.4.2.1 Bulk Modulus

We first discuss bulk modulus, as shown in Figure 4.2 a). Conventional DFT obtained αU's bulk modulus to be 133GP in Ref.[105] and 136 GPa in Ref.[144] using FPLMTO, and 141 GPa using PAW here. As we discussed above in section 4.4.1.2, the more accurate experimental values are all below 115 GPa at 300 K, and are estimated to be 114.4 GPa at 0 K[172]. In comparison, our DFT + *U* calculations obtained 127.1 and 124 GPa at U_{eff} = 1.24 and 1.5 eV, respectively, which are lower and closer to the experimental values.

4.4.2.2 Volume

Next we discuss volume. It is true that some earlier full potential calculations[103, 105] using only conventional DFT already reproduced αU's volume with error <0.5%, while pseudopotential PAW calculations of ours[34] and those in Refs.[108, 113, 165] gave errors of about 2%. From these results one may be tempted to assume that the pseudopotential approximation introduces a significant error, which would confuse validation of DFT + *U* in this system. However, the difference between full potential and pseudopotential volume results for αU are entangled with other aspects of calculations.

For instance, full potential studies in Refs.[103, 105] used the so called PW-91[173] GGA functional, while we used PBE[30] GGA functional in Ref[34]. Moreover, as we have already discussed in Ref.[34], there are also differences in structural relaxation: Pseudopotential calculations[34, 108, 113, 165] almost always fully relaxed all structural degrees of freedom of αU simultaneously with optimization algorithms like conjugate-gradient. In comparison, the full potential calculations in Ref.[103] did not relax the structural parameter that determines the atomic positions at all, but just lattice constants and obtained αU's volume to be 20.41/20.76 Å^3/atom from noSOC/SOC calculations, respectively. Ref.[105] performed sequential iterative relaxation of the lattice constants and the structural parameter, and obtained volumes of 20.40/20.67 Å^3/atom from noSOC/SOC calculations, respectively, which are only slightly smaller than those of Ref.[103]. A more recent FPLMTO study[144] that also used PBE[5] GGA functional and fully relaxed all structural degrees of freedom simultaneously using conjugate-gradient algorithm predicted αU's equilibrium volume to be 20.34 Å^3/atom from DFT-SOC calculations, which is >0.3 Å^3/atom (or 1.5%) smaller than the two previous full potential results. Comparing to the experimental value of 20.53 Å^3/atom at 45 K[125] (corrected to be 20.48 Å^3/atom at 0 K), the volume from this full potential calculation[144] is still underestimated by about 0.2 Å^3/atom (1%). We have shown in Ref.[34] that DFT + *U* will increase the calculated volume for αU, and hence is expected to bring it closer to the experimental volume value, consistent with the improvement for bulk modulus as we discussed in section 4.4.2.1 above.

4.4.2.3 Electronic Structure

Besides volume and bulk modulus, we have also shown in Ref.[34] that DFT + *U* can improve the calculated electronic structure for αU. Specifically, as shown in FIG. 8 and FIG. 11 of Ref. [34], DFT + *U* at U_{eff} = 1.24 eV shifts upwards some bands, intensifies the DOS peak directly below the Fermi level, and reduce the *f*-orbital occupation relative to DFT. Comparing to the latest photoelectron spectra of αU (001) single crystal[115, 116], these are improvements over conventional DFT, and are similar to the improvement seen in the FPLMTO calculations of αU based on many-body quasiparticle self-consistent GW (QSGW) method, which is potentially more accurate than DFT + *U*[119]. These evidences all serve to support that DFT + *U* is applicable for αU and can yield improved results compared to conventional DFT.

4.4.3 The magnetic moments issue

The final issue is that DFT + *U* may result in magnetic ground state solutions, which are not believed to occur in nature for U metal, although their existence (or non-existence) is uncertain for U-Zr alloy due to lack of experimental data—note both U and Zr are paramagnetic ("nonmagnetic") in ground state, but two "nonmagnetic" metals can still have a alloyed phase to be magnetic, for example UCu_2. We showed in Ref.[34] that for U metal and U-rich U-Zr alloys magnetic solutions generally do emerge within the empirical U_{eff} range of 1-1.5 eV. For example, the maximum local spin moments for αU, βU, and γU are 0.00/0.05, 1.00/1.46, and 0.22/1.36 μB/atom from DFT + *U* calculations at U_{eff} = 1/1.24 eV, respectively. Those magnetic solutions suggest that the present DFT + *U* approach is not completely satisfactory. Nevertheless, such an imperfection is to be expected given that DFT + *U* is equivalent to the DFT + DMFT formalism wherein the DMFT impurity problem is solved within Hartree-Fock approximation[159]. Hartree-Fock can only incorporate correlations via real, static self-energies which amount to splitting in the spin and orbital sectors. The Hartree-Fock self-energy therefore often exaggerates polarization as compared to the complex, frequency dependent self-energy that can be obtained exactly using quantum Monte-Carlo[174].

However, one should not discount DFT + *U* just because it predicts a magnetic solution. For our particular cases of U and U-Zr, we have shown above that the ground state properties of energy, volume, and bulk modulus for U and U-Zr can be improved with DFT + *U* despite some errors in the moments. This result is in agreement with the theme of an earlier study[175] in which the energetics of the six known allotropes of Pu metal were concluded to be well reproduced by the DFT plus orbital polarization (DFT + OP) calculations despite the fact that significant local magnetic moments were also obtained in the calculations (> 2.0 μB/atom, see FIG. 3 of Ref. [34]), in contradiction with experiments[176].

Furthermore, we hope that future work will address this problem of spurious moments using DFT + DMFT, with which the static moments will perhaps not be predicted, while the same or better quantitative improvements are expected for the other properties. As an example, for δPu, one of the allotropes of Pu, DFT + *U* also resulted in a magnetic solution in Ref.[177], while DFT + DMFT using quantum Monte-Carlo produced a mildly correlated Fermi liquid with no magnetism[178], which is consistent with experiment. Another factor to consider besides the solution to the DMFT impurity problem is the double-counting correction scheme, which could also be responsible for pushing the system into an excessively correlated regime. So far only the so-called fully localized limit (FLL) double-counting have been explored for U and U-Zr, but there are other choices which could be more appropriate. In particular, the so-called around the mean field (AMF) scheme has been shown to give magnetic polarization a much larger energy penalty than the FLL[149]. Returning to the example of δPu, the FLL based DFT + *U* also resulted in a magnetic solution in Ref.[177], but AMF based DFT + *U* in Ref.[150] yielded a nonmagnetic ground state in agreement with experiment results that also reproduced other equilibrium properties well, all being significant improvement over the conventional DFT. Further study is needed to assess to what extent different double counting correction schemes in DFT + *U* might reduce or remove the moments in the range of physical U_{eff} values. Even in light of the present DFT + *U* results, given that energetics, volume, bulk modulus and aspects of electronic structure can be generally improved, we believe it would be misguided to abandon the approach just because of the emergence of magnetic moments.

4.5 Conclusions

In summary, our review of existing experimental and full potential *ab initio* data from the literature suggests that DFT based on GGA seems to underestimate the volume and overestimate the bulk modulus of γU considerably. We show in Ref. [34] and here that the key properties of γU's volume and bulk modulus that were in poor agreement with experiment from DFT + *U* calculations using $U_{\text{eff}} = 2$ eV seem actually to be quite reasonably well reproduced by DFT + *U* at or near $U_{\text{eff}} = 1$eV, which is evidently better or as good as conventional DFT. γ(U,Zr)'s volume and enthalpy also seems to be improved by DFT + *U* at or near $U_{\text{eff}} = 1$eV. However, much uncertainty still exists for these high temperature BCC phases γU and γ(U,Zr) due to lacking of sufficient and direct low temperature experimental data because they are both thermodynamically and mechanically unstable at our *ab initio* modeling temperature of 0 K and must be treated with the constrained structural relaxation approach in our calculations. Errors that appear at larger U_{eff} in γ(U,Zr) are certainly a concern and show limitations of using just a single U_{eff} value, but do not undermine the potential value of the approach using more appropriate U_{eff} values.

The ground state phase αU is a more appropriate case to validate *ab initio* approaches. We show that DFT overestimates the bulk modulus of αU by over 20 GPa comparing to most accurate experimental results measured with multiple methods, even when calculated using full potential methods. The difference between some previous full potential results and our PAW results on αU's volume is analyzed to be due to not only the pseudopotential approximation but also the differences in GGA functional and structural relaxation methods. A more recent full potential calculation using FPLMTO with the same GGA functional and structural relaxation method as ours still underestimates αU by about 1%. DFT + *U* gives lower bulk modulus and larger volume for αU than DFT, and hence improving them comparing to experiments. They are consistent with DFT + *U*'s improvement over DFT in the calculated electronic structure of αU comparing to experimental photoelectron spectra.

The emergence of magnetic moments in U metal and some U-Zr alloy systems is a concern, but does not seem to keep DFT + *U* from providing other improved ground state properties when compared to conventional DFT. Furthermore, this artifact can potentially be avoided if we use alternative double counting terms in DFT + *U*, or go beyond the Hartree-Fock approximation and use DFT + DMFT, whereby the DMFT impurity problem is solved exactly via quantum Monte-Carlo.

5 CALPHAD Modeling and *Ab initio* Calculations of the Np and Np-Zr systems

Note: This chapter has been published as a peer-reviewed article[35] in Journal of Nuclear Materials, and the article was adapted for use in this thesis document.

5.1 Chapter Abstract

A thermodynamic description of Np-Zr alloys is developed using the CALPHAD method based on available experimental information on phase equilibria and select *ab initio* energetics. The present thermodynamic description shows improvements compared to previous models in the predicted phase diagram when comparing to assessed reliable experimental data. *Ab initio* density functional theory (DFT) calculations are also performed on all known stable solid phases of Np-Zr alloys and the end member Np and Zr metals. Comparing to the formation energetics predicted from the CALPHAD models of both this work and a previous study (J. Nucl. Mater. 409, 1 (2011)) we find that DFT with the generalized gradient approximation (GGA) to the exchange-correlation potential overestimates the formation enthalpies of Np and Np-Zr by about 0.15 eV/atom, and the so-called DFT + U approach with a U_{eff} of near 0.65 eV can reduce this error by about 0.07-0.10 eV. Our comprehensive comparision between existing CALPHAD, *ab initio* and experimental results for Np-Zr indicates a need for further experiments on the phase equilibrium.

5.2 Introduction

Np-Zr is an important alloy system for nuclear fuels due to its potential uses in multiple applications. For example, Np-Zr-H can be used in the hydride fuel as an integral fuel-moderator system, since the concentration of hydrogen in the hydride is comparable to that of hydrogen in liquid water of LWR cores [179]. In addition, the Np-Zr-H alloys are also considered as the actinide hydride targets in fast reactors, which were proposed to reduce the actinide content in nuclear waste [180]. Furthermore, Np-Zr is a binary component of the U-Pu-Zr-MA (MA = Minor Actinides Np, Am, Cm) alloy, which is a promising metallic fuel for fast nuclear reactors [179]. Recent research activities on phase equilibria of the U-Pu-Zr-MA systems [23, 162, 181] have contributed to understanding of the phase behavior of the actinide alloys for desiging new actinide materials.

Because of the importance of the Np-Zr system in nuclear engineering applications, it is necessary to study thermodynamics of the Np-Zr alloys, and to provide a reasonable thermodynamic description of this system for constructing reliable actinide thermodynamic databases.

Up to now, thermodynamic modeling of the Np-Zr system has been performed by two research groups [12, 182]. However, the optimized Np-Zr phase diagrams in the two studies [12, 182] still leave some uncertainty unresolved, which motivates further thermodynamic modeling of this system. One aim of this work is to develop a CALPHAD model of the Np-Zr system, which can be utilized for the thermodynamic modeling of multi-component actinide systems in the future. Moreover, it has recently been found that the DFT + U method can provide useful energetic calculations of the U-

Zr alloys [33, 34] for phase diagram development. Therefore, it is interesting to see if DFT + *U* calculations can also be applied to the Np-Zr system to assist in the thermodynamic modeling.

5.3 Literature Review

5.3.1 Experimental Data on Np-Zr Phase Diagrams

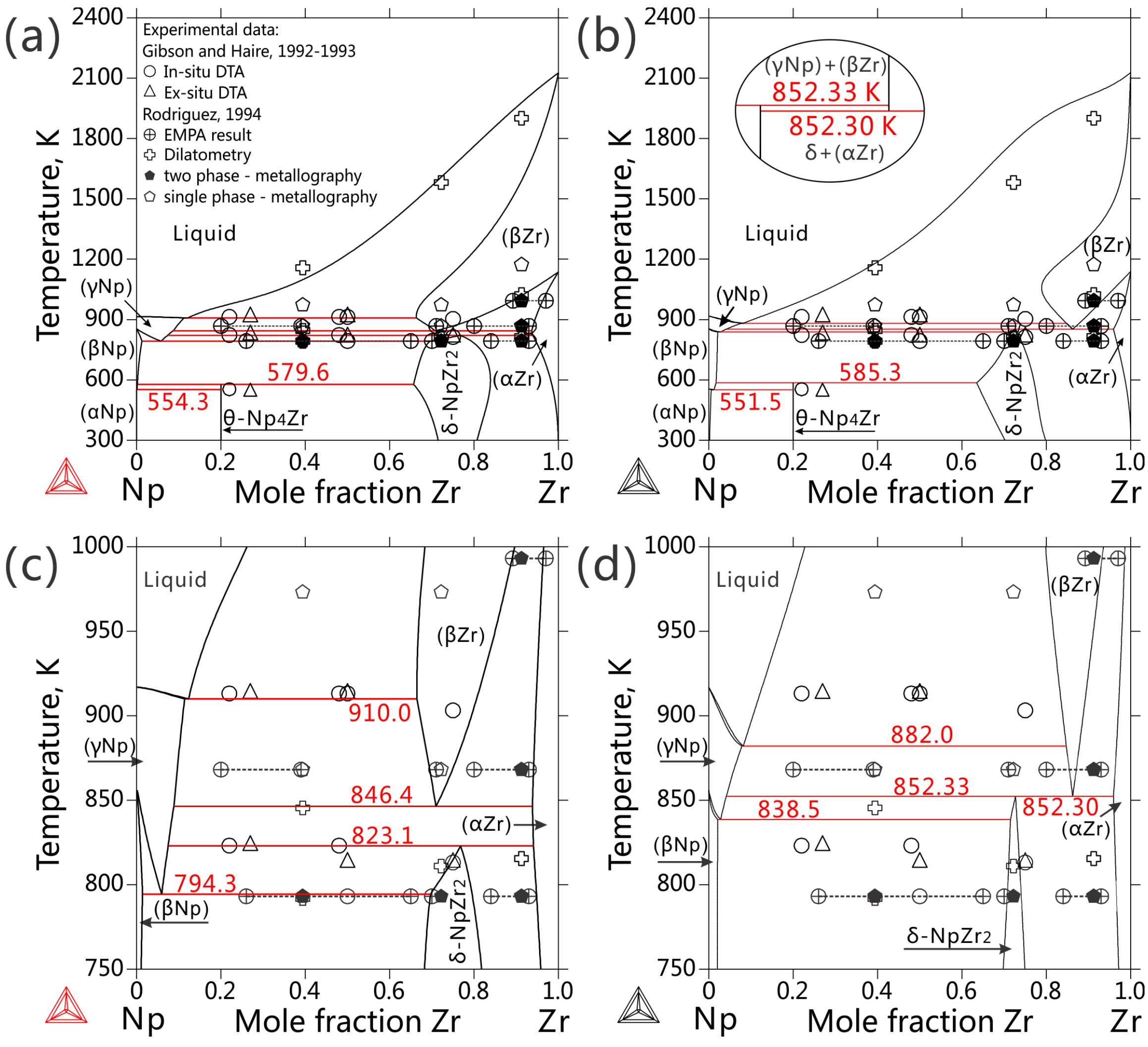

Figure 5.1. Comparison of the phase diagram of Np-Zr between the CALPHAD modeling and experimental data [183-185]. (a) calculated phase diagram in this work and experimental data; (b) calculated phase diagram in the work by Bajaj *et al*. [182] and experimental data [183-185]; (c) magnified part of (a); (d) magnified part of (b).

All of the experimental information on Np-Zr of which we are aware that can be used in thermodynamic modeling is summarized in Figure 5.1 (a). Firstly, a major source of experimental phase equilibria data was from the research group of Gibson *et al*. [183, 184], who provided the invariant equilibria temperatures of the Np-Zr phase diagram using both in-situ and ex-situ Differential Thermal Analysis (DTA) measurements [183, 184]. Using the so-called in-situ DTA measurement invented by Gibson *et al*. [183, 184], pure elemental Np and Zr were placed together in a Ta or Al_2O_3 crucible and the Np-Zr alloying proceeded upon fusion of Np. However, since the melting temperature of pure Zr is higher than the maximum operating temperature (1200 ºC), it is hard to confirm that an equilibrium alloy was achieved during the in-situ DTA measurement, which was why some ex-situ (regular) DTA were also performed using arc-melted alloys. As shown in in Figure 5.1 (a), the differences between in-situ and ex-situ are relatively small. Therefore, it is reasonable to set a relatively high weight during the optimization on the reported temperatures of the invariant reaction of the Np-Zr system. However, it should be noted that the invariant reaction type and the phases involved were not determined completely in the study by Gibson *et al*. [183, 184]. Later Rodriguez *et al*. [185] also studied this binary experimentally. As shown in in Figure 5.1, they determined the tie-line by electron microprobe analysis (EMPA), measured some phase transition temperatures through dilatometry, and studied the microstructures of several phase regions using metallography. However, their tie-line construction is suggested to be inaccurate on the Np-rich corner (for example, see tie-lines for (γNp)+(βZr) and (γNp)+δ at 793 and 868 K in Figure 5.1 (c)), since we found it is hard to fit their values consistently with other experimental data during the thermodynamic optimization. The possible reasons for the tie-line issues are uncertain, as the details of their EPMA measurement methodology were not reported [185]. Rodriguez *et al*. [185] also used dashed lines to sketch the constructed phase boundaries, which usually means large uncertainties in the measurements. In addition, Rodriguez *et al*. [185] indicated that the BCC solution phases (γNp) and (βZr) have continuous mutual solubility in the whole composition range, which is not supported by later experiments [21]. As a consequence, in this work, the EMPA results from Rodriguez *et al*. [185] were assigned with a relatively low weight in the thermodynamic optimization. Finally, a third experiment by Okamoto *et al*. [21] performed X-ray diffraction on (γNp) and (βZr) up to 973 K, which provided direct evidence for a lack of continuous mutual solubilty between the two phases. Okamoto *et al*. [21] also estimated the decomposition temperature of the δ phase to be around 823 K.

Despite the above mentioned studies, the phase diagram and phase equillibria of the Np-Zr system are still not well established. For example, except for the reaction temperature, the invariant reaction type has not been fully determined. Also, as summarized in in Figure 5.1, experimental data of the solubility of Zr in Np allotropes are also mostly lacking. Moreover, although there are some efforts measuring the temperatures of phase transitions involving the θ phase, the crystalline structure of the θ phase is still undetermined, and thus so far it can only be considered as a stoichiometric phase in the CALPHAD modeling. Besides phase diagram data, to the best of our knowledge, there is also no available direct measurement of the thermodynamic properties of the Np-Zr alloys. Therefore, we hope that by integrating *ab initio* calculations and CALPHAD modeling in this work we can provide some reasonable prediction of the thermodynamic properties of this binary alloy, such as the enthalpy of formation of the solid phases.

5.3.2 Reported *Ab initio* Calculations and Thermodynamic Modeling of Np-Zr

So far there are two CALPHAD models available for the Np-Zr system [12, 182]. The first is performed by Kurata [12], which we did not reproduce and compare our results to in this work because 1) the thermodynamic parameters of the δ phase is not provided in Ref. [12], and 2) the calculated phase diagram shown in Ref. [12] shows complete mutual solubility between (γNp) and (βZr), which is not consistent with the commonly accepted experimental observation [21] discussed in Section 5.3.1.

A second study is reported by Bajaj *et al.* [182]. They performed *ab initio* calculations using the KKR-ASA-CPA model (KKR: Korringa-Kohn-Rostoker, ASA: Atomic Sphere Approximation, CPA: Coherent Potential Approximation) to explore the mutual solubility of the BCC (γNp, βZr) structure,. Their calculated enthalpies of formation for (γNp, βZr) referencing to pure BCC γNp and βZr are positive at 0 K over the whole composition range, which is consistent with Okamoto *et al.*'s experimental results [21]. However, it seems that the phase diagram calculated by Bajaj *et al.* [182] using CALPHAD did not capture well some features of the assessed reliable experimental data shown in Figure 5.1, as we will discuss in detail in Section 5.6.

5.4 Thermodynamic Models used in the CALHPAD modeling

Thermodynamic models used in this work for the stable phases in the Np-Zr system are summarized in Table 5.1.

Table 5.1. Thermodynamic models and optimized CALPHAD type parameters for different phases of the Np-Zr system in this work

Phase	Model	Thermodynamic parameters (Energy unit: J/mol·atom)
Liquid	(Np,Zr)	${}^{0}L_{\mathrm{Np,Zr}}^{\mathrm{Liquid}} = 1142.97$
		${}^{1}L_{\mathrm{Np,Zr}}^{\mathrm{Liquid}} = 10193.88$
(αNp)	(Np,Zr)	${}^{\mathrm{o}}G_{\mathrm{Zr}}^{(\alpha\mathrm{Np})} = 5804 + {}^{\mathrm{o}}G_{\mathrm{Zr}}^{\mathrm{SER}}$
		${}^{0}L_{\mathrm{Np,Zr}}^{(\alpha\mathrm{Np})} = 52892.37$
(βNp)	(Np,Zr)	${}^{\mathrm{o}}G_{\mathrm{Zr}}^{(\beta\mathrm{Np})} = 5331 + {}^{\mathrm{o}}G_{\mathrm{Zr}}^{\mathrm{SER}}$
		${}^{0}L_{\mathrm{Np,Zr}}^{(\beta\mathrm{Np})} = 23559.89$
(γNp,βZr)	(Np,Zr)	${}^{0}L_{\mathrm{Np,Zr}}^{(\gamma\mathrm{Np},\beta\mathrm{Zr})} = 12335.36 + 3.973 \cdot T$
		${}^{1}L_{\mathrm{Np,Zr}}^{(\gamma\mathrm{Np},\beta\mathrm{Zr})} = 4304.16$
(αZr)	(Np,Zr)	${}^{\mathrm{o}}G_{\mathrm{Np}}^{(\mathrm{aZr})} = 19000 + {}^{\mathrm{o}}G_{\mathrm{Np}}^{\mathrm{SER}}$
		${}^{0}L_{\mathrm{Np,Zr}}^{\beta} = -2109.31$
θ	$(\mathrm{Np})_{0.8}(\mathrm{Zr})_{0.2}$	${}^{\mathrm{o}}G_{\mathrm{Np:Zr}}^{\theta} = -635.02 + 0.8 \cdot {}^{\mathrm{o}}G_{\mathrm{Np}}^{\mathrm{SER}} + 0.2 \cdot {}^{\mathrm{o}}G_{\mathrm{Zr}}^{\mathrm{SER}}$
δ	$(\mathrm{Zr})_{1/3}(\mathrm{Np,Zr})_{2/3}$	${}^{\mathrm{o}}G_{\mathrm{Zr:Zr}}^{\delta} = 527.5 + {}^{\mathrm{o}}G_{\mathrm{Zr}}^{\mathrm{SER}}$
		${}^{\mathrm{o}}G_{\mathrm{Zr:Np}}^{\delta} = 7676.68 - 10.05 \cdot T + 1/3 \cdot {}^{\mathrm{o}}G_{\mathrm{Zr}}^{\mathrm{SER}} + 2/3 \cdot {}^{\mathrm{o}}G_{\mathrm{Np}}^{\mathrm{SER}}$
		${}^{0}L_{\mathrm{Zr:Np,Zr}}^{\delta} = -17744.92 + 32.474 \cdot T$
		${}^{1}L_{\mathrm{Zr:Np,Zr}}^{\delta} = -7535.08 + 9.768 \cdot T$

5.4.1 Solution phase

There are six solution phases in the Np-Zr system: (αZr) with hcp structure, (βZr) and (γNp) with BCC structure, (αNp) with orthorhombic_AC structure, and (βNp) with tetragonal_AD structure.

These solution phases can be modeled with the substitutional solution model by the following equation:

$$G_{\mathrm{m}}^{\phi} = x_{\mathrm{Np}} \, {}^{\mathrm{o}}G_{\mathrm{Np}}^{\phi} + x_{\mathrm{Zr}} \, {}^{\mathrm{o}}G_{\mathrm{Zr}}^{\phi} + RT\left(x_{\mathrm{Np}} \ln x_{\mathrm{Np}} + x_{\mathrm{Zr}} \ln x_{\mathrm{Zr}} \right) + {}^{\mathrm{ex}}G_{\mathrm{m}}^{\phi} \tag{5}$$

where x_{Np} and x_{Zr} are the mole fraction of Np and Zr, respectively. Note that different from Bajaj's work, we only considered αZr with hcp structure as the ground state phase of Zr metal, and the reason is discussed in detail in Section 5.1 below.

5.4.2 Intermetallic Compounds

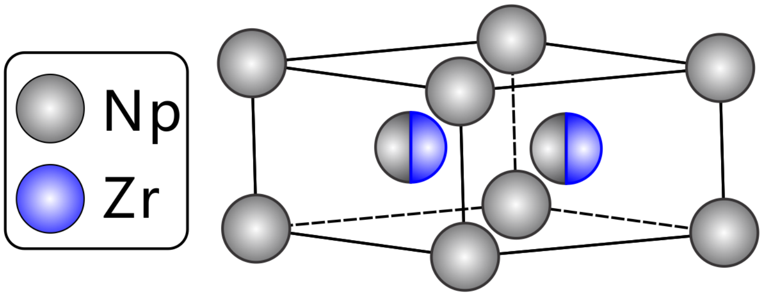

Figure 5.2. The Hexagonal_C32 structure of the δ-NpZr phase.

There are two intermetallic phases in the Np-Zr system: θ and δ. The crystal structure of the θ(Np,Zr) phase remains undetermined although there has been a suggestion [21] that it is isomorphic with θ(Pu,Zr), whose crystal structure is also only partially known [186]. Consequently, the θ phase is modeled as a stoichiometric phase in this work. On the other hand, the crystal structure of the δ phase was determined [22] to be a C32 structure with prototype AlB_2, which is the same to the δ phase in the U-Zr system, both isomorphic with the ω phase of pure Zr [128]. As illustrated in Figure 5.2, the C32 structure has two distinct Wyckoff sites—site I (i.e., the corners of the lattice box) has Wyckoff symbol 1*a* and fractional coordinate (0, 0, 0), while site II (i.e., the two internal positions in the lattice box) has Wyckoff symobol 2*d* and fractional coordinates (1/3, 2/3, 1/2) and (1/3, 2/3, 1/2). Ref. [22] determined that for the δ phase of Np-Zr, site I is occupied only by Zr but site II is occupied by both Np and Zr with an occupancy of 50 to 67 at.% Zr.

Table 5.2. Crystal information on Np and Zr allotropy and their solution phases used in the *ab initio* modeling of this work

Phase	Structure Name	Space Group	Composition (Zr at.%)	Unit Cell Size (atoms/cell)	SQS used?	*k*-point mesh	Expt. Source
αNp	Orthorhombic_A$_c$	Pnma	0	8	No	5×5×5	Ref. [187]
(αNp)			6.3	16	Yes	5×5×5	Ref. [22]
βNp	Tetragonal_A$_d$	P4/nmm	0	4	No	6×6×6	Ref. [188]
(βNp)			3.3	16	Yes	4×4×4	Ref. [21]
γNp	Bcc_A2	$Im\bar{3}m$	0	1	No	17×17×17	Ref. [188]
(γNp, βZr)			6.3 25.0 50.0 75.0 93.8	16	Yes	6×6×6	Ref. [21]
βZr			100	1	No	17×17×17	Ref. [83]
δ	Hexagonal_C32	P6/mmm	33.3 66.7	3 15	No Yes	9×9×13 6×6×6	Ref. [21]
ωZr			100	3	No	9×9×13	Ref. [128]
(αZr)	Hcp_A3	P6$_3$/mmc	93.8	16	Yes	4×4×4	Ref. [22]
αZr			100	2	No	8×8×8	Ref. [82]
θ	Tetragonal (not clear)	P4/ncc	20	80	No	Not calculated	Ref. [21]*

* Ref. [21] suggests it isomorphic with θ(Pu,Zr) whose structure has only been partially solved in Ref.[186]

Thermodynamic models of both θ and δ phases are described using the sublattice model according to the work by Sundman and Ågren [71, 189]. For instance, the Gibbs energy expression of δ phase can be expressed as:

$$G_{\mathrm{m}}^{\delta} = y_{\mathrm{Np}}^{\mathrm{II}}\,{}^{o}G_{\mathrm{Zr:Np}}^{\delta} + y_{\mathrm{Zr}}^{\mathrm{II}}\,{}^{o}G_{\mathrm{Zr:Zr}}^{\delta} + 2/3\,RT(y_{\mathrm{Np}}^{\mathrm{II}}\ln_{\mathrm{Np}}^{\mathrm{II}} + y_{\mathrm{Zr}}^{\mathrm{II}}\ln_{\mathrm{Zr}}^{\mathrm{II}}) + y_{\mathrm{Np}}^{\mathrm{II}}y_{\mathrm{Zr}}^{\mathrm{II}}L_{\mathrm{Zr:Np,Zr}}^{\delta} \qquad (5)$$

where $y_{\mathrm{Np}}^{\mathrm{II}}$ and $y_{\mathrm{Zr}}^{\mathrm{II}}$ are the site fraction of Np and Zr in the second sublattice, respectively; ${}^{o}G_{\mathrm{Zr:Np}}^{\delta}$ and ${}^{o}G_{\mathrm{Zr:Zr}}^{\delta}$ are the Gibbs energies of the two end-members Zr_1Np_2 and Zr_1Zr_2 , respectively—both of them of course have the same C32 structure of the δ phase, and the second end member Zr_1Zr_2 is in fact the ω phase of Zr metal; $L^{\delta}_{\mathrm{Zr:Np,Zr}}$ represents the interaction energy term between Np and Zr in the second sublattice in the presence of only Zr in the first sublattice. Note in the subscripts of ${}^{\circ}G^{\delta}_{\mathrm{Zr:Np}}$, ${}^{\circ}G^{\delta}_{\mathrm{Zr:Zr}}$ and $L^{\delta}_{\mathrm{Zr:Np,Zr}}$, we use a colon to separate the first and the second sublattice.

5.5 *Ab initio* Calculations

The stable solid phases of elemental Np and Zr metals and Np-Zr alloys are summarized in Table 5.2. All these phases except the θ phase are calculated in this work. Among them, elemental Np and Zr metal phases, that is, αNp, βNp, γNp, αZr, ωZr and βZr are modeled using their primitive unit cells [82, 83, 128, 187, 188]. Np-Zr alloy phases, that is (αNp), (βNp), (αZr), (γNp, βZr), and δ, all have some chemical disorder in the structure. These phases are therefore modeled using supercells that are generated based on their experimental crystal structures [21, 22, 82, 187, 188] and the Special Quasi-random Structure (SQS) method [84] as implemented in the Alloy Theory Automated Toolkit (ATAT) [85]. Firstly, the low and intermediate temperature terminal solution phases (αNp), (βNp) and (αZr) are each studied by one 16-atom supercell with composition 6.3, 6.3 and 93.8 at.%Zr (i.e., containing 1, 1, and 15 Zr atoms), respectively. The solute concentrations have exceeded the experimental solubility limit, but we believe they are acceptable model systems to probe the dilute alloying effect, as the solute atoms are at least 4.6, 5.8, and 7.6 Å apart in these cells, respectively. Secondly, the high temperature solution phases (γNp) and (βZr) both have BCC lattice, although they are not completely miscible, as we discussed above. For the convenience of discussion, we still designate them with a single phase label (γNp, βZr) henceforth. They are studied together by five 16-atom supercells with composition 6.3, 25.0, 50.0, 75.0, 93.8 at.% Zr (i.e., containing 1, 4, 8, 12, and 15 Zr atoms), respectively. Among them, the three structures at 25.0, 50.0, 75.0 at.% Zr are exactly the same to those recommended by Jiang *et al*. [86]. The other two structures at 6.3 and 93.8 at.% Zr are generated and selected using the same guidelines as used by Jiang *et al*. [86]. The 16-atom cell has already been found to reach convergence in terms of energy vs. number of atoms for the BCC phase of the testing systems in Ref. [86]. We therefore assume the 16-atom cell is also adequate to represent the disordered BCC phase in the present system of Np-Zr. Finally, the intermediate solution phase δ(Np,Zr)'s crystal structure has been introduced in Section 3 above. Here we calculate two relevant structures of this alloyed phase. The first structure has 50 at.% Zr occupation on site II with the overall chemical formula of $NpZr_2$ (i.e., $Zr_1(Np_{0.5}Zr_{0.5})_2$ in sublattice notation). We find that different from δ(U,Zr)[34], we need 15 atoms to converge the energy and therefore a 15-atom SQS supercell is selected and used in this study. This structure can be considered as a realistic representative of the δ(Np,Zr) phase because its site II occupation is both within the stability range—in fact, it is close to the minimum in the enthalpy of formation curve for δ(Np,Zr) from CALPHAD—and also convenient for constructing SQS cells. The second structure has 0 at.% Zr occupation on site II with the overall chemical formula of Np_2Zr (i.e., Zr_1Np_2 in sublattice notation). Although its occupation on site B is beyond the stability range, it is calculated here because it is one of the two perfectly ordered end members in CALPHAD modeling of δ(Np,Zr) with the sublattice model $(Zr)_1(Np,Zr)_2$ (the other one Zr_1Zr_2 is exactly ωZr, as mentioned above).

All *ab initio* calculations are performed in the general framework of Density Functional Theory (DFT) [28, 29] using the Vienna *Ab initio* Simulation Package

(VASP) [72, 73]. The electron-ion interaction is described with the projector-augmented-wave (PAW) method [74] as implemented by Kresse and Joubert [75]. The PAW potentials used treat $6s^2 6p^6 7s^2 5f^4 6d^1$ and $4s^2 4p^6 5s^2 4d^2$ as valence electrons for Np and Zr, respectively. The exchange-correlation functional parameterized in the Generalized Gradient Approximation (GGA) [76] by Perdew, Burke and Ernzerhof (PBE) [30] is used. The stopping criteria for self-consistent loops used are 0.1 and 1 meV tolerance of total free energy for the electronic and ionic relaxation, respectively. The electronic and ionic optimizations are performed using a Davidson-block algorithm [190] and a Conjugate-gradient algorithm [191], respectively. We do not explicitly set force as a stopping criterion, but when the total free energy is converged according to the criteria above, the Hellmann-Feynman forces on atoms are generally < 0.03 eV/Å for low-symmetry systems, and < 0.001 eV/Å for high-symmetry ones. A cutoff energy of 450 eV is used throughout all calculations. The Brillouin zone is sampled with Monkhorst–Pack k-point meshes [78] given in Table 5.2. We have tested that such k-point meshes and cutoff energy converge the total energy to less than 3 meV/atom, with errors of closer to 1 meV/atom in most cases. The partial occupancies are set using the Methfessel-Paxton method [129] of order one with a smearing width of 0.2 eV. All calculations have included spin polarization.

In a previous study[34], we found that the so-called DFT + U [119, 159] functional with a reasonable Hubbard U parameter can provide some improvement in some calculated ground state properties of U and U-Zr compared to the standard DFT functional when both of them are based on the Generalized Gradient Approximation (GGA) to the exchange-correlation potential as parametrized by PBE[30]. Therefore, we also explore DFT + U for Np and Np-Zr in this study, under the assumption that the valence f-electrons in Np may also contain some level of correlation that can be improved with a DFT + U treatment, as was found for U. Following Ref.[34], we use the DFT + U form suggested by Dudarev *et al.* [31] which does not introduce explicit local exchange J term but only an effective Hubbard U term that depends on $U_{\mathrm{eff}} = U - J$. This approach also recovers the standard DFT functional exactly when $U_{\mathrm{eff}} = 0$. DFT + U potential is applied only on Np sites in Np metal and Np-Zr alloy, and is not used at all in elemental Zr metal. In comparing the performance of the standard DFT functional with the DFT + U functional, we will refer to the two functionals as DFT and DFT + U, respectively. These names should not be confused with the theories that are usually referred to with the same acronyms. We combat the metastability issue of DFT + U using the U-ramping method [132] with modifications described in Ref.[34].

Regarding the relativistic effects, VASP always includes the mass-velocity and Darwin corrections using methods of Refs. [134, 135] and thus all of our calculations are at least scalar-relativistic. In more accurate calculations, we have included the spin-orbit coupling (SOC) effect in the *LS*-coupling limit. For convenience, in this paper we will designate calculations as SOC and noSOC, respectively for those with and without SOC included. SOC uses quantization axis (0, 0, 1) (i.e., z axis) and starts with the charge density from noSOC and relaxes both the magnitude and direction of the magnetic moments self-consistently. All noSOC calculations treat magnetism collinearly while SOC treats magnetism non-collinearly.

We define the enthalpy of formation for any Np and Np-Zr phase, elemental or alloyed, as $E^{\mathrm{form}}_{\mathrm{Np}_{1\text{-}x}\mathrm{Zr}_x} = E^{\mathrm{o}}_{\mathrm{Np}_{1\text{-}x}\mathrm{Zr}_x} - (1\text{-}x)\, E^{\mathrm{o}}_{\alpha\mathrm{Np}} - xE^{\mathrm{o}}_{\alpha\mathrm{Zr}}$, where $\mathrm{Np}_{1\text{-}x}\mathrm{Zr}_x$ is the chemical formula, x

is the mole fraction of Zr with 0 ≤ x ≤ 1, and $E^{\mathrm{o}}_{\mathrm{Np}_{1\text{-}x}\mathrm{Zr}_x}$, $E^{\mathrm{o}}_{\alpha\mathrm{Np}}$ and $E^{\mathrm{o}}_{\alpha\mathrm{Zr}}$ are the calculated total energy per atom at zero temperature for $\mathrm{Np}_{1\text{-}x}\mathrm{Zr}_x$ and the two references αNp and αZr, respectively. Similarly, we define the enthalpy of mixing specifically for the alloyed phase (γNp, βZr) as $E^{\mathrm{mix}}_{\mathrm{Np}_{1\text{-}x}\mathrm{Zr}_x}=E^{\mathrm{o}}_{\mathrm{Np}_{1\text{-}x}\mathrm{Zr}_x}-(1\text{-}x)E^{\mathrm{o}}_{\gamma\mathrm{Np}}\text{-}xE^{\mathrm{o}}_{\beta\mathrm{Zr}}$, for which γNp and βZr are used as the references. The two enthalpies can be straightforwardly converted to each other using the differences in energies between the two sets of references.

All structural degrees of freedom — volume, ion position, and cell shape — are fully relaxed for all structures in both DFT and DFT + *U* calculations with and without SOC included, except for those of γNp and (γNp, βZr) which are only volume-relaxed. We find γNp and (γNp, βZr) are mechanically unstable at low temperature, similarly to γU [87, 97] and (γU, βZr)[34]. To mitigate the strong mechanical instability in our zero temperature calculations, we follow the practices of previous calculations [34, 66, 105] to constrain ion positions and lattice shape and perform only volume relaxation for γNp and (γNp, βZr). The atomic radius for Np and Zr is 1.55 and 1.60 Å in Np and Zr metal [136], respectively, differing only by 3%. As a result of this small size mismatch, the cell-internal relaxations that are being excluded are expected to be small, as found in Ref.[34]for U and U-Zr.

5.6 Results and Discussion

The PARROT module in the Thermo-Calc software package version 3.0 was employed for the current thermodynamic optimization[89]. Reliable experimental data discussed in Section 2 were adopted during the thermodynamic modeling. Since BCC is the phase shown in most of the invariant reactions, the preliminary optimization steps focused on adjusting the invariant reactions with the BCC phase involved. The liquid phase was optimized as the second step, and the thermodynamic parameters of the intermetallic compounds were adjusted in the PARROT module as the final step.

Table 5.2 lists the evaluated thermodynamic parameters of our CALPHAD model. We emphasize that the optimization of these parameters in this work is done primarily by fitting to experimental phase diagram data. The only three *ab initio* energetic inputs used in the optimization of the CALPHAD model are $^{\mathrm{o}}G_{\mathrm{Zr}}^{(\alpha\mathrm{Np})}$,, $^{\mathrm{o}}G_{\mathrm{Zr}}^{(\beta\mathrm{Np})}$, and $^{\mathrm{o}}G_{\mathrm{Np}}^{(\alpha\mathrm{Zr})}$, which are the lattice stabilities of pure Zr with the structures of αNp (orthorhombic_AC) and βNp (Tetragonal_AD), as well as that of pure Np with the structure of αZr (Hcp_A3), respectively. These three values are not available in the standard CALPHAD database, and are here roughly estimated by 0 K energies from DFT calculations for $^{\mathrm{o}}G_{\mathrm{Zr}}^{(\alpha\mathrm{Np})}$and $^{\mathrm{o}}G_{\mathrm{Zr}}^{(\beta\mathrm{Np})}$ and from DFT + *U* (U_{eff}=0.65 eV) calclations for $^{\mathrm{o}}G_{\mathrm{Np}}^{(\alpha\mathrm{Zr})}$, as listed in Table 5.2. Excepting the above three values, no other *ab initio* energetics, especially the enthalpy of mixing for (γNp, βZr), are used in the CALPHAD model fitting. They are only used as references to cross-validate with CALPHAD models *a posteriori*.

5.6.1 Low Temperature Stability of Pure Zr

The previous work by Bajaj *et al*. [182] developed two CALPHAD models by considering αZr (hcp_A3) and ωZr (Hexagonal_C32) as the ground state of Zr metal, respectively (refered to as Model 1 and Model 2, respectively in Ref.[182] and in our discussion below). Bajaj *et al*. explained in Ref. [182] that the reason was because their *ab initio* calculations found αZr's energy to be about 1 kJ/mole higher than ωZr. However, it is more commonly accepted in the literature[192, 193] that αZr is the ground state phase of Zr metal. Facing the discrepancy, we also performed *ab initio* calculations of pure Zr metal.

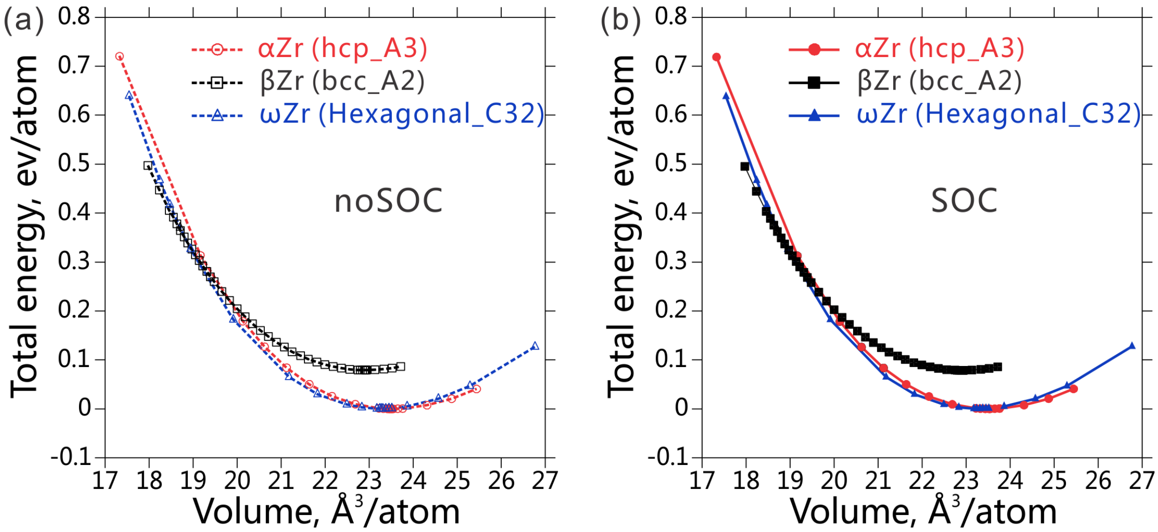

Figure 5.3. Total energy for Zr metal as a function of volume. noSOC means that spin-orbit coupling effect was not considered in the *ab initio* calculations, while SOC means the spin-orbit coupling was taken into account.

Figure 5.3 shows the total energy as a function of volume we calculated for all the three stable solid phases of Zr metal ─ αZr (hcp_A3), ωZr (Hexagonal_C32) and βZr (BCC_A2). We see that at the equilibrium volumes (i.e., zero pressure), the total energy is in the order αZr < ωZr < βZr. This shows that our DFT-PAW calculations correctly reproduce the better accepted experimental finding [192, 194] that αZr is the most stable ground state phase at zero temperature and pressure, with total energy 96.485 J/mole lower than ωZr. This result also matches those of some recent *ab initio* calculations using both FPLMTO [66] and PAW [195]. To explain the difference between our and Bajaj *et al.* [182]'s *ab initio* results for Zr metal, we point out that one possible reason may be due to structure relaxation. Although Bajaj *et al.* [182] did not describe the details of their structural relaxation, our earlier calculations performing only one-step automatic full structure relaxation also obtained αZr to be less stable than ωZr. It is only our later calculations manually performing a series of constant volume relaxation to most accurately identify the equilibrium volume and energy that reproduced the correct phase stability reported here.

As a consequence, only the hcp_A3 structure (αZr) as the ground state is optimized in this work. Furthermore, comparisons will be made only to Model 1 of Ref. [182] that considered hcp_A3 (αZr) as the stable Zr phase.

5.6.2 Comparison of Calculated Phase Diagrams and Experimental Data

As discussed in Section 2.1 above, the transition temperatures of invariant reations in the Np-Zr system have been well determined in the experiments by Gibson and Haire [183, 184] using both in-situ and ex-situ DTA measurements and should be considered as the most reliable experimental data so far that CALHPAD model of Np-Zr should reproduce. As shown in Figure 5.1 (a) and (c), our present CALPHAD model reproduced these transition temperatures rather well. As a first example, our model predicted the two transition temperatures of 823.1 and 910 K that are in excellent agreement with the empty circle (in-situ) and triangle (ex-situ) DTA experimental data points of Gibson and Haire [183, 184] in Figure 5.1 (c). In comparison, we note in Figure 5.1 (d) that Bajaj *et al.* [182]'s Model 1 predicted the corresponding two temperatures to be 882 and 852.3 K respectively, which are are about 30 K away from the experimental DTA data points. Another example of how our CALPHAD reproduces well the invariant reaction data can be seen by comparing the difference in the temperatures for the two invariant reactions, $(\gamma Np) + (\beta Zr) = \delta$ and $(\beta Zr) = \delta + (\alpha Zr)$. Our model predicts the two reaction temperatures to be 846.4 and 823.1, respectively, differing by 23.3 K. In addition to the excellent agreement for the second temperature 823.1 K that we have already discussed above, the first temperature 846.4 K is also in excellent agreement with the Dilatometry data point of Rodriguez marked by an open cross. We note that Bajaj *et al*. [182]'s Model 1 predicted this difference to be only 0.03 K (852.33 vs. 852.30 K), which seems to be very small considering the measured values and that thermal analysis has a typical measurement uncertainty as high as 0.1 K. Another improvement in the present model compared to Bajaj *et al*. [182]'s Model 1 is that our model predicted solubility boundaries of (*β*Zr) that did not show the unusual curvature that Bajaj *et al*. [182]'s Model 1 predicted between 900 and 1200 K. This type of curvature, while not necessarily incorrect, does seem very uncommon in binary alloy phase diagrams. Overall, the above comparisons between experimental data and the calculated phase diagrams of this work and Ref. [182] indicate that the thermodynamic model in this work may have provided an improved thermodynamic description of the Np-Zr system.

5.6.3 Calculation of Thermodynamic Properties

5.6.3.1 *Ab initio* Energetic Calculations of the Elemental Np and Terminal Solution Phases

Now we validate *ab initio* approaches (i.e., DFT vs. DFT + *U*; noSOC vs. SOC) in modeling the correlation and relativistic effects in Np and Np-Zr. To avoid any bias, we compare *ab initio* energetics to the predictions from both the CALPHAD model of this work as well as CALPHAD Model 1 of Bajaj *et al*. [182]. We will see that the conclusion to be reached below is unaffected by which CALPHAD model we compare to.

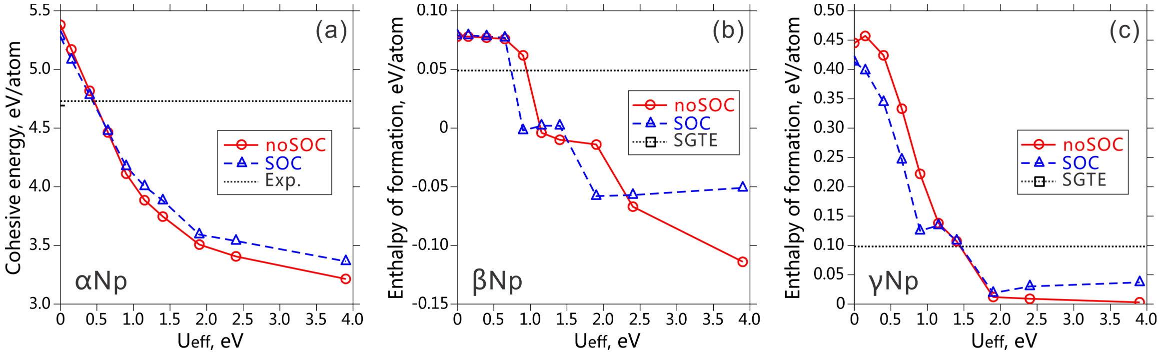

Figure 5.4. *Ab initio* energetics for Np metal at 0 K: (a) cohesive energy for αNp, and enthalpy of formation for (b) βNp and (c) γNp. The data from SGTE and experiments are considered at 298 K. Experimental data in (a) are taken from Ref. **[136]**.

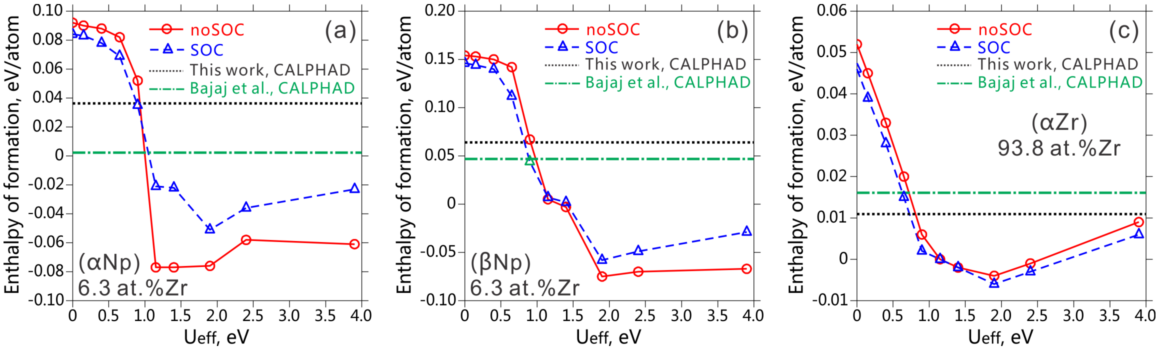

Figure 5.5. Comparison of the enthalpy of formation for Np-Zr alloy phases at 0 K: (a) (αNp) (6.3 at.% Zr); (b) (βNp) (6.3 at.% Zr); (c) (αZr) (93.8 at.% Zr). The CALPHAD values are calculated at 298 K. The model 1 by Bajaj *et al.* **[182]** considering HCP as the stable structure for pure Zr is used for comparison.

First, we focus the comparison on all the three known stable solid phases of Np metal as well as the low and intermediate temperature terminal solution phases of Np-Zr alloy in Figure 5.4 and Figure 5.5, respectively. The remaining two phases δ(Np,Zr) and (γNp, βZr) are subject to uncertainty due to the controversy on αZr vs. ωZr as ground state phase and the constrained relaxation approach employed to mitigate the mechanical instability, respectively, and we will discuss them separately later. Figure 5.4 and Figure 5.5 show that, similar to U and U-Zr[34], Np and Np-Zr's energetics are significantly overestimated by DFT (i.e., at U_{eff}= 0 eV). This overestimation can be seen by comparing the DFT values to the experimental cohesive energy of αNp [136], the SGTE data for pure elements [69], and the enthalpies predicted by the two CALPHAD models. On the other hand, DFT + U gives smaller formation energies and thus better agreement with the above references. The energetics also evolve as functions of U_{eff} in three stages, similar to those for U and U-Zr[34]. The first stage is between 0 to 1 eV, the second 1 to 2 eV, and the third > 2 eV. The *ab initio* curves in general cross the experimental or CALPHD reference values at U_{eff} between 0.65 to 0.9 eV.

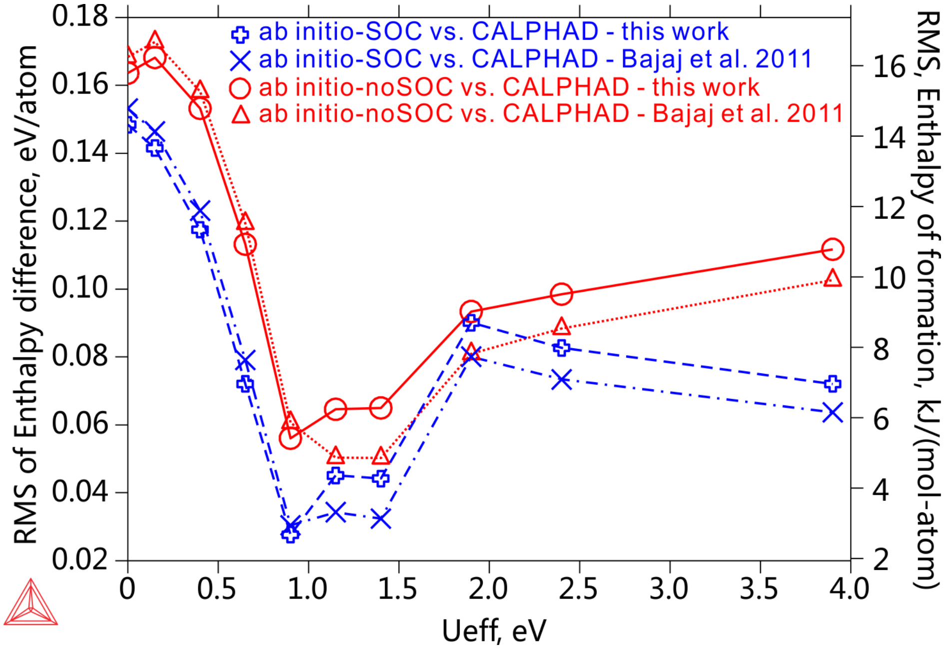

Figure 5.6. RMS of enthalpy differences between *ab initio* and CALPHAD in this work. βNp, γNp, (αNp) (6.3 at.% Zr), (βNp) (6.3 at.% Zr) and (αZr) (93.8 at.% Zr) are considered. The lines connecting the *ab initio* results are used for guiding the eyes.

Figure 5.6 summarizes the comparison in Figure 5.4 and Figure 5.5 and shows the root mean square (RMS) of enthalpy differences between *ab initio* and measured or CALPHAD modeled energetics. At this level of comparison there is no visible difference in the RMS values calculated referencing to the CALPHAD model of this work and to CALPHAD Model 1 of Bajaj *et al.* [182]. Note that we include only formation energies relative to the end members in Figure 5.6. The overall cohesive energy of the stable end members αNp is not considered here as it does not impact phase stability being modeled here. However, the trend in calculated cohesive energy with U_{eff} for αNp is similar to those found for the formation energies of other phases, with an optimal U_{eff} of around 0.6 eV. as shown in Figure 5.4 (a). Overall, Figure 5.6 shows two qualitative features that are the most important: (1) the RMS of enthalpy differences for the SOC case keeps going down from 0 to 0.9 eV, reaches minimum at 0.9 eV, and gradually increases thereafter; (2) the RMS of enthalpy differences from SOC calculations are clearly smaller than that of noSOC. Quantitatively, the average RMS of differences is 0.151, 0.076 and 0.029 eV/atom when SOC is included, and 0.166, 0.116 and 0.058 eV/atom when SOC is not included at $U_{\mathrm{eff}} = 0$, 0.65 and 0.9 eV, respectively. These statistics show that (1) DFT yields RMS errors in the enthalpies of about 0.15 eV/atom (these errors are typically due to overestimating the formation energies compared to experimentally derived values), and DFT + U can reduce the error by roughly 0.07-0.1 eV/atom when using an U_{eff} of around 0.65-0.9 eV; (2) Adding SOC will typically lower the RMS error in enthalpy by about 0.03 eV/atom. These results suggest that the modeling of Np and Np-Zr seems to be improved by the use of DFT + U and by adding SOC, which is consistent with our findings on U and U-Zr [33]

5.6.3.2 Enthalpy of Formation for the δ and BCC Phases

Given the fairly good agreement between DFT + U and CALPHAD energetics for the better established models of phases discussed above in Section 5.3.1, we proceed to discuss the *ab initio* results for the more controversial phases δ(Np,Zr) and (γNp, βZr), whose energetics are shown in Figure 5.7 and Figure 5.8, respectively.

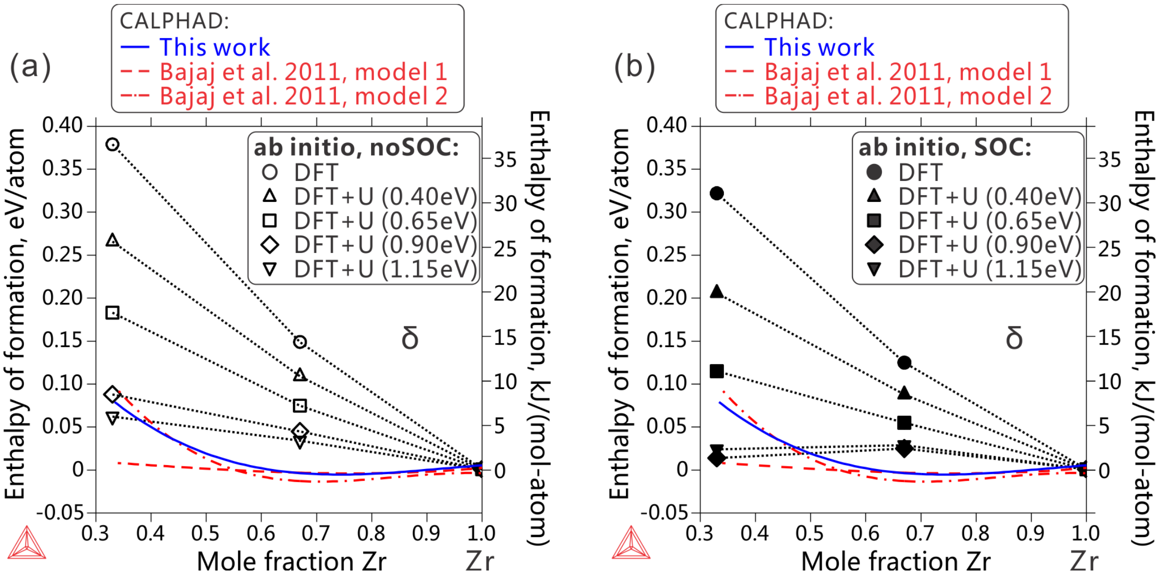

Figure 5.7. Comparison of the enthalpy of formation of the δ phase between *ab initio* calculations and CALPHAD modeling. The dotted lines connecting the *ab initio* results are used for guiding the eyes. Model 1 in the work by Bajaj *et al*. [182] takes hcp as the stable structure for pure Zr, while model 2 takes the ω phase. (a) Is the case for *ab initio* calculations with noSOC and (b) is the case for *ab initio* calculations with SOC.

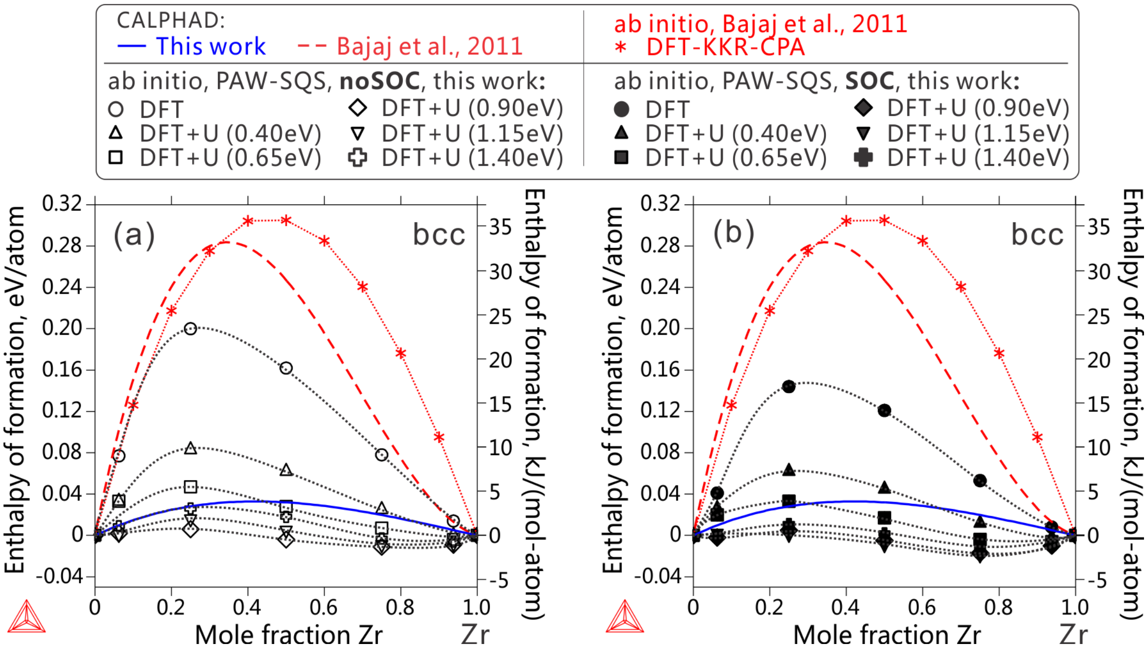

Figure 5.8. Comparison of the enthalpy of mixing of the BCC structure between *ab initio* calculations and CALPHAD modeling. The dotted lines connecting the *ab initio* results are used for guiding the eyes. (a) Is the case for *ab initio* calculations with noSOC and (b) is the case for *ab initio* calculations with SOC.

Figure 5.7 shows the enthalpy of formation for δ(Np,Zr). Firstly we note that our

CALPHAD predicted enthalpy is in agreement with that from Bajaj *et al.*'s model 1 [182] that also considered αZr as the ground state of Zr. The value from Bajaj *et al.*'s Model 2 that treated ωZr as the ground state is also plotted in Figure 7 for the sake of completeness, but we will not discuss it below. An evident feature is that the CALPHAD curves from both our model and Bajaj *et al.*'s Model 1 are concave upward, with a minimum near 66.7 at.% Zr. In comparsion, our *ab initio* curves are also concave upward at $U_{\mathrm{eff}} \leq 0.65$ eV but turn into concave downward when $U_{\mathrm{eff}} \geq 0.9$ eV. Such result suggests that although $U_{\mathrm{eff}} = 0.9$ eV is the statistical optimal U_{eff} value when only considers enthalpy at a single composition, as shown in Figure 5.6 above, it fails to reproduce the qualitative curvature of the energy curve of δ(Np,Zr) when we consider several compositions. This curvature is essential to reproduce if the energetics are going to predict a stable δ(Np,Zr) phase at approximately the right composition. At the smaller $U_{\mathrm{eff}} = 0.65$ eV, the correct curvature is still reproduced, and in terms of quantitative difference, the *ab initio* calculated enthalpy is also reasonably close to that of the CALPHAD data near the two ends of the curve although somewhat larger in the middle at 66.7 at.% Zr. It is possible that a minor improvement in agreement between the DFT + *U* and CALPHAD values may be obtained through exploring additional U_{eff} values between 0.65 and 0.9 eV, but considering the range of intrinsic uncertainty in both CALPHAD and *ab initio* predictions, further search is probably not too meaningful and thus is not performed. Overall, for δ(Np,Zr) we find the difference in *ab initio* and CALPHAD energies are very similar to those found for the better constrained phases discussed in Section 5.3.1, in that DFT also significantly overestimates the energetics for δ(Np,Zr) by about 0.15 eV/atom, and DFT + *U* reduces the error by about 0.10 eV/atom using U_{eff} near 0.65 eV.

Figure 5.8 shows the enthalpy of mixing for (γNp, βZr). Again, we also note the difference between the CALPHAD result of this work and Bajaj *et al.*'s [182], the former being slightly positive (~0.025 eV/atom) while the later quite substantially positive (~0.3 eV/atom). We have shown above that our CALPHAD model gives phase boundary that matches existing experimental data equally or better than Bajaj *et al.*'s [182], which in some sense may suggest that the present CALPHAD model's values may be more trustworthy.

To further revolve the discrepancy, we compare them to *ab initio* results. Someone may have the concern that the CALPHAD model in this work was fitted in a way that biased it towards better match with DFT + *U* results. This concern is not true, at least for the present phase of (γNp, βZr). As we already mentioned above, our CALPHAD model is developed mainly by fitting to experimental phase boundary data with the only *ab initio* inputs being the energies for pure Zr metal with the crystal structures of αNp and βNp and that for pure Np metal with the crystal structure of αZr. No *ab initio* input is used in our CALPHAD model for for (γNp, βZr), and hence our CALPHAD and *ab initio* results can be used to validate each other.

Figure 5.8 shows that DFT calculations also give large and positive mixing enthalpy, although our DFT-PAW-SQS results are somewhat smaller than Bajaj *et al.*'s DFT-KKR-CPA result [182], which may be due to the differences between PAW and KKR and between SQS and CPA. However, all the previous comparisons discussed in Sections 5.3.1 and 5.3.2, as well as our previous work on U-Zr [33, 34]have suggested that DFT + *U* results in smaller energetics than DFT that are expected to be closer to experimental and/or robust CALPHAD results. We find that this is again the case here for (γNp, βZr), because the DFT + *U* (0.65 eV)-SOC enthalpy curve in Figure 5.8 is again very close to our CALPHAD curve. Both of them also show the same asymmetry that the Np-rich end is higher, although such an asymetry is more pronounced in the *ab initio* data. Such a match between our *ab initio* and CALPHAD results that are essentially independently obtained validates both the CALPHAD and *ab initio* values. Therefore, we argue that (γNp, βZr) possibly also has a slightly positive enthalpy, similar to the BCC phase (γU, βZr) in the U-Zr system as found in Ref.[34]. However, due to lack of direct experimental thermochemical data, the controversy on this high temperature phase cannot be completely resolved at present, and further experimental validation is needed.

Finally, we note that our finding that DFT + *U* can provide improved energetics for Np metal and Np-Zr alloys is in consistent with the conclusion of another work of Bajaj *et al*. that assessed DFT + *U*'s on Np metal[196]. Their suggested optimal Hubbard U for Np metal alone is around 2.2 eV, and because they set the exchange J to 1 eV, the optimal U_{eff} is 2.2-1 = 1.2 eV, which is close to our suggested U_{eff} value of 0.65-0.9 eV for Np and Np-Zr's overall modeling. Bajej *et al*. pointed out that "large changes in volumes supplemented by magnetic transitions" happen when U_{eff} is larger than the optimized U_{eff} region. We note here that similar to what have observed in U and U-Zr system[34], at the empirical optimal U_{eff} region of 0.65-0.9 eV, volume from DFT + *U* for Np and Np-Zr is also improved comparing to experimental data and those unphysical expansion is not present. There is indeed some emergence of small magnetic moments, which can be unphysical for at least Np metal, suggesting the DFT + *U* model for Np and Np-Zr is not fully correct in its treatment of the electronic structure. However, the use of

DFT + *U* still seems to yield improved energetic results compared to DFT.

5.6.3.3 Model Predicted Excess Entropy of Mixing for the Liquid

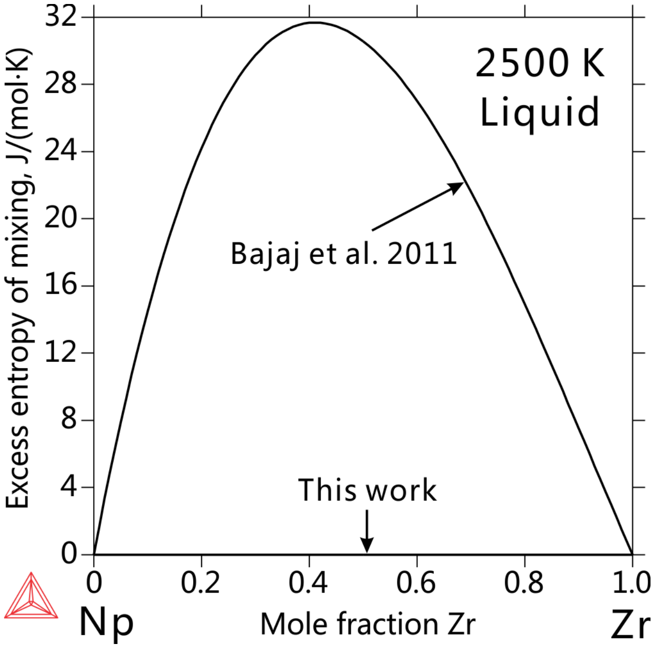

Figure 5.9. Comparison of the excess entropy of mixing of the liquid phase at 2500 K between this work and Bajaj *et al*. [182].

The comparison of excess entropy of mixing for the liquid phase at 2500 K from this work and Bajaj *et al*. [182] is shown in Figure 5.9. The excess entropy of mixing of a metallic liquid is expected to be in the range of −10 to 5 J/(mol·atom·K) [90, 92, 197]. While the model from this work produces excess entropies of mixing in this range the values from Bajaj *et al*. [182] are outside this range, which possibly is contributing to the improvements in the predicted phase boundary and enthalpy we discussed before.

5.7 Conclusions

The thermodynamic description of the Np-Zr system has been re-optimized in CALPHAD modeling. A set of self-consistent thermodynamic parameters have been achieved. These parameters can be employed to describe the known experimental data for the Np-Zr phase diagram, and to predict reasonable thermodynamic properties of the Np-Zr alloys.

Ab initio DFT calculations for Np-Zr are performed and used to both guide some limited aspects of the CALPHAD model fitting and provide validation of a DFT + U approach for obtaining more accurate energies. For Np metal and Np-Zr alloy, the PBE parametrization of the GGA functional is found to overestimate the formation enthalpies of Np and Np-Zr compounds by about 0.15 eV/atom, and the so called DFT + U method with a reasonable U_{eff} of near 0.65 eV can reduce this error by about 0.07-0.10 eV. Spin Orbit Coupling (SOC) also lowers the formation enthalpies of Np and Np-Zr by about 0.03 eV/atom. These statistics are quite consistent both when comparing to the CALPHAD model of this work and one from a previous study[182]. These results suggest that use of the DFT + U method with a U_{eff} near 0.65 eV for Np can provide improved energetics for Np-Zr and possibly other alloys of Np and transition metals.

This work provides a CALPHAD model for the Np-Zr systems that shows some improvements in the model predicted phase diagram compared to the previous models. However, a robust and comprehensive thermodynamic understanding of the Np-Zr system will need additional experimental investigation to validate the current modeling results, resolve existing controversies and suggest further improvements.

6 CALPHAD Modeling and *Ab initio* Calculations of the Np-U System

Note: The contents of this chapter are under preparation to be submitted to Journal of Nuclear Materials for peer-review and publication as an article.

6.1 Chapter Abstract:

A thermodynamic model for the Np-U system is developed based on fitting only to available experimental thermodynamic and phase stability data using the CALPHAD method. The model reproduces well the experimental phase boundaries of the liquid and body centered cubic (BCC) phases that are both stable at high temperature, but cannot find satisfactory fitting at the same time for both the compound phase ζ and the terminal solution phases α(Np) and β(Np) at low temperature. Comparison with a previous CALPHAD model suggests that consistent thermodynamic optimizations for ζ and α(Np) and β(Np) may not be possible, indicating that the corresponding experimental data—which were measured by different experimental techniques for the two phase regions—may not be fully consistent. Validations of density functional theory (DFT) in its standard form and the so-called DFT plus Hubbard *U* (DFT + *U*) modification are performed on all the four terminal solution phases α(Np), β(Np), α(U), and β(U) with small solute concentrations in addition to the BCC solution phase γ(Np,U) in the whole composition range. Overall, compared to DFT, DFT + *U* with the same empirical U_{eff} ranges—0.65-0.9 eV for Np and 1-1.5 eV for U—that we previously established in the Np-Zr and U-Zr systems predict similar or improved enthalpies when compared to both the present and the previous CALPHAD models. Finally, we predict enthalpy of formation and site

occupations for ζ phase. The *ab initio* results for ζ should be of value for assisting the development of an improved CALPHAD model for the Np-U system.

6.2 Introduction

This work is motivated by the need to better understand the phase stability and thermodynamic properties of the U-Pu-Zr-MA (MA= minor actinides Np, Am and Cm) alloy systems for their safe, effective, and economical use as metallic nuclear fuels[4]. We previously developed a thermodynamic model using CALHAD method and validated the *ab initio* approaches of density functional theory (DFT) in its standard form[28, 29] and one of its so-called DFT plus Hubbard U (DFT + U) modifications[31] for each of the U-Zr[33, 34] and the Np-Zr[35] systems. We now continue to work on the Np-U system, on the one hand to develop a CALPHAD model for the one remaining binary system in the Np-U-Zr ternary system, and on the other hand to continue validating *ab initio* approaches on a system that contains more than one actinide components. A major question we hope to answer is regarding the empirical U_{eff} for Np and U that we established individually in the Np-Zr and U-Zr systems that contain only one actinide element. Does DFT + U using the same or similar ranges of U_{eff}'s still provide improved enthalpy for Np-U? The answer to this question is critical to determine if the DFT + U approach with U_{eff} established in a few benchmark systems can be applied more broadly on other metallic fuel systems through use of transferable U_{eff} values. Moreover, so far we have been mainly using CALPHAD to validate *ab initio* approaches, but have not yet significantly used the validated *ab initio* approach to assist CALPHAD modeling, for example as has been done for non-actinide alloys.[198-206] The Np-U system provides an opportunity to use *ab initio* calculations to make some predictions on the ζ phase that may help better CALPHAD modeling of the Np-U system.

The remaining of this chapter proceeds as follows. Section 2 describes the details of the CALPHAD and *ab initio* methodology. Section 3 presents and discusses the results, including calculated phase diagram for Np-U from CALPHAD, validations of *ab initio* methods on α(Np), β(Np), α(U), β(U) and BCC γ(Np,U) phases, and *ab initio* predictions for ζ phase. Finally, Section 4 summarizes this chapter.

6.3 Methodology

6.3.1 CALPHAD Methodology

6.3.1.1 Summary of Experimental Data for Np-U

Mardon and Pearce[19] investigated the Np-U equilibrium diagram using thermal analysis, dilatometry and X-ray techniques, and the obtained data are summarized in Figure 6.1. Six solid phases exist in the Np-U system, as summarized in Table 6.1: α(Np), β(Np), α(U), and β(U) terminal solution phase, BCC single solution phase, and ζ compound phase. BCC phase is labeled γ(Np,U) here because it is the solution of γNp and γU. Mardon and Pearce used δ to label the compound phase[19]. However, to distinguish that it has a different structure from δ phases of U-Zr and Np-Zr and recognizing that it was suggested to be isomorphous with ζ phase of Pu-U[11], we label it ζ here.

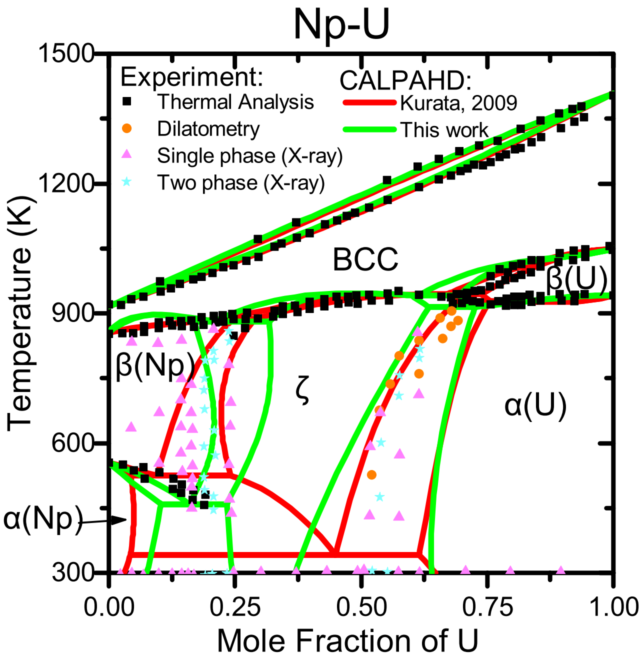

Figure 6.1. Phase diagram of the Np-U system from the CALPHAD models of this work and Kurata[12], compared to the experimental data of Mardon and Pearce[19].

Table 6.1. Stable solid phases of the Np-U system, their crystal structures and settings in *ab initio* calculations.

Phase	Structure name	Space group	Composition (U at.%)	Unit cell size (atoms/cell)	SQS used?	*k*-point mesh	Expt. Source
α(Np)	Orthorhombic_A_c	Pnma	6.3	16	Yes	8×8×4	Ref. [19]
β(Np)	Tetragonal_A_d	P4/nmm	6.3	16	Yes	6×6×4	Ref. [19]
γ(Np, U)	Bcc_A2	$Im\bar{3}m$	25.0 50.0 75.0	16	Yes	6×6×6	Ref. [19]
β(U)	Tetragonal_A_b	$P6_2/mnm$	96.7	30	Yes	4×4×6	Ref. [19]
α(U)	Orthorhombic_A20	Cmcm	93.8	16	Yes	8×8×4	Ref. [19]
ζ	Tetragonal	$R\bar{3}m$	0-100	58	No	2×2×2	Ref. [11, 15]

As shown in Figure 6.1, Mardon and Pearce[19]'s work suggested that γNp and γU are completely miscible with each other. The solubility of U in β(Np), and of Np in α(U) and β(U) are quite large; the only intermediate phase ζ was also suggested to stable over large ranges of composition and temperature. Correspondingly, the two-phase fields between ζ and the four terminal solution phases are very small.

Table 6.2. Wyckoff sites of ζ phase given in the conventional tetragonal setting. This whole table, including the atomic environment is quoted from Ref.[207] and provided here for easier reference. The original experimental crystal structure data are from Ref.[15]

Site	Wyckoff label	Site symmetry	Atomic environment	Coordination number
1	36i	1	14-vertex Frank-Kasper Pu_{14}	14
2	18h	.m	pseudo Frank-Kasper Pu_{13}	13
3	18h	.m	14-vertex Frank-Kasper Pu_{14}	14
4	18h	.m	15-vertex Frank-Kasper Pu_{15}	15
5	18h	.m	pseudo Frank-Kasper Pu_{13}	13
6	18h	.m	pseudo Frank-Kasper Pu_{13}	13
7	18h	.m	14-vertex Frank-Kasper Pu_{14}	14
8	18f	.2	icosahedron Pu_{12}	12
9	6c	3m	16-vertex Frank-Kasper Pu_{16}	16
10	6c	3m	16-vertex Frank-Kasper Pu_{16}	16

Focusing on ζ, Mardon and Pearce[19] argued that its crystal structure is cubic and isomorphous with ζ phase in the U-Pu system[11]. However ζ U-Pu is now generally accepted to be rhombehedral in the primitive setting and tetragonal in conventional with space group $R\bar{3}m$ thanks to the study of Lawson *et al*.[15]. Its Wyckoff sites have also been determined[15], as quoted from Ref.[207] in Table 6.2. Its site occupation is nevertheless still unknown at any composition in its stable range. However, the crystal structure for ζ Np-U has, to our knowledge, never been fully explored beyond the initial study of Mardon and Pearce[19]. Besides crystal structure, it is expected that the phase equilibrium data for ζ Np-U[19] also has sizable uncertainties since it is difficult to obtain equilibrium samples at low temperatures. Due to such uncertainties, in the CALPHAD model for the Np-U system by Kurata[12], the Gibbs free energy for ζ was estimated by extrapolating the phase boundary to the two ends of Np and U metals. We will see in the next section that the uncertainty in both crystal structure and phase boundary of ζ phase presents a major challenge for thermodynamic modeling of the Np-U system.

6.3.1.2 Thermodynamic Modeling of Np-U

Table 6.3. Thermodynamic model and optimized CALPHAD type parameters for stable phases of the Np-U system.

Phase	Model	Thermodynamic parameters (Energy unit: J/mole·atom)
Liquid	(Np,U)	${}^{0}L_{\mathrm{Np,U}}^{\mathrm{Liquid}} = 0$
α(Np)	(Np,U)	${}^{o}G_{\mathrm{U}}^{\alpha(\mathrm{Np})} = 4266 + 0.416 \cdot T + {}^{o}G_{\mathrm{U}}^{\mathrm{SER}}$
		${}^{0}L_{\mathrm{Np,U}}^{\alpha(\mathrm{Np})} = -10413.603 + 1.002 \cdot T$
β(Np)	(Np,U)	${}^{o}G_{\mathrm{U}}^{\beta(\mathrm{Np})} = 11420 + 2.206 \cdot T + {}^{o}G_{\mathrm{U}}^{\mathrm{SER}}$
		${}^{0}L_{\mathrm{Np,U}}^{\beta(\mathrm{Np})} = -40533.601 + 28.627 \cdot T$
γ(Np, U)	(Np,U)	${}^{0}L_{\mathrm{Np,U}}^{\gamma(\mathrm{Np,U})} = 578$
β(U)	(Np,U)	${}^{o}G_{\mathrm{Np}}^{\beta(\mathrm{U})} = 13579 + {}^{o}G_{\mathrm{Np}}^{\mathrm{SER}}$
		${}^{0}L_{\mathrm{Np,U}}^{\beta(\mathrm{U})} = -20142.460 - 2.128 \cdot T$
		${}^{1}L_{\mathrm{Np,U}}^{\beta(\mathrm{U})} = -10101.902$
α(U)	(Np,U)	${}^{o}G_{\mathrm{Np}}^{\alpha(\mathrm{U})} = 11178 + {}^{o}G_{\mathrm{Np}}^{\mathrm{SER}}$
		${}^{0}L_{\mathrm{Np,U}}^{\alpha(\mathrm{U})} = -27917.331 + 7.677 \cdot T$
		${}^{1}L_{\mathrm{Np,U}}^{\alpha(\mathrm{U})} = -12441.161 + 3.843 \cdot T$
ζ	(Np,U)$_1$(Np,U)$_2$	${}^{o}G_{\mathrm{Np}}^{\zeta} = 9508.271 + {}^{o}G_{\mathrm{Np}}^{\mathrm{SER}}$
		${}^{o}G_{\mathrm{U}}^{\zeta} = 946.266 + 3 \cdot {}^{o}G_{\mathrm{U}}^{\mathrm{SER}}$
		${}^{o}G_{\mathrm{Np_2U_1}}^{\zeta} = -7622.189 - 6.349 \cdot T + 2 \cdot {}^{o}G_{\mathrm{Np}}^{\mathrm{SER}} + {}^{o}G_{\mathrm{U}}^{\mathrm{SER}}$
		${}^{o}G_{\mathrm{Np_1U_2}}^{\zeta} = 18073.114 + 6.349 \cdot T + {}^{o}G_{\mathrm{Np}}^{\mathrm{SER}} + 2 \cdot {}^{o}G_{\mathrm{U}}^{\mathrm{SER}}$
		${}^{0}L_{\mathrm{Np,U:Np}}^{\zeta} = -11701.428 + 4.108 \cdot T$
		${}^{0}L_{\mathrm{Np,U:U}}^{\zeta} = 6871.720 - 0.121 \cdot T$

Thermodynamic models used in this work for the stable phases in the Np-Zr system are summarized in Table 6.3. All solid phases except ζ are modeled with the substitutional solution model, while ζ is described using the two-sublattice model (Np,U)$_1$(Np,U)$_2$ based on the theory of Sundman and Ågren [71, 189]. We note the

CALPHAD model of Kurata that we will compare to next describes all phases include ζ using substitutional solution models[12]. The PARROT module in the Thermo-Calc software package was employed for the current thermodynamic optimization[89].

6.3.2 *Ab initio* Methodology

The stable solid phases of the Np-U system has been modeled in the structure, composition and setting given in Table 6.1. All structures except that for ζ are modeled with supercells that are generated using the Special Quasi-random Structure (SQS) method [84] as implemented in the Alloy Theory Automated Toolkit (ATAT) [85]. The cells are the same as were used in our previous studies of the Np-Zr and U-Zr system[34, 35]. The elemental reference structures αNp, βNp, γNp, αU, βU, and γU have been calculated in Refs[34, 35] and the results of these previous studies are used here whenever necessary.

Table 6.4. Groups of the lattice sites of ζ in *ab initio* calculations according to atomic environment.

Group	Wyckoff sites	Atomic environment
I	1, 3, 7	14-vertex Frank-Kasper Pu_{14}
II	2, 5, 6	pseudo Frank-Kasper Pu_{13}
III	4	15-vertex Frank-Kasper Pu_{15}
IV	8	icosahedron Pu_{12}
V	9, 10	16-vertex Frank-Kasper Pu_{16}

ζ is modeled using its 58-atom rhombohedral primitive unit cell and the site occupations are explored with the following approach. The 10 Wyckoff sites are firstly divided into groups based on their atomic environment given in Table 6.2. The atomic environment considers more information than site symmetry and coordination number alone do, and is expected to be more effective at characterizing the most important structural characteristics of an atomic site. For example, Ref.[208] showed that atomic environment could be used effectively classify cubic intermetallic structure types. As tabulated in Table 6.4, the ten lattice sites are grouped into five lattice site groups based on the atomic environment of each site: group I contains site 1, 3 and 7, group II contains site 2, 5, 6, group III contains site 4, group IV contains site 8, and group V contains site 9, 10. Such grouping is a necessary approximation to handle the large number of 10 Wyckoff sites as enumerating possible occupations of the 10 sites even by assuming full occupation of either Np or U on each site requires one to calculate 2^{10}=1024 structures, not to mention modeling any fractional occupation.. After the grouping, each group is explored by assuming full occupation of either Np or U and thus a total of 2^5=32 structures are calculated, covering the whole 0-100 at.%U composition range.

All *ab initio* calculations are performed in the general framework of DFT[28, 29] using the Vienna *Ab initio* Simulation Package (VASP)[72, 73]. The electron-ion interaction is described with the projector-augmented-wave (PAW) method[74] as implemented by Kresse and Joubert[75]. The PAW potentials used treat $6s^2 6p^6 7s^2 5f^4 6d^1$ and $6s^2 6p^6 7s^2 5f^3 6d^1$ as valence electrons for Np and U, respectively. The exchange-correlation functional parameterized in the generalized gradient approximation (GGA)[76] by Perdew, Burke and Ernzerhof (PBE)[30] is used. The stopping criteria for self-consistent loops used are 0.1 meV and 1 meV tolerance of total free energy for the electronic and ionic relaxation, respectively. Cutoff energy of 450 eV is used throughout all calculations. The partial occupancies are set using the Methfessel-Paxton method[129] of order one with a smearing width of 0.2 eV. The electronic and ionic optimizations are performed using a Davidson-block algorithm[190] and a Conjugate-gradient algorithm[209], respectively. Following our practice to mitigate the mechanical instability of BCC U-Zr and Np-Zr[34, 35], only volume relaxation is performed for BCC γ(Np,U) structures. All other systems have volume, lattice shape and ion positions fully optimized.

Spin polarization is included in all calculations. In our previous validations on U-Zr and Np-Zr binaries, spin-orbit coupling (SOC) was found to affect the calculated enthalpy by about 0.02 and 0.03 eV/atom[34, 35], respectively, which are relatively small compared to the differences in the average errors in enthalpy between DFT and DFT + U—about 0.08 and 0.10 eV/atom for U-Zr and Np-Zr at the statistically optimal U_{eff} values of U_{eff}(U)=1.24 and U_{eff}(Np)=0.9 eV, respectively. Because our objective is mainly to assess the relative accuracy of DFT and DFT + U, we do not include SOC here to reduce the computational costs. Future work can be performed to include SOC and decide what is the best absolute accuracy that DFT + U can attain.

The DFT + U functional proposed by Dudarev *et al.*[31] is used. This form of DFT + U does not introduce explicit local exchange J term but only an effective Hubbard U term that depends on $U_{\mathrm{eff}} = U - J$. This approach also recovers the standard DFT functional exactly when $U_{\mathrm{eff}} = 0$. DFT + U potential is applied both on U and Np sites. For historical reasons we did not set $J = 0$ as one conveniently does but instead to 0.6 and 0.51 eV for Np and U, respectively and vary U up to 3 eV. This detail is provided here merely to explain why we discussed results at some awkward U_{eff} values like 0.99 and 1.24 that were obtained from 1.5 - 0.51 and 1.75 - 0.51. In the future, one should be able to reproduce our results as long as the same U_{eff}'s are used, regardless of what specific pair of U and J is used to reach the U_{eff}. Note the standard DFT corresponds to the point at (U_{eff}(Np), U_{eff}(U)) = (0,0). The metastable solution issue of DFT + U is combated using the *U*-ramping method[132] with modifications described in Ref.[34].

Enthalpy of formation of a given structure is defined as:

$$E^{\mathrm{form}}(\mathrm{Np}_{x_{\mathrm{Np}}}\mathrm{U}_{x_{\mathrm{U}}}) = E(\mathrm{Np}_{x_{\mathrm{Np}}}\mathrm{U}_{x_{\mathrm{U}}}) - x_{\mathrm{Np}}E(\alpha\mathrm{Np}) - x_{\mathrm{U}}E(\alpha\mathrm{U}) \quad (6)$$

where *E* is total energy per unit amount (e.g., per atom), $\mathrm{Np}_{x_{\mathrm{Np}}}\mathrm{U}_{x_{\mathrm{U}}}$ and αNp (αU) are the alloy and the constituent elemental metal references for Np (U), respectively, and x_{Np} (x_{U}) are the mole fractions of Np (U) in the alloy with $x_{\mathrm{Np}}+x_{\mathrm{U}}=1$. Eq. (1) is slightly modified for the enthalpy of mixing for BCC γ(Np,U), which is defined as in Eq. (1) except by referencing to BCC γNp and γU in place of αNp and αU.

Following our practice to mitigate the mechanical instability of BCC U-Zr and Np-Zr[34, 35], only volume relaxation is performed. The BCC volume mismatch between Np and U are about 13% from DFT. DFT + *U* predicts larger volumes for Np and U, and the volume mismatch reduces to 6% for example at (U_{eff}(Np), U_{eff}(U))=(0.6, 0.99) eV. Based on our testing on the 10 BCC alloys formed by V, Nb, Ta, Mo and W, which are stable in BCC structure unlike Np and U, we estimated that the overestimation in enthalpy of mixing due to the lack of ion relaxation are about 0.013 and 0.006 eV/atom corresponding to the volume mismatch from DFT and DFT + *U*, respectively and the corresponding values should be similar or smaller at 25 and 75 at.%. These values themselves are quite small, comparable to the intrinsic uncertainty of the two modeling approaches as well as our estimation of these energies using other BCC alloys. However, we will see that the enthalpy of mixing for BCC Np-U is also small. We will discuss the implication of neglecting ion relaxation in the next section.

6.4 Results and Discussion

6.4.1 CALPHAD Phase Diagram

Table 6.3 lists the evaluated thermodynamic parameters of our CALPHAD model for the Np-U system. These parameters were obtained by optimizing the phase boundaries using only the experimental data of Mardon and Pearce[19] as reference. The resulting phase diagram is plotted in Figure 6.1, which also includes the phase diagram from the CALHAD model published in Ref. [12] by Kurata and the experimental data of Mardon and Pearce[19] for comparison. Note Mardon and Pearce's data were obtained using four different experimental techniques. Among them thermal analysis and dilatometry data should be on phase boundary, while X-ray data only show whether they are in a single- or two-phase field, and may not necessarily be on phase boundary. Some noticeable differences between the two CALHPAD models include that we treated ζ using the sublattice model, while Kurata substitutional solution model and also that we used temperature-dependent interaction parameters for α(Np) and β(U), while Kurata did not.

It is clear from Figure 6.1 that both the models of this work and Kurata reproduce the liquidus, solidus in addition to the BCC phase boundaries rather satisfactorily. The solidus and liquidus are quite close and both of them are almost straight lines connecting the melting point of Np and U. Such features of phase diagram are consistent with the two elements forming very close to ideal solution in both the liquid and the BCC phases and each having quite similar and small entropies of melting.

On the other hand, the two CALPHAD phase diagrams show significant differences at low temperature, in particular near the Np-rich side. Specifically, some key differences include: 1) on bottom left, Kurata's results show a very large two-phase field of α(Np)+ζ that actually is overlapped with most of the thermal analysis experimental points (black square) expected to correspond to the α(Np)+β(Np) two-phase field. Our results do not show this overlap and seem to have reasonably reproduced the boundaries of α(Np)+β(Np). 2) On the middle left, the two models show opposite curvatures for the two phase field of ζ+β(Np) on both sides.. Because X-ray data are not necessarily on the phase boundary, we can only compare if the sing- and two-phase data are located in the corresponding phase fields. We see that Kurata's ζ+β(Np) two-phase field includes many of the X-ray single-phase data points (magenta triangle); our model also included some of those two-phase points as well, but much less. However, Kurata's model correctly covers all the two-phase data (cyan star) expected to be in ζ+β(Np), while we missed some but the left boundary of ζ+β(Np) are still close to the missed points. We therefore cannot be sure which model reflects the reality better for ζ+β(Np). 3) The previous two differences lead to ζ phase field being wider from Kurata on the top, while extending to lower temperature (below 300 K) at the bottom from our model. 4) The phase boundary for the two-phase field of α(Np)$_+$ζ is also different between the two models. Unfortunately on relevant experimental data are available nearby, and thus the two models thus cannot be evaluated in this aspect. 5) Finally, on the right, the ζ+ α(U) two phase-field also is also somewhat different between the two models although the curvatures of the phase boundaries are similar. Both models unfortunately included most or even all of the single-phase X-ray data near in ζ+ α(U) two phase-field. In short, while our model may shows some aspects of improvement, significant uncertainty still remain for the low temperature phases of ζ, α(Np), β(Np) and α(U).

Before proceeding to the next section, we comment that in our thermodynamic optimization for the Np-U system, when we adjust the model to reproduce the thermal analysis data (black square) for α(Np)+β(Np) better than Kurata we end up with worse match with the X-ray single- and two- phase data. If on the contrary, we optimize the model for better phase boundaries of β(Np) and ζ, we end up with worse match for α(Np)+β(Np), and a model somewhat close to the result from Kurata's model. Based on our experience, we think this indicates that the two sets of experimental data are likely not totally consistent with each other. Moreover, neither of the two CALPHAD models seem to like a very narrow α(U) + ζ two-phase field that the X-ray data of Mardon and Pearce suggest. Going forward, we suggest that future experiments can focus on determining the solubility limit of in U in α(Np) and β(Np), the stability range of ζ to lower temperatures, preferably down to 300 K. Determining the solubility limit of Np in α(U) is also helpful. Without further new experimental data, it is expected that *ab initio* modeling of ζ may provide some helpful information, which helps motivate our effort to model ζ described in Sec. 3.3.

6.4.2 Validation of *Ab initio* Methods on α(Np), β(Np), α(U), β(U) and γ(Np,U)

In this section we compare *ab initio* enthalpies for α(Np), β(Np), α(U), β(U) and γ(Np,U) to those from both of the two CALPHAD models. As we mentioned in Introduction, the major motivation is to see if DFT + *U* with the empirical ranges of U_{eff} parameters that we validated individually in the Np-Zr and the U-Zr system—0.65-0.99 eV and 1-1.5, respectively for Np and U—also predicts equally or more accurate enthalpy than DFT.

Before we start, it is essential to note first that both CALPHAD and *ab initio* enthalpies have their own intrinsic error bars. On the CALPHAD side, from comparison above, the two CALPHAD models for the Np-U system encounter some uncertainty for the lower temperature phases of α(Np), β(Np), ζ, and α(U). Even though the two models both reproduced the experimental phase boundaries for the BCC phase rather satisfactorily, some degrees of freedom are still allowed in how the total free energy is partitioned between enthalpy and entropy and how large the total free energy is, which depends on the state of the liquid phase that is in equilibrium with the BCC phase. For example, in our recent work on U-Zr we found that two earlier CALPHAD models[11, 40] predicted very similar BCC phase boundaries as our model[33], however the enthalpy of mixing for the BCC phase from them were about 0.08-0.09 eV/atom (7.7-8.8 kJ/mole) larger at 50.at% Zr than that from our model. One of the models[11] also predicted the excess entropy of mixing for the liquid phase to be about 0.10 eV/atom (10 kJ/mole) larger than the other two[33, 40]. On the *ab initio* side, DFT was found, on average, to overestimate the CALPHAD predicted enthalpies by about 0.10 and 0.16 eV/atom (9.7 and 15.4 kJ/mole) for U metal and U-Zr alloy[34] and Np metal Np-Zr alloy[35], respectively. DFT + U was found to reduce the difference, but not to totally zero. The smallest average difference between DFT + U and CALPHAD enthalpies for the U-Zr system[34] was found at $U_{\mathrm{eff}}(\mathrm{U}) = 1.24$ eV, which was still about 0.02-0.03 eV/atom (1.9-2.9 kJ/mole) depending on which CALPHAD model we compared to; for the Np-Zr system, the corresponding smallest average difference was found to be 0.03-0.06 eV/atom (2.9-5.8 kJ/mole) at $U_{\mathrm{eff}}(\mathrm{Np}) = 0.9$ eV.

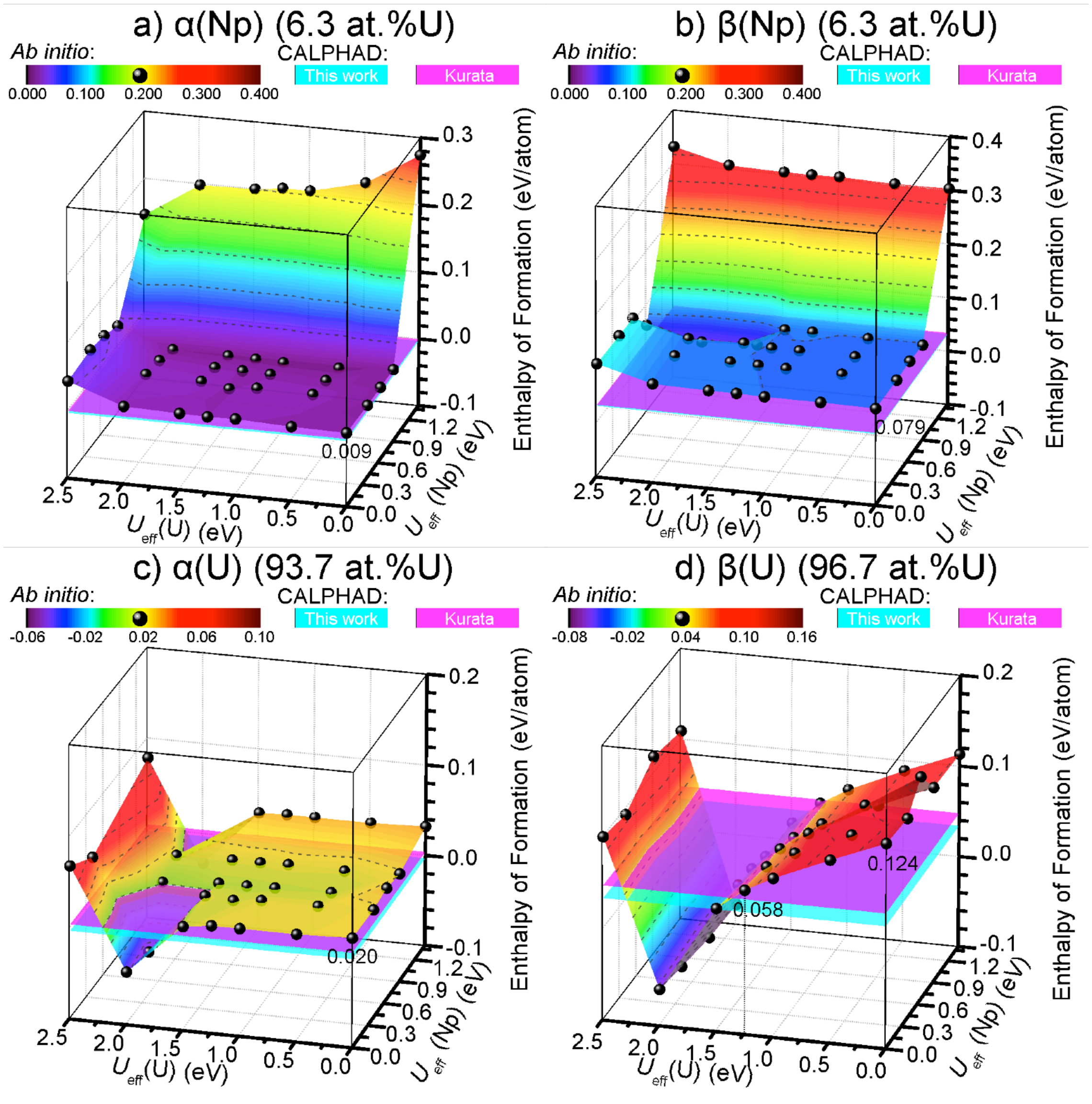

Figure 6.2. Enthalpy of formation for a) α(Np) (6.3 at.%U), b) β(Np) (6.3 at.%U), c) α(U) (93.7 at.%U), and d) β(U) (96.7 at.%U) from *ab initio* at different U_{eff}(Np) and U_{eff}(U) compared with those from the CALPHAD models of this work (cyan) and Kurata (magenta)[12]. Only the points marked with black balls are actually calculated data, and the surfaces connecting them are from spline interpolation as guides to the eyes.

The existence of error bars for both *ab initio* and CALPHAD enthalpies have important implications for the validation of *ab initio* methods against CALPHAD predictions. Because CALPHAD predicted enthalpies are estimations but not necessarily true values, the best empirical U_{eff} for the Np-U system may not be exactly the same value with which DFT + U enthalpy is precisely the same as CALPAHD for any given alloy. Instead, any conclusion from the comparison must be drawn statistically, which is the reason why we are looking at all the stable solid phases of Np-U as given in Table 6.1 except ζ for which the reference CALPHAD models are expected to have large uncertainty.

Let us start by looking at the four terminal solution phases α(Np), β(Np), α(U), and β(U) in Figure 6.2. We first discuss the qualitative trend of how the enthalpy is dependent on U_{eff}(Np) and U_{eff}(U). A first observation is that the enthalpy is negligibly affected by U_{eff}(U) for the two Np-rich systems in panels a) and b) and negligibly affected by U_{eff}(Np) for the two U-rich systems in panels c) and d), respectively. More specifically, in panels a) and b), both the systems contain 6.3 at.% U and their enthalpies calculated at the same U_{eff}(Np) are almost the same when U_{eff}(U) varies in the range of 0-2.0 eV, and are only slightly larger at U_{eff}(U) = 2.5 eV. Similarly, panels c) and d) show that the two U-rich systems' enthalpies change little at the same U_{eff}(U) when U_{eff}(Np) varies in the range of 1-1.4 eV. This general trend is expected because its host atoms dominate the energy of a dilute system. Note in c), an exception exists at U_{eff}(U) = 2 eV with two points above while all the other points below the CALPHAD enthalpy planes. Considering that the trend is so well followed, we believe the two points above the CALPHAD planes are metastable solutions of DFT + U. Unfortunately, although we have tried using the U-ramping method (see Sec. 6.3.2) to obtain more stable solutions but have not been able to converge a lower energy state. Next we consider how the energy changes as a function of the host atom's U_{eff}. Interestingly, this time it shows three different behaviors. In a) and b), the *ab initio* enthalpy surfaces are almost horizontal planes when U_{eff}(Np) is between 0 and 0.9 eV and rise very steeply when it is larger. In c), the *ab initio* enthalpy surface also essentially levels out between U_{eff}(U) = 0 and 1.5 eV, drops between 1.5 and 2 eV, and rises afterwards. In d), the *ab initio* enthalpy surface drops continues between U_{eff}(U) = 0 and 2 eV and rises afterwards. The gradient of descending is nevertheless again different between the range of 0-1.5 eV and the range of 1.5-2 eV. At this point the physical origins of the three different behaviors are not clear.

Now we consider how the *ab initio* enthalpies compare with CALPHAD. Figure 6.2 shows that despite the different in the predicted phase boundaries, the two CALPHAD model gives very similar or almost the same enthalpies. In panels a) – c), enthalpies at different U_{eff}'s are essentially the same when U_{eff}(Np) is between 0 – 0.9 eV and U_{eff}(U) is between 0 -1.5 eV—including the point of DFT with U_{eff}(Np)=U_{eff}(U)=0, which are all very close to the corresponding CALPHAD values. However, in panels d), the enthalpy from DFT is too large (0.124 eV/atom) compared to the reference values of 0.034 and 0.048 eV/atom from the CALPHAD models of this work and Kurata, respectively. The DFT + U is found to predict lower enthalpy, which can improve the agreement with the CALPHAD. In particular, if we take U_{eff}(U) to be the value that we found to predict enthalpies of U-Zr to be statistically closest to CALPHAD in Ref.[34] (U_{eff}(U) = 1.24 eV) we get a formation energy of 0.058 eV/atom, which is in fairly good agreement with the two CALPHAD values.

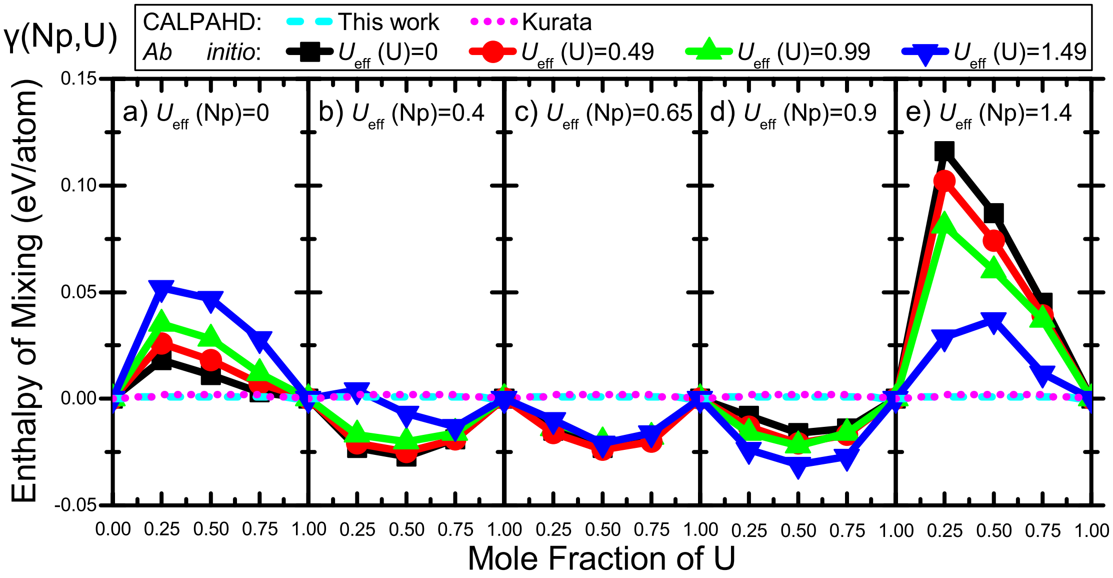

Figure 6.3. Enthalpy of mixing for γ(Np,U) from *ab initio* compared with those from the CALPHAD models of this work (cyan) and Kurata (magenta)[12]. The results from U_{eff}(Np) = a) 0, b) 0.4, c) 0.65, d) 0.9, e) 1.4 eV are shown in the respective panel. In all panels the results from U_{eff}(U) = 0 (black), 0.49 (red), 0.99 (green) and 1.49 (blue) eV are shown as different curves. Only the points marked with symbols are actually calculated data, and the lines connecting them are from spline interpolation as guides to the eyes.

The previous discussion only looks at one individual composition point in each phase, next let us look at the BCC γ(Np,U) phase's enthalpy of mixing over the whole composition range of 0 to 100 at.% U in Figure 6.3. We show results calculated at U_{eff}(U) = 0, 0.49, 0.99 and 1.49 eV as black, red, green, and blue curves, respectively in each of the five panels of a) to e) calculated at U_{eff}(Np) = 0, 0.4, 0.65, 0.9 and 1.4 eV, respectively. Again we start our discussion with qualitative features. Firstly, the enthalpy decreases initially and then increase when U_{eff}(Np) increases from 0 to 1.4 eV. Second, when increasing U_{eff}(U), the enthalpy increases in panels a) and b), essentially does not change in panel c), while decreases in panels d) and e). Third, both U_{eff}(U) and U_{eff}(Np) play a significant role in the enthalpy changes. However, U_{eff}(Np) has a somewhat larger effect than U_{eff}(U). For example, the maximum change in enthalpy with U_{eff}(Np) at fixed U_{eff}(U) is about 0.15 eV/atom across panels, while the maximum change in U_{eff}(U) at fixed U_{eff}(Np) is about 0.1 eV/atom in panel e), and generally much less in all the other four panels of a) to d).

Now we compare *ab initio* enthalpies to those predicted by CALPHAD, which are almost zero in the whole composition range from both models. Figure 6.3 shows that DFT predicts the enthalpy of mixing for γ(Np,U) to be positive, about 0.02 eV/atom at the maximum near 25 at.%U, and is reasonably close to the CALPHAD values. In the previous section, we estimated that due to the neglect of ion relaxation the calculated enthalpy of mixing may reduce by about 0.013 eV/atom at 50 at.% corresponding to DFT calculated volume mismatch between BCC Np and U. If we subtract the ion relaxation energy from DFT enthalpy of mixing, the resulting enthalpy will be smaller but should remain positive around 25 at.%U. Positive enthalpies suggest the possible existence of a miscibility gap although the values are small enough that it may not be observable at the high temperatures where γ(Np,U) is stable. For DFT + *U* enthalpies, we can rule out that those in panel e) are probably too large, in agreement with the results that U_{eff}(Np) = 1.4 eV is larger than the validated U_{eff}(Np) range of 0.65-0.9 eV. The single blue curve of U_{eff}(U) = 1.49 eV in panel a) shows a maximum also near 25 at.%U to be around 0.05 eV/atom, which is probably also too large, in agreement with what we showed in Ref.[155] that although 1-1.5 eV is the general empirical U_{eff} range for U and U-Zr, the individual empirical U_{eff} for BCC γU and γ(U,Zr) phases are approximately on the smaller end of 1 eV. If we take the statistically optimal U_{eff} values for U-Zr and Np-Zr (U_{eff}(Np) = 0.9 eV[35] and U_{eff}(U) = 1.24 eV[34]), or the individual empirical U_{eff} values specifically for the BCC high temperature phase of U-Zr and Np-Zr (U_{eff}(Np) near 0.65 eV[35] and U_{eff}(U) near 0.99 eV[155]), then our results suggest that the enthalpy of mixing for BCC γ(Np,U) is negative. Further, the ion relaxation energy, although very small due to the reduced volume mismatch—estimated to be about 0.006 eV/atom at 50 at.%U corresponding to the calculated volume mismatch from DFT + U at (U_{eff}(Np), U_{eff}(Np))=(0.6,0.99) eV, will also bring down the enthalpy slightly. Quantitatively, most of the DFT + U curves in panels b) – d) are also about 0.02 eV/atom or less away from the CALPHAD curves, which are possible and should be within the uncertainty of these modeling approaches, as we discussed in the beginning of this section. Moreover, the negative enthalpy of mixing in the whole composition range suggests that γ(Np,U) should have no miscibility gap, which is consistent with the fact that Mardon and Pearce did not find any evidence for the existence of a BCC miscibility gap in their experimental study of the Np-U system[19], nor did either of the CALPHAD models predicts one. In short, CALPHAD, DFT and DFT + U predict almost zero, slightly positive and mostly slightly negative enthalpy of mixing for BCC γ(Np,U), respectively. Although they differ qualitatively by sign, the absolute differences are small in the sense that they are comparable with the error bars of these modeling approaches. We thus cannot be sure which prediction is closer to the true situation except that the enthalpy of mixing for BCC γ(Np,U) must be small, be it positive or negative. We hope future experimental studies can provide more constraints on these energies.

6.4.3 *Ab initio* predictions for ζ phase

Results in the previous section suggests that for Np-U DFT + U enthalpies are either on par with or more accurate than DFT when using U_{eff}(Np) and U_{eff}(U) in the statistically optimal ranges found from previous studies of U-Zr and Np-Zr[34, 35, 155](U_{eff}(Np) = 0.65-0.99 eV and U_{eff}(U) = 1-1.5 eV) for the solid phases of Np-U we have discussed so far—α(Np), β(Np), α(U), β(U) and γ(Np,U). Now we turn our attention to the remaining phase of ζ. As reviewed above, CALPHAD modeling faces significant uncertainty for this phase, and here we present *ab initio* predictions of the enthalpy of formation and site occupations for ζ as functions of composition. We hope results of this section can assist development of improved CALPHAD model for the Np-U system, for example by guiding the sublattice modeling of ζ. Results from both DFT and DFT + U at (U_{eff}(Np), U_{eff}(U)) = (0.65, 1.24) eV are shown.

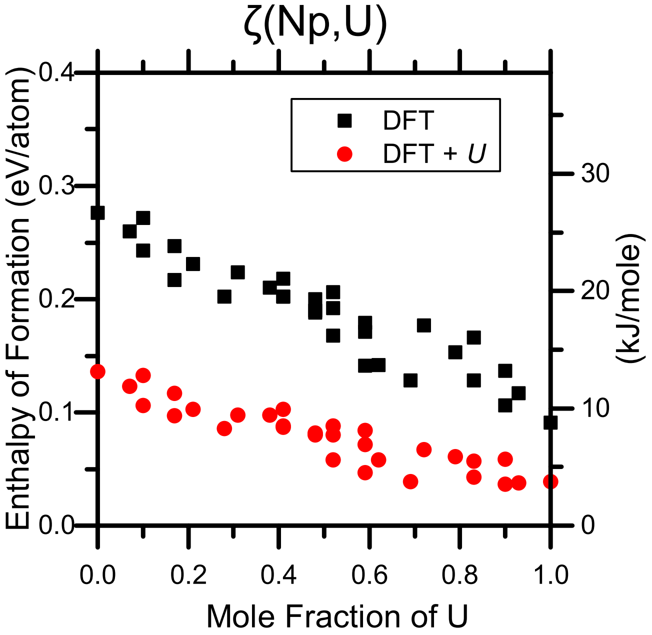

Figure 6.4. Enthalpy of formation for ζ from DFT and DFT + U at (U_{eff}(Np), U_{eff}(U)) = (0.65, 1.24) eV.

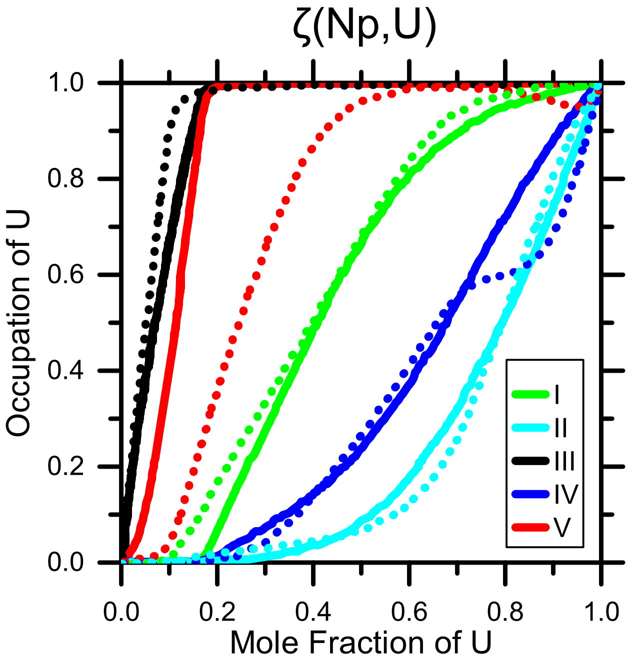

Figure 6.5. Site occupations for ζ predicted by DFT (solid) and DFT + U (dash) at (U_{eff}(Np), U_{eff}(U)) = (0.65, 1.24) eV for the five lattice site groups I-V defined in Table 6.4.

Figure 6.4 shows enthalpy of formation for ζ as a function of composition. DFT values are black squares while DFT + U are red circles. With increasing mole fraction of U, the enthalpy is decreased, suggesting that it is possible that ζ is easier to form on the U-rich side. The relative stability change as a function of composition is smaller predicted by DFT + U than DFT. In terms of absolute values, those from DFT are around 0.27 eV/atom on the Np end and 0.10 eV/atom on the U end. As expected, DFT + U again predicts much smaller enthalpy than DFT in the whole composition range, similar as we have been finding in the U-Zr and Np-Zr systems and also for β(U) at 96.7 at.%U above. Specifically, the DFT + U enthalpy is about 0.14 eV/atom on the Np end, while 0.05 eV/atom on the U end. The average difference between DFT and DFT + U enthalpies is about 0.10 eV/atom, which suggests the Hubbard U potential in DFT + U have a significant effect for ζ phase. One may doubt that our results for ζ are wrong because the formation energy of a compound phase stable at low temperature should be negative, while all of our *ab initio* enthalpies, both from DFT and DFT + U are positive. We think that these may in part because that we only sampled those end members with several lattice sites grouped together and with them fully occupied by only one element, and the actual ζ alloy may have lower calculated enthalpy of formation. Another reason may be that although ζ is stable at room temperature, it is not stable at 0 K, which is actually the situation assumed by Kurata's CALPHAD model[12], as shown in Figure 6.1. If this assumption is true, then a good reference can be some compound phase stable at finite temperatures, for example σ phase of the Mo-Re system, for which Ref.[202] reported enthalpies of formation to be about 0.04 to 0.10 eV/atom from *ab initio* calculations at 0 K. Our DFT + U enthalpies are close to this range, while DFT enthalpies, particularly on the Np-rich end are too high.

Based on the enthalpy results, we predict the site occupation of ζ as a function of composition in Figure 6.5. The occupation was obtained using the compound energy formalism[71, 210] with the *ab initio* calculated enthalpy of formation as model parameters. Again we consider the situation with the lattice site grouping given in Table 6.4. Alternative ways of grouping are possible, but given the uncertainty in *ab initio* methods and also considering the limited experimental data available for ζ, we did not pursue them in this study. We first compare DFT and DFT + U results. Figure 6.5 shows DFT and DFT + U predict in general qualitatively and even quantitatively similar lattice site occupation curves despite the significant difference in enthalpy of formation shown above. The most significant difference is only for the occupation curve of lattice site group V (red), which contains lattice sites 9, and 10. For this group V DFT suggests a sharp increase of U occupation with increasing U mole fraction, while DFT + *U* predicts a more gradual increase. Another difference is that DFT + *U* predicted two small kinks for lattice site group IV (blue) and V (red) near 80 at.%U, which are most possibly wrong and due to artifacts induced by metastable solutions of DFT + *U* for some end members. In fact, the relative enthalpy differences between different end members predicted by DFT + *U* are much smaller than DFT, making DFT + *U* more susceptible to some small numerical convergence errors than the DFT. We do not think these errors are significant to the extent that makes the DFT + *U* results totally untrustworthy because the two kinks only happen on the U-rich end and for two lattice site groups, which means that probably only a few of the end members were affected. Moreover, the DFT + *U* enthalpies also do not show any odd point far from the main data cluster near the U-rich end, similar to the case for the DFT enthalpies, which suggests the error in energy due to metastable solutions should be very small—otherwise the wrong points would have stood out.

We now comment on the predicted occupation curves in Figure 6.5. With increasing mole fraction of U, U atoms like to occupy lattice sites in group III (black) first, then group V (red), I (green), IV (blue) and finally II (cyan), which manifests in Figure 6.5 as different slopes of the five occupation curves. In particular, group III (black), which contains only lattice site 4 is almost totally occupied by U when the overall U mole fraction is larger than about 0.2. This suggests that lattice site 2 is possibly only occupied by U atom in the actual ζ alloy. Lattice sites 9 and 10 in group V (red) also like to be occupied by U more than Np, while lattice sites in groups II and IV may be occupied more easily by Np than U. Finally, lattice site group I, which contains sites 1, 3 and 7 have intermediate U occupation in a large range of compositions, and thus site 1, 3 and 7 possibly do not have strong preference between Np and U. Overall, we expect that the *ab initio* predicted site occupations may provide some useful information for future thermodynamic description of ζ phase with sublattice model, as Ref.[202] exemplified in the Mo-Re system.

6.5 Conclusions

A CALPHAD model was developed for the Np-U system that reproduces the experimental BCC and liquid phase boundaries well but faces major uncertainty for the phase fields at lower temperatures, in particular that of the ζ phase. Suggestions of possible issues in existing experimental data and for future experimental studies were given.

DFT + U enthalpies are either on par with or more accurate than DFT when using U_{eff}(Np) and U_{eff}(U) in the ranges of 0.65-0.99 eV and 1-1.5 eV ranges, respectively that we determined in our previous studies of the Np-Zr and U-Zr systems containing either only Np or only U. Specifically, DFT and DFT + U enthalpies both match CALPHAD closely for α(Np), β(Np), α(U), but DFT overestimates the enthalpy for β(U) by about 0.08 eV/atom (7.7 kJ/mole) while DFT + U could reproduce CALPHAD approximately using U_{eff}(U) near 1.24 eV, which is the statistically optimal U_{eff} for U that we established individually in the U-Zr system (U_{eff}(Np) has a negligible effect in this case). For γ(Np,U), DFT predicts slightly positive enthalpy of mixing while DFT + U slightly negative, which could be an improvement considering that no miscibility gap was found experimentally and that neither did the two CALPHAD models predict one, but this is really uncertain due to the small differences in enthalpy that are comparable to the error bar of the modeling approaches. Furthermore, DFT predicts very large enthalpies for the end members of intermediate phase ζ, about 0.187 eV/atom on average while DFT predicts 0.081 eV/atom, which is possibly an improvement as it seems unusual for an intermediate phase stable at room temperature to have enthalpy larger than 0.15 eV/atom, while 0.04-0.08 eV/atom may be possible as found for σ phase of the Mo-Re system[202]. Our results suggest that U_{eff} is largely determined by nature of the element and the chemical bonding, but less by the crystal structure and composition and thus similar U_{eff} ranges determined in one system may be transferable to closely related systems—from U-Zr and Np-Zr to Np-U in our case.

Finally, predictions of the enthalpy of formation and site occupations of ζ phase were made with both DFT and DFT + U, which may help future CALPHAD modeling of the Np-U system. DFT and DFT + U at (U_{eff}(Np), U_{eff}(U)) = (0.65, 1.24) eV calculated enthalpies for ζ differ by about 0.10 eV/atom (9.6 kJ/mole) on average over the whole composition range, which suggests that the Hubbard U potential in DFT + U has a large effect for this phase in the Np-U system. The predicted site occupations may be of value for the sublattice modeling of ζ phase in future CALPHAD studies.

7 CALPHAD Modeling and *Ab initio* Calculations of the Np-U-Zr Systems

Note: The contents of this chapter are under preparation to be submitted to Journal of Nuclear Materials for peer-review and publication as an article.

7.1 Chapter Abstract

A thermodynamic model for the Np-U-Zr ternary system is developed based on Muggianu extrapolation of the models for the U-Zr, Np-Zr, and Np-U binary systems that we developed previously, all employing the CALPHAD method. This model is shown to capture reasonably the phase stability of the high temperature phases of the Np-U-Zr system through comparison with available experimental phase equilibrium data. *Ab initio* calculations are performed on 28 compositions of body centered cubic (BCC) Np-U-Zr that are evenly distributed overs the whole ternary composition space. Both density functional theory (DFT) in its standard form and the so-called DFT plus Hubbard *U* (DFT + *U*) modification are employed, based on the generalized gradient approximation (GGA). Comparing to the enthalpy of mixing predicted by CALPHAD, root mean square (RMS) errors for DFT are 0.093 eV/atom (9.0 kJ/mole). However, RMS errors vs. CALPHAD for DFT + *U* values are reduced to 0.009 to 0.036 eV/atom (0.9 to 3.5 kJ/mole) when the effective Hubbard *U* parameters U_{eff} for Np and U vary in the range of 0.65-0.9 and 1-1.5 eV, respectively. In particular, the smallest RMS error of 0.009 eV/atom (0.9 kJ/mole) is obtained when U_{eff}'s of 0.65 and 0.99 eV are used for Np and U, respectively. The improvement in enthalpy provided by DFT + *U* in these U_{eff} ranges is found to be generally consistent amongst the 28 compositions (i.e., the comparisons are

not mixtures of better and worse cases at different compositions). Such ranges of empirical U_{eff} for Np and U are in agreement with the values previously determined for the Np-Zr and U-Zr systems, suggesting that similar U_{eff} parameters may be applicable for modeling other Np and/or U containing metallic alloys with different structure and composition. Using both CALPHAD and *ab initio* approaches, the solution behavior (in particular the miscibility gap), atomic volume and volume of mixing for the BCC phase, and the solidus and liquidus surface of the Np-U-Zr systems are predicted and discussed.

7.2 Introduction

Actinide rich metallic nuclear fuels are promising candidates for future generation fast nuclear reactors because of their advantages such as thermal conductivity, burn-up and recycling. over traditional oxides fuels[4]. However, several issues must be addressed in using metallic fuels. Firstly, the melting temperatures of the constituent actinide metals[211]—for example, U (1408 K), Np (917 K), Pu (913 K)—are close to or even lower than many fast reactor's design operating temperatures (870-1300 K)[2]. Moreover, metallic fuels have considerable constituent redistribution and interaction with the cladding during burnup. It was suggested[4] that alloying the actinides with transition metals like Zr and Mo can both boost the melting temperature and suppress the constituent's diffusion and interaction with the cladding. Understanding the underlying mechanisms for such improvements are important for better design and safe and optimal use of the fuels.

Fundamentally, melting temperature, constituent redistribution, and cladding interaction are all strongly tied to the phase stability of the fuels. However, due to their radioactivity, toxicity, and scarcity, experimental measurement of the fuel phase stability is often quite difficult and expensive. Take U-Pu-Zr-MA (MA=Np, Am, Cm) metallic fuel as an example. Among all its ternary subsystems, to the best of our knowledge only U-Pu-Zr has systematic experimental phase diagram data presently available[13]. To gain additional knowledge of these systems, we have previously studied[33-35, 155, 212] the Np, U, Zr unary and the Np-Zr, U-Zr and Np-U binary systems with *ab initio* calculations and CALPHAD modeling. It is a natural next step to study their parent ternary system Np-U-Zr.

To our knowledge, experimental study of the phase diagram of the Np-U-Zr ternary system has only been reported once in Ref.[185], in which Rodríguez, *et al*. probed the U-rich corner around the three temperatures of 793, 868 and 973 K. Due to the limited composition and temperature space studied, Rodríguez, *et al*. still left the phase diagram of Np-U-Zr largely undetermined. Furthermore, Rodríguez, *et al*. suggested in the same study[185] that BCC Np and Zr are completely miscible, which is in disagreement with more recent experiment results on the Np-Zr binary system[21, 183, 184]. We also found it difficult to accommodate Rodríguez, *et al*.'s data for Np-Zr[185] with other experimental data[21, 183, 184] in our CALPHAD modeling of the Np-Zr binary system[35]. Therefore, we shall in the following we will compare our model results with the experimental data of Rodriguez, *et al*.[185], but we will not use the data of Rodriguez, *et al*. to adjust our model parameters for Np-U-Zr. Besides Ref.[185], we did not find any other experimental thermochemical or phase equilibria data for Np-U-Zr, nor any CALPHAD model of Np-U-Zr reported previously.

The goals of this study are as follows. First, to develop a CALPHAD model for the Np-U-Zr ternary system. Due to the scarcity of experimental data for the Np-U-Zr ternary system itself, thermodynamic modeling of this system faces more uncertainty than other more common metal alloys. However, we will use our previous studies of the binary subsystems to restrain the uncertainty to some extent so that our current work can formulate an initial quantitative model of the Np-U-Zr system that future work can continue to refine. We will also suggest some phase fields and composition ranges where experimentalist can work on to help improve the thermodynamic assessment. Second, we found in our earlier studies[34, 35] that calculations using density functional theory (DFT)[28, 29] in its standard form based on the generalized gradient approximation (GGA)[30] to the exchange-correlation potential tend to overestimate the enthalpy of U-Zr and Np-Zr by about 0.1 and 0.15 eV/atom and those based on a so-called DFT plus Hubbard U (DFT + U) functional[31] can reduce such errors to approximately 0.03 and 0.05 eV/atom and better when the effective Hubbard U parameter U_{eff}'s in the DFT + U functional are in the range of 0.65-0.9 and 1-1.5 eV for Np and U, respectively. It is interesting to test 1) if DFT also overestimates the enthalpy of Np-U-Zr to similar extent and 2) if such empirical U_{eff} parameters determined individually in binary systems containing only one actinide element still apply to systems containing two or more actinide elements. Demonstration that the U_{eff} values are transferable from the binaries to the ternary system is an important step in circumventing the limit in or as some people believe, the lack of predictive power for DFT + U on actinide alloys. Finally, the alloying behavior of the Np-U-Zr system is interesting from a fundamental point of view. For example, different miscibility behaviors of BCC Np, U and Zr are expected in each of the three binary systems. BCC Np and BCC Zr are suggested by more recent experimental studies[21, 183, 184] to always phase separate until they melt, as mentioned above; BCC

U and BCC Zr also show a miscibility gap[41] but dissolve into a single solid solution phase at higher temperature before melting, while BCC Np and BCC U do not seem to show any stable miscibility gap[19]. It is interesting to see if these qualitative solution behaviors of the three binary systems can be explained by the enthalpy of mixing from the current modeling study. If yes, we hope to predict the solution behavior of the whole ternary BCC Np-U-Zr phase, which has little been studied except for the three binary sides so far..

This chapter proceeds as follows. Section 2 describes the details of the CALPHAD and *ab initio* methodology. Section 3 validates the CALPHAD model and *ab initio* methods for Np-U-Zr. Section 4 presents and discusses CALPHAD and *ab initio* predictions for Np-U-Zr, including BCC phase's solution behavior and its atomic volume and volume of mixing, as well as the liquid phase boundary. Finally, Section 5 summarizes this study.

7.3 Methodology

7.3.1 CALPHAD Methodology

We develop the thermodynamic model of the Np-U-Zr system by extrapolating the CALPHAD models of the three binary subsystems U-Zr, Np-Zr and Np-U that we developed earlier[33, 35, 212] using the Muggianu symmetric scheme[32].

We describe the details by taking the BCC phases as an example. When phase separated, they are labeled γ(Np), γ(U), β(Zr) or their combinations (e.g., γ(Np)+β(Zr) miscibility gap) following the respective label of the elemental BCC phases. BCC and BCC+BCC' are also used in this work to denote single-phase and two-phase BCC regions. In our previous assessments of the U-Zr[33] and Np-Zr[35] systems, the BCC phases were found to be well modeled using the substitutional solution model. Although for the Np-U system uncertainty exists for the low temperature part due to the lack of reliable experimental data, we found in our assessment[212] that the BCC phase of Np-U can also be reliably modeled using the substitutional solution model. The expression of the Gibbs free energy of BCC Np-U-Zr in the Muggianu symmetric scheme[32] is:

$$\begin{aligned} G_{\mathrm{Np,U,Zr}}^{\mathrm{BCC}} &= (x_{\mathrm{Np}}\,{}^{\circ}G_{\mathrm{Np}}^{\mathrm{BCC}} + x_{\mathrm{U}}\,{}^{\circ}G_{\mathrm{U}}^{\mathrm{BCC}} + x_{\mathrm{Zr}}\,{}^{\circ}G_{\mathrm{Zr}}^{\mathrm{BCC}}) + RT(x_{\mathrm{Np}}\ln x_{\mathrm{Np}} + x_{\mathrm{U}}\ln x_{\mathrm{U}} + x_{\mathrm{Zr}}\ln x_{\mathrm{Zr}}) \\ &+(x_{\mathrm{Np}}x_{\mathrm{U}}L_{\mathrm{Np,U}}^{\mathrm{BCC}} + x_{\mathrm{Np}}x_{\mathrm{U}}L_{\mathrm{Np,U}}^{\mathrm{BCC}} + x_{\mathrm{Np}}x_{\mathrm{Zr}}L_{\mathrm{Np,Zr}}^{\mathrm{BCC}} + x_{\mathrm{Np}}x_{\mathrm{U}}x_{\mathrm{Zr}}L_{\mathrm{Np,U,Zr}}^{\mathrm{BCC}}) \end{aligned} \tag{7}$$

where x_i is the mole fraction, ${}^{\circ}G_i^{\mathrm{BCC}}$ is the Gibbs energy of elemental BCC metal, and $L_{i,j}^{\mathrm{BCC}}$ and $L_{i,j,k}^{\mathrm{BCC}}$ are the binary and ternary interaction parameter for specie *i*/*j*/*k*=Np, U, Zr. Collectively, the first term is the linear Gibbs energy of mixing, the second term the contribution of ideal entropy of mixing to the Gibbs energy, and the third term the excess Gibbs energy of mixing as described by the Redlich–Kister polynomial [70]. We currently set the ternary interaction parameter $L_{\mathrm{Np,U,Zr}}^{\mathrm{BCC}}$ to zero in our model (i.e., assuming weak and negligible ternary interactions). This assumption is supported by Rodríguez, *et al.*'s conclusion[185] that the experimentally measured solidus temperatures of Np-U-Zr were "in agreement with the values expected from a linear interpolation of the solidus temperatures of the binary compounds". The standard element reference (SER) [69] is used as the Gibbs energy reference state. Finally, it is important to note that the CALPHAD parameters for the BCC phases in the three binary sub-systems[33, 35, 212] are not from fitting to *ab initio* results but only to experimental data.

We do not include any compound phase in our model besides those found in the binary systems: δ phases of both U-Zr and Np-Zr, and ζ phase of Np-U. They are modeled using the sublattice model, as detailed in Refs[33, 35, 212]. Note that the ζ phase of Np-U was also labeled δ in the experimental phase diagram of Mardon and Pearce[19]. To distinguish that it has a different structure from δ phases of U-Zr and Np-Zr and recognizing that it is actually is isomorphous with ζ phase of Pu-U[11], we label the compound phase of Np-U ζ here (as in Ref. [212]). Our decision to not include any ternary compound is supported by the finding of no ternary compound in the samples studied Rodríguez, *et al.*[185].

The remaining phases are terminal solution phases α(Np), β(Np), α(U), and β(U). They are also modeled using the substitutional model, same as explained above for the BCC phases.

7.3.2 *Ab initio* Methodology

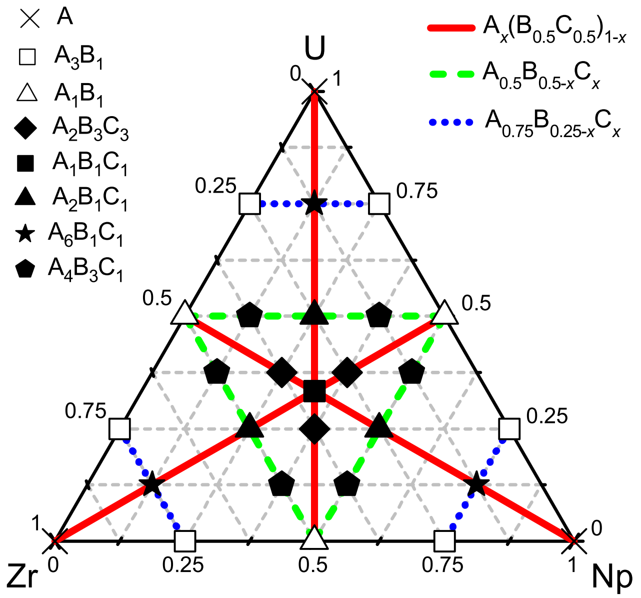

Figure 7.1. The 28 compositions of BCC Np-U-Zr studied in *ab initio* calculations and the three representative series of isopleth paths that they form.

Table 7.1. Supercell structures used in *ab initio* calculations of BCC Np-U-Zr.

Supercell[1]	Number of compositions	Cell size (atoms/cell)	*k*-Point mesh
A	3	1	17×17×17
A_3B_1	6	16	6×6×6
A_1B_1	3	16	6×6×6
$A_2B_3C_3$	3	64	2×2×2
$A_1B_1C_1$	1	36	3×3×3
$A_2B_1C_1$	3	32	4×4×4
$A_6B_1C_1$	3	64	2×2×2
$A_4B_3C_1$	6	64	2×2×2

[1] A/B/C=Np, U, Zr

Totally 28 compositions of BCC Np-U-Zr are calculated, as illustrated in Figure 7.1. They are modeled using 8 different supercell structures listed in Table 7.1. Among them, except for the unary structure A that uses the one-atom BCC primitive cell, all supercells are generated using the special quasirandom structure (SQS) method[84], as implemented in the Alloy Theoretic Automated Toolkit (ATAT)[85, 213]. A_3B_1 and A_1B_1 binary as well as $A_1B_1C_1$, $A_2B_1C_1$, $A_6B_1C_1$, and $A_2B_3C_3$ ternary structures were generated and tested by one of us previously in Mo-Nb, Ta-W and Cr-Fe binary systems[86], and Mo-Nb-Ta and Mo-Nb-V ternary systems[27], respectively. Additionally, we generate the $A_4B_3C_1$ structure in this study following the same approach as Ref.[27]. The supercell size and the Monkhorst–Pack[78] *k*-point mesh used to sample Brillouin zone for each supercell are listed in Table 7.1. For the BCC U-Zr, Np-Zr and Np-U binary supercells, we tested and found the *k*-point meshes used could converge the energy to at least 3 meV/atom, and thus here for BCC Np-U-Zr ternary supercells, similar *k*-point meshes adjusted based on supercell sizes are used. Note that the unary and binary structures listed in Table 7.1 were already calculated in our previous studies[33-35, 212] and they are included here for completeness. All *ab initio* data we present in this study are only calculated at these 28 compositions, and additional data at other compositions we show next are generated by spline interpolation and they only serve as guides to the eye.

All *ab initio* calculations are performed in the general framework of DFT[28, 29] using the Vienna *Ab initio* Simulation Package (VASP)[72, 73]. The electron-ion interaction is described with the projector-augmented-wave (PAW) method[74] as implemented by Kresse and Joubert[75]. The PAW potentials used treat $6s^2 6p^6 7s^2 5f^4 6d^1$, $6s^2 6p^6 7s^2 5f^3 6d^1$ and $4s^2 4p^6 5s^2 4d^2$ as valence electrons for Np, U and Zr, respectively. The exchange-correlation functional parameterized in the generalized gradient approximation (GGA)[76] by Perdew, Burke and Ernzerhof (PBE)[30] is used. The stopping criteria for self-consistent loops used are 0.1 meV and 1 meV tolerance of total free energy for the electronic and ionic relaxation, respectively. Cutoff energy of 450 eV is used throughout all calculations. The partial occupancies are set using the Methfessel-Paxton method[129] of order one with a smearing width of 0.2 eV. The electronic and ionic optimizations are performed using a Davidson-block algorithm[190] and a Conjugate-gradient algorithm[209], respectively.

Spin polarization is included in all calculations. In our previous validations on U-Zr and Np-Zr binaries, spin-orbit coupling (SOC) was found to affect the calculated enthalpy by about 0.02 and 0.03 eV/atom[34, 35], respectively, which are relatively small compared to DFT-GGA's error in enthalpy that are about 0.10 and 0.15 eV/atom, respectively, and hence we do not include it here to reduce the computational costs.

The DFT + U functional proposed by Dudarev *et al.*[31] is used. This form of DFT + U does not introduce explicit local exchange J term but only an effective Hubbard U term that depends on $U_{\mathrm{eff}} = U\text{-}J$. This approach also recovers the standard DFT functional exactly when $U_{\mathrm{eff}} = 0$. DFT + U potential is applied only on U and Np sites, but not on any Zr site. For historical reasons we did not set set $J = 0$ as one conveniently does but instead to 0.6 and 0.51 eV for Np and U, respectively and vary U from 0.75 to 2 eV. Putting them together results in a grid of (U_{eff}(Np), U_{eff}(U)) pairs as illustrated in Figure 7.2. In the future, one should be able to reproduce our results as long as the same U_{eff}'s are used, regardless of what specific pair of U and J is used to reach the U_{eff}. *Ab initio* data presented next that correspond to (U_{eff}(Np), U_{eff}(U)) points beyond those marked by filled circle on the grid in Figure 7.2 are generated by spline interpolation and they only serve as guides to the eye. Note the standard DFT corresponds to the (U_{eff}(Np), U_{eff}(U)) = (0,0) point on the grid. The metastability issue of DFT + U is combated using the U-ramping method[132] with modifications described in Ref.[34].

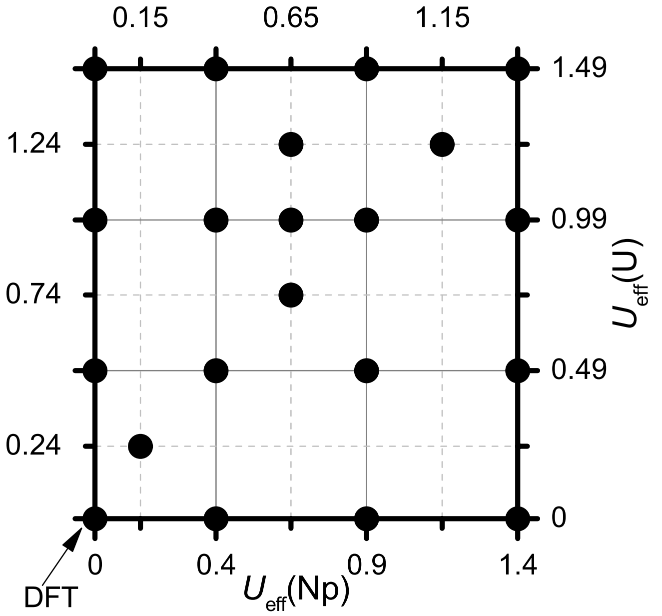

Figure 7.2. U_{eff} used for Np and U in DFT + U calculations.

Enthalpy (volume) of mixing of BCC Np-U-Zr is defined as:

$$X^{\text{mix}}(\text{Np}_{x_{\text{Np}}}\text{U}_{x_{\text{U}}}\text{Zr}_{x_{\text{Zr}}}) = X(\text{Np}_{x_{\text{Np}}}\text{U}_{x_{\text{U}}}\text{Zr}_{x_{\text{Zr}}}) - x_{\text{Np}}X(\text{Np}) - x_{\text{U}}X(\text{U}) - x_{\text{Zr}}X(\text{Zr}) \quad (8)$$

where X is enthalpy (volume) per unit amount (e.g., per atom), $\text{Np}_{x_{\text{Np}}}\text{U}_{x_{\text{U}}}\text{Zr}_{x_{\text{Zr}}}$ and Np, U, Zr are the alloy and the constituent BCC elemental metal references, respectively, and x_{Np}, x_{U}, x_{Zr} are the mole fractions of Np, U, Zr in the ternary alloy with $x_{\text{Np}}+x_{\text{U}}+x_{\text{Zr}}=1$.

Following our practice to mitigate the mechanical instability of BCC U-Zr and Np-Zr[34, 35], only volume relaxation is performed. The BCC volume mismatches between Np and Zr, Np and U, and U-Zr are about 26%, 13%, and 13%, respectively from DFT. DFT + U predicts larger volumes for Np and U, and the volume mismatches for the three binary systems become 16%, 6% and 10%, respectively for example at (U_{eff}(Np), U_{eff}(U))=(0.6, 0.99) eV. Based on our testing on the 10 BCC alloys formed by V, Nb, Ta, Mo and W, which are stable in BCC structure unlike Np and U, we estimated that the overestimation in enthalpy of mixing due to the lack of ion relaxation are about 0.026, 0.013, and 0.013 eV/atom, respectively for BCC Np-Zr, Np-U, and U-Zr corresponding to the volume mismatches from DFT, while 0.016, 0.006 and 0.009 eV/atom corresponding to those from DFT + U at 50.at.%; the corresponding values should be similar or smaller at 25 and 75 at.%. These values themselves are quite small, comparable to the intrinsic uncertainty of the two modeling approaches as well as our estimation of these energies using other BCC alloys. If one does not agree that they are small, pointing out that at least the error of 0.026 eV for Np-Zr at 50 at.% is significant, we mention that DFT enthalpy at that point is larger than CALPHAD by 0.162-0.032=0.130 eV/atom, which means the intrinsic error of DFT dominates the effect of ion relaxation. As a results, neglecting ion relaxation should not affect the quantitative comparison in *ab initio* and CALHPAD enthalpies of mixing for BCC phase of the Np-U-Zr system in this study.

7.4 Model Validations

7.4.1 CALPHAD Model

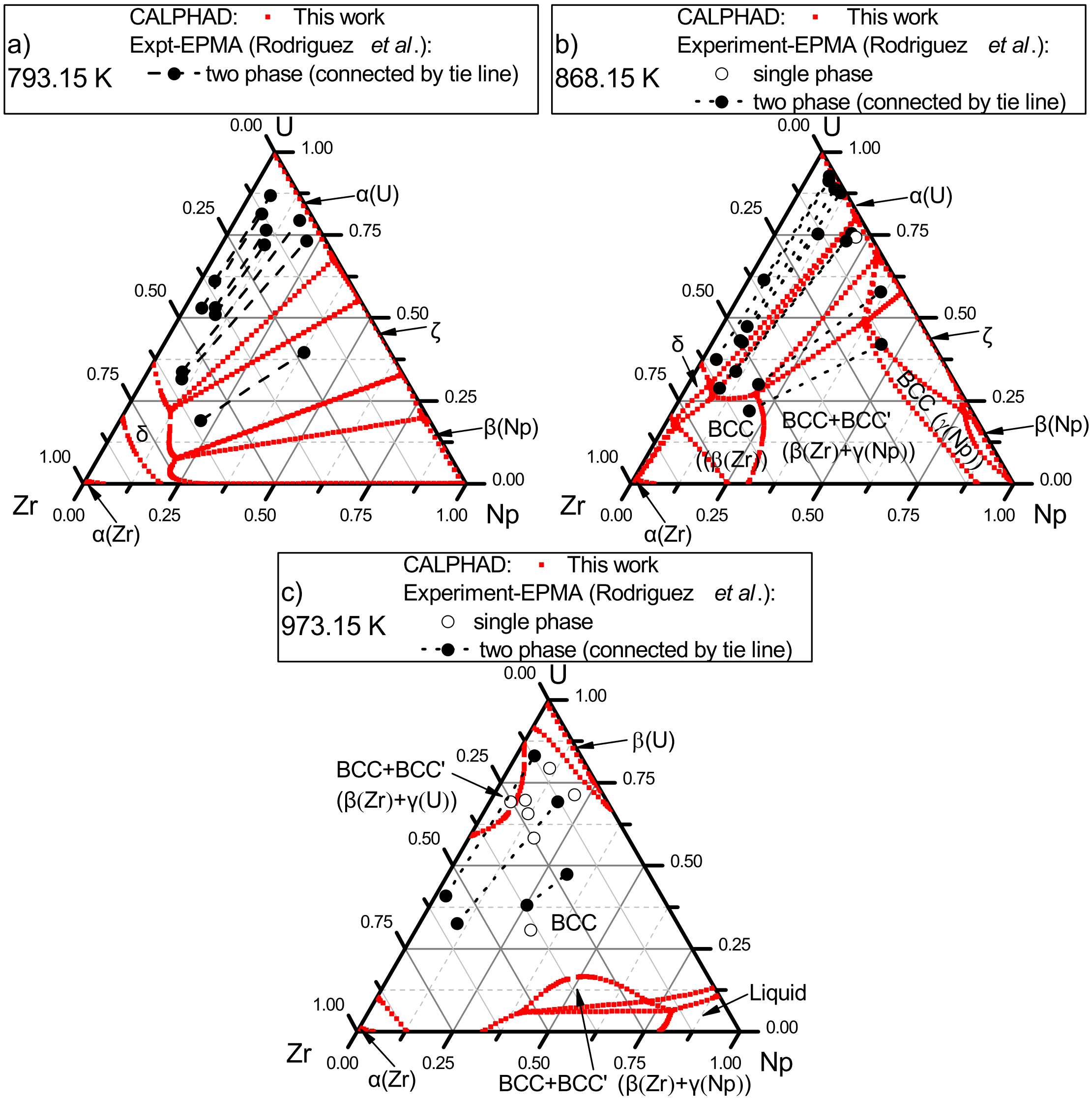

Figure 7.3. Isothermal sections of the phase diagram of Np-U-Zr at a) 793.15 K, b) 868.15 K, and c) 973.15 K. Greek phase labels for dominant component(s) of single-phase and BCC two-phase regions are given. Additionally, BCC and BCC+BCC’ are used to denote BCC single- and two-phase regions, respectively.

As mentioned in the Introduction, to our knowledge the study by Rodríguez *et* *al.*[185] is the only experimental phase diagram research on the Np-U-Zr system to date. We therefore first compare in Figure 7.3 our model predicted isothermal sections at 793.15, 868.15 and 973.15 K to the experimental electron probe microanalysis and metallographic analysis data of Rodríguez *et al.*[185]. At 793.15 K shown in Figure 7.3 a), most of the experimental data are expected to reflect the equilibration of α(U) and δ phases as suggested by CALPHAD. However, the points that are expected to lie on the phase boundary of δ have x(U) that are about 0.1-0.3 larger than those predicted by CALPHAD. The result that δ phase in Np-U-Zr is stable at x(U) smaller than 0.5 as the experimental data suggested is surprising because the phase boundary of δ phase in U-Zr is rather accurately determined by many recent experimental studies we reviewed and quite well reproduced in our study of U-Zr in Ref.[33]. It seems unlikely that the addition of small content of Np would lead to such a substantially larger δ phase homogeneity range. In fact, the phase boundary of δ phase of Np-Zr, which is also rather well measured in experiments and reproduced in our model for Np-Zr[35], shows smaller homogeneity range than δ phase of U-Zr, so δ Np-U-Zr is expected to have smaller content of U. On the other hand, those experimental points near the U end that likely correspond to α(U) have x(U) to be 0.1 or more larger than those predicted by the CALPHAD model. Again, that Zr only has very small solubility in α(U) (x(Zr) <0.02) has now been rather well accepted, as we reviewed in Ref.[33]. The two remaining experimental points at 793.15 K in the middle of the triangle do not have any single-phase region nearby from CALPHAD but they may represent β(Zr) and γ(Np) as seen at 868.15 K in Figure 7.3 b). In fact, at this slightly higher temperature, although still showing some scatter, most of the experimental data suggests δ and α(U) to have substantially increased and decreased content of *x*(U), respectively and the boundaries of the two phases are now quite close to CALPHAD. More encouraging are the two pairs of points in the middle of the triangle, which are very close to the β(Zr) and γ(Np) BCC phase boundaries. Considering experimental data at the two temperatures together, large changes in *x*(U) (>0.1) for α(U) and δ with only 75 K difference in temperature seem unusual, especially the widening with increasing temperature. It is possible that data at one temperature are biased, likely those at 793.15 K if we assume the CALPHAD model is reasonably accurate. Finally, going further up to 973.15 K, we cannot find a good match with the remaining three pairs of experimental two-phase points. However, it is rather clear in Figure 7.3 c) that near the U-Zr side, the two tie lines both essentially cross a single-phase point, which does not make physical sense. Altogether, the above analysis is in agreement with Rodríguez *et al.*'s comment[185] to their own data that due to the very small size of the phases identified, "the resulting microanalysis values are relatively inaccurate". We suggest that the data at 793.15 and 973.15 K need further verification, and those at 868.15 might be relatively reasonable. Finally, let us take a step back and assume that Rodríguez *et al.*'s data at 793.15 and 868.15 K do not have any issue (tie lines crossing single phase points at 973.15 K are issues beyond doubt), then our CALPHAD model predicts rather inaccurate α(U) and δ phase boundaries at 793.15 K, but seems to do a fair job predicting them at 868.15 K; our CALPHAD model also seems to predict the BCC phase boundary rather well, at least at 868.15 K. We believe this suggests that our model captures reasonably the phase stability of the high temperature phases of the Np-U-Zr system, although the uncertainty is larger for the low temperature part.

Table 7.2. Melting temperature at U-rich corner of Np-U-Zr compared with solidus and liquidus

temperatures predicted from CALPHAD in this work.

Sample[1]	x(Np)	x(U)	x(Zr)	Expt. (K) Melting T	CALPHAD (K) Solidus T	CALPHAD (K) Liquidus T
R1	0.30	0.30	0.40	1243	1257	1507
R2	0.11	0.67	0.22	1373	1436	1552
R3	0.05	0.70	0.25	1443	1505	1614
R4	0.05	0.80	0.15	1437	1447	1515
R5	0.15	0.55	0.30	1228	1429	1588
R6	0.20	0.70	0.10	1338	1328	1389
R7	0.30	0.45	0.25	1267	1278	1438
R9	0.16	0.60	0.24	1323	1400	1532
R10	0.08	0.69	0.23	1388	1467	1572
R11	0.10	0.80	0.10	1355	1390	1443

[1] Sample label and melting temperature from TABLE 3 of Rodriguez, *et al.*[185].

Rodríguez *et al*. [185] also measured the melting temperatures of the same samples above using dilatometer. However, the melting point for multicomponent alloy is not unambiguously defined—depending on the temperature change direction during dilatometer measurement, it usually refers to solidus temperature if heating and liquidus if cooling. Rodríguez *et al.*[185] did not make this distinction explicitly although they provided in Fig.2 of Ref.[185] a dilatometric heating curve between 793.15 and 973.15 K and commented in the conclusion section that the solidus temperatures of Np-U-Zr are close to linear interpolation of those of the binary systems, as we mentioned above, which both suggest that what they measured were solidus temperatures. This supposition is further supported by the fact that our CALPHAD predicted solidus temperatures are much closer than the liquidus to the melting temperatures that Rodríguez *et al.* reported in Ref.[185]. As Table 7.2 shows, except for sample R5, the differences in our model predicted solidus and Rodríguez *et al.*'s dilatometric melting temperatures differ only by

10 to 79 K with the average being 40 K, while the corresponding differences for liquidus temperatures are much larger, from 50 to 264 K with the average being 155 K. For sample R5, the solidus and liquidus temperatures differ from the dilatometric melting temperatures by 201 and 360 K, respectively. We think this sample may be affected by some unknown problem, because it is very close in compositions to other samples and it seems highly unlikely that the CALPHAD errors suddenly surge at this single point. Overall, if we assume what Rodríguez *et al.*[185] measured were indeed solidus temperatures and exclude sample R5, the agreement between our CALHPAD model and the experiment is again reasonably good.

7.4.2 *Ab initio* Method

In this section we use CALPHAD predicted enthalpy as reference in lieu of experimental thermochemical data to validate *ab initio* methods for the Np-U-Zr system. As supported by the comparisons to the experimental data of Rodríguez *et al.*[185] in last section, we assume our CALPHAD model for the Np-U-Zr system to be reasonably accurate for the BCC phase and take it as our best estimate as if it is exact to validate DFT and DFT + U at different U_{eff} parameters by comparing *ab initio* calculated enthalpy of mixing for the BCC phase with CALPHAD. We think such comparison is meaningful because errors in *ab initio* enthalpies were found to be much larger than the uncertainty in CALPHAD for example in the U-Zr[33, 34] and Np-Zr[35] binary systems for which our CALPHAD models should be sufficiently robust thanks to the many reliable experimental data available.

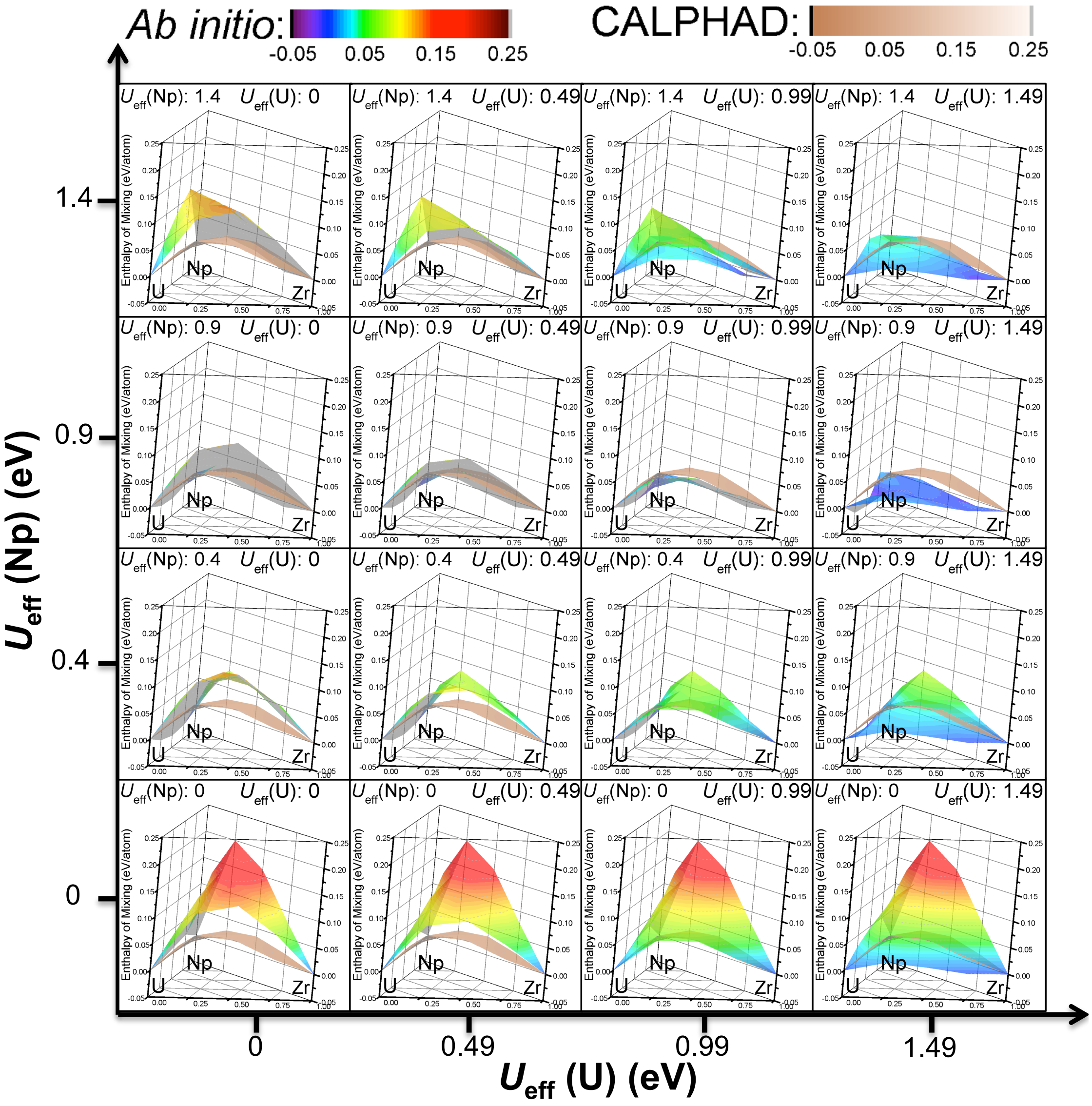

Figure 7.4. Enthalpy of mixing for BCC Np-U-Zr from CALPHAD (300 K) and *ab initio* (0 K) at different U_{eff}'s. DFT corresponds to the point at U_{eff}(Np)= U_{eff}(Np)=0 (bottom left), while DFT + U to all others.

The representative results are presented in Figure 7.4. Firstly, the enthalpy surface from DFT (bottom left) is significantly higher than the CALPHAD one, most evidently on the Np-Zr rich side. The highest point of DFT enthalpy surface is near the point of x(Np)=0.75 and x(U)=0, with a mixing enthalpy of 0.200 eV/atom (19.3 kJ/mole), while the corresponding CALPHAD value is 0.028 eV/atom (2.7 kJ/mole), about seven times smaller. The difference is smaller but still sizable on the U-Zr rich side, although relatively small on the Np-U side. Averaging over the 28 calculated compositions except for the three end points of BCC Np, U and Zr elemental metals, the root mean square (RMS) of the differences between DFT and CALPHAD enthalpy is 0.093 eV/atom (9.0 kJ/mole).

Now we look at DFT + U results. Navigating on the U_{eff} grid first in the bottom row of Figure 7.4. where U_{eff} (Np) is kept at 0 but U_{eff} (U) is varied from 0 to 1.49 eV, the *ab initio* enthalpy surface not surprisingly adjusts lower on the U rich side but remains largely unchanged in the Np-rich end. The reverse is true if we look at the first column where U_{eff} (U) is kept at 0 but U_{eff} (Np) is varied from 0 to 1.4 eV. If we go along the diagonal, not surprisingly enthalpy drops on both the Np and the U sides. Overall, it seems that *ab initio* enthalpy becomes lower when both or either of U_{eff}(Np) and U_{eff}(Np) increase from 0 (i.e., only the standard DFT is applied) to nonzero values. However, when U_{eff}(Np) and U_{eff}(U) are too large (e.g., larger than 0.9 eV for the former and 1.24 for the later), *ab iniito* enthalpy either continues to reduce and becomes overly small or bounce back and become larger compared to CALPHAD. Moreover, near the Np-U side, the DFT enthalpy is already reasonably close to CALPHAD's. However, the change in enthalpy there is also quite small even when largely different U_{eff}(Np) and U_{eff}(U) are used in DFT + U. Most encouragingly, when U_{eff}(Np) and/or U_{eff}(U) values are individually optimized to match CALPHAD for Np-Zr and/or U-Zr, enthalpy does not become worse near the Np-U side, but instead is still in general improved, although by smaller extent as the concentration of Zr decreases. Therefore, a consistent set of U_{eff} seems to apply to the BCC Np-U-Zr phase in the whole composition space.

Table 7.3. Root mean square (RMS) of the differences in enthalpy of mixing for BCC Np-U-Zr

between CALPHAD (300 K) and *ab initio* (0 K) at different U_{eff}'s averaged over compositions illustrated in Figure 7.2. DFT corresponds to the point at U_{eff}(Np)= U_{eff}(Np)=0 (bottom left), while DFT + U to all others. The units of enthalpy and U_{eff} are eV/atom and eV, respectively.

U_{eff} (Np) U_{eff} (U)	0	0.15	0.4	0.65	0.9	1.15	1.4
1.49	0.073		0.025		0.036		0.024
1.24				0.016		0.018	
0.99	0.077		0.020	0.009	0.017		0.029
0.74				0.014			
0.49	0.085		0.032		0.019		0.047
0.24		0.065					
0	0.093		0.044		0.032		0.064

A natural question to ask is then at what values of U_{eff} (Np) and U_{eff} (U) are enthalpies from CALPHAD and *ab initio* closest? This question is answered in Figure 7.5, which presents RMS of the differences between the two enthalpies at the U_{eff} grid we have illustrated in Figure 7.2. These actual *ab initio* data along with spline interpolated values at U_{eff} values not calculated are visualized in Figure 7.5 as a three-dimensional (3D) surface of the RMS of differences plotted as a function of (U_{eff} (Np), U_{eff} (U)). It is clear from Figure 7.5 that a minimum exists at (U_{eff} (Np), U_{eff} (U)) ≈ (0.65, 0.99) eV, at which values the RMS of the differences in *ab initio* and CALPHAD enthalpy is 0.009 eV/atom (0.9 kJ/mole). Moreover, when U_{eff} for Np and U vary in the range of 0.65-0.9 and 1-1.5 eV, respectively, which are the empirical U_{eff} parameter ranges determined individually in binary systems of U-Zr [34]and Np-Zr[35] containing only one actinide element, the average RMS difference is only slightly higher, at 0.036 eV/atom (3.5 kJ/mole) or less, as given in Table 7.3. It should be noted that the same ranges of U_{eff} have been individually determined in our previous studies of U-Zr[34] and Np-Zr[34], in which not only BCC but also all other stable solid phases at ambient conditions were examined.

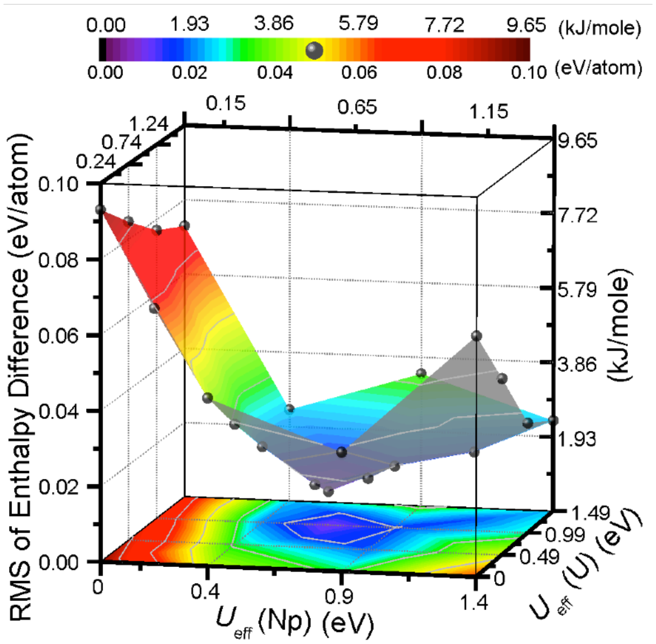

Figure 7.5. Root mean square (RMS) of the differences in enthalpy of mixing for BCC Np-U-Zr between CALPHAD (300 K) and *ab initio* (0 K) at different U_{eff}'s. DFT corresponds to the point at U_{eff}(Np)= U_{eff}(Np)=0 (bottom left), while DFT + U to all others. *Ab initio* calculated values are marked black balls and the remaining in the surface are their spline interpolations. The bottom plane is projection of the 3D surface.

Our finding that the same small ranges of U_{eff} for Np and U can help improve the calculated enthalpy for Np and U based metallic actinide systems of different systems (e.g., the unary/binary/ternary; containing one or two actinides), compositions (e.g., across the whole BCC ternary in this study), and crystal structure (different solid phases) suggests that U_{eff} should be predominately determined by the species and has reasonable transferability to different chemical and structural environments. This result implies that consistent or similar U_{eff} determined in some benchmark systems may be applied to model alternative systems of different structure and composition, so long as the main chemical bonding characteristic remain similar to the validated systems. For example, we expect the U_{eff} we determined for Np and U to be of value for modeling other metallic alloys of Np and U, and we encourage future study to test this assertion.

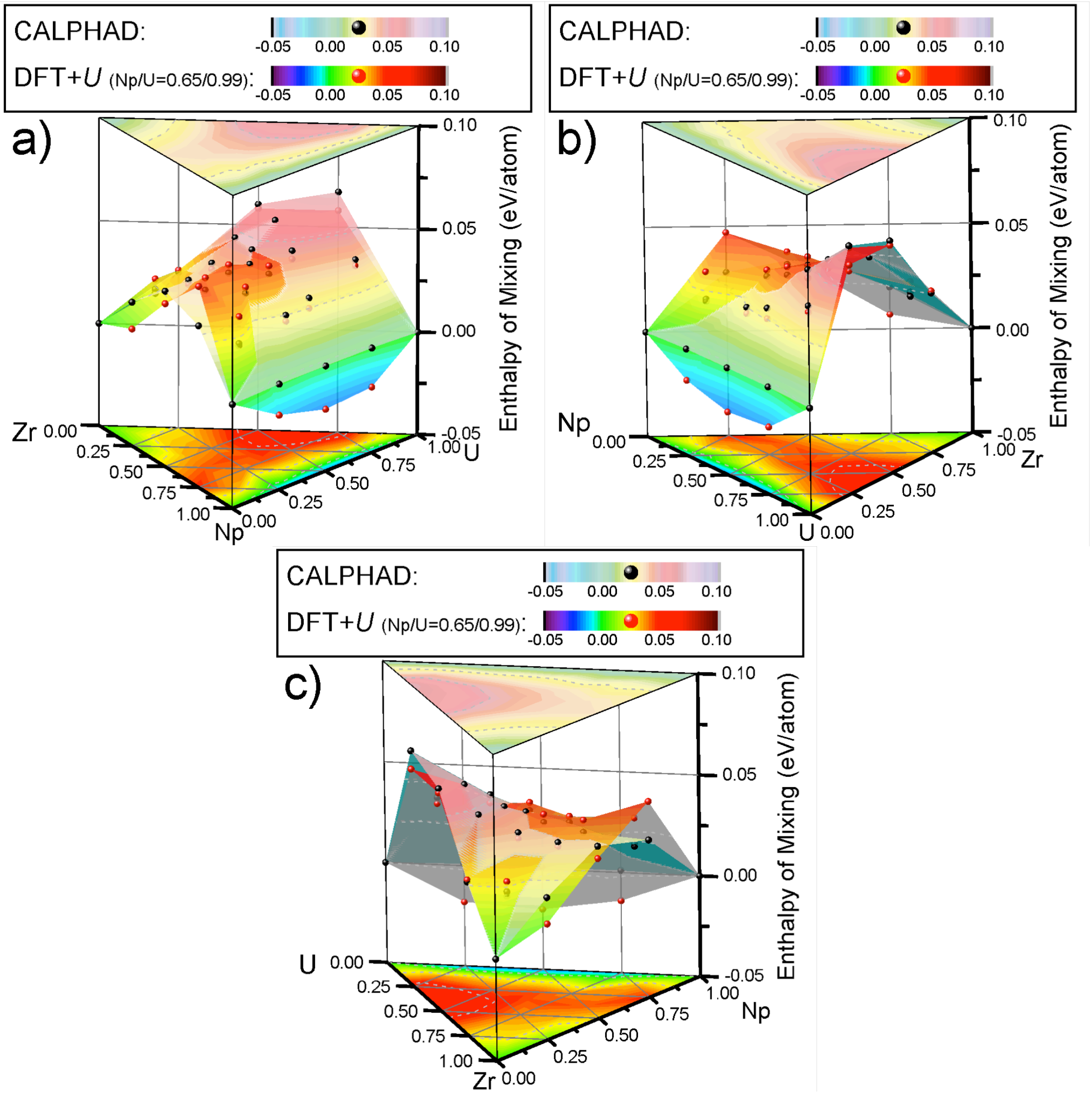

Figure 7.6. Enthalpy of mixing for BCC Np-U-Zr from CALPHAD and DFT + U at (U_{eff}(Np), U_{eff}(U))=(0.6, 0.99) eV viewed from a) Np-, b) U-, and c) Zr-rich corner. The front of CALPHAD and DFT + U surface is filled by the color palette given in the legend, while the back of them is filled by dark cyan and gray, respectively. The top and bottom plane are projections of the CALPHAD and DFT + U 3D surface, respectively. See Figure 7.4 for the result from DFT.

7.5 Model Predictions

This section presents and discusses some predictions for the Np-U-Zr system from both CALPHAD and *ab initio* modeling. All DFT + U results are calculated at the validated (U_{eff}(Np), U_{eff}(U)) values of (0.65, 0.99) eV. DFT results are also given as reference.

7.5.1 BCC Np-U-Zr solution behavior

We briefly discussed enthalpy of mixing for the BCC phase in Figure 7.4 above. The focus then was on how *ab initio* enthalpies change and compare with CALPHAD at different U_{eff}'s. Now let us take a close look in Figure 7.6 at the data calculated at (U_{eff}(Np), U_{eff}(U)) = (0.65, 0.99) eV. Viewing from all of the three Np-, U- and Zr-rich corners, it is not surprising that the DFT + U enthalpy surface is always very close to that of CALPHAD. Quantitatively, the magnitude of the overall mixing enthalpy of BCC Np-U-Zr is not very large—the maximum and average values of the *ab initio* calculated compositions are 0.058 and 0.029 eV/atom, respectively. The DFT + U enthalpies are even slightly negative at x(Zr)=0 for Np-U, with minimum being -0.020 eV/atom (see the red balls at the bottom of the cyan area in Figure 7.6 a) and b)), although the corresponding CALPHAD value is 0. Negative values are, however, fully consistent with the known phase stability and thermodynamics in this system, as discussed in Ref.[212]. In general, we note the following trends. The enthalpy is very small (<0.02 eV/atom) when Zr content is either high (x(Zr)>0.75) or very low (x(Zr)<0.1), which manifests in the enthalpy projection on the bottom plane as green area near the Zr end and the Np-U side; in the middle, however, the enthalpy increases to larger than 0.05 eV/atom and the projection there shows a large red area. Figure 7.6 c) also clearly shows that in the middle region, the enthalpy is smaller when Np and U concentration is about the same. In fact, a saddle point seems to exist for the overall enthalpy surface near x(Np)= x(U)=0.375 and *x*(Zr)= 0.25.

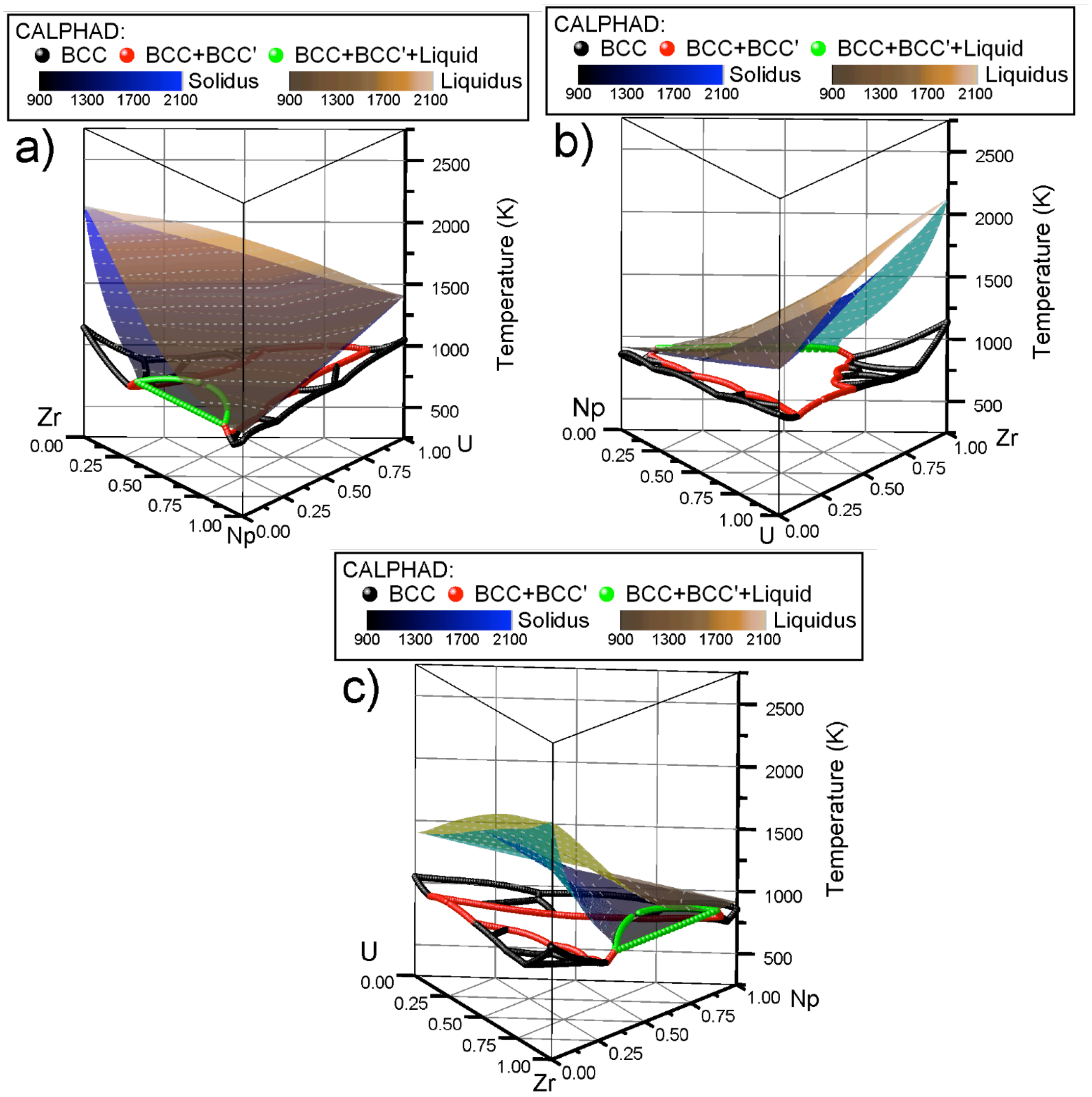

Figure 7.7. Phase diagram of Np-U-Zr showing only BCC and Liquid phases viewed from a) Np-, b) U-, and c) Zr-rich corner. The surface outlined by red, black and the inner curled piece of green curves is the lower while the surface of Solidus is the upper boundary of BCC single-phase region. The surface outlined by red and green curves is the upper boundary of BCC+BCC' two phase (i.e., miscibility gap) region. Green curves outline the interface shared between solidus and BCC+BCC' miscibility gap. The front of solidus and liquidus surface is filled the color palette given in the legend, while the back of them is filled by dark cyan and dark yellow, respectively.

What phase diagram of Np-U-Zr will result from such mixing enthalpies? This question is answered in Figure 7.7 showing the stable phase boundaries of the BCC and liquid phases. The phase space is divided by three surfaces: liquidus, solidus and the BCC lower boundary. The first two are plotted in Figure 7.7 as color filled 3D surfaces, but the BCC lower boundary is outlined by curves made of color balls—specifically, the red, black and the inner curled piece of green curves. Obviously, above liquidus is the liquid phase; between liquidus and solidus is the two-phase mixture of BCC and liquid; and above the BCC lower boundary and below the solidus is the BCC single phase. Below the BCC lower boundary are various phases that are equilibrating with BCC, in particular the BCC+ BCC' miscibility gap, the top boundary of which is outlined in Figure 7.7 by red and green curves. Figure 7.7 shows that 1) BCC+ BCC' miscibility gap does not show up when Zr content is either high or very low (i.e., near either the Zr end or the Np-U side); 2) the majority of the BCC+BCC' miscibility gap dissolves into a single BCC phase when temperature rises, however, a part of it near the Np-Zr side never becomes single BCC phase but melts into liquid directly from BCC+BCC', which is why an interface between solidus and BCC+BCC' miscibility gap curves exists. Such an interface is outlined by the two green curves.

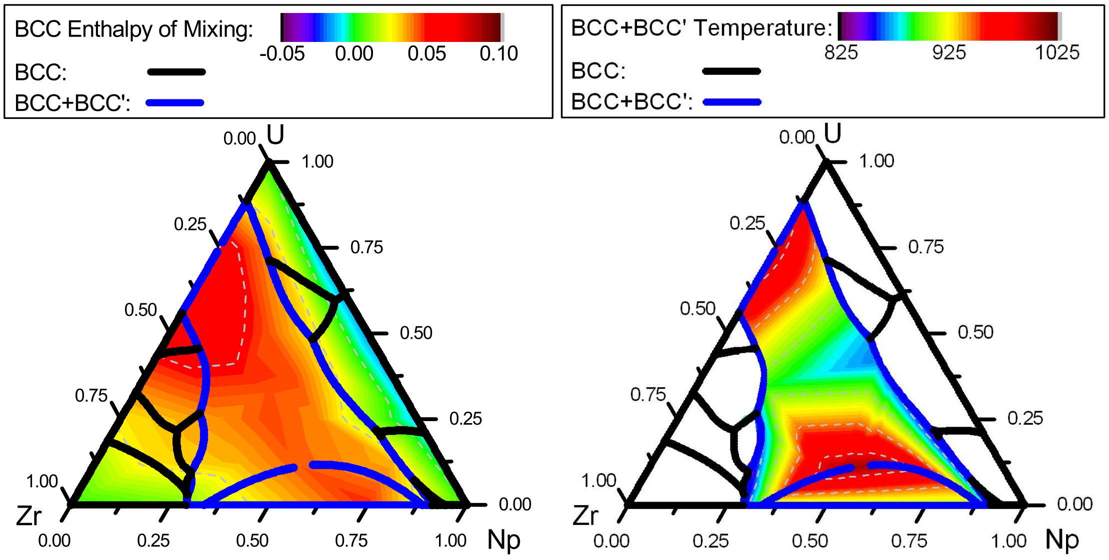

Figure 7.8. Projections of BCC Np-U-Zr's stable phase boundary from CALPHAD compared to enthalpy of mixing from DFT + *U* at (U_{eff}(Np), U_{eff}(U))=(0.6, 0.99) eV on the left and miscibility gap temperature from CALPHAD on the right. The units for enthalpy and temperature are

eV/atom and K, respectively.

The solution behavior of BCC Np-U-Zr can be explained well from the enthalpy of mixing predicted by DFT + *U* at (U_{eff}(Np), U_{eff}(U))=(0.6, 0.99) eV, which we show in Figure 7.8. On the left, the color contour of the enthalpy of mixing shows that BCC+BCC' exists only where the mixing enthalpy is high (red region), which is totally expected, because when it takes more energy to mix, the alloy would prefer to stay phase separated. The opposite is not true, however. Approximately between x(Zr)= 0.44 and 0.82 on the U-Zr side, some area is also high (red) in BCC mixing enthalpy, but does not show any miscibility gap. That is because the alloy is less stable there in BCC+BCC' phase than the competing phases—we see multiple phase boundaries corresponding to the competing phases in that region. Another aspect of the BCC miscibility gap can also be explained by the mixing enthalpy. On the right of Figure 7.8, we show the temperature of BCC+BCC' miscibility gap upper boundary (i.e, where BCC+BCC' completely dissolves into single BCC, or, in the small area at the bottom, starts to melt). Such transition is expected to be due to entropy counterbalancing the positive mixing enthalpy and thus the higher the enthalpy, the higher the transition temperature. We see that the temperature is higher (red) on the two ends than in the middle, which is in excellent agreement with the existence of a saddle point in the mixing enthalpy near the middle, as we discussed above. Finally, one may notice that our calculated enthalpy is slightly higher on the U-Zr side than the Np-Zr side (difference <0.02 eV/atom) which if true means higher miscibility gap temperature range. However, the difference of 0.02 eV/atom is almost certainly within the error bar of our model and we cannot tell if the difference is real besides calling the two enthalpies as very close.

Overall, this section predicts and explains the following three aspects of the solution behavior of BCC Np-U-Zr: 1) The Np-U rich side does not show stable BCC+BCC' miscibility gap, because the mixing enthalpy is very small, possibly even slightly negative. 2) The Np-Zr rich side does not show stable single BCC phase because the melting temperature of Np is too low so that the BCC+BCC' miscibility gap cannot wait for the entropy effects to counterbalance the positive mixing enthalpy before melting. 3) The U-Zr rich side has similar positive mixing enthalpy as Np-Zr, and the melting temperature of U is higher, so the BCC+BCC' miscibility gap shows up first but dissolves into a single BCC phase that is stable above about 1000 K until the solidus temperature, which we discuss in the next section. We leave it for further study to explain the electronic structure origin of the relative magnitude of the mixing enthalpy of BCC Np-U-Zr.

7.5.2 BCC Np-U-Zr atomic volume and volume of mixing

Figure 7.9 presents atomic volume and volume of mixing for BCC Np-U-Zr calculated both by DFT and DFT + U at (U_{eff}(Np), U_{eff}(U)) = (0.65, 0.99) eV. The numerical values of atomic volume are also tabulated in Table 7.4. Let us first look at atomic volume on the left of Figure 7.9. We find that Zr has the largest atomic volume (22.92 Å^3/atom), followed by U, which is 20.13 and 20.98 from DFT and DFT + U, respectively, while Np is smallest—17.60 and 19.46 Å^3/atom from DFT and DFT + U, respectively. It seems that DFT predicts that atomic volumes of BCC Np, U and Zr differ significantly—relative to that of Np, the difference between Np and Zr is astonishingly 31%, while even between Np and U, the difference is larger than 14%. DFT + U brings the two figures to around 18% and 8%, respectively. The trend in relative atomic volume difference is in good correspondence with the qualitative trend of the mixing enthalpy discussed above, with that from DFT to be considerably larger than DFT + *U* because DFT predicts much larger differences in atomic volume among the three BCC metals. Furthermore, going from the Zr end to the Np-U side, atomic volume reduces only slightly if *x*(Zr) remains larger than about 0.5, which manifests in the projections as a large triangle of pink on the top and red at the bottom for DFT and DFT + *U*, respectively. The Np-Zr side seems to have similar (from DFT) or even somewhat larger (from DFT + *U*) atomic volume than the U-Zr side in this region, even though elemental BCC U has larger atomic volume than BCC Np. After *x*(Zr) becomes smaller, atomic volume starts to reduce steeply. For example, projection at the bottom changes color in the order of light red, yellow, green and cyan with decreasing Zr concentration. The DFT projection on the top shows similar changes.

Table 7.4. Atomic volume of BCC Np-U-Zr from DFT and DFT + U at (U_{eff}(Np), U_{eff}(U))=(0.6, 0.99) eV (unit: eV/atom). The same values are given multiple times where the isopleth paths cross.

Isopleth path	x(Np)	x(U)	x(Zr)	DFT	DFT + U
$Np_x(U_{0.5}Zr_{0.5})_{1-x}$	0.000	0.500	0.500	21.97	22.53
	0.250	0.375	0.375	21.74	22.52
	0.333	0.333	0.333	21.53	22.43
	0.500	0.250	0.250	20.98	22.32
	0.750	0.125	0.125	19.53	21.74
	1.000	0.000	0.000	17.60	19.46
$Np_{0.5}U_{0.5-x}Zr_x$	0.500	0.500	0.000	19.47	20.49
	0.500	0.375	0.125	20.13	21.56
	0.500	0.250	0.250	20.98	22.32
	0.500	0.125	0.375	21.84	22.94
	0.500	0.000	0.500	22.49	23.26
$Np_{0.75}U_{0.25-x}Zr_x$	0.750	0.250	0.000	18.33	20.30
	0.750	0.125	0.125	19.53	21.74
	0.750	0.000	0.250	20.90	23.14
$U_x(Np_{0.5}Zr_{0.5})_{1-x}$	0.500	0.000	0.500	22.49	23.26
	0.375	0.250	0.375	21.80	22.69
	0.333	0.333	0.333	21.53	22.43
	0.250	0.500	0.250	21.06	22.04
	0.125	0.750	0.125	20.50	21.41
	0.000	1.000	0.000	20.13	20.81
$U_{0.5}Zr_{0.5-x}Np_x$	0.000	0.500	0.500	21.97	22.53
	0.125	0.500	0.375	21.68	22.43
	0.250	0.500	0.250	21.06	22.04
	0.375	0.500	0.125	20.28	21.51
	0.500	0.500	0.000	19.47	20.49
$U_{0.75}Zr_{0.25-x}Np_x$	0.000	0.750	0.250	21.10	21.84
	0.125	0.750	0.125	20.50	21.41
	0.250	0.750	0.000	19.76	20.68
$Zr_x(Np_{0.5}U_{0.5})_{1-x}$	0.500	0.500	0.000	19.47	20.49
	0.375	0.375	0.250	21.05	22.14
	0.333	0.333	0.333	21.53	22.43
	0.250	0.250	0.500	22.17	22.81
	0.125	0.125	0.750	22.63	22.87
	0.000	0.000	1.000	22.92	22.92
$Zr_{0.5}Np_{0.5-x}U_x$	0.500	0.000	0.500	22.49	23.26
	0.375	0.125	0.500	22.34	23.01
	0.250	0.250	0.500	22.17	22.81
	0.125	0.375	0.500	22.14	22.70
	0.000	0.500	0.500	21.97	22.53
$Zr_{0.75}Np_{0.25-x}U_x$	0.250	0.000	0.750	22.80	23.09
	0.125	0.125	0.750	22.63	22.87
	0.000	0.250	0.750	22.43	22.80

In terms of volume of mixing given on the right of Figure 7.9, DFT and DFT + U results are very similar in terms of qualitative features, both showing a maximum on the Np-Zr side near x(Zr) between 0.25 and 0.5 (red areas on the projection planes). The quantitative differences between the DFT and DFT + *U* surfaces are largest on the Np-Zr side, following by that on the U-Zr side, while smallest on the Np-U side. This trend is in agreement with the relative differences in the mixing enthalpy between DFT and DFT + *U*. Also, both the U-Zr and the Np-Zr side show a maximum near x(Zr)=0.25, in excellent agreement with the trend in mixing enthalpy from DFT + *U* shown in Figure 7.6 c). The volume of mixing both from DFT and DFT + *U* however shows the Np-Zr side to be considerably larger than the U-Zr side, while in terms of enthalpy of mixing, DFT, as shown in the bottom left panel of Figure 7.4 predicts the same relative order as volume of mixing, but DFT + *U* shows the opposite relative order—the DFT + *U* mixing enthalpy is slightly higher on the U-Zr side in Figure 7.6We think the fact that DFT + *U* shows different relative magnitudes between volume and enthalpy of mixing for the Np-Zr and the U-Zr side while DFT does not is possibly because that DFT + *U* captures some electronic structure effects so the enthalpy is no longer mainly affected by size effects as characterized by atomic volume. We leave it for future study to analyze the details of the bonding characteristics and electronic structure to test this hypothesis.

7.5.3 Solidus and liquidus of Np-U-Zr

The solidus and liquidus temperatures of Np-U-Zr predicted by our CALHAD model are plotted in Figure 7.7. The liquidus temperature is very close to those expected from linear interpolations of the melting points of elemental Np, U and Zr metals, which we have also seen in Table 7.2. The solidus temperature surface is very close to the liquidus on the Np-U side, as is evident in Figure 7.7 a), only slightly lower on the U-Zr side seen in Figure 7.7 b), but is significantly smaller on the Np-Zr side. As shown in Figure 7.7 c), in the whole region marked with green (i.e., the interface between solidus and BCC+BCC' miscibility gap), the solidus temperature stays essentially unchanged when *x*(Zr) increases from about 0.1 to 0.65. Even after *x*(Zr)>0.65, there is still a large difference between the liquidus and solidus. The situation is largely alleviated if content of U is increased, for example when *x*(U)>0.5, which is expected to be the case for most metallic fuels.

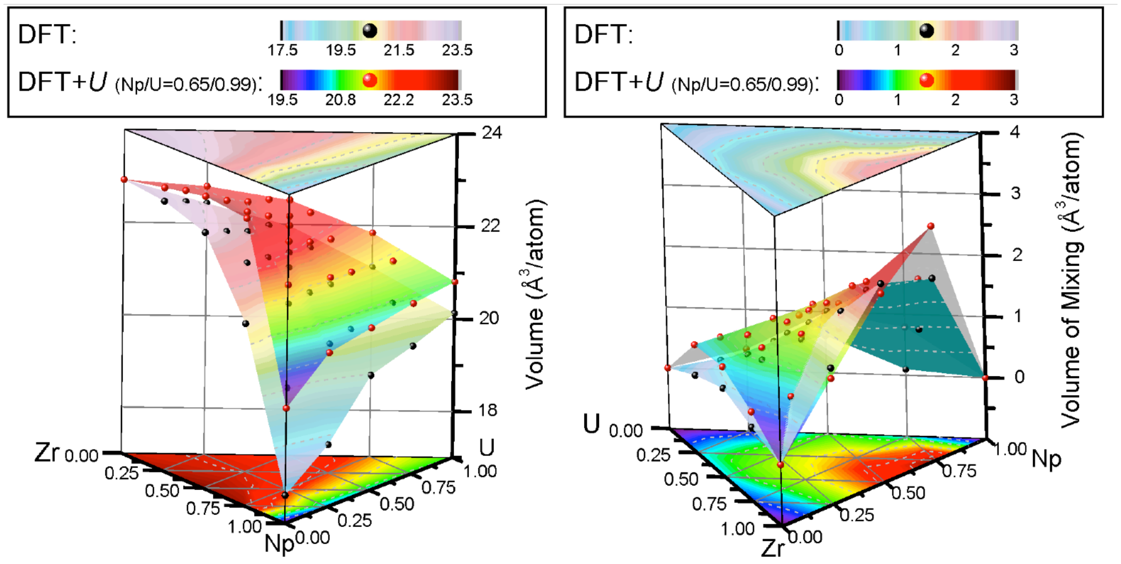

Figure 7.9. Atomic volume and volume of mixing for BCC Np-U-Zr from DFT and DFT + *U* at (U_{eff}(Np), U_{eff}(U))=(0.6, 0.99) eV. The front of DFT and DFT + *U* surface is filled by the color palette given in the legend, while the back of them is filled by dark cyan and gray, respectively. The top and bottom flat surfaces are projections of the DFT and DFT + *U* 3D surfaces, respectively.

7.6 Conclusions

A CALPHAD model for the Np-U-Zr system is developed based on Muggianu extrapolation of our previous models for the constituent binary systems. Comparing the model predicted isothermal sections and liquidus temperatures with available experimental data suggests that our model has reasonably characterized the high temperature phase diagram of the Np-U-Zr system, but faces much certainty for the low temperature part, in particular on the compound phases like δ and ζ, which require further experimental work.

Ab initio calculations are performed at 28 compositions of BCC Np-U-Zr with both DFT and DFT + U, both based on GGA-PBE. For BCC Np-U-Zr, DFT is found to on average overestimate the enthalpy of mixing by 0.093 eV/atom (9.0 kJ/mole). DFT + U predicts lower values than DFT, which are on average 0.009 to 0.036 eV/atom (0.9 to 3.5 kJ/mole) different from those by CALPHAD when U_{eff} for Np and U vary in the range of 0.65-0.9 and 1-1.5 eV, respectively, which are the same small ranges of U_{eff} we previously validated individually in the Np-Zr and U-Zr systems that contain only one actinide element. At (U_{eff}(Np,), U_{eff}(U))=(0.65, 0.99) eV, DFT + U seems to consistently improve the enthalpy in the whole composition space of the BCC Np-U-Zr phase, resulting a minimal average difference from CALPHAD, 0.009 eV/atom (0.9 kJ/mole). Therefore, U_{eff} is expected to be predominately determined by nature of the element and chemical bonding, while crystal structure and composition should play secondary roles. As a result, similar U_{eff} (Np) and U_{eff} (U) parameter as we determined may be applicable for modeling other Np and/or U based metallic alloys with different structure and composition, of which we again call for further testing.

Our model predicts enthalpy of mixing for BCC Np-U-Zr to be very small both near the Np-U side and at the Zr-rich end. In the intermediate region, mixing enthalpy is relatively lower when x(Np) and x(U) are about equal and a saddle point near x(Np)=x(U)=0.375 and x(Zr)=0.25 exists for the mixing enthalpy surface. The composition regions with higher mixing enthalpy is in excellent agreement with the projected composition range of the BCC+BCC' miscibility gap, and even the magnitude of the mixing enthalpy shows good qualitative correspondence with the miscibility gap dissolution temperature. Near the Np-Zr side, the miscibility gap does not turn into single BCC but instead melts directly when temperature increases due to the low melting point of Np, while near the Np-U side miscibility gap does not emerge due to the small mixing enthalpy. Atomic volume for BCC Np-U-Zr is highest near the Zr end, then U and smallest near the Np end. DFT + *U* predicts larger atomic volume than DFT for Np and U, bringing them closer to that of Zr and the relative change between DFT and DFT + *U* predicted atomic volume is larger for Np than U. Volume of mixing for BCC Np-U-Zr results show consistent picture as enthalpy of mixing. Liquidus of the Np-U-Zr system is close to linear interpolation of the melting points of the elemental metals, and solidus are very close to the liquidus near the Np-U side, slightly lower near the U-Zr side, and significantly smaller near the Np-Zr side. A large BCC+liquid two-phase region exists near the Zr end of the Np-Zr side.

8 Concluding Remarks

8.1 Summary

We addressed two problems in this thesis: 1) the lack of quantitative and accurate thermodynamic models and 2) the problem of obtaining accurate *ab initio* energetics for the *f* electron containing metallic fuel systems of Np-U-Zr. To address the first challenge, our work developed thermodynamic models for the U-Zr and Np-Zr systems that we have shown to be of good accuracy. For the Np-U and Np-U-Zr systems, we developed models that were limited by the very scarce experimental data on these systems but should also be accurate at the high temperatures at which metallic fuels are deployed in reactors. We also showed that the *ab initio* enhanced CALPHAD modeling approach is a promising route for future studies aiming at further improvement at low temperature.

To address the second challenge, we established an *ab initio* method based on DFT + U and a set of empirical U_{eff} ranges for Np and U. In Chapter 3 we showed that for the U-Zr binary system, compared to two previous CALHPAD models [11, 40] and also the one developed in this work, DFT-GGA's average errors in enthalpy characterized by the RMS of differences in enthalpy from CALPHAD were about 0.10 and 0.07 eV/atom without and with SOC included in the calculations, respectively. Such errors were assessed on the low and intermediate temperature phases (not including the more controversial BCC γ(U,Zr) phase) for which the three CALHPAD models predict very similar enthalpies. DFT + U was found to reduce the errors when U_{eff}(U) of 1-1.5 eV was used and the smallest average errors of about 0.04 and 0.02 eV/atom were obtained at U_{eff}(U)=1.24 eV when the calculations were without and with SOC included, respectively. Similarly, for the Np-Zr binary system, in Chapter 5 we showed that DFT-

GGA's average errors in enthalpy were about 0.17 and 0.15 eV/atom without and without SOC included, respectively. Such errors were assessed on phases excluding BCC γ(Np,Zr) and C32 δ(Np,Zr) for which available CALPHAD models should be robust. Again both the CALPHAD model of Ref.[182] and the one developed in this work were used as references. DFT + *U* was found to reduce the errors in enthalpy by about 0.07 to 0.12 eV using U_{eff}(Np) of 0.65 to 0.9 eV. We then showed in Chapter 6 that this same set of U_{eff}(Np) and U_{eff}(U) could yield enthalpies for the Np-U system that were more accurate or on par with DFT. For example, for ζ phase DFT predicted very high enthalpy of formation (0.1-0.27 eV/atom depending on composition) unusual for a compound phase stable at room temperature, while DFT + *U* using (U_{eff}(Np), U_{eff}(U)) = (0.65, 1.24) eV again predicted enthalpies that were smaller by about 0.10 eV/atom on average than DFT, which are expected to be more reasonable. Finally, in Chapter 7, we showed that for the BCC phase of Np-U-Zr, DFT overestimated the enthalpy of mixing predicted by the CALPHAD model of this work by 0.093 eV/atom, which is calculated without SOC at 28 compositions distributed evenly on the whole ternary space. DFT + *U* reduced the error to 0.009-0.036 eV/atom using U_{eff}(Np) and U_{eff}(U) in the ranges of 0.65-0.9 and 1-1.5 eV, respectively, which were the same ranges of empirical U_{eff} we determined individually for Np and U in the U-Zr and Np-Zr systems that contain only one actinide component. These results collectively suggest that DFT + *U* can improve the accuracy of calculated enthalpy for Np-U-Zr using a consistent set of U_{eff} parameter's for Np and U that are transferable between the unary, binary and ternary systems. Such transferability further suggests that U_{eff} should be predominately determined by the nature of the element and chemical bonding, with crystal structure and composition playing only secondary roles. We therefore expect that comparable ranges of U_{eff} determined in this study may be applicable in the modeling of other similar metallic fuel systems containing Np and U to predict more accurate energetics.

Overall, work in this thesis increases the understanding of the phase stability, thermodynamic properties, and correlation and relativistic effects for minor actinide-containing metallic nuclear fuels. Practically, these understandings can guide better design and use of existing metallic nuclear fuels. Moreover, the *ab initio* methods and CALPHAD models established in this thesis are expected to be applicable for studying additional properties and other related systems of metallic nuclear fuels and thus are of academic value. This thesis also demonstrated that the *ab initio* enhanced CALPHAD modeling approach could be an effective tool to probe phase stability and thermodynamic properties of multicomponent alloys even when they contain constituents as challenging to study as actinides.

8.2 Suggestions for Future Work

In the future, several research areas can be built on the development of this thesis.

1). ***Ab initio* enhanced CALPHAD modeling of Pu and heavier actinide containing alloy systems**. A number of Pu containing systems already have many experimental data and some thermodynamic models available, while Am and Cm containing systems remain much less studied. Due to time and resource limit, we only finished some preliminary *ab initio* studies of Pu containing systems in early stage of the thesis research. Nevertheless, we demonstrated the effectiveness of *ab initio* enhanced CALPHAD modeling approach in our study of Np-U-Zr and expect that this approach could possibly be extended to these new systems. In the future, if further understanding is obtained from these additional actinide materials, a multicomponent thermodynamic model can be formulated for the full U-Pu-Zr-MA alloys, which can provide important insights for the design and optimization of metallic fuels.

Similarly, we have also only focused on Zr as the transition metal components in this thesis. Recently, Mo based metallic fuels have been suggested to have lower constitution migration, better fuel-cladding resistance and higher thermo conductivity than the Zr fuels[214]. More researches would be needed to better understand the mechanisms of such improvements.

2) ***Ab initio* predictions of crystal structure of intermediate compound phases of Np-U-Zr**. As we reviewed in Chapter 1, θ phase of the Np-Zr system has unknown Wyckoff site positions and occupations although its space group has been determined. Future work can perform *ab initio* search of Wyckoff site positions with, for example, some evolutionary algorithms[215]. Such a search may not be very fruitful with the standard DFT because the relative energetic differences between competing structures may be too small compared to the accuracy that DFT can attain. We hope that DFT + U could provide some improvement with the empirical U_{eff} ranges we determined, so that it becomes possible to identify some promising candidates, if complete determination is still not possible. After that, we can further perform *ab initio* predictions of the site occupations for θ Np-Zr, similar to what we did for ζ Np-U in Chapter 5. These *ab initio* predictions could help guide more accurate thermodynamic modeling of the lower temperature part of the corresponding alloy systems where the intermediate phases are stable, which are often challenging to study experimentally due to issues like metastable competing phases that need very long annealing time to avoid. Moreover, such studies

are potentially useful to help understand the bonding characteristics of actinide intermetallic compounds, which often have complex crystal structures due to *f* electron bonding.

3) **Thermodynamic modeling of additional materials containing Np-U-Zr**, for example mixed oxide (MOX) nuclear fuel containing mixtures of U, Np and Pu oxides. In particular, we expect that our CALPHAD models for the U-Zr and Np-Zr systems to of good accuracy and can be used as starting points for thermodynamic modeling of other systems containing them.

4) **Finite temperature *ab initio* modeling of metallic nuclear fuels**. The *ab initio* calculations in this thesis did not consider finite temperature effects like lattice vibrations and electronic entropies. Metallic fuels are used at finite operating temperatures at which the stable phase is often the BCC solution phase. In fact, BCC phases of many actinides have been found to be to be mechanically unstable at low temperature[97], which was why in this thesis we only performed volume relaxation for them. Now that we have established an effective *ab initio* approach at 0 K and determined its error range, we can build on this foundation to include the finite temperature effects of phonon contribution and electronic entropy. In this way, predictions on properties like Gibbs free energy and thermal conductivity at finite temperature—for example at the desired reactor operating temperatures—can be made.

5) **Dynamical many-body theory based *ab initio* modeling of metallic nuclear fuels**. This thesis only used static mean-field many body theory of DFT and DFT + *U*. This choice was an approximation we made because we were dealing with a large number of systems and phases at multiple compositions. With the advance in both

theoretical methodology and computing power, we envision that dynamical many-body approaches like *GW*[216] and dynamical mean field theory (DMFT)[159] will become practice for *ab initio* study of practical systems of metallic nuclear fuels. As we discussed in in Chapter 3, we expect these advanced approaches to be able to properly address the concerns people currently have on static mean fuel theory of DFT + *U* like the magnetic moments that are predicted for U and Np containing systems. We also expect including dynamic correlation effects can help improve the accuracy of the calculated energetics. Results from this study can contribute towards such endeavors. For example, we determined theoretically the Hubbard *U* for the solid phases of U and U-Zr in Chapter 2, which could be used in DMFT studies of these materials. The one-particle static real band energy from this work can also be used as starting point for calculating the many-particle dynamic complex self-energy.

6) **Multi-scale modeling of metallic fuels.** This thesis only worked at the electronic and the macroscopic scale in *ab initio* and CALPHAD modeling, respectively. In fact, modeling at the scales intermediate between them can be pursued with the help of our work. At the atomic scale, *ab initio* results can be used as the input parameters for example in atomistic simulations using the Bozzolo– Ferrante–Smith (BFS) method[217], as has been applied to study the interaction of U-Zr fuel with cladding elements of Fe, Ni and Cr[218]. Similarly, our *ab initio* results can also guide the development of empirical potentials for Np-U-Zr and its subsystems. Beeler *et al.*[219] and Moore *et al.*[220] developed semi-empirical Modified Embedded Atom Method (MEAM) potential for U and U-Zr, respectively based on *ab initio* results from standard DFT. Our *ab initio* results can be used in similar ways to develop MEAM potentials for Np-U-Zr and all of its

subsystems, where we would expect the improvement offered by DFT + U may help increase the accuracy of the developed potentials. Development of such atomic scale potentials may enable predictions of properties that are difficult to model by electronic scale *ab initio* calculations, for example, the melting point of the fuels—a property that is very important but for many systems and at many compositions is still not known. In addition, at the mesoscale, phase-field modeling can benefit from the thermodynamic models and phase diagrams we developed, and modeling at this scale is well suited to study the constituent redistribution phenomenon from which metallic fuels notoriously suffer, as exemplified in Ref.[221].

9 Appendix: Supplementary Material for Chapter 3

To best validate *ab initio* approaches in terms of calculated volume, we need to use the most accurate and appropriate experimental volume data. We face two issues here. Firstly, many experimental structural data for U metal exist. Donohue[222] compiled a review of the structural data for U metal in 1974. However, only after significant advancement in analytical instrument and sample preparation technique was the structure of βU first determined in 1988[80]. We need to review existing experimental data taking into consideration of such new development. Secondly, all experimental data are measured at finite *T*. However, our current *ab initio* calculations do not include the zero-point and any finite *T* effects. To validate our calculations, we use the so-called Debye-Grüneisen quasi-harmonic model[143] to estimate these effects and correct the experimental data to 0 K.

This supplementary material contains three sections. Section 9.1 details our evaluation of experimental structural data for U metal. Section 9.2 gives the results for Debye-Grüneisen quasi-harmonic modeling of U metal and Zr metal. Finally, Section 9.3 summarizes the best experimental volume data from our evaluation and the corresponding values corrected to 0 K.

9.1 Evaluating Experimental Structural Data for U Metal

The accuracy of experimental data is decided by the analytical technique and the sample used in the measurement. We evaluate and select the most accurate experimental data for U metal based on the following criteria as suggested by Refs. [80, 96]: 1) Technique: Diffraction techniques are more accurate than dilatometry; neutron diffraction is more accurate than X-ray diffraction. 2) Sample: pure U metal is more accurate than U alloy; single-crystal bulk is more accurate than poly-crystal bulk at low *T*, and powder is more accurate at high *T*. We refer to Refs.[80, 96] for the physical reasons underlying such criteria.

9.1.1 αU

Best experimental data: 1) Barrett *et al.*[125], which has data at 4.2-298 K; 2) Lawson *et al.*[80], which has data at 298-919 K

Justification: The former is from X-ray/neutron diffraction measurements of αU single crystal and is the standard structural reference for αU at low *T*. The latter is the latest high-resolution neutron diffraction measurement performed on powder sample of U metal at room *T* and above. The two give exactly the same volume at 298 K. Other earlier data for αU compiled by Donohue[222] are mostly from poly-crystal bulk sample and are expected to be less accurate.

Note αU has charge density waves[96] at 43, 38 and 22 K that expand the lattice and is not modeled in our study. We therefore should validate our results against experimental data above 43 K.

9.1.2 βU

Best experimental data: Lawson *et al.*[80], which has data at 955 and 1030 K:

Justification: Same as above. Note it is the work that finally determined the structure of βU. We did not find any more recent experiential structural study of U metal.

9.1.3 γU

Table 9.1. Experimental lattice constant and volume of γU

Source	T (K)	Lattice constant (Å)	Volume (Å^3/atom)
Wilson&Rundle [Ref. [81]]	Room T[a]	3.474	20.96
	1073	3.49	21.20
Thewlis [Ref. [223]]	1078	3.524	21.88
Bochvar *et al.* [Ref. [224]]	1078	3.524	21.88
Chiotti *et al.* [Ref. [225]]	298[b]	3.474	20.96
	1045	3.5321	22.03
	1073	3.534	22.07
	1123	3.538	22.14
	1173	3.542	22.22
	1223	3.5458	22.29
	1273	3.5498	22.37
	1323	3.5535	22.44
	1373	3.5572	22.51
Lawson *et al.* [Ref. [80]]	1060	3.5335	22.05

[a] Linear extrapolation to pure U from U-Mo data at room T.

[b] Linear extrapolation to 298 K from high T (1045-1373 K) data of U metal.

We compile a summary of γU's experimental lattice constant and volume in Table 9.1. Firstly, we pointed out that the value at 1073 K (800°C) from Wilson and Rundle[81] should be significantly underestimated, which was first noted by Thewlis[223] to give "unreasonably high" density. As listed in Table 9.1 and potted in Figure 9.1, the single point from Wilson and Rundle[81] at 1074 K is significantly smaller than data from all the other four sources—the four themselves being very close to each other. Secondly, we also note that the two extrapolated data at 300 K from Wilson and Rundle[81] and Chiotti *et al.*[225], respectively are also underestimated despite the two match each other perfectly, which we suggest may be a coincidence. The first from Wilson and Rundle[81] is based on linear extrapolation of bcc U-Mo alloy data measured at 17.3-31.2 at.%Mo to 0, assuming Vegard's law holds. However, Ref.[67] shows that U-Mo has considerable positive deviation from Vegard's law between 17.3 and 31.2 at.%Mo. The second from Chiotti *et al.*[225] is obtained by linear extrapolation from high temperature data for γU between 1045 and 1373 K to 298 K. As we see in Figure 9.1, αU shows considerable deviation from linear thermal expansion below 935 K and it is reasonable to expect γU also has nonlinear thermal expansion behavior and therefore such linear extrapolation to 298 K is not very physical. We will come back to this point at section 9.2. Finally, we give:

Best experimental data: 1) Lawson *et al.*[80], which has data at1060 K; 2) Chiotti *et al.*[225], which has data at 1045-1373 K.

Justification: Same reason for the first reference as that for βU. The latter matches the first very well; it also provides data at multiple *T*'s up to the melting point. The other two sources (Thewlis[223] and Bochvar *et al.*[224]) also give very close results.

9.2 Quasiharmonic Theory for the Zero-Point and Finite *T* Effects

We estimate the zero-point and finite *T* effects by performing the so called Debye-Grüneisen quasi-harmonic modeling[143]. With this theory, we are able to estimate the volume expansion from 0 K to finite *T* with the input of only total energy vs. volume, which we obtain from *ab initio* calculations of the rigid lattice at 0 K. The model needs Poisson's ratio as a model parameter. For U metal and Zr metal, we use their experimental value (0.23 and 0.34, respectively); we could not find experimental Poisson's ratio for U-Zr alloy and thus use linear composition average of the Poisson's ratios for U and Zr metals. The so called Slater approximation is used for the Grüneisen constant[143].

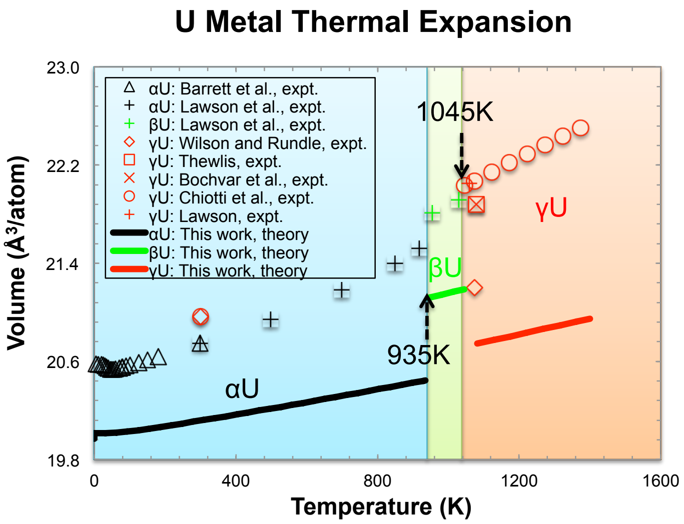

Figure 9.1. Thermal expansion of U metal from quasi-harmonic theory and experiment. See section 9.1 for references to the plotted experimental data. Two points exist at 0 K, corresponding to the rigid lattice and the zero-point of the vibrating lattice, respectively.

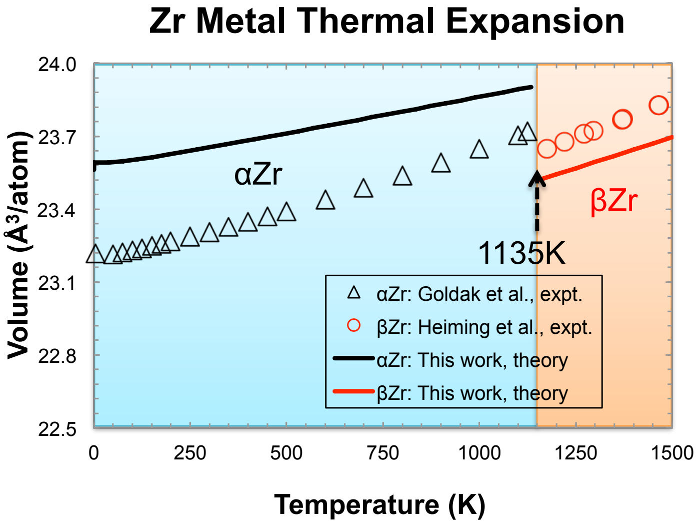

Figure 9.2. Thermal expansion of Zr metal from quasiharmonic theory and experiment. The experimental references for αZr and βZr are Goldak *et al.*[82] and Heiming *et al.*[83], respectively. Two points exist at 0 K, corresponding to the rigid lattice and the zero-point of the vibrating lattice, respectively.

Our results are shown in Figure 9.1 and Figure 9.2 for U metal and Zr metal, respectively. The experimental data we review in section 9.1 are also plotted therein for comparison. The theoretical values are based on our DFT-noSOC calculations. We are not concerned with the absolute difference between experimental and theoretical volume here, which is discussed in the body of the article. Here we focus on relative volume expansion. in Figure 9.1 and Figure 9.2 show that in terms of relative volume expansion, model prediction matches experimental data qualitatively at room temperature or below. For example, the experimental volume expansion for αU between 50 and 298 K is 0.21 Å^3/atom; the model gives 0.10 Å^3/atom. Similarly for volume expansion of αZr between 4.2 and 300 K, experiment and theory give 0.09 and 0.06 Å^3/atom, respectively. However, model prediction becomes worse at higher temperature, which manifests in the two figures as the increased difference between the slopes of the theoretical and experimental curves at higher temperatures; the phenomenon is also more significant for U metal than Zr metal. Such results are expected as at higher temperature, there are stronger anharmonic effects that are not properly modeled in the quasi-harmonic theory; U metal presumably also has stronger anharmonic effects than Zr metal. One may then think that if we want to get better estimation of the 0 K volume for the high *T* phases (e.g., γU) we should apply the quasi-harmonic correction on the extrapolated volume at room *T* rather than their actually measured values at high *T*. Unfortunately, the validity of this hypothesis largely depends on how well the extrapolation performs. In most cases, the extrapolation assumes a linear volume vs. temperature dependence (e.g., Chiotti *et al.*[225]). While linear model gives good fitting at high temperature, as demonstrated by the experimental data for γU and βZr, it is clearly not the case at lower temperatures. For example, we see the slopes of experimental volumes (i.e., thermal expansion coefficient) for αU and αZr increase considerably between 300 and 900 K. If we assume that the slope of γU/βZr changes in a similar manner as αU/αZr in this intermediate *T* region, linear extrapolation significantly underestimates the volume, as we have analyzed in section 9.2. In fact, simple graphical estimation shows that the error of such linear extrapolation is significantly larger than that of the quasiharmonic model. Due to this reason, we apply the quasi-harmonic theory to correct the actually measured volumes of γU/βZr at their actual measurement temperatures, not to the extrapolated data at room temperature. Because the theory shows increased uncertainty at high *T*, we should put most weight on low *T* phases (e.g., αU/αZr) in our model validation.

9.3 Summary of Experimental Volumes for U, Zr Metals and U-Zr Alloys

Table 9.2. Experimental volume for U, Zr metals and U-Zr alloys (Å^3/atom).

System	Expt. Vol. (var. *T*)	Expt. Vol. (corrected to 0 K)	Source
αU	20.53 (45 K)	20.48	Barrett *et al.* [Ref. [125]]
βU	21.81 (955 K)	21.19	Lawson *et al.* [Ref. [80]]
γU	22.05 (1060 K)	21.46	Lawson *et al.* [Ref. [80]]
γ(U,Zr)-25at.%Zr	22.37 (room *T*)	22.15	Huber&Ansari [Ref. [126]]
γ(U,Zr)-50at.%Zr	22.29 (room *T*)	22.07	
γ(U,Zr)-75at.%Zr	22.75 (room *T*)	22.63	
βZr	23.70 (1253 K)	23.10	Heiming *et al.* [Ref. [83]]
δ(U,Zr)-66.7at.%Zr	22.49 (room *T*)	22.36	Akabori *et al.* [Ref. [49]]
ωZr	22.75 (room *T*)	22.65	Jamieson [Ref. [128]]
αZr	23.22 (4.2 K)	23.19	Goldak *et al.* [Ref. [82]]

Based on the review in section 9.1 and the model estimation in section 9.2, we summarize the experimental volume (original at finite *T* and estimated value at 0 K) for U, Zr metals and U-Zr alloys in Table 9.2.

10 References

[1] N. Cerullo, G. Lomonaco, Generation IV reactor designs, operation and fuel cycle, in: I. Crossland (Ed.) Nuclear Fuel Cycle Science and Engineering, Woodhead Publ Ltd, Cambridge, 2012, pp. 333-395.

[2] Y. Guerin, G.S. Was, S.J. Zinkle, Materials Challenges for Advanced Nuclear Energy Systems, MRS Bull., 34 (2009) 10-14.

[3] A.E.T.D.R.T.P.V. Waltar, Fast spectrum reactors, Springer, New York; London, 2011.

[4] G.L. Hofman, L.C. Walters, T.H. Bauer, Metallic fast reactor fuels, Prog. Nucl. Energy, 31 (1997) 83-110.

[5] Y. Chang, Technical rationale for metal fuel in fast reactors, Nucl Eng Technol, 39 (2007) 161-170.

[6] Y.S. Kim, G.L. Hofman, S.L. Hayes, Y.H. Sohn, Constituent redistribution in U-Pu-Zr fuel during irradiation, J. Nucl. Mater., 327 (2004) 27-36.

[7] J.L. Smith, E.A. Kmetko, Magnetism or bonding: A nearly periodic table of transition elements, J. Less-Common Met., 90 (1983) 83-88.

[8] M. Kurata, T. Inoue, C. Sari, Redistribution Behavior of Various Constituents in U-Pu-Zr Alloy and U-Pu-Zr Alloy Containing Minor Actinides and Rare-Earths in a Temperature-Gradient, J. Nucl. Mater., 208 (1994) 144-158.

[9] J. Roberto, T. Diaz de la Rubia, Basic Research Needs for Advanced Nuclear Systems, U.S. Department of Energy, 2006.

[10] M. Kurata, Thermodynamic assessment of the Pu-U, Pu-Zr, and Pu-U-Zr systems, Calphad, 23 (1999) 305-337.

[11] M. Kurata, Thermodynamic database on U-Pu-Zr-Np-Am-Fe alloy system I - Re-evaluation of U-Pu-Zr alloy system, IOP Conf. Ser.: Mater. Sci. Eng., 9 (2010) 012022.

[12] M. Kurata, Thermodynamic database on U-Pu-Zr-Np-Am-Fe alloy system II - Evaluation of Np, Am, and Fe containing systems, IOP Conf. Ser.: Mater. Sci. Eng., 9 (2010) 012023.

[13] M. Kurata, 2.05 - Phase Diagrams of Actinide Alloys, in: J.M.K. Rudy (Ed.) Comprehensive Nuclear Materials, Elsevier, Oxford, 2012, pp. 139-195.

[14] M. Akabori, T. Ogawa, A. Itoh, Y. Morii, The lattice stability and structure of δ-UZr2 at elevated temperatures, J. Phys.: Condens. Matter, 7 (1995) 8249-8257.

[15] A.C. Lawson, J.A. Goldstone, B. Cort, R.J. Martinez, F.A. Vigil, T.G. Zocco, J.W. Richardson, M.H. Mueller, Structure of ζ-phase plutonium-uranium, Acta Crystallogr. Sect. B, 52 (1996) 32-37.

[16] F.H. Ellinger, R.O. Elliott, E.M. Cramer, The Plutonium - Uranium System, J. Nucl. Mater., 1 (1959) 233-243.

[17] D.T. Cromer, Crystal Structure of Zeta-Pu-Zr, Ideal Formula $Pu_{28}Zr$, Acta Crystallogr. Sect. B, 35 (1979) 14-19.

[18] A.F. Berndt, Room temperature lattice constants of alloys of plutonium in alpha-uranium, J. Nucl. Mater., 9 (1963) 53-58.

[19] P.G. Mardon, J.H. Pearce, An Investigation of the Neptunium-Uranium Equilibrium Diagram, J. Less-Common Met., 1 (1959) 467-475.

[20] P.G. Mardon, J.H. Pearce, J.A.C. Marples, Constitution Studies On the Neptunium Plutonium Alloy System, J. Less-Common Met., 3 (1961) 281-292.

[21] Y. Okamoto, R.G. Haire, J.K. Gibson, T. Ogawa, The investigation of selected Np-Zr alloys by X-ray diffraction up to 700 degrees C, J. Alloys Compd., 232 (1996) 302-306.

[22] M.M. Gensini, R.G. Haire, J.K. Gibson, Investigation of the Neptunium-Zirconium System by X-Ray-Diffraction, J. Alloys Compd., 213 (1994) 402-405.

[23] K.T. Moore, G. van der Laan, Nature of The 5f States in Actinide Metals, Rev. Mod. Phys., 81 (2009) 235-298.

[24] P. Soderlind, G. Kotliar, K. Haule, P.M. Oppeneer, D. Guillaumont, Computational modeling of actinide materials and complexes, MRS Bull., 35 (2010) 883-888.

[25] Y.A. Chang, S.L. Chen, F. Zhang, X.Y. Yan, F.Y. Xie, R. Schmid-Fetzer, W.A. Oates, Phase diagram calculation: past, present and future, Prog. Mater. Sci., 49 (2004) 313-345.

[26] S.L. Shang, Y. Wang, D. Kim, Z.K. Liu, First-principles thermodynamics from phonon and Debye model: Application to Ni and Ni3Al, Comp. Mater. Sci., 47 (2010) 1040-1048.

[27] C. Jiang, First-principles study of ternary bcc alloys using special quasi-random

structures, Acta Mater, 57 (2009) 4716-4726.

[28] P. Hohenberg, W. Kohn, Inhomogeneous Electron Gas, Phys. Rev. B, 136 (1964) 864-871.

[29] W. Kohn, L.J. Sham, Self-Consistent Equations Including Exchange and Correlation Effects, Phys. Rev., 140 (1965) 1133-1138.

[30] J.P. Perdew, K. Burke, M. Ernzerhof, Generalized gradient approximation made simple, Phys. Rev. Lett., 77 (1996) 3865-3868.

[31] S.L. Dudarev, G.A. Botton, S.Y. Savrasov, C.J. Humphreys, A.P. Sutton, Electron-energy-loss spectra and the structural stability of nickel oxide: An LSDA+U study, Phys. Rev. B, 57 (1998) 1505-1509.

[32] Y.M. Muggianu, M. Gambino, J.P. Bros, ENTHALPIES OF FORMATION OF LIQUID ALLOYS BISMUTH-GALLIUM-TIN AT 723K - CHOICE OF AN ANALYTICAL REPRESENTATION OF INTEGRAL AND PARTIAL THERMODYNAMIC FUNCTIONS OF MIXING FOR THIS TERNARY-SYSTEM, Journal De Chimie Physique Et De Physico-Chimie Biologique, 72 (1975) 83-88.

[33] W. Xiong, W. Xie, C. Shen, D. Morgan, Thermodynamic Modeling of the U-Zr System - A Revisit, J. Nucl. Mater., 443 (2013) 331-341.

[34] W. Xie, W. Xiong, C.A. Marianetti, D. Morgan, Correlation and relativistic effects in U metal and U-Zr alloy: validation of ab initio approaches, Phys. Rev. B, 88 (2013) 235128.

[35] W. Xiong, W. Xie, D. Morgan, Thermodynamic evaluation of the Np–Zr system using CALPHAD and ab initio methods, J. Nucl. Mater., 452 (2014) 569-577.

[36] A. Riyas, P. Mohanakrishnan, Studies on physics parameters of metal (U–Pu–Zr) fuelled FBR cores, Ann. Nucl. Energy, 35 (2008) 87-92.

[37] L. Leibowitz, R.A. Blomquist, A.D. Pelton, Thermodynamics of the uranium-zirconium system, J. Nucl. Mater., 167 (1989) 76-81.

[38] M. Kurata, T. Ogata, K. Nakamura, T. Ogawa, Thermodynamic assessment of the Fe-U, U-Zr and Fe-U-Zr systems, J. Alloys Compd., 271 (1998) 636-640.

[39] P.Y. Chevalier, E. Fischer, Thermodynamic modelling of the O-U-Zr system, J. Nucl. Mater., 257 (1998) 213-255.

[40] P.Y. Chevalier, E. Fischer, B. Cheynet, Progress in the thermodynamic modelling of

the O-U-Zr ternary system, Calphad, 28 (2004) 15-40.

[41] R. Sheldon, D. Peterson, The U-Zr (Uranium-Zirconium) system, Bulletin of Alloy Phase Diagrams, 10 (1989) 165-171.

[42] D. Summers-Smith, The constitution of uranium-zirconium alloys, J. Inst. Met., 83 (1955) 277-282.

[43] A. Maeda, Y. Suzuki, T. Ohmichi, Uranium Activity of Uranium-Rich U--Zr Alloys by Knudsen Effusion Mass Spectrometry, J. Alloys Compd., 179 (1992) L21-L24.

[44] M. Kanno, M. Yamawaki, T. Koyama, N. Morioka, Thermodynamic Activity Measurements of U-Zr Alloys by Knudsen Effusion Mass-Spectrometry, J. Nucl. Mater., 154 (1988) 154-160.

[45] S. Kaity, J. Banerjee, M.R. Nair, K. Ravi, S. Dash, T.R.G. Kutty, A. Kumar, R.P. Singh, Microstructural and thermophysical properties of U-6 wt.%Zr alloy for fast reactor application, J. Nucl. Mater., 427 (2012) 1-11.

[46] F.A. Rough, A.E. Austin, A.A. Bauer, J. Robert Doig, The stability and existence range of the Zirconium-Uranium epsilon phase, in: Report No. BMI-1092, Battelle Memorial Institute, Ohio, 1956, pp. 36.

[47] J.F. Duffey, C.A. Bruch, Delta phase field of U-Zr equilibrium diagram, Trans. AIME, 212 (1958) 17-19.

[48] S.T. Zegler, The uranium-rich end of the uranium-zirconium system, in: USAEC REP.ANL-6055, 1962.

[49] M. Akabori, A. Itoh, T. Ogawa, F. Kobayashi, Y. Suzuki, Stability and structure of the δ phase of the U-Zr alloys, J. Nucl. Mater., 188 (1992) 249-254.

[50] C.B. Basak, S. Neogy, D. Srivastava, G.K. Dey, S. Banerjee, Disordered bcc gamma-phase to delta-phase transformation in Zr-rich U-Zr alloy, Philos. Mag., 91 (2011) 3290-3306.

[51] C.B. Basak, Microstructural evaluation of U-rich U-Zr alloys under near-equilibrium condition, J. Nucl. Mater., 416 (2011) 280-287.

[52] T. Matsui, T. Natsume, K. Naito, Heat-Capacity Measurements of U0.80Zr0.20 and U0.80Mo0.20 Alloys from Room-Temperature to 1300-K, J. Nucl. Mater., 167 (1989) 152-159.

[53] Y. Takahashi, K. Yamamoto, T. Ohsato, H. Shimada, T. Terai, M. Yamawaki, Heat-

Capacities of Uranium Zirconium Alloys from 300-K to 1100-K, J. Nucl. Mater., 167 (1989) 147-151.

[54] H. Loeffler, V. Synecek, M. Simerska, G. Wendrock, P. Bartuska, R. Kroggel, On the mode of decomposition of Al-Zn alloys, Phys. Status Solidi A, 65 (1981) 197-204.

[55] S.A. Mey, Reevaluation of the Al-Zn System, Z. Metallkd., 84 (1993) 451-455.

[56] W. Xiong, M. Selleby, Q. Chen, J. Odqvist, Y. Du, Phase equilibria and thermodynamic properties in the Fe-Cr system, Crit. Rev. Solid State Mater. Sci., 35 (2010) 125-152.

[57] W. Xiong, P. Hedstrom, M. Selleby, J. Odqvist, M. Thuvander, Q. Chen, An improved thermodynamic modeling of the Fe-Cr system down to zero kelvin coupled with key experiments, CALPHAD: Comput. Coupling Phase Diagrams Thermochem., 35 (2011) 355-366.

[58] H. Baker, ASM Handbook: alloy phase diagrams, 1992.

[59] A.N. Holden, Metallography of the ε phase in the uranium-zirconium system, U. S. A. E. C., TID-7523 (1956) 40-64.

[60] G.B. Fedorov, E.A. Smirnov, Heat Capacity of Uranium-Zirconium Systems, At. Energ., 25 (1968) 795-797.

[61] T. Murakami, T. Kato, M. Kurata, H. Yamana, Electrochemical formation of uranium-zirconium alloy in LiCl-KCl melts, J. Nucl. Mater., 394 (2009) 131-135.

[62] K. Nagarajan, R. Babu, C.K. Mathews, Enthalpy of formation of UZr_2 by calorimetry, J. Nucl. Mater., 203 (1993) 221-223.

[63] B. Beeler, B. Good, S. Rashkeev, C. Deo, M. Baskes, M. Okuniewski, First principles calculations for defects in U, J. Phys.: Condens. Matter, 22 (2010) 505703.

[64] G.Y. Huang, B.D. Wirth, First-principles study of diffusion of interstitial and vacancy in α U－Zr, J. Phys.: Condens. Matter, 23 (2011) 205402.

[65] A. Landa, P. Soderlind, P.E.A. Turchi, L. Vitos, A. Ruban, Density-functional study of Zr-based actinide alloys: 2. U-Pu-Zr system, J. Nucl. Mater., 393 (2009) 141-145.

[66] A. Landa, P. Soderlind, P.E.A. Turchi, Density-functional study of the U-Zr system, J. Alloys Compd., 478 (2009) 103-110.

[67] A. Landa, P. Soderlind, P.E.A. Turchi, Density-functional study of U-Mo and U-Zr alloys, J. Nucl. Mater., 414 (2011) 132-137.

[68] T. Ogawa, T. Iwai, Thermochemical modelling of U-Zr alloys, J. Less-Common Met., 170 (1991) 101-108.

[69] A.T. Dinsdale, SGTE data for pure elements, Calphad, 15 (1991) 317-425.

[70] O. Redlich, A.T. Kister, THERMODYNAMICS OF NONELECTROLYTE SOLUTIONS - X-Y-T RELATIONS IN A BINARY SYSTEM, Ind. Eng. Chem., 40 (1948) 341-345.

[71] M. Hillert, The compound energy formalism, J Alloy Compd, 320 (2001) 161-176.

[72] G. Kresse, J. Hafner, Ab initio Moleculear Dynamics for Liquid Metals, Phys. Rev. B, 47 (1993) 558-561.

[73] G. Kresse, J. Furthmuller, Efficient iterative schemes for ab initio total-energy calculations using a plane-wave basis set, Phys. Rev. B, 54 (1996) 11169-11186.

[74] P.E. Blochl, Projector Augmented-Wave Method, Phys. Rev. B, 50 (1994) 17953-17979.

[75] G. Kresse, D. Joubert, From ultrasoft pseudopotentials to the projector augmented-wave method, Phys. Rev. B, 59 (1999) 1758-1775.

[76] D.C. Langreth, J.P. Perdew, Theory of Nonuniform Electronic Systems .1. Analysis of the Gradient Approximation and a Generalization That Works, Phys. Rev. B, 21 (1980) 5469-5493.

[77] A.I. Liechtenstein, V.I. Anisimov, J. Zaanen, Density-functional Theory and Strong Interactions: Orbital Ordering in Mott-Hubbard Insulators, Phys. Rev. B, 52 (1995) R5467-R5470.

[78] H.J. Monkhorst, J.D. Pack, Special Points for Brillouin-Zone Integrations, Phys. Rev. B, 13 (1976) 5188-5192.

[79] G.H. Lander, M.H. Mueller, Neutron Diffraction Study of α-Uranium at Low Temperatures, Acta Crystallogr., B26 (1970) 129-136.

[80] A.C. Lawson, C.E. Olsen, J.W.J. Richardson, M.H. Mueller, G.H. Lander, Structure of β-uranium, Acta Crystallogr., B44 (1988) 89-96.

[81] A.S. Wilson, R.E. Rundle, The Structures of Uranium Metal, Acta Crystallogr., 2 (1949) 126-127.

[82] J. Goldak, L.T. Lloyd, C.S. Barrett, Lattice Parameters Thermal Expansions and Gruneisen Coefficients of Zirconium 4.2 to 1130 Degrees K, Phys. Rev., 144 (1966) 478-

484.

[83] A. Heiming, W. Petry, J. Trampenau, W. Miekeley, J. Cockcroft, The Temperature-Dependence of the Lattice-Parameters of Pure Bcc Zr and Bcc Zr-2 at-Percent-Co, J. Phys.: Condens. Matter, 4 (1992) 727-733.

[84] A. Zunger, S.H. Wei, L.G. Ferreira, J.E. Bernard, Special Quasirandom Structures, Phys. Rev. Lett., 65 (1990) 353-356.

[85] A. van de Walle, M. Asta, G. Ceder, The Alloy Theoretic Automated Toolkit: A user guide, Calphad, 26 (2002) 539-553.

[86] C. Jiang, C. Wolverton, J. Sofo, L.Q. Chen, Z.K. Liu, First-principles study of binary bcc alloys using special quasirandom structures, Phys. Rev. B, 69 (2004) 214202.

[87] P. Soderlind, B. Grabowski, L. Yang, A. Landa, T. Bjorkman, P. Souvatzis, O. Eriksson, High-temperature phonon stabilization of gamma-uranium from relativistic first-principles theory, Phys. Rev. B, 85 (2012) 060301.

[88] http://www.thermocalc.se, in.

[89] B. Sundman, B. Jansson, J.O. Andersson, The Thermo-Calc Databank System, CALPHAD: Comput. Coupling Phase Diagrams Thermochem., 9 (1985) 153-190.

[90] H. Okamoto, Reevaluation of thermodynamic models for phase diagram evaluation, J. Phase Equilib., 12 (1991) 623-643.

[91] W. Xiong, Y. Du, X. Lu, J.C. Schuster, H. Chen, Reassessment of the Ce–Ni binary system supported by key experiments and ab initio calculations, Intermetallics, 15 (2007) 1401-1408.

[92] W. Xiong, Y. Kong, Y. Du, Z.K. Liu, M. Selleby, W.H. Sun, Thermodynamic investigation of the galvanizing systems, I: Refinement of the thermodynamic description for the Fe-Zn system, CALPHAD: Computer Coupling of Phase Diagrams and Thermochemistry, 33 (2009) 433-440.

[93] G.B. Fedorov, E.A. Smirnov, Specific heat of uranium-zirconium alloys, Soviet Atomic Energy, 25 (1968) 795-797.

[94] F.L. Oetting, M.H. Rand, E.F.J. Westrum, I.A.E. Agency, V.A. Medvedev, The Chemical Thermodynamics of Actinide Elements and Compounds: Part 1 The Actinide Elements, International Atomic Energy Agency, 1976.

[95] P. Chiotti, V. Akhachinskij, I. Ansara, M. Rand, The Chemical Thermodynamics of

Actinide Elements and Compounds: Part 5, The Actinide Binary Alloys, International Atomic Energy Agency, Vienna, 1981.

[96] G.H. Lander, E.S. Fisher, S.D. Bader, The Solid-State Properties of Uranium - a Historical-Perspective and Review, Adv. Phys., 43 (1994) 1-111.

[97] P. Soderlind, Theory of the crystal structures of cerium and the light actinides, Adv. Phys., 47 (1998) 959-998.

[98] H.L. Skriver, O.K. Andersen, B. Johansson, Calculated Bulk Properties of Actinide Metals, Phys. Rev. Lett., 41 (1978) 42-45.

[99] P. Soderlind, O. Eriksson, B. Johansson, J.M. Wills, Electronic-Properties of f-Electron Metals Using the Generalized Gradient Approximation, Phys. Rev. B, 50 (1994) 7291-7294.

[100] J. Akella, S. Weir, J.M. Wills, P. Soderlind, Structural stability in uranium, J. Phys.: Condens. Matter, 9 (1997) L549-L555.

[101] L. Vitos, J. Kollar, H.L. Skriver, Local density approximation versus generalized gradient approximation: full charge density study of the atomic volume of the light actinides, J. Alloys Compd., 271 (1998) 339-341.

[102] J.C. Boettger, M.D. Jones, R.C. Albers, Structural properties of crystalline uranium from linear combination of Gaussian-type orbitals calculations, Int. J. Quantum Chem., 75 (1999) 911-915.

[103] M.D. Jones, J.C. Boettger, R.C. Albers, D.J. Singh, Theoretical atomic volumes of the light actinides, Phys. Rev. B, 61 (2000) 4644-4650.

[104] L. Nordstrom, J.M. Wills, P.H. Andersson, P. Soderlind, O. Eriksson, Spin-orbit coupling in the actinide elements: A critical evaluation of theoretical equilibrium volumes, Phys. Rev. B, 63 (2001) 035103.

[105] P. Soderlind, First-principles elastic and structural properties of uranium metal, Phys. Rev. B, 66 (2002) 085113.

[106] M. Penicaud, Calculated Equilibrium Properties, Electronic Structures and Structural Stabilities of Th, Pa, U, Np and Pu, J. Phys.: Condens. Matter, 12 (2000) 5819-5829.

[107] M. Penicaud, Calculated structural stabilities of U, Np, Pu and Am; new high-pressure phases for Am and Pu, J. Phys.: Condens. Matter, 14 (2002) 3575.

[108] C.D. Taylor, Evaluation of first-principles techniques for obtaining materials parameters of alpha-uranium and the (001)alpha-uranium surface, Phys. Rev. B, 77 (2008) 094119.

[109] J.H. Li, Q.B. Ren, C.H. Lu, L. Lu, Y. Dai, B.X. Liu, Structure, formation energies and elastic constants of uranium metal investigated by first principles calculations, J. Alloys Compd., 516 (2012) 139-143.

[110] S. Adak, H. Nakotte, P.F. de Chatel, B. Kiefer, Uranium at high pressure from first principles, Physica B, 406 (2011) 3342-3347.

[111] S.K. Xiang, H.C. Huang, L.M. Hsiung, Quantum Mechanical Calculations of Uranium Phases and Niobium Defects in Gamma-Uranium, J. Nucl. Mater., 375 (2008) 113-119.

[112] B. Beeler, B. Good, S. Rashkeev, C. Deo, M. Baskes, M. Okuniewski, First-principles calculations of the stability and incorporation of helium, xenon and krypton in uranium, J. Nucl. Mater., 425 (2012) 2-7.

[113] B. Beeler, C. Deo, M. Baskes, M. Okuniewski, First principles calculations of the structure and elastic constants of α, β and γ uranium, J. Nucl. Mater., 433 (2013) 143-151.

[114] G.Y. Huang, B.D. Wirth, First-principles study of bubble nucleation and growth behaviors in alpha U-Zr, J. Phys.: Condens. Matter, 24 (2012) 415404.

[115] C.P. Opeil, R.K. Schulze, M.E. Manley, J.C. Lashley, W.L. Hults, R.J. Hanrahan, J.L. Smith, B. Mihaila, K.B. Blagoev, R.C. Albers, P.B. Littlewood, Valence-band UPS, 6p core-level XPS, and LEED of a uranium (001) single crystal, Phys. Rev. B, 73 (2006) 165109.

[116] C.P. Opeil, R.K. Schulze, H.M. Volz, J.C. Lashley, M.E. Manley, W.L. Hults, R.J. Hanrahan, J.L. Smith, B. Mihaila, K.B. Blagoev, R.C. Albers, P.B. Littlewood, Angle-Resolved Photoemission and First-Principles Electronic Structure of Single-Crystalline Alpha-U(001), Phys. Rev. B, 75 (2007) 045120.

[117] A.N. Chantis, R.C. Albers, M.D. Jones, M. van Schilfgaarde, T. Kotani, Many-body electronic structure of metallic alpha-uranium, Phys. Rev. B, 78 (2008) 081101.

[118] Z. Fisk, J.L. Smith, H.R. Ott, B. Batlogg, Heavy Fermion Behavior in Uranium-Compounds, J. Magn. Magn. Mater., 52 (1985) 79-84.

[119] V.I. Anisimov, F. Aryasetiawan, A.I. Lichtenstein, First-principles calculations of the electronic structure and spectra of strongly correlated systems: The LDA+U method, J. Phys.: Condens. Matter, 9 (1997) 767-808.

[120] A.B. Shick, W.E. Pickett, Magnetism, spin-orbit coupling, and superconducting pairing in UGe2, Phys. Rev. Lett., 86 (2001) 300-303.

[121] A.N. Yaresko, V.N. Antonov, P. Fulde, Localized U 5f electrons in UPd3 from LDA+U calculations, Phys. Rev. B, 67 (2003) 155103.

[122] A.N. Yaresko, V.N. Antonov, B.N. Harmon, Electronic structure and x-ray magnetic circular dichroism in uranium compounds. III. Heavy-fermion compounds, Phys. Rev. B, 68 (2003) 214426.

[123] J.G. Yu, R. Devanathan, W.J. Weber, First-principles study of defects and phase transition in UO2, J. Phys.: Condens. Matter, 21 (2009) 435401.

[124] M. Cococcioni, S. de Gironcoli, Linear response approach to the calculation of the effective interaction parameters in the LDA+U method, Phys. Rev. B, 71 (2005) 035105.

[125] C.S. Barrett, M.H. Mueller, R.L. Hitterman, Crystal Structure Variations in Alpha Uranium at Low Temperatures, Phys. Rev., 129 (1963) 625-629.

[126] J.G. Huber, P.H. Ansari, The Superconductivity of Bcc U-Zr Alloys, Physica B+C, 135 (1985) 441-444.

[127] V.N. German, A.A. Bakanova, L.A. Tarasova, Y.N. Sumulov, Phase Transformation of Titanium and Zirconium Shock Waves, Sov. Phys. Solid State, 12 (1970) 490-&.

[128] J.C. Jamieson, Crystal Structures of Titanium, Zirconium, and Hafnium at High Pressures, Science, 140 (1963) 72-73.

[129] M. Methfessel, A.T. Paxton, High-Precision Sampling for Brillouin-Zone Integration in Metals, Phys. Rev. B, 40 (1989) 3616-3621.

[130] O. Bengone, M. Alouani, P. Blochl, J. Hugel, Implementation of the projector augmented-wave LDA+U method: Application to the electronic structure of NiO, Phys. Rev. B, 62 (2000) 16392-16401.

[131] B. Dorado, B. Amadon, M. Freyss, M. Bertolus, DFT+U calculations of the ground state and metastable states of uranium dioxide, Phys. Rev. B, 79 (2009) 235125.

[132] B. Meredig, A. Thompson, H.A. Hansen, C. Wolverton, A. van de Walle, Method

for locating low-energy solutions within DFT plus U, Phys. Rev. B, 82 (2010) 195128.

[133] J.W. Ross, D.J. Lam, Magnetic Susceptibility of Single-Crystal Alpha-Uranium, Phys. Rev., 165 (1968) 617-&.

[134] L. Kleinman, Relativistic Norm-Conserving Pseudopotential, Phys. Rev. B, 21 (1980) 2630-2631.

[135] A.H. Macdonald, W.E. Pickett, D.D. Koelling, A Linearized Relativistic Augmented-Plane-Wave Method Utilizing Approximate Pure Spin Basis Functions, J. Phys. C., 13 (1980) 2675-2683.

[136] C. Kittel, Introduction to solid state physics, Wiley, Hoboken, NJ, 2005.

[137] G.B. Fedorov, E.A. Smirnov, Thermodynamic properties of the γ-phase in the uranium-zirconium system, At. Energ., 21 (1966) 837-840.

[138] Y. Wang, S. Curtarolo, C. Jiang, R. Arroyave, T. Wang, G. Ceder, L.Q. Chen, Z.K. Liu, Ab initio lattice stability in comparison with CALPHAD lattice stability, Calphad, 28 (2004) 79-90.

[139] P.E.A. Turchi, I.A. Abrikosov, B. Burton, S.G. Fries, G. Grimvalle, L. Kaufman, P. Korzhavyi, V.R. Manga, M. Ohno, A. Pisch, A. Scott, W.Q. Zhang, Interface between quantum-mechanical-based approaches, experiments, and CALPHAD methodology, Calphad, 31 (2007) 4-27.

[140] G. Grimvall, B. Magyari-Kope, V. Ozolins, K.A. Persson, Lattice instabilities in metallic elements, Rev. Mod. Phys., 84 (2012) 945-986.

[141] S. Bajaj, A. Landa, P. Soderlind, P.E.A. Turchi, R. Arroyave, The U-Ti system: Strengths and weaknesses of the CALPHAD method, J. Nucl. Mater., 419 (2011) 177-185.

[142] A. Berche, N. Dupin, C. Gueneau, C. Rado, B. Sundman, J.C. Dumas, Calphad thermodynamic description of some binary systems involving U, J. Nucl. Mater., 411 (2011) 131-143.

[143] V.L. Moruzzi, J.F. Janak, K. Schwarz, Calculated Thermal-Properties of Metals, Phys. Rev. B, 37 (1988) 790-799.

[144] T. Le Bihan, S. Heathman, M. Idiri, G.H. Lander, J.M. Wills, A.C. Lawson, A. Lindbaum, Structural behavior of alpha-uranium with pressures to 100 GPa, Phys. Rev. B, 67 (2003) 134102.

[145] A. Jain, G. Hautier, C.J. Moore, S.P. Ong, C.C. Fischer, T. Mueller, K.A. Persson, G. Ceder, A high-throughput infrastructure for density functional theory calculations, Comput. Mater. Sci., 50 (2011) 2295-2310.

[146] P. Soderlind, L. Nordstrom, Y.M. Lou, B. Johansson, Relativistic Effects on The Thermal Expansion of The Actinide Elements, Phys. Rev. B, 42 (1990) 4544-4552.

[147] M.S.S. Brooks, Relativistic corrections to the atomic volumes of the actinide metals, J. Phys. F, 13 (1983) 103-108.

[148] L.F. Bates, D. Hughes, THE MAGNETIC SUSCEPTIBILITY OF METALLIC URANIUM, Proc. Phys. Soc. Lond, B, 67 (1954) 28-37.

[149] E.R. Ylvisaker, W.E. Pickett, K. Koepernik, Anisotropy and magnetism in the LSDA plus U method, Phys. Rev. B, 79 (2009) 035103.

[150] A.B. Shick, V. Drchal, L. Havela, Coulomb-U and magnetic-moment collapse in delta-Pu, Europhys. Lett., 69 (2005) 588-594.

[151] Y. Baer, J.K. Lang, High-Energy Spectroscopic Study of the Occupied and Unoccupied 5f and Valence States in Th and U Metals, Phys. Rev. B, 21 (1980) 2060-2062.

[152] J.G. Tobin, K.T. Moore, B.W. Chung, M.A. Wall, A.J. Schwartz, G. van der Laan, A.L. Kutepov, Competition between delocalization and spin-orbit splitting in the actinide 5f states, Phys. Rev. B, 72 (2005) 085109.

[153] M.S.S. Brooks, Calculated ground state properties of light actinide metals and their compounds, Physica B+C, 130 (1985) 6-12.

[154] N. Spector, Ground-State Configuration of Neutral Uranium (U I), Phys. Rev. A, 8 (1973) 3270-3273.

[155] W. Xie, C.A. Marianetti, W. Xiong, D. Morgan, Applicability of DFT + U to U-Zr alloys, J. Nucl. Mater., Accepted (2014).

[156] P. Söderlind, A. Landa, P.E.A. Turchi, Comment on “Correlation and relativistic effects in U metal and U-Zr alloy: Validation of <i>ab initio</i> approaches”, Phys. Rev. B, 90 (2014) 157101.

[157] P. Söderlind, B. Sadigh, V. Lordi, A. Landa, P.E.A. Turchi, Electron correlation and relativity of the 5f electrons in the U–Zr alloy system, J. Nucl. Mater., 444 (2014) 356-358.

[158] J.F. Herbst, R.E. Watson, I. Lindgren, Coulomb Term U and 5f Electron-Excitation Energies for Metals Actinium to Berkelium, Phys. Rev. B, 14 (1976) 3265-3272.

[159] G. Kotliar, S.Y. Savrasov, K. Haule, V.S. Oudovenko, O. Parcollet, C.A. Marianetti, Electronic structure calculations with dynamical mean-field theory, Rev. Mod. Phys., 78 (2006) 865-951.

[160] J.M. Wills, M. Alouani, P. Andersson, A. Delin, O. Eriksson, O. Grechnyev, Full-potential electronic structure method: energy and force calculations with density functional and dynamical mean field theory, Springer, Berlin, Heidelberg, New York, 2010.

[161] P. Blaha, K. Schwarz, G.K.H. Madsen, D. Kvasnicka, J. Luitz, WIEN2k, An Augmented Plane Wave + Local Orbitals Program for Calculating Crystal Properties, Vienna University of Technology, Vienna, Austria, 2001.

[162] C.B. Basak, N. Prabhu, M. Krishnan, On the formation mechanism of UZr2 phase, Intermetallics, 18 (2010) 1707-1712.

[163] E. Zen, Validity of "Vegard's Law", Am. Mineral., 41 (1956) 523.

[164] J. Hafner, A Note on Vegard and Zen Laws, J. Phys. F, 15 (1985) L43-L48.

[165] A. Dewaele, J. Bouchet, F. Occelli, M. Hanfland, G. Garbarino, Refinement of the equation of state of alpha-uranium, Phys. Rev. B, 88 (2013) 134202.

[166] C.S. Yoo, H. Cynn, P. Soderlind, Phase diagram of uranium at high pressures and temperatures, Phys. Rev. B, 57 (1998) 10359-10362.

[167] E.S. Fisher, H.J. McSkimin, Adiabatic Elastic Moduli of Single Crystal Alpha-Uranium, J. Appl. Phys., 29 (1958) 1473-1484.

[168] E.S. Fisher, Temperature Dependence of Elastic Moduli in Alpha Uranium Single Crystals, Part IV. (298° to 923° K), J. Nucl. Mater., 18 (1966) 39-54.

[169] S. Yamanaka, K. Yamada, T. Tsuzuki, T. Iguchi, M. Katsura, Y. Hoshino, W. Saiki, Mechanical and thermal properties of uranium intermetallic compounds, J. Alloys Compd., 271 (1998) 549-556.

[170] A.C. Lawson, B. Martinez, J.A. Roberts, B.I. Bennett, J.W. Richardson, Melting of the light actinides, Philos. Mag. B, 80 (2000) 53-59.

[171] J.C. Lashley, B.E. Lang, J. Boerio-Goates, B.F. Woodfield, G.M. Schmiedeshoff, E.C. Gay, C.C. McPheeters, D.J. Thoma, W.L. Hults, J.C. Cooley, R.J. Hanrahan, Jr.,

J.L. Smith, Low-temperature specific heat and critical magnetic field of α-uranium single crystals, Phys. Rev. B, 63 (2001) 224510.

[172] A.C. Lawson, H. Ledbetter, Coupled temperature dependences of volume and compressibility, Philos. Mag., 91 (2011) 1425-1440.

[173] J.P. Perdew, Y. Wang, Accurate and Simple Analytic Representation of the Electron-Gas Correlation-Energy, Phys. Rev. B, 45 (1992) 13244-13249.

[174] E. Gull, A.J. Millis, A.I. Lichtenstein, A.N. Rubtsov, M. Troyer, P. Werner, Continuous-time Monte Carlo methods for quantum impurity models, Rev. Mod. Phys., 83 (2011) 349-404.

[175] P. Soderlind, B. Sadigh, Density-functional calculations of α, β, γ, δ, δ', and ε plutonium, Phys. Rev. Lett., 92 (2004) 185702.

[176] J.C. Lashley, A. Lawson, R.J. McQueeney, G.H. Lander, Absence of magnetic moments in plutonium, Phys. Rev. B, 72 (2005) 054416.

[177] S.Y. Savrasov, G. Kotliar, Ground state theory of delta-Pu, Phys. Rev. Lett., 84 (2000) 3670-3673.

[178] C.A. Marianetti, K. Haule, G. Kotliar, M.J. Fluss, Electronic coherence in delta-Pu: A dynamical mean-field theory study, Phys. Rev. Lett., 101 (2008) 056403.

[179] B.A. Pudjanto, K. Konashi, M. Kato, T. Terai, M. Yamawaki, Thermodynamic analysis on the Np-Zr-H system, Journal of Nuclear Materials, 344 (2005) 89-93.

[180] B.A. Pudjanto, K. Konashi, T. Terai, M. Yamawaki, Thermodynamic analysis of Np-Zr-H, Am-Zr-H, Pu-Zr-H systems, Journal of Physics and Chemistry of Solids, 66 (2005) 665-670.

[181] A.J. Schwartz, H. Cynn, K.J.M. Blobaum, M.A. Wall, K.T. Moore, W.J. Evans, D.L. Farber, J.R. Jeffries, T.B. Massalski, Atomic structure and phase transformations in Pu alloys, Prog. Mater Sci., 54 (2009) 909-943.

[182] S. Bajaj, A. Garay, A. Landa, P. Söderlind, P. Turchi, R. Arróyave, Thermodynamic study of the Np-Zr system, J. Nucl. Mater., 409 (2011) 1－8.

[183] J.K. Gibson, R.G. Haire, High-Temperature DTA of Transuranium Materials with Application to the Np-Zr Phase-Diagram, Thermochim. Acta, 207 (1992) 65-78.

[184] J.K. Gibson, R.G. Haire, Investigation of the Neptunium-Zirconium Phase-Diagram by Differential Thermal-Analysis, J. Nucl. Mater., 201 (1993) 225-230.

[185] R.J. Rodriguez, C. Sari, A.J.C. Portal, Investigation of the Np-Zr and U-Zr-Np Systems, J. Alloys Compd., 209 (1994) 263-268.

[186] A.F. Berndt, Theta Phase in Plutonium-Zirconium System, J. Less-Common Met., 12 (1967) 82-83.

[187] W.H. Zachariasen, Crystal Chemical Studies of the 5f-series of Elements. XVII. The Crystal Structure of Neptunium Metal, Acta Crystallogr., 5 (1952) 660-664.

[188] W.H. Zachariasen, Crystal Chemical Studies of the 5f-Series of Elements. XVIII. Crystal Structure Studies of Neptunium Metal at Elevated Temperatures, Acta Crystallogr., 5 (1952) 664-667.

[189] B. Sundman, J. Ågren, A regular solution model for phase with several components and sublattices, suitable for computer applications, Journal of Physics and Chemistry in Solids, 42 (1981) 297-301.

[190] E.R. Davidson, Matrix Eigenvector Methods, in: G.H.F. Diercksen, W. S. (Eds.) Methods in Computational Molecular Physics, D. Reidel Publishing Company, Bad Windsheim, West Germany, 1982, pp. 95-113.

[191] M.P. Teter, M.C. Payne, D.C. Allan, Solution of Schrödinger's equation for large systems, Physical Review B, 40 (1989) 12255-12263.

[192] S.K. Sikka, Y.K. Vohra, R. Chidambaram, Omega-Phase in Materials, Prog. Mater Sci., 27 (1982) 245-310.

[193] J. Zhang, Y. Zhao, C. Pantea, J. Qian, L.L. Daemen, P.A. Pigg, R.S. Hixson, C.W. Greeff, G.T.G. Iii, Y. Yang, L. Wang, T. Uchida, Experimental constraints on the phase diagram of elemental zirconium, Journal of Physics and Chemistry of Solids, 66 (2005) 1213-1219.

[194] J.Z. Zhang, Y.S. Zhao, C. Pantea, J. Qian, L.L. Daemen, P.A. Rigg, R.S. Hixson, C.W. Greeff, G.T. Gray, Y.P. Yang, L.P. Wang, Y.B. Wang, T. Uchida, Experimental constraints on the phase diagram of elemental zirconium, J. Phys. Chem. Solids, 66 (2005) 1213-1219.

[195] Y.J. Hao, L. Zhang, X.R. Chen, L.C. Cai, Q. Wu, D. Alfe, Ab initio calculations of the thermodynamics and phase diagram of zirconium, Phys. Rev. B, 78 (2008).

[196] S. Bajaj, C. Sevik, T. Cagin, A. Garay, P.E.A. Turchi, R. Arroyave, On the limitations of the DFT plus U approach to energetics of actinides, Comp. Mater. Sci., 59

(2012) 48-56.

[197] W. Xiong, Y. Du, X. Lu, J.C. Schuster, H. Chen, Reassessment of the Ce-Ni binary system supported by key experiments and ab initio calculations, Intermetallics, 15 (2007) 1401-1408.

[198] C. Zhang, J. Zhu, A. Bengtson, D. Morgan, F. Zhang, W.S. Cao, Y.A. Chang, Modeling of phase stability of the fcc phases in the Ni-Ir-Al system using the cluster/site approximation method coupling with first-principles calculations, Acta Materialia, 56 (2008) 2576-2584.

[199] C. Zhang, J. Zhu, A. Bengtson, D. Morgan, F. Zhang, Y. Yang, Y.A. Chang, Thermodynamic modeling of the Cr-Pt binary system using the cluster/site approximation coupling with first-principles energetics calculation, Acta Materialia, 56 (2008) 5796-5803.

[200] C. Zhang, J. Zhu, D. Morgan, Y. Yang, F. Zhang, W.S. Cao, Y.A. Chang, Thermodynamic modeling of the Cr-Ir binary system using the cluster/site approximation (CSA) coupling with first-principles energetic calculation, Calphad-Computer Coupling of Phase Diagrams and Thermochemistry, 33 (2009) 420-424.

[201] J. Zhu, C. Zhang, W. Cao, Y. Yang, F. Zhang, S. Chen, D. Morgan, Y.A. Chang, Experimental investigation and thermodynamic modeling of the Ni-Al-Ru ternary system, Acta Materialia, 57 (2009) 202-212.

[202] Y. Yang, C. Zhang, S.L. Chen, D. Morgan, Y.A. Chang, First-principles calculation aided thermodynamic modeling of the Mo-Re system, Intermetallics, 18 (2010) 574-581.

[203] P.E.A. Turchi, V. Drchal, J. Kudrnovsky, C. Colinet, L. Kaufman, Z.K. Liu, Application of ab initio and CALPHAD thermodynamics to Mo-Ta-W alloys, Phys. Rev. B, 71 (2005).

[204] B.P. Burton, A. van de Walle, First principles phase diagram calculations for the octahedral-interstitial system HfOX, 0 <= X <= 1/2, Calphad, 37 (2012) 151-157.

[205] X.L. Liu, C.Z. Hargather, Z.K. Liu, First-principles aided thermodynamic modeling of the Nb-Re system, Calphad, 41 (2013) 119-127.

[206] G. Ghosh, A. van de Walle, M. Asta, G.B. Olson, Phase stability of the Hf-Nb system: From first-principles to CALPHAD, Calphad, 26 (2002) 491-511.

[207] P. Villars, K. Cenzual, J. Daams, R. Gladyshevskii, O. Shcherban, V. Dubenskyy,

N. Melnichenko-Koblyuk, O. Pavlyuk, I. Savysyuk, S. Stoyko, L. Sysa, (U0.4Pu0.6), in: P. Villars, K. Cenzual (Eds.) Structure Types, Springer-Verlag Berlin Heidelberg, 2008.

[208] J.L.C. Daams, J.H.N. Vanvucht, P. Villars, Atomic-Environment Classification of the Cubic Intermetallic Structure Types, J. Alloys Compd., 182 (1992) 1-33.

[209] M.P. Teter, M.C. Payne, D.C. Allan, Solution of Schrodinger-Equation for Large Systems, Phys. Rev. B, 40 (1989) 12255-12263.

[210] S.G. Fries, B. Sundman, Using Re-W sigma-phase first-principles results in the Bragg-Williams approximation to calculate finite-temperature thermodynamic properties, Phys. Rev. B, 66 (2002).

[211] D.R. Lide, CRC handbook of chemistry and physics, CRC, Boca Raton, Fla.; London, 2003.

[212] W. Xie, W. Xiong, D. Morgan, CALPHAD modeling and ab initio calculations of the Np-U system, in, 2013.

[213] A. van de Walle, Multicomponent multisublattice alloys, nonconfigurational entropy and other additions to the Alloy Theoretic Automated Toolkit, Calphad, 33 (2009) 266-278.

[214] Y.S. Kim, G.L. Hofman, A.M. Yacout, T.K. Kim, U-Mo alloy fuel for TRU-burning advanced fast reactors, J. Nucl. Mater., 441 (2013) 520-524.

[215] A.R. Oganov, I. Wiley, Modern methods of crystal structure prediction, (2010).

[216] F. Aryasetiawan, O. Gunnarsson, The GW method, Rep Prog Phys, 61 (1998) 237-312.

[217] G. Bozzolo, J. Ferrante, J.R. Smith, Method for Calculating Alloy Energetics, Phys. Rev. B, 45 (1992) 493-496.

[218] G. Bozzolo, H.O. Mosca, A.M. Yacout, G.L. Hofman, Atomistic modeling of the interaction of cladding elements (Fe, Ni, Cr) with U-Zr fuel, J. Nucl. Mater., 414 (2011) 101-108.

[219] B. Beeler, C. Deo, M. Baskes, M. Okuniewski, Atomistic properties of gamma uranium, J. Phys.: Condens. Matter, 24 (2012).

[220] A.P. Moore, B. Beeler, M. Baskes, M. Okuniewski, C.S. Deo, Atomistic Ordering in Body Centered Cubic Uranium-Zirconium Alloy, MRS Online Proceedings Library, 1514 (2013) 27-35.

[221] Y.S. Kim, S.L. Hayes, G.L. Hofman, A.M. Yacout, Modeling of constituent redistribution in U-Pu-Zr metallic fuel, J. Nucl. Mater., 359 (2006) 17-28.

[222] J. Donohue, The structures of the elements, Wiley, New York, 1974.

[223] J. Thewlis, STRUCTURES OF URANIUM, Nature, 168 (1951) 198-199.

[224] A.A. Bochvar, S.T. Konobeevskii, A.S. Zaimovskii, G.I. Sergeev, V.I. Kutaitsev, N.F. Pravdiuk, B.M. Levitskii, Investigation of the metallography of plutonium, uranium and their alloys, The Soviet Journal of Atomic Energy, 5 (1958) 811-829.

[225] P. Chiotti, H. Klepfer, R. White, Lattice Parameters of Uranium from 25 to 1132 C, Trans. Amer. Soc. Metals, 51 (1959) 772-782.